UNIVERSITA' DEGLI STUDI DI PARMA

Dottorato di ricerca in Scienze degli Alimenti

Ciclo XXIX

The CFD technique in food processing: a tool to improve the development of new products and processes

Coordinatore:
Chiar.mo Prof. Furio Brighenti

Tutor:
Chiar.mo Prof. Davide Barbanti

Dottorando:
Matteo Cordioli

A pessima,
mia gioia
mia vita

Introduction

What is Computational Fluid Dynamic?

- Fundamental governing equations
- Discretization techniques
- Numerical solving

Performing CFD analysis with commercial code

- Pre-processing
- Solving
- Post-processing

Aim of the thesis

Study of heat exchange

- Study 1: *Computational Fluid Dynamics (CFD) Modelling and Experimental Validation of Thermal Processing of Canned Fruit Salad in Glass Jar.*
- Study 2: *Investigation and modelling of natural convection and conduction heat exchange: study on food systems with modified starch by means of Computational Fluid Dynamics (CFD).*
- Study 3: *Computational Fluid Dynamics (CFD) techniques to investigate the effects of jar geometry and starch concentration on thermal treatment of food systems.*
- Study 4: *Development and validation of CFD models of thermal treatment on milk whey proteins dispersion in static and continuous process condition.*

Study of fluid motion

- Study 5: *Study and optimization of a CO_2 sparger for carbonated beverages and beer by means of CFD modelling.*
- Study 6: *Development of a geometry with specific wall shear stress characteristics by means of Computational Fluid Dynamics (CFD) techniques.*
- Study 7: *Evaluation of the performances of a plate fine heat exchanger for liquid food with different kinds of vortex generators using CFD methods.*

Short CV and list of publications

Introduction

"Challenges in mathematical modelling […] is not to produce the most comprehensive descriptive model but to produce the simplest possible model that incorporates the major features of the phenomenon of interest"

Howard Emmons

Mathematical modelling is generally understood as the process of applying mathematics to a real-world problem with the aim of understanding the latter and investigating important questions that arise from it. The **Figure 1** shows the key steps in modelling process.

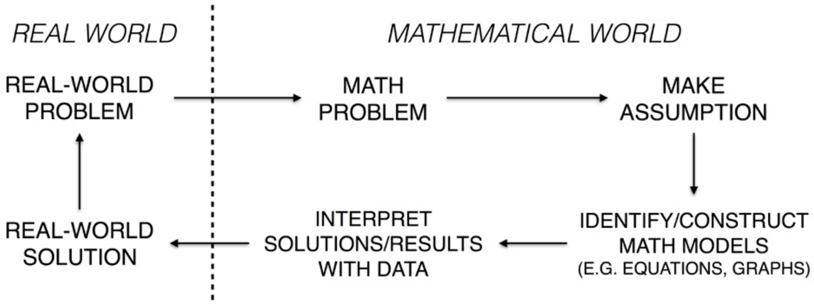

Figure 1 Flow diagram of mathematical modelling process [adapted from *math4theaching*]

The primary aim of a modeller is to undertake experiments on the mathematical representation of a real-world problem, instead of undertaking experiments in the real world. However, the real-world systems are complex and several interrelated components are involved, so a good model must try to incorporate all critical elements and interrelated components. This is not always possible, and the elements left out create model limitation. Significant problems arise when key aspects of the real-world system are inadequately treated in a model or are ignored to avoid complications which may lead to incomplete models.

Starting from these limitations and pitfalls, a good model can be formulated, if a modeller asks himself the following question about the model, as highlighted by Banerjee (2014):

1) Does the structure of the model resemble the system being modelled?
2) Why is the selected model appropriate to use in a given application?
3) How well does the model perform?
4) What assumptions and data were used in producing model output for the specific application?
5) What is the accuracy of the model output?

Moreover, as a rule of thumb the model should not be extrapolated beyond the region of fit. It is important to understand that the model is not the reality and one should not distort reality to fit the models. It is imperative to be aware of the limitations inherent models. Finally, there is no best model, only better models.

After brief introduction about the meaning and powerful of models, in the next paragraph a brief overview about models classification. First, it's possible to divide the models in functions of the type of outcome they predict. *Deterministic models* ignore random variation, and so always predict the same outcome from a given starting point. On the other hand, the *stochastic models* predict the distribution of possible outcomes, considering the statistical component present in nature. A second method of distinguishing between types of models is to consider the level of understanding on which the model is based. *Mechanistic models* use a large amount of theoretical information and generally describes what happens at one level in the hierarchy by considering process at lower levels. While, in the *empirical models*, no account is taken of the mechanism by which changes to the system occur: its merely noted that they do occur, and the model tries to account quantitatively for changes associated with different conditions. The four categories above explained represent extremes of a range of model types: between them a whole spectrum of model types can be identify. Furthermore, the two methods of classification (deterministic/stochastic and mechanistic/empirical) are complementary. For example, a deterministic model may be either mechanistic or empirical (but not stochastic).

As introduced in the previous pages, the purpose of a mathematical model is to capture relevant features of a complex object or process, based on existing theoretical understanding of the phenomena and available measurements. Complexity of modelling is not obvious. Often for simple studies, simple models are sufficient. However, modelling of food products and food processes is a complicated task due to the lack of knowledge concerning mechanisms, the difficulty to performing experimentation and obtaining numerous reliable data and the uncertainties concerning food properties (Trystram, 2012).

The modelling and simulation research should be directed towards main phenomenological aspects, whose main are heat, mass and momentum which take place in almost all unit operations in food processing (e.g. sterilization, drying, baking). In applying momentum, heat, and mass transfer on food processing, one must consider that food industry usually deals with difficult raw materials. As biological materials, in many cases they are of non-uniform and variable consistency, with no-homogenous and isotropic behaviour. The shape of the products is often irregular and sometimes changes during the processing. Moreover, almost all food undergo physical properties changes during processing (e.g. conductivity, viscosity and density). Also from the process point of view there are many variables to take into consideration. In many cases, the processing results depend on the combination of time and temperature because, in addition to temperature changes, biochemical and microbiological changes take place during processing. As consequence, heat transfer and reaction kinetics considerations must be considered in designing thermal processes of foods.

Because of these complexities, the unsteady state momentum, heat and mass transfer partial differential equations can be solved analytically only with several simplifying assumptions. To solve complex systems its necessary to shift toward numerical methods, which offer an efficient and powerful tool for simulating and comprehending transport processes in the food industry. The main difference between analytical and numerical solutions of mathematical modelling is that with the first the result is a univocal solution while with the second the result comes from a process of approximation. The numerical solutions can never have the same generality as analytical solutions but can give good results in any instance, also the more complex. Despite the differences between the various numerical methods, the starting point is always a set of different equations: the Navier-Stokes equations coupled with the energy and mass transfer equations for predicting momentum, heat and mass transfer. At these base equations may be added other models, such kinetic model, in function of the phenomena taken into account (Yanniotis and Stoforos, 2014).

Nowadays, a powerful tool for the numerical solution of the equations governing the flow of fluids often coupled with the energy and mass transfer equations and other equations, as stated above, is Computational Fluid Dynamics (CFD). This technique results in rapid progression due to the development of advanced computer design and analysis tools, like CFD software, as the tackle complex problems in fluid mechanics and heat transfer, and many other physical processes with important industrial applications. Since the first computer implementation of CFD in the 1950s, it has continued to be developed contemporaneously with the digital computer (Norton and Sun, 2006). Moreover, the application of CFD has been both inevitable and progressive through the years, as the high costs and time consumption associated with experimentation has often precluded the desire to produce efficient and in-depth results (Norton and Sun, 2006).

Nowadays, CFD programs are the standard numerical tools which predict not only fluid flow behaviour, but also the heat and mass transfer, phase change (such as freezing or boiling), chemical reaction (such as combustion), mechanical movement and stress or deformation of solid. This wide range of applications permit to apply CFD techniques to a variety of industrial field, generating billions of Euros worldwide within a vast range of specialization (Xia and Sun, 2002). General applications of CFD in the food industry have also been reviewed by some

Authors (Norton and Sun, 2006; Scott and Richardson, 1997; Xia and Sun, 2002). These reviews have concluded that CFD is a powerful and pervasive tool for process and product improvement in food processing industry. Some of the many fascinating subjects in which CFD has been applied include baking (Chhanwal et al., 2011), thermal sterilization (Abdul Ghani et al., 1999), pasteurization (Kiziltals et al., 2010), mixing (Metcalfe and Lester, 2009), refrigeration (Moureh et al., 2009), spray-freeze drying (Kuriakose and Anandharamakrishnan, 2010), fluidized drying (Markowski et al., 2010), cleaning process (Jensen et al., 2005), protein denaturation (Bouvier et al., 2014), phase change (Lian et al., 2006) and bottle rinsing (Meister et al., 2012).

CFD techniques have led to an improvement in both quality and safety alongside reducing energy consumption used in industrial processes, and has reduced the amount of empiricism associated with a design process (Norton and Sun, 2006). Moreover, it is undisputed that CFD will continue to provide explanations for more fluid flow, heat and mass transfer phenomenon, leading to a better understanding of physical and chemical phenomena at the base of food transformations.

References

Abdul Ghani, A. G., Farid, M. M., Chen, X. D. & Richards, P., (1999). Numerical Simulation of Natural Convection Heating of Canned Food by Computational Fluid Dynamics. *Journal of Food Engineering*, 41(1), 55–64.

Banerjee, S., (2014). *Mathematical modeling: models, analysis and applications*. CRC Press. Boca Raton (FL).

Bouvier, L., Moreaua, A., Ronse, G., Six, T., Petit, J. & Delaplace, G., (2014). A CFD Model as a Tool to Simulate Beta-Lactoglobulin Heat-Induced Denaturation and Aggregation in a Plate Heat Exchanger. *Journal of Food Engineering*, 136, 56–63.

Chhanwal, N., Indrani, D., Raghavarao, K. S. M. S. & Anandharamakrishnan, C., (2011). Computational Fluid Dynamics Modeling of Bread Baking Process. *Food Research International*, 44(4), 978–983.

Glen, M., & Lawson, D., (2008). *An introduction to mathematical modelling*. Biomathematics and Statistics Scotland. Edinburgh (UK).

http://math4teaching.com/2011/04/16/what-is-mathematical-modeling/

Jensen, B. B. B., Friis, A., Bénézech, Th., Legentilhomme, P. & Lelièvre, C., (2005). Local Wall Shear Stress Variations Predicted by Computational Fluid Dynamics for Hygienic Design. *Food and Bioproducts Processing*, 83(1), 53–60.

Kiziltals, S., Erdogdu, F. & Palazoglu, T. K., (2010). Simulation of Heat Transfer for Solid-Liquid Food Mixtures in Cans and Model Validation under Pasteurization Conditions. *Journal of Food Engineering*, 97(4), 449–456.

Kuriakose, R. & Anandharamakrishnan, C., (2010). Computational Fluid Dynamics (CFD) Applications in Spray Drying of Food Products. *Trends in Food Science & Technology*, 21(8), 383–398.

Lian, G., Moore, S. & Heeney, L., (2006). Population Balance and Computational Fluid Dynamics Modelling of Ice Crystallisation in a Scraped Surface Freezer. *Chemical Engineering Science*, 61(23), 7819–7826.

Markowski, M., Białobrzewski, I. & Modrzewska, A., (2010). Kinetics of Spouted-Bed Drying of Barley: Diffusivities for Sphere and Ellipsoid. *Journal of Food Engineering*, 96(3), 380–387.

Meister, C., Velten, K. & Methner, F. J., (2012). Modelling and Simulation of Bottle Rinsing. *International Journal of Food Science and Technology*, 47(7), 1468–1478.

Metcalfe, G. & Lester, D., (2009). Mixing and Heat Transfer of Highly Viscous Food Products with a Continuous Chaotic Duct Flow. *Journal of Food Engineering*, 95(1), 21–29.

Moureh, J., Tapsoba, S., Derens, E. & Flick, D., (2009). Air Velocity Characteristics within Vented Pallets Loaded in a Refrigerated Vehicle with and without Air Ducts. *International Journal of Refrigeration*, 32(2), 220–234.

Norton, T. & Sun, D.W., (2006). Computational Fluid Dynamics (CFD) – an Effective and Efficient Design and Analysis Tool for the Food Industry: A Review. *Trends in Food Science & Technology*, 17(11), 600–620.

Scott, G. & Richardson, P., (1997). The Application of Computational Fluid Dynamics in the Food Industry. *Trends in Food Science & Technology*, 8(4), 119–124.

Trystram, G., (2012). Modelling of Food and Food Processes. *Journal of Food Engineering*, 110(2), 269–277.

Xia, B. & Sun, D.W., (2002). Applications of Computational Fluid Dynamics (CFD) in the Food Industry: A Review. *Computers and Electronics in Agriculture*, 34(1–3), 5–24.

Yanniotis, S. & Stoforos, N. G., (2014). Modelling Food Processing Operations with Computational Fluid Dynamics: A Review. *Scientia Agriculturae Bohemica*, 45(1), 1–10.

What is Computational Fluid Dynamics?

1. *Fundamental governing equations*

The Computational Fluid Dynamics codes are developed around numerical algorithms that solve the nonlinear partial differential equations governing all fluid flow, heat transfer, and associated phenomena. These equations can be considered as mathematical formulations of the conservation laws of fluid mechanics. When applied to a fluid continuum, these conservation laws relate the rate of change of a desired fluid property to external forces and if these laws are imposing over a discrete spatial region in the flow domain, it is possible to achieve a systematic account of the change in mass, momentum and energy as the fluid crosses the region boundaries.

The three conservation laws and the related equations, named Navier-Stokes equations, can be summarized as follow:

a) <u>*Conservation of mass*</u> (continuity equation), which states that the mass flow entering a fluid element must balance exactly with the flow leaving it. Mathematically result:

$$\frac{\partial \rho}{\partial t} + \frac{\partial \rho}{\partial t}\left(\rho u_j\right) = 0$$

b) <u>*Conservation of momentum*</u> (Newton's second law of motion), which states that the sum of the external forces acting on the fluid particle is equal to its rate of change of linear momentum. Can be expressed as:

$$\frac{\partial \rho}{\partial t}(\rho u_i) + \frac{\partial}{\partial x_j}\left(\rho u_i u_j\right) = \frac{\partial}{\partial x_j}\left[-p\delta_{ij} + \mu\left(\frac{\partial u_i}{\partial x_j} + \frac{\partial u_j}{\partial x_i}\right)\right] + \rho g_i$$

c) <u>*Conservation of energy*</u> (first law of thermodynamics), which states that the rate of change of energy of a fluid particle is equal to the heat addition and the work done on the particle. Resulting in:

$$\frac{\partial}{\partial t}(\rho C_a T) + \frac{\partial}{\partial x_j}\left(\rho u_j C_a T\right) - \frac{\partial}{\partial x_j}\left(\lambda \frac{\partial T}{\partial x_j}\right) = s_T$$

where t is time (s), ρ is density (kg m^{-3}), u is velocity component (m s^{-1}), g acceleration due to gravity (9.81 m s^{-2}), x, y, z cartesian coordinates (m), T temperature (K), C_a specific heat capacity (W kg^{-1} K^{-1}), s_T thermal sink or source (W m^{-3}), λ thermal conductivity (W m^{-1} K^{-1}). Starting from these equations some clarifications need to be made. The density variations in the flow domain, caused by the buoyancy can be model in different ways. One of the main algorithm considered to estimate this value is the Boussinesq approximation which assume that the density differential in the flow are only required in the momentum equation. Mathematically can be expressed as:

$$\rho = \rho_{ref}\left[1 - \beta\left(T - T_{ref}\right)\right]$$

Where β is thermal expansion coefficient (K^{-1}).

However, the Navier-Stokes equations in the form above mentioned have a limited amount of applications in the food process due to the oversimplified assumption. As consequence, additional models, which mainly influence the dynamics of a system, must be considered. In simple terms, the governing equations may need to be fortified with additional approximations or physical models to fully represent the modelled flow regime. Some of these supplementary models needed in food processing include turbulence estimation, multiphase systems, porous media and non-Newtonian flow behaviour. However, this is not the place to deepen these models because the aim of this section was only to introduce the basic equations of CFD techniques.

2. *Discretization techniques*

As assessed in the previous paragraph, the Navier-Stokes equations are solved over a discrete spatial volume. Thus, the first step toward obtaining a numerical solution involves the discretization of the geometric domain and conversion of the governing equations into a system of algebraic equations. As consequence, the discretization process results of great importance to guarantee accurate and precise numerical results. Of the many existing techniques, the most important include finite difference, finite elements and finite volumes. The first one are of limited use in many problems due to the difficulties to handling complex geometries. Regard the finite element technique, only few commercial packages exist, due to the difficulties involved in the programming and implementation of these techniques. With the finite volume technique, these difficulties can be overcome.

Finite difference

In this technique, at each nodal point of the grid used to describe the fluid-flow domain, the Taylor series expansions are used to generate finite-difference approximations to the partial derivatives of the governing equations. These derivatives, replaced by finite-difference approximations, yield and algebraic equation for the flow solution at each grid point. The finite-difference discretization can be applied to any type of grid system. However, the method is applied to structure grids since it requires a mesh having a high degree of regularity (there are limitation on the amount of grid stretching or distortion that can be imposed to maintain accuracy).

Finite volume method

The finite-volume method discretizes the integral form of the conservation equations directly in the physical space. In this technique, the domain is divided into a finite number of contiguous control volumes, and at centroid of each volume, the variable values are calculated. Interpolation is used to express variable values at the control volume surface and suitable quadrature formulae are applied to approximate the surface and volume integrals. Since the finite-volume method works with control volumes and not the grid intersection points, it has the capacity to accommodate any type of grid. Hence, instead of structured grids, unstructured grids can be employed that allow many options for the definition of the shape and location of the control volumes. From this, the possibility to combine triangles and quadrilaterals mesh in the case of two dimensions or tetrahedral and hexahedra in three dimensions. This type of unstructured mesh offers greater flexibility for handling complex geometries.

3. *Numerical solving*

Through the discretization process it's possible to obtain, starting form governing equations, a system of linear or nonlinear algebraic equations that needs to be solved by some numerical methods. The size and complexity of this equations depends on the dimensionality and geometry of the physical problem. Regardless the type of equations, efficient and robust methods to solve them are required. Today two kinds of numerical methods are available: direct methods and iterative methods. The direct method can permit to solve only simple problems, so in this paragraph only the iterative method is taken into consideration. In an iterative method, one guesses the solution, and used the equation to systematically improve the solution until it reaches some level of convergence. The accuracy of solution depends on the targeted number of significant figures you wish to obtain for each single variable. The smaller the acceptable error, the higher the number of iterations, but this will achieve greater accuracy. Moreover, more accurate solutions can be obtained through refining the grid and for an unsteady problem by employing smaller time intervals.

In most commercial CFD codes, the system of algebraic equations is usually solved iteratively and three important aspects must be respect for iterative convergence. First, all the discretized equations (mass, momentum, energy, etc.) are deemed to be converged when they reach a specified tolerance at every nodal location. Second, the numerical solution non-longer changes with additional iterations. Third, overall mass, momentum, energy and scalar balances are obtained. During the numerical procedure, the imbalances of the discretized equations are monitored and these defects are commonly referred as “residuals”. For satisfactory convergence, the residuals should diminish as the numerical process progresses. In the likelihood that the imbalances grow, as reflected by increasing residual values, the numerical solution is thus classified as being unstable (divergent).

References

Sun, D.W., (2007). *Computational Fluid Dynamics in Food Processing*. CRC, Boca Raton.

Tu, J., Yeoh, G.H. & Liu, C., (2008). *Computational Fluid Dynamics: A Practical Approach*. Elsevier.

Performing CFD analysis with commercial code

A CFD study can be divided into three different software environments, closely connected each other, representing an equally important section of the modelling process. The first environment, known as *pre-processor*, embodies the most important phase of model definition. The success of simulation relies upon the modelling constraints and conditions input by the user via mathematical statements to the processor. The second environment, i.e. the *solver*, takes these mathematical statements, structures them into a solvable arrangement, and solve for the specified boundary conditions by iterative methods. Finally, the third environment, the *post-processor*, is employed to visualize the solution obtained.

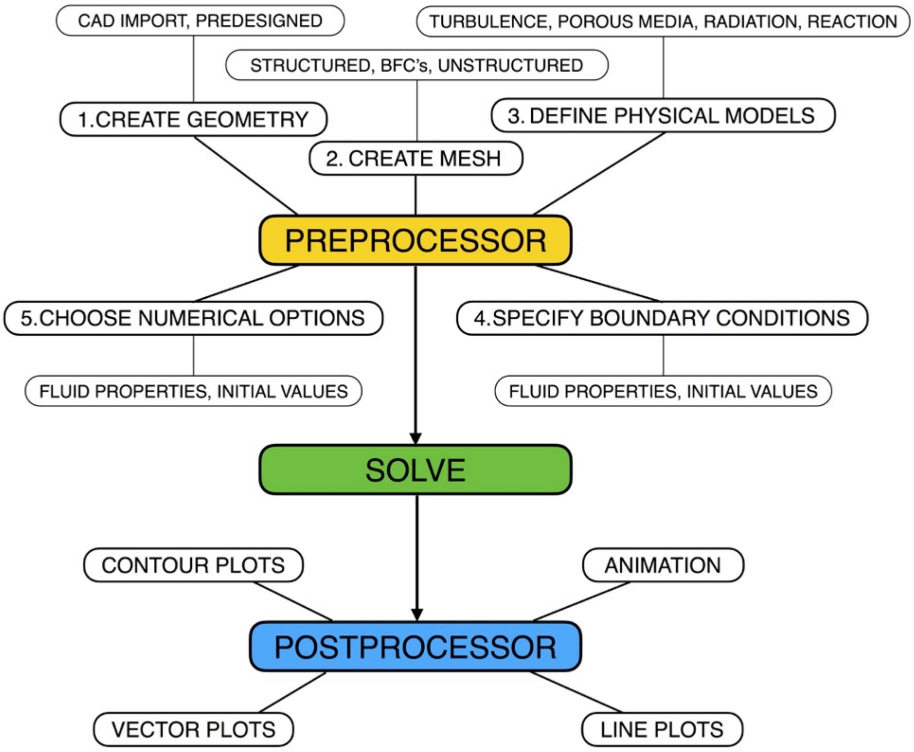

Figure 2 Flow diagram of CFD analysis.
[*adapted from Sun (2007)*]

1. *Pre-processing*

The pre-processor of CFD software holds all the raw data and mathematical statements attributable to the potential success of a modelling exercise. The main task facing a user in the pre-processing environment include problem consideration, geometry creation or import, mesh development, physical property set-up, and numerical implementation.

Problem identification

The first step in a CFD study is to consider the physics of the problem taken into consideration. In doing this, the user determines the physical processes that can be accurately represented in a

CFD model and expound suitable mathematical strategies to determine the desired variables. In this phase, it's important to highlight what are the results you are looking for, the degree of accuracy required and closely connected with this how quickly you need the results. From these consideration result evident the importance to known the phenomena involved in the studied process to avoid misleading results.

Domain creation and mesh development

The second stage in model development is geometry design and mesh specification. Usually the geometry is defined by importing it from any standard CAD program. This stage results of great importance to reduce the time of calculation in model development. The identification of domain of interest must be conducted with attention to comprise all phenomena involved in the studied system. Typically, the domain boundaries were chosen in function of the availability of information in these regions (e.g. experimental measurements). Moreover, in this phase some geometric approximation can be introduced, such as the application of symmetry plans or the shift from 3D to 2D geometry to reduce the time of calculation.

CFD requires the subdivision of the domain into a number of smaller, non-overlapping subdomains in order to solve the flow physics within the domain geometry that has been previously created. This results in the generation of a mesh (or grid) of cells (elements or control volumes) overlaying the whole domain of interest. As described in ***Introduction***, the equations describing physical phenomena are solved numerically in each of these cells and the discrete values of the flow properties such as the velocity, pressure, temperature and other parameters of interest are determined. This gave the CFD solution of the problem considered, therefore the accuracy of solutions is governed by the number of cells within the computational domain. In general, the provision of a large number of cells leads to the attainment of an accurate solution. Usually, the mesh definition stage consists of object-orientated automatic grid generator, that allows mesh to be defined around the modelled geometry. However, in a lot of case (e.g. when the geometry is complex or domain composed by different sub-domains) a large amount of effort by the user is required to obtain a good quality of mesh, which results a compromise between the desired accuracy and solution cost.

For relatively simple geometries, an overlay mesh of structured cells that generally comprises a regular distribution of rectangular (for 2D domain)/hexahedral (for 3D domain) cells can be readily realized. For more complex geometries, the meshing by triangular (for 2D domain)/tetrahedral (for 3D domain) cells allows the flexibility of mesh generation for geometries having complicated shape boundaries. It is also not uncommon and in some practices a requirement to embrace a combination of structured and unstructured meshes (named hybrid meshes) for more realistic simulations within flow domains that may include many inherent complex geometrical intricacies. In the last years, new cells geometries were taken into consideration to fill the domain of interest. The application of this cells, named polyhedral, is still in its infancy. Nevertheless, polyhedral meshing has shown thus far to have many advantages over tetrahedral meshing regard the accuracy and efficiency of the numerical computations.

The grid quality of generated mesh depends mainly on the cell shape and can be evaluate by different parameters, the main relevant are aspect ratio and skewness. The grid aspect ratio of the cell can be defined as the ratio between the length of the longest and the shortest edge of the cell. Starting from the ideal value of 1 (for equilateral triangle or square in 2D and cube or tetrahedron in 3D geometries), it is recommended that aspect ratio is maintained within the range of 0.2 and 5. It's important to avoid large aspect ratio mainly in important regions of domain, as they can degrade the solution accuracy and may result in possible poor iterative convergence (or divergence) during the numerical computations. The next aspect concerning the cell shape deals with grid distortion or skewness, which relates to the angle between the grid lines. It's desirable that the angle between the grid lines results approximately of 90°. If the cells angle results lower than 45° or higher than 135°, the mesh can often exhibit a deterioration of the computational results or leads to numerical instabilities.

Finally, it is desirable that a grid independent study is performed to analyse the suitability of the mesh number and to yield an estimate of the numerical errors in the simulation. In simple terms with grid independent analysis it is satisfied that the solution results independent from the mesh resolution. Practically, this evaluation was carried out by solving the model with an increasing number of mesh until the solution result doesn't change.

Define the physical properties of the domain

The third step in pre-processing stage is to define the physical models and to set up the physical properties. This phase of pre-processing requires both knowledge regarding the initial status of the model and a preconception of the potential solution. First is necessary to define if the properties of the system and the boundary conditions change with the time. If doesn't change with the time the analysis was time independent and simulation was at steady state, otherwise if conditions change with the time, the analysis became time dependent and simulation became transient. In the case of transient simulation, it's necessary to define also the time interval (or time steps) in which the solver solve the governing equations. This setting is important as the definition of mesh dimension because if the time step is too large the data obtained may be far from the real solution, while if time step is too small the time of calculation becomes infinite. Usually the time step is choosing as function of the gradient of variation of different variable considered in the model. Furthermore, different dimensionless parameters (e.g. Courant number) have been developed over the years to calculate the correct time step.

Once defined this characteristic the next step is to select the state of matter (solid or liquid) that compose the domain or subdomains (if are more than one) and the physical and thermal properties of each. As example, regard fluid domain density and dynamic viscosity must be defined, while for problems with heat transfer, additional specification of the thermal properties such as thermal conductivity and specific heat is required.

Define the boundary conditions

The fourth step in the pre-process stage deals with the specification of permissible boundary conditions. As example, where there exist inflow and outflow boundaries within the domain, suitable fluid flow boundary conditions are required to accommodate the fluid to enter and leave the flow domain. Appropriate boundary conditions are also required to be assigned for external stationary solid wall boundaries.

Furthermore, to take advantage of special geometrical features that the solution region may possess, symmetric and cyclic boundary conditions can be employed to speed up the computations and enhance the computational accuracy by placing an additional number of cells at the simplified geometry.

2. Solving

The solver environment within CFD software organizes the mathematical input from the pre-processor into numerical arrays and solves them by an iterative method. A CFD user, whether applying in-house or commercial codes regard the solution step needs to gain the necessary insights pertaining initialization, solution control, monitoring solution, CFD calculation and checking for convergence. The knowledge of these processes permit to better navigate the “black box” operations that reside in the solution code. The solution procedure can be described as reported in **Figure 3**.

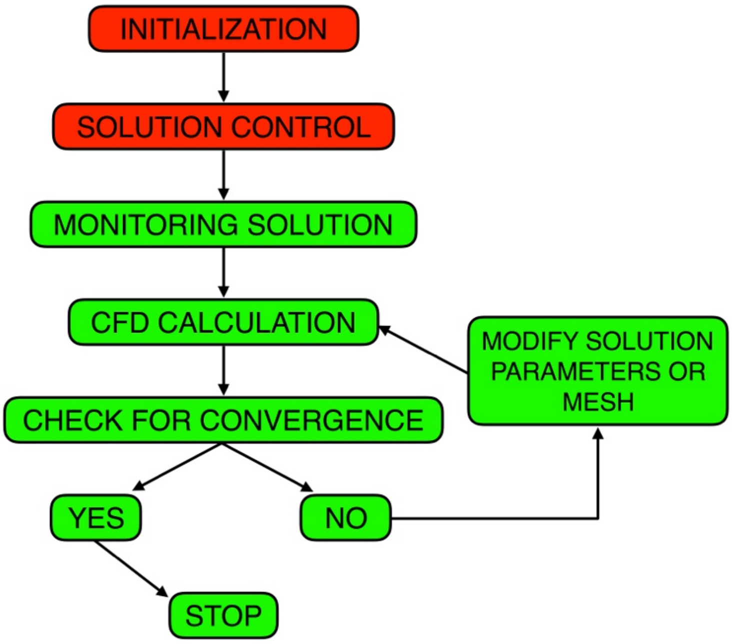

Figure 3 Flow diagram of solution process
[*adapted from Tu et al., (2008)*]

Initialization and solution control

Iterative procedure generally involves all the discrete values of the flow properties and other transport parameters of interest to be initialized before calculating a solution. In theory, initial conditions can be purely arbitrary. However, in practice, there are many advantages to impose initial conditions intelligently. Good initial conditions are crucial to the iterative procedure because if these are closed to the final steady-state solution the equations will converge quicker and the computational time results shorter. Conversely if the initial conditions result far from reality, the computational efforts increase. Moreover, improper values may lead to the iterative procedure misbehaving and possibly “blowing-up” or diverging.

The same importance has the choice of appropriate parameters in the solution control, in particular the specification of appropriate discretization (interpolation) schemes and selection of suitable iterative solvers. As saw in the previous chapter, most of commercial code adopt the finite volume method as their standard numerical solution technique. The algebraic forms of the fluid governing equations are approximated by the application of finite volume cell in space. At each face of the cell volume, surface fluxes of the transport variable can be determined through different interpolation schemes. The common schemes available are: First-Order Upwind, Second-Order Upwind, Second-Order Central and Quadratic Upstream Interpolation Convective Kinetics (QUICK). Another example of a discretization method used in CFD is the segregated solver, semi-implicit method for pressure-linked equations (SIMPLE), and its descendants, which have now become traditional techniques employed by many commercial packages to solve the discretized general equations. Once defined the interpolation scheme, iterative solvers, so-called number crunching engines for numerical calculations, are employed to resolve the algebraic equations. The simplest method from the various classes of iterative methods is the Jacobi method and the direct improvement named Gauss-Siedel method. In this method the iteration process stop when the maximum difference between variable values at two iteration fall below some predetermined value of acceptable error. The smaller the acceptable error, the more accurate the solution will be but it is noted that this is achieved with a more number of iterations.

Monitoring convergence

This step in the solving phase can be dived into three process: monitoring solution, CFD calculation and checking for convergence. Convergence can usually be assessed by progressively tracking the imbalances that are accentuated by the advancement of the numerical calculations of the algebraic equations through each iteration step. These imbalances measure the overall conservation of the flow properties and are commonly known as residuals. If these values increase along the iterative process the solutions diverge, while if the residual tend to move downward along the process the solutions converge. A converged solution is achieved when the residual fall below some converge criteria set by CFD user. Besides examining the residuals, it is important to follow the trend of variables considered (e.g. temperature, flow rate, pressure) to ascertain the convergence of the numerical computations. In addition to monitoring residual and variable histories, it is good practice to check also the overall mass and heat balance for the fluid flow. The net imbalance should be minimized as low as possible to ensure adequate property conservation.

3. Post-processing

The Post-process environment allows the user to visualize and scrutinize the resulting field solution. The ability to present the computational results effectively is an invaluable design tool. There are many ways to show the data obtained from solving phase, each of this can assist the CFD user to better analyse and visualize the relevant physical characteristics within the problem analysed. Probably, thanks to the commercial software, the ways to shown the results are endless. The focus of the next paragraph was on the most used tools, such as X-Y plots, vector plots, contour plots, animation and data report output. Along the years the interpretation step is progressively fortified in commercial software packages to reduce the effort of CFD users in the data interpretation.

X-Y plots

These plots are mainly two-dimensional graphs that represent the variation of one dependent transport variable against independent one. These graphs are therefore a popular way of directly comparing the numerical data with the experimental measured values. They are usually meant to be very easily identifiable: the reader can read the results without resorting to any mental or arithmetic interpolation.

Vector plots

A vector plot provides the means whereby a vector quantity is displayed at discrete points (e.g. vector with arrows) whose orientation indicates direction and whose size (or colour) indicates magnitude. It generally presents a perspective view of the flow field in two dimensions.

Contour plots

In CFD, contour plots are one of the most commonly found graphic representations of data. A contour line (also known as isoline) can be described as a line indicative of some property that is constant in space (the equivalent in three dimensions is isosurface). In contrast to X-Y plots, contours plots like vector plots provide a global description of the fluid flow in one view. Therefore, contour plots is not employed for precision evaluation of the numerical values but to give an overview of the phenomenon considered.

Animation

Animation represent not only a technical record of quantitative results, it is also an artistic work of art. Some examples that animation has assisted in enhancing the physical representation of the fluid flow processes are the movement of particles with the fluid in multiphase flows, moving geometries such as mixing tanks and heat propagation during thermal treatment. It is undoubtedly an effective visualization tool also for marketing purposes.

Data report output

It is generally impractical to view the raw data of a CFD simulation especially on a mesh that may entail thousands or millions of grid points. However, other alphanumeric reporting approaches can be adopted. Such reports may be helpful to qualitatively check the numerical solution or, of greater interest, to extract the quantitative results for post analysis purpose (such as experimentally validation of the process). Data of several pertinent transport variables can be tracked and dumped into format/unformatted files to adequately describe the time-development response of the fluid flow process.

References

Sun, D.W., (2007). *Computational Fluid Dynamics in Food Processing*. CRC, Boca Raton.

Tu, J., Yeoh, G.H. & Liu, C., (2008). *Computational Fluid Dynamics: A Practical Approach*. Elsevier.

Aim of the thesis

The aim of this PhD thesis was to improve the knowledge of the Computational Fluid Dynamics techniques applied to complex systems such as foods.

The work was composed by a series of experiences involving the applications of CFD in different food processing. The objective was to demonstrate how this technique can improve the development of new products and processes, reducing the time consumption and cost, and improving a better understanding of physical phenomena at the base of the food processing.

The work can be divided into two main sections, representing two physical fields of application of CFD techniques.

Study of heat exchange

In this section the core was the heat treatment such as sterilization and pasteurization, in batch (for example the treatment of food in cans or jars) and in continuous conditions. This theme can be divided into two subtopics: heat treatments after and before packaging. Regarding the first one, three experience were carried out: study of the heat exchange in liquid-solid system (Cordioli et al., 2015); systems where the heat exchange vary from convection to conduction along the thermal treatment itself (Cordioli et al., 2016); and evaluation, on convection/conduction systems, of the effect of different jar geometry (paper to be submitted). About the bulk thermal treatment, a comparative study was carried out on the denaturation/aggregation of whey protein solutions in continuo and static conditions (paper submitted to publishing).

Study of fluid motion

The aim of this part was the study of the fluid motion inside the processing plant. For this topic, three experiences were carried out. The first one concerns the study and optimization of a mixing system for carbonated beverages (Rinaldi et al., 2016). The aim of the second experience was to develop a plant geometry suited to obtain specific values of wall shear stress on fluid/wall interfaces (paper to be submitted). Finally, the last one was a theoretically study to evaluate the performance of a plate-fin heat exchanger with different kinds of vortex generators (paper to be submitted).

References

Cordioli, M., Rinaldi, M., Copelli, G., Casoli, P. & Barbanti, D., (2015). Computational Fluid Dynamics (CFD) Modelling and Experimental Validation of Thermal Processing of Canned Fruit Salad in Glass Jar. *Journal of Food Engineering*, 150, 62–69.

Cordioli, M., Rinaldi, M. & Barbanti, D., (2016). Investigation and Modelling of Natural Convection and Conduction Heat Exchange: Study on Food Systems with Modified Starch by Means of Computational Fluid Dynamics. *International Journal of Food Science & Technology*, 51(4), 854-864.

Rinaldi, M., Cordioli, M., Barbanti, D. & Dall'Aglio, M., (2016). Study and optimization of CO_2 sparger for carbonated beverages and beer by means of CFD modelling. *International Journal of Food Engineering*.

Study of heat exchange

Computational Fluid Dynamics (CFD) Modelling and Experimental Validation of Thermal Processing of Canned Fruit Salad in Glass Jar

Matteo Cordioli[1], Massimiliano Rinaldi[1], Gabriele Copelli[2], Paolo Casoli[2] and Davide Barbanti[1]

[1]Department of Food Science, University of Parma, Parco Area delle Scienze 47/A, 43124 Parma, Italy
[2]Department of Industrial Engineering, University of Parma, Parco Area delle Scienze 181/A, 43124 Parma, Italy

Published in *Journal of Food Engineering*
DOI:10.1016/j.jfoodeng.2014.11.003

Abstract

In this paper the heat transfer of a fruit salad during the pasteurization treatment was investigated. The objective of the paper was to develop and validate a computational fluid dynamics (CFD) model for predicting the temperature profiles during the thermal processing of this sample. Samples of a commercial fruit salad, composed of five different fruits with different shapes, sizes and thermal properties, submerged in water/sugar syrup, were submitted to thermal treatments in a pilot plant and temperature profiles at different locations were experimentally recorded. Results showed that the slowest heating point (SHP) was positioned at 19-20% of the can height: fruit closest to the SHP such as pear presented the lowest *F value.* Moreover, *F values* resulted to be influenced by the distance from the jar bottom as function of natural convection motion of the syrup. CFD model simulations data were then successfully validated against the experimental ones: results, expressed as RMSE, showed a good fitting between calculated and experimental data, both for syrup (mean RMSE 1.47 °C) and fruit pieces (mean RMSE 1.63°C). In addition, *F values* calculated from both experimental and simulated temperatures resulted very similar with only little differences. In conclusion, the proposed approach and mathematical model can thus be usefully applied for the simulation and prediction of thermal processes of canned fruit salad for process design and optimization.

Keywords: CFD, Thermal processing, Canned fruit salad, Natural convection, Conduction.

1. *Introduction*

In the food industry, a great number of fruits and vegetables are packaged in cans or jars, filled with an appropriate sugar syrup or brine, and thermally processed in order to increase their shelf life through the inactivation of both spoilage microorganisms and enzymes (Kiziltas et al., 2010).

Heat transfer mechanisms in canned food are conduction for solid and high viscosity liquid foods, natural convection for low viscosity liquid foods, convection plus conduction for liquid foods with solid particles and convection followed by conduction for liquid foods containing starch or viscosity modifiers (Chen and Ramaswamy, 2007).

Moreover, it is widely known that quality as well as nutritional characteristics of foods can be dramatically reduced by the thermal stabilisation processes. Hence, time and temperature combination during the heating and the cooling cycles must be properly assessed to guarantee both effectiveness (inactivation of microorganisms and enzymes) and efficiency (retention of sensory and nutritional characteristics as well as limiting of costs). As a consequence, the thermal process must be properly designed by studying the thermal properties of foods and the mechanism of heat transfer during the treatment. These purposes are normally achieved by a relevant number of experimental trials with an increase in costs and time consumption thus reducing the possibility to have fast, efficient and in-depth results (Sun, 2007).

In order to overcome these limits, in the last years, process design in the food industry has been increasingly carried out by using numerical solutions of process governing equations, modelling and calculation methods (Weng, 2005).

Among these, Computational Fluid Dynamics (CFD), has found widespread application in many areas of food processing such as spray drying, baking, sterilization, heat exchangers design, chilling, mixing, fermentation and in the agri-food industry (Sun, 2007).

CFD is a simulation tool which uses powerful computers and applied mathematics to model fluid flow situations for the prediction of heat, mass, momentum transfer and optimal design in industrial processes (Anandharamakrishnan, 2011; Chhanwal et al., 2012; Kuriakose and Anandharamakrishnan, 2010; Xia and Sun, 2002). Several works deal with CFD simulations of canned foods: Kumar et al. (1990) simulated the natural convection in canned thick viscous liquid foods; Ghani et al. (1999, 2002) studied the natural convection heating of canned foods in vertical and horizontal positions, showing faster heating in the vertical can, which is expected due to the enhancement of natural convection caused by its greater height. The effect of the inclination of container walls and geometry modification on the sterilization process was also investigated by Varma and Kannan (2005).

A few works have been published on the CFD simulation studies of canned foods with solid/liquid mixture. These include heat transfer and liquid flow prediction during the sterilization of large particles in a cylindrical vertical can (Rabiey et al., 2007) and the heat transfer in canned peas under pasteurization (Kiziltas et al., 2010). Ghani and Farid (2006) analysed and successfully modelled the thermal sterilization process of canned solid-liquid food mixture (pineapple slices with governing liquid) in metal cans, indicating that natural convection effects in the liquid played a significant role in the evolution of temperature. In the same way, Dimous and Yanniotis (2011) studied the temperature profile, the velocity profile and the slowest heating zone in a still can filled with food items with cylindrical-conical shape such as asparagus. With regard to pineapples, Padmavati and Anandharamakrishnan (2013) investigated the effect of size reduction of the product (pineapple slices vs. tidbits) on the effectiveness of heat transfer during thermal processing.

However, the scientific literature still lacks a comprehensive simulation study for the prediction of temperature changes of solid-liquid mixtures where solids with different shapes and thermal characteristics are dispersed in the liquid phase.

In this paper, samples of commercial fruit salad (composed of five different fruits with various geometries and thermal properties) were canned in glass jars and submitted to heat treatment. The objectives of this work were (i) to study the temperature distribution and the thermal behaviour of both fruit pieces and syrup during the process and (ii) to develop and experimentally validate a computational fluid dynamics (CFD) model of the process itself.

2. *Materials and Methods*

2.1. Plant and process details

The thermal treatment of fruit salad and sugar syrup in glass jar was studied taking into consideration only the heating phase of the thermal process as commercial sterility is generally achieved at the end of this stage. Tests were carried out in a small scale static pasteuriser (JBT FoodTech, Parma, Italy), controlled by PLC. Inside the pasteuriser (width = 550 mm; length = 730 mm) water was sprayed over the containers from two nozzles at a rate of 2800 $l\ h^{-1}$ with a spread angle of 120°. Hot water temperature was set at 93°C and samples were heated from 22 to 85°C at the slowest heating point (SHP). The water was heated and cooled through a "tube in tube" heat exchanger where the heating and cooling media were water vapour and icy water, respectively. The jar was positioned at the centre of the pasteuriser between the nozzles and was surrounded with other jars (filled with the same product) hence reproducing as better as possible the operating conditions of the actual industrial process.

During preliminary trials, no temperature variations were observed among jars placed in various positions of the plant and also along the circumpherence of a single jar. This was due to the high water flow and to the nozzles with high spreads angle, allowing homogeneous temperature distribution inside the pasteurizer.

Three repeated thermal treatments were performed on three different jars in order to evaluate the average temperatures and standard deviations of syrup and fruit pieces, as described below (*paragraph 2.3*). The overall coefficient of variation (standard deviation/average temperature *100), both for syrup and fruit pieces resulted lower than 5 % and hence, for a clear reading, in Figures only average values (without error bars) are reported.

2.2. Sample characteristics

The fruit salad was composed of five different fruits (percentage expressed by weight): peach (52%), pear (38%), pineapple (5%), grape (3%) and cherry (2%). The pH value and the water activity of syrup and fruit mixture were measured at 25°C. pH value resulted 3.79 ±0.05, and it was obtained with a pH meter (Jenway, Staffordshire, UK), previously calibrated with standard solutions at pH = 4.02 and 7.00. Water activity value (a_w) was 0.988 ±0.005 and it was determined with an Aqualab 4TE (Decagon Devices, Inc., WA, USA), previously calibrated with saturated salt solutions of $MgNO_3$ ($a_w = 0.543 \pm 0.007$), NaCl ($a_w = 0.754 \pm 0.006$) and bi-distilled water ($a_w = 0.999 \pm 0.001$) at a constant temperature of 25°C.

Peach and pear were cubic with sides of 10 and 8 mm, respectively. Pineapple had truncated pyramid geometry (such as a titbit, with a thickness of 5 mm and major edge of 10 mm). Cherry had a hemispherical geometry with a radius of 8 mm, with a spherical hole at the centre (due to destoning) with a radius of 4 mm. The grape had an ellipsoidal geometry, with major and minor axis of 8 and 5 mm, respectively (**Figure 1**). The fruits were inserted into the jar simulating an industrial filling process in the order peach, pear, pineapple, grape and cherry. The jar was then filled with 16.7% (w/w) sucrose solution measured with an electronic refractometer (Sinotech, Fujian, China). The solid/liquid ratio was 61:39 (w/w), the same as those of commercial samples. The jar used for the trials had a filling volume of 372 ml, diameter = 86.0 mm; height = 90.5 mm. Glass thickness was measured with a calliper at different locations on the side and bottom surfaces of the container and resulted in an average value of 3.5 mm. Prior to experiments, the jar was hermetically closed with a screw metal cap with a diameter of 86 mm.

2.3. Data acquisition

The temperatures inside the jar were measured using thermocouples (K-type; Ni/Al-Ni/Cr) connected to a multimeter acquisition system (Yokogawa Electric Corporation, Tokyo, Japan). A stainless steel multipoint temperature probe was positioned along the central axis of the jar through a hole made in the centre of the cap. This multipoint probe (length = 97.5 mm; diameter = 3.5 mm) included four thermocouples spaced every 13 mm from the tip of the probe in order to record the syrup temperature at four different heights (17.5, 30.5, 43.5 and 56.5 mm) from the bottom of the jar. The temperature of fruit pieces was obtained by using five wire thermocouples (diameter = 0.9 mm, Gauge number = 20) inserted at the core of each fruit (**Figure 2b**). The temperature at half the height of the outer wall of the jar was also measured by sticking a thermocouple on the external sufarce with a 1 cm^2 of an appropriate scotch tape. Data obtained from the external wall of jars were used as temperature values for boundary conditions of the model. Both for multipoint probe and single thermocouples, an acquisition rate of 2 s was used and time-temperature data were collected in an Excel® ASCII worksheet.

3. CFD modelling

3.1. Geometry of fruit salad in the glass jar

The process of thermal treatment of fruit salad in a glass jar was simulated by means of a multidimensional CFD (Computational Fluid Dynamic) model. The observed spatial placement of the fruit salad inside the container was replicated in a 3D CAD model. In order to reduce the computational effort required by the solution of the CFD model, the spatial domain was assumed to be symmetric with regard to two perpendicular planes through the vertical axis of the jar, hence only a quarter of the jar needed to be simulated.

The fruit pieces were spatially arranged on a regular grid (8 rows evenly distributed over the full jar height), and the spacing carefully chosen in order to obtain a solid/liquid content ratio as close as possible to that measured in the experimental tests. The resulting spatial arrangement of the fruit pieces in the model of the jar is depicted in **Figure 2a**.

The model geometry was then imported into the ICEM CFD® software (Canonsburg, Pennsylvania, USA) and discretized into an unstructured tetrahedrical mesh. The maximum element dimension was chosen taking into consideration the domain (solid, fluid and glass). The values of maximum element edge dimension for the different fruit pieces inside the jar, together with syrup and glass are reported in **Table 1**.

Following the approach used by Kiziltas et al. (2010) and Dimou et al. (2011), in order to reduce the complexity of multiphase fluid calculation, the headspace was not considered in the simulation assuming the jar completely filled with product.

In order to accurately calculate the flow field near the wall of the jar, six layers of flat prismatic wedge element were used for the discretization of the fluid domain. The optimal number of wall boundary layers needed to obtain an appropriate level of accuracy was identified by means of a layer-independence analysis, which suggested a value for the dimension of the first element near the wall equal to 0.04 mm with a height ratio of 1.2 between layers. The final mesh with solid and fluid elements consists of $3*10^6$ elements (**Figure 3**).

3.2. Numerical model

The evaluation of the field of fluid flow and thermal exchange occurring in the considered domain due to natural convection required numerical solution of the generalized transport equations:

a) Continuity Equation

$$\frac{\partial \rho}{\partial t} + \nabla \cdot (\rho V) = 0 \quad (1)$$

b) Momentum Equation

$$\frac{\partial \rho V}{\partial t} + \nabla \cdot (\rho V \cdot V) = \nabla \cdot \left(-p\delta + \mu(\nabla V + (\nabla V)')\right) + S_M \qquad (2)$$

c) Energy Equation

$$\frac{\partial \rho h_{total}}{\partial t} - \frac{Dp}{Dt} + \nabla \cdot (\rho V h_{total}) = \nabla \cdot (k\Delta T) + S_E \qquad (3)$$

Where t is the time (s), V is the velocity vector (m s^{-1}), ρ is the density (kg m^{-3}), p is the pressure (Pa), μ is dynamic viscosity (Pa s), h_{total} is the specific total enthalpy (J).

The software Ansys® CFX 14.5 (Canonsburg, Pennsylvania, USA) was chosen for the calculation. Natural convection was modelled using the Boussinesq approximation, which uses a constant density fluid model, but applies a local body gravitational force throughout the fluid that is a linear function of thermal expansivity β and of the local temperature difference. The buoyancy source is added to the momentum equation as follows:

$$S_M = -\rho_{REF} \cdot \beta \cdot (T - T_{REF}) \cdot g \quad (4)$$

Where ρ_{ref} and T_{ref} are the density and temperature (°C) at the boundary wall condition and g is the gravitational force.

No internal energy source terms (S_E) were taken into account.

3.3. Boundary conditions

A uniform time varying temperature condition was applied to all the external surfaces of the jar and corresponded to that measured in the experimental tests. The value of initial temperature of fruit and syrup was 22°C, while the variation of the outer wall temperature with time during the heat treatment is showed in **Figure 4** (black dotted line).

Transition in a free convection boundary layer depends both on the relative magnitude of the buoyancy and on the viscous forces in the fluid and, ususally, they are correlated in terms of the Rayleigh number. For vertical plates, as glass walls, the critical Rayleigh number (*Ra*) for the transition between laminar and turbulent flow is approximately 10^9 (Incropera, 2006); since the maximum *Ra* estimated using the maximum temperature difference and the maximum viscosity remained lower than 10^6 during the whole thermal treatment, laminar flow was adopted for all the simulations. The *Ra* value was calculated by the following equation:

$$Ra = \frac{g\beta(T_S - T_\infty)x^3}{v\alpha} \quad (5)$$

where $g = 9.81$ (m s^{-2}), $x = 0.087$ (m) height of jar, $T_s - T_\infty = 71$ (K) maximum temperature difference inside the jar, $v = 7.9*10^{-4}$ (m^2 s^{-1}) kinematic viscosity, $\beta = 2.57*10^{-4}$ (K^{-1}) volumetric thermal expansion coefficient, $\alpha = 1.56*10^{-7}$ (m^2 s^{-1}) thermal diffusivity.

An adaptive time step option was used in order to maintain the Courant number low enough in order to accurately solve the transient heating phase. A good accuracy can be reached setting the maximum Courant number value lower of 1 (Boz et al., 2014); as a consequence a maximum time step of 0.5 s has been reached during the calculation. High resolution advection schemes were adopted for all simulations, in order to achieve second order accuracy. The convergence criterion was defined as residual root mean square (RMS) value lower than 10^{-4}.

3.4. Thermal and physical properties

Values of thermal and physical properties such as density ρ (kg m^{-3}), viscosity μ (Pa s), specific heat C_p (J kg^{-1} K^{-1}) and thermal conductivity k (W m^{-1} K^{-1}) of fruits, syrup and glass were needed for the definition of the model and the values used are summarized in **Table 1**. The viscosity of the syrup was assumed to be a function of temperature and a linear interpolation from experimental data was used. By means of properties data also the thermal diffusivity α (m^2 s^{-1}) of each fruit was calculated by means of:

$$\alpha = \frac{k}{\sigma * C_p} \quad (6)$$

and reported in **Table 1**.

3.5. Model validation

The developed model was validated by comparing experimental temperature measurements at specific points inside the glass jar with predicted ones. The accuracy of the model prediction was assessed by determining root mean square error (*RMSE*) and lethality (F_{Ts}^{z}).

The equation for *RMSE* determination can be expressed as:

$$RMSE = \sqrt{\frac{\sum_{i=1}^{n}(T_E - T_P)^2}{N}} \quad (7)$$

where T_P is simulated temperature and T_E is measured temperature, at time *t*. The effect of heat treatment and time with respect to the survival of a microorganism can be quantified by the following F_{Ts}^{z} value equation (Holdsworth and Simpson, 2007):

$$F_{Ts}^{z} = \int_0^t 10^{\left(\frac{T-T_{ref}}{z}\right)} dt \qquad (8)$$

Lethality was calculated as an equivalent heating time at a constant temperature (T_{ref}) of 90°C and a *z* value of 12.9 °C as characteristic for *Alicyclobacillus acidoterrestris* as suggested by Silva and Gibbs (2004) for high acidity shelf stable fruit products.

4. *Results and discussion*

4.1. Validation results

The simulation results were in agreement with the experimental data for both the syrup and the fruits, as shown in **Table 2**, where validation parameters at each measurement point are reported (4 and 5 points for syrup and fruits, respectively). No significant differences were observed between experimental and simulated *F values*, confirming the accuracy and the reliability of the developed mathematical model. In addition, in **Figure 4** and **5** temperature profiles of the experimental and simulated treatment for syrup and fruit pieces are compared, respectively. The variations in the results of the model may be due to the distribution of the fruit pieces inside the container, the combined effects of the experimental and model assumptions such as Boussinesq approximation and the thermal properties of the materials. Furthermore, during the experiments, the location of the temperature sensor may change the liquid flow pattern and, hence, affects the temperature profile of the sugar solution. In the simulation, small-scale instabilities were produced by the buoyancy effect. The buoyancy-produced structures might have directly interacted and coupled with the existing local turbulence and laminar modelling could not successfully predict this effect with little deviations between experimental and simulated data.

4.2. Slowest heating point (SHP) and temperature profile

The identification of the slowest heating point (SHP) inside the container was considered of basic importance for the effectiveness of thermal processing of our samples. The temperature distribution inside the jar was then measured at different time steps in order to describe the convective movement of the SHP.

When a fluid is subjected to a rapid temperature increase adjacent to a solid wall, part of the fluid in the wall neighbourhood expands resulting in an increase in the local pressure with significant effects in heat transfer due to thermal buoyancy effects in a gravitational force field

(Aktas and Farouk, 2003). In a similar way, during thermal processing of solid-liquid mixtures, such as canned fruit salad, syrup closer to the can walls receives the heat (undergoes heat flux) thus resulting in volume expansion and density decrease while the syrup far from the walls is still at lower temperature. This phenomenon leads to development of an upward buoyancy force with a motion due to density differences. This movement also carries the colder fluid upward by viscous drag. The fluid flowing upward is deflected by the top surface of the can and starts moving in a radial direction and, by becoming heavier, starts to move downwards through the stack of fruits. Consequently, its temperature decreases as it comes in contact with colder pieces of fruits and syrup, and a new cycle starts from the bottom. These convective movements create a recirculating flow thus increasing the rate of heat transfer. This observation is similar to the results obtained by other Authors for natural convection heating mechanism (Ghani et al., 1999; Padmavati and Anandharamakrishnan, 2013). The maximum value of liquid velocity was observed close to the wall of the jar (due to the higher temperature gradient between the jar wall and the thin liquid layer close to the wall). When solid and impermeable particles were distributed into the fluid, the velocity profile changed due to the heat exchange and surface deflections: the flow was very slow through the stack of solid particles in the horizontal direction while on the contrary it showed an increase between solids in the vertical direction.

In the case of pure convection heating of liquids, the slowest heating point (SHP) is located at about 10-15% of the can height (Padmavati and Anandharamakrishnan, 2013), but in the case of solid-liquid food mixtures heated by a combination of conduction and convection, SHP location is more complex to determine. Under our experimental conditions, the SHP of the canned fruit salad was not at the geometric centre of the can or at a can height of 10-15% but at an intermediate position between these (19-20% of the can height). The position of SHP is well shown by the *F value* of the various fruits: pear pieces presented the lowest *F value* because this kind of fruit was positioned closer to the SHP.

The natural convection effects also influenced the heating of the fruit pieces. As shown in **Table 2**, the fruits positioned close to the top of the jar showed a simulated *F value* higher than those placed close to the bottom: grape = 9.68 min, peach = 5.30 min.

When there is a marked effect of natural convection heating, thermal stratification takes place (observation based on the fluid movement due to buoyancy effects explained above). **Figure 6** shows temperature stratification for the syrup during heating phase, at 4 different time steps (5, 10, 20 and 30 min), while **Figure 7** reports the temperature stratification along the fruit pieces at the same time steps (both figures come from the graphical representation of the mathematical model).

5. Conclusions

In this study, a 3D CFD model was developed in order to predict the temperature profiles, to identify the slowest heating point (SHP) and to describe the flow field during the pasteurization process of a fruit salad composed of five kinds of fruit canned in a glass jar and filled with 16.7% sugar syrup.

Calculated experimental $F_{90}^{12.9}$ *values* resulted different between the various fruits and, in particular, they were a function of position, characteristic dimensions and thermal properties; moreover, experimental *F values* were also greatly influenced by the natural convection motion of the syrup. Pear pieces showed the lowest pasteurizing value while grape the highest one: the first presented a high characteristic dimension (4 mm) and was positioned near the SHP while the latters had a lowest dimension (2.5 mm) and was positioned at the top of the jar where syrup presented the highest temperature.

Concerning the proposed CFD model, an appreciable agreement, expressed as RMSE, between simulated and experimental values of temperature both for syrup (1.47 °C) and fruit pieces (1.63 °C) was obtained: the model can be thus considered successfully validated and applicable for the simulation and prediction of thermal processes of canned fruit salad.

Finally, an increase in the reliability of the model by minimizing the differences with experimental data could be achieved by enhancing temperature measurements inside syrup and fruits with reference to position inside the jar during the thermal process.

References

Akhijahani, H. S., & Khodaei, J., (2013). Investigation of specific heat and thermal conductivity of rasa grape (*Vitis vinifera* L.) as a function of moisture content. *World Applied Sciences Journal*, 22, 939-947.

Aktas, M.K., & Farouk, B., (2003). Numerical simulation of developing natural convection in an enclosure due to rapid heating. *International Journal of Heat and Mass Transfer*, 46, 2253-2261.

Anandharamakrishnan, C. (2011). Applications of computational fluid dynamics in food processing operations. In A. D. Murphy (Ed-), *Computational fluid dynamics: theory, analysis and applications-Chapter 9* (pp. 297-316). New York: Nova Publishers.

ASHRAE, (2006). Thermal properties of foods. *Handbook refrigeration-Chapter 9*.

Boz, Z., Erdogdu, F., & Tutar, M., (2014). Effects of mesh refinement, time step size and numerical scheme on the computational modeling of temperature evolution during natural-convection heating. *Journal of Food Engineering*, 123, 8-16.

Chen, C.R., & Ramaswamy, H.S., (2007). Visual basic computer simulation package for thermal process calculations. *Chemical Engineering and Processing*, 46, 603-613.

Chhanwal, N., Tank, A., Raghavarao, K.S.M.S., & Anandharamakrishnan, C., (2012). Computational fluid dynamics applications in bread baking process. *Food and Bioprocess Technology*, 5, 1157-1172.

Dimou, A., & Yanniotis, S., (2011). 3D numerical simulation of asparagus sterilization in a still can using computational fluid dynamics. *Journal of Food Engineering*, 104, 394-403.

Ghani, A. G., & Farid, M. M., (2006). Using the computational fluid dynamics to analyse the thermal sterilization of solid-liquid food mixture in cans. *Innovative Food Science and Emerging Technologies*, 7, 55-61.

Ghani, A. G., Farid, M. M., & Chen, X. D., (2002). Numerical simulation of transient temperature and velocity profiles in a horizontal can during sterilization using computational fluid dynamics. *Journal of Food Engineering*, 51, 77-83.

Ghani, A. G., Farid, M. M., Chen, X. D., & Richards, P., (1999). Numerical simulation of natural convection heating of canned food by computational fluid dynamics. *Journal of Food Engineering*, 41, 55-64.

Holdsworth, D., & Simpson, R., (2007). *Thermal processing of packaged foods, food engineering series*. New York: Springer.

Incropera, F. P, DeWitt D. P., Bergman T. L., & Lavine, A. S., (2006). *Fundamental of heat and mass transfer*. John Wiley & Sons.

Kiziktas, S., Erdogdu, F., & Palazoglu, T.K., (2010). Simulation of heat transfer for solid-liquid food mixtures in cans and model validation under pasteurization conditions. *Journal of Food Engineering*, 97, 449-456.

Kumar, A., Bhattacharya, M., & Blaylock, J., (1990). Numerical simulation of natural convection heating of canned thick viscous liquid food products. *Journal of Food Science*, 55, 1403-1411.

Kuriakose, R., & Anandharamakrishnan, C., (2010). Computational fluid dynamics (CFD) applications in spray drying of food products. *Trends in Food Science and Technology*, 21, 383-398.

Padmavati, R., & Anandharamakrishnan, C., (2013). Computational Fluid Dynamics Modeling of the Thermal Processing of Canned Pineapple Slices and Titbits. *Food Bioprocess Techology*, 6, 882-895.

Rabiey, L., Flick, D., & Duquenoy, A., (2007). 3D simulations of heat transfer and liquid flow during sterilization of large particles in a cylindrical vertical can. *Journal of Food Engineering*, 82, 409-417.

Rahman, M.S., (2008). *Food properties Handbook*. Boca Raton: CRC.

Silva, F. V., & Gibbs, P., (2004). Target selection in designing pasteurization processes for shelf-stable high-acid fruit products. *Critical Reviews in Food Science and Nutrition*, 44(5), 353-360.

Sun, D.W., (2007). *Computational fluid dynamics in food processing*. Boca Raton: CRC.

Varma, M. N., & Kannan, A., (2005). Enhanced food sterilization through inclination of the container walls and geometry modifications. *International Journal of Heat and Transfer*, 48, 3753-3762.

Weng, Z.J., (2005). Thermal processing of canned foods. In: Sun, Da-Wen (Ed.), *Thermal Food Processing-New Technologies and Quality Issues – Chapter 11*. Boca Raton: CRC-Taylor and Francis.

Whitelock, D.P., Brusewitz, G.H., & Ghajar, A.J., (1999). Thermal/physical properties affect predicted weight loss of fresh peaches. *American Society of Agricultural Engineers*, 42, 1047-1053.

Xia, B., & Sun, D.W., (2002). Review: applications of computational fluid dynamics (CFD) in the food industry. *Computers and Electronics in Agriculture*, 34, 5-24.

Table 1. Thermal properties, rheological characteristic and maximum element edge dimension for all the different kinds of fruit, together with syrup and glass.

Food	**ρ (kg m^{-3})**	**μ (Pa s)**	**C_p (J kg^{-1} K^{-1})**	**k (W m^{-1} K^{-1})**	**α (m^2 s^{-1})**	***Max edge length^g (mm)***
Syrup (16.7% sugar)	1074^g	$0.0258-0.00023*T^g$	-	-		0.50
Peach	930^a	-	3700^a	0.581^b	$1.69\ 10^{-7}$	1.70
Pear	1000^b	-	3800^c	0.595^b	$1.57\ 10^{-7}$	1.50
Pineapple	1010^d	-	3490^d	0.549^d	$1.56\ 10^{-7}$	0.80
Grape	1320^c	-	3325^e	0.273^e	$0.69\ 10^{-7}$	0.45
Cherry	1049^b	-	3730^c	0.511^c	$1.31\ 10^{-7}$	0.26
Glass	2500^f	-	750^f	1.400^f		2.00

[a] Whitelock et al. (1999);
[b] Rahman (2008);
[c] ASHRAE 2006 Handbook-refrigeration;
[d] Padmavati and Anandharamakrishnan (2013);
[e] Akhijahani and Khodaei (2013);
[f] Incropera et al. (2006);
[g] experimental value.

Table 2. Validation results (RSD < 5%).

Point of measurement		***RMSE***	$F_{90}^{12.9}$ **(min)**		
			Experimental	***Simulated***	$\Delta F_{90}^{12.9}$
Syrup	17.5 mm	0.68	0.40	0.36	0.04
	30.5 mm	0.79	1.19	1.01	0.18
	43.5 mm	1.77	2.52	2.55	0.03
	56.5 mm	2.65	4.04	4.99	0.95
	Average	***1.47***			***0.30***
Peach		1.14	5.41	5.30	0.11
Pear		2.31	1.56	1.63	0.07
Pineapple		1.78	5.03	5.13	0.10
Grape		1.61	9.70	9.68	0.02
Cherry		1.31	7.27	7.31	0.04
Average		***1.63***			***0.07***

Figure 1. Visual comparison of the different kinds of fruits used in the experiments.

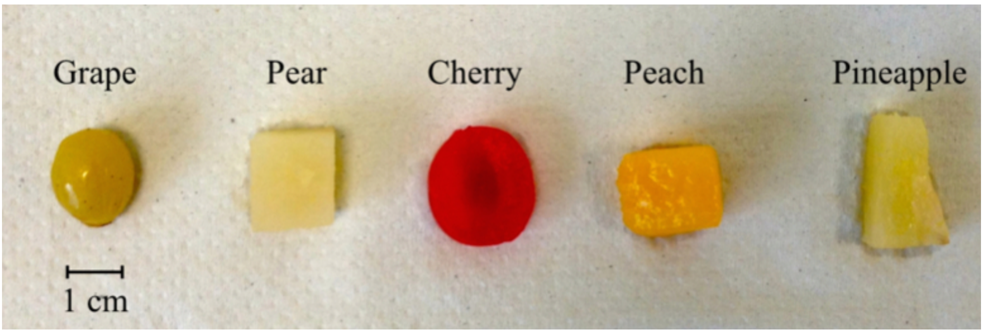

Figure 2. 3D model of the distribution of the fruits inside the jar (panel **a**) and thermocouple location (panel **b**).

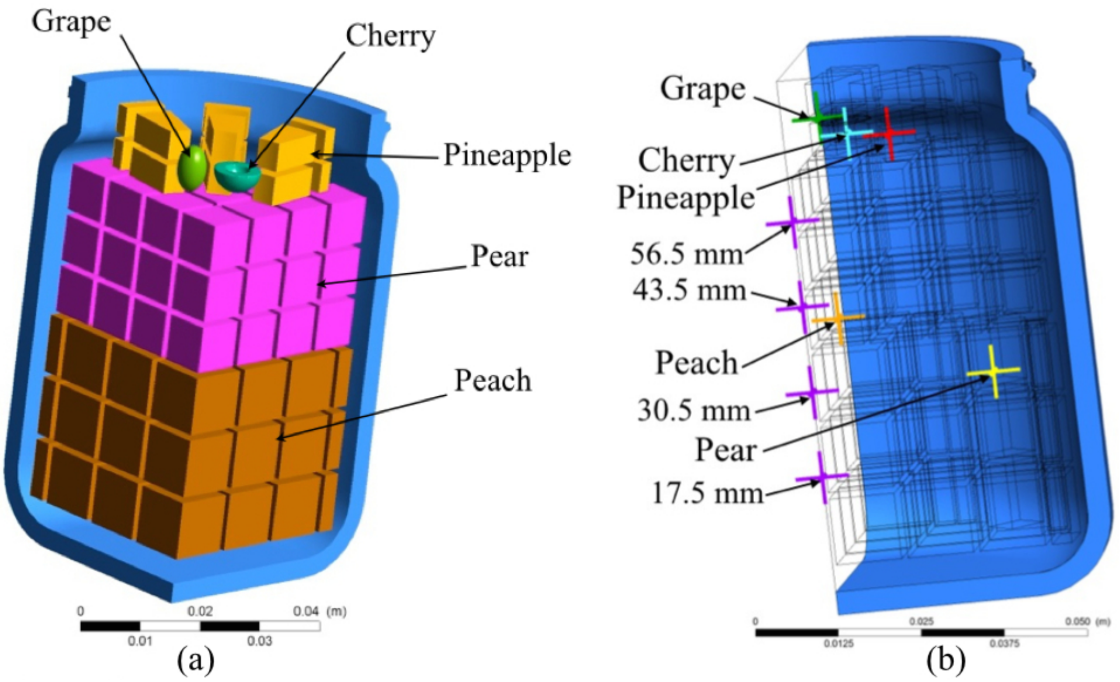

(a)

(b)

Figure 3. 3D model of the fruits inside the jar with the mesh element.

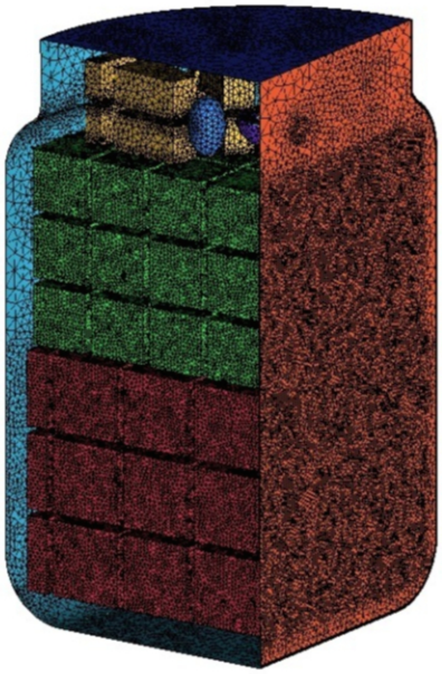

Figure 4. Comparison of temperature profile in syrup between experimental test and mathematical model (RSD < 5%).

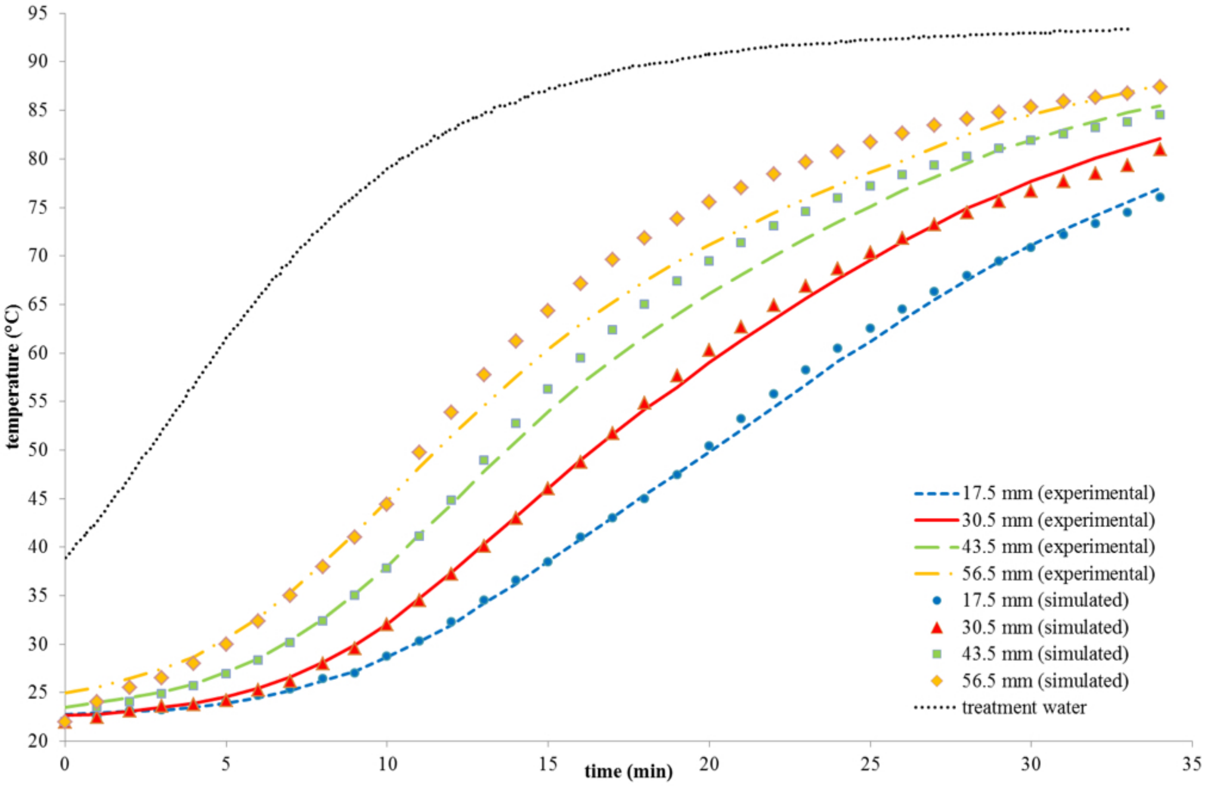

Figure 5. Comparison of the temperature profile in fruit pieces between experimental test and mathematical model (RSD < 5%).

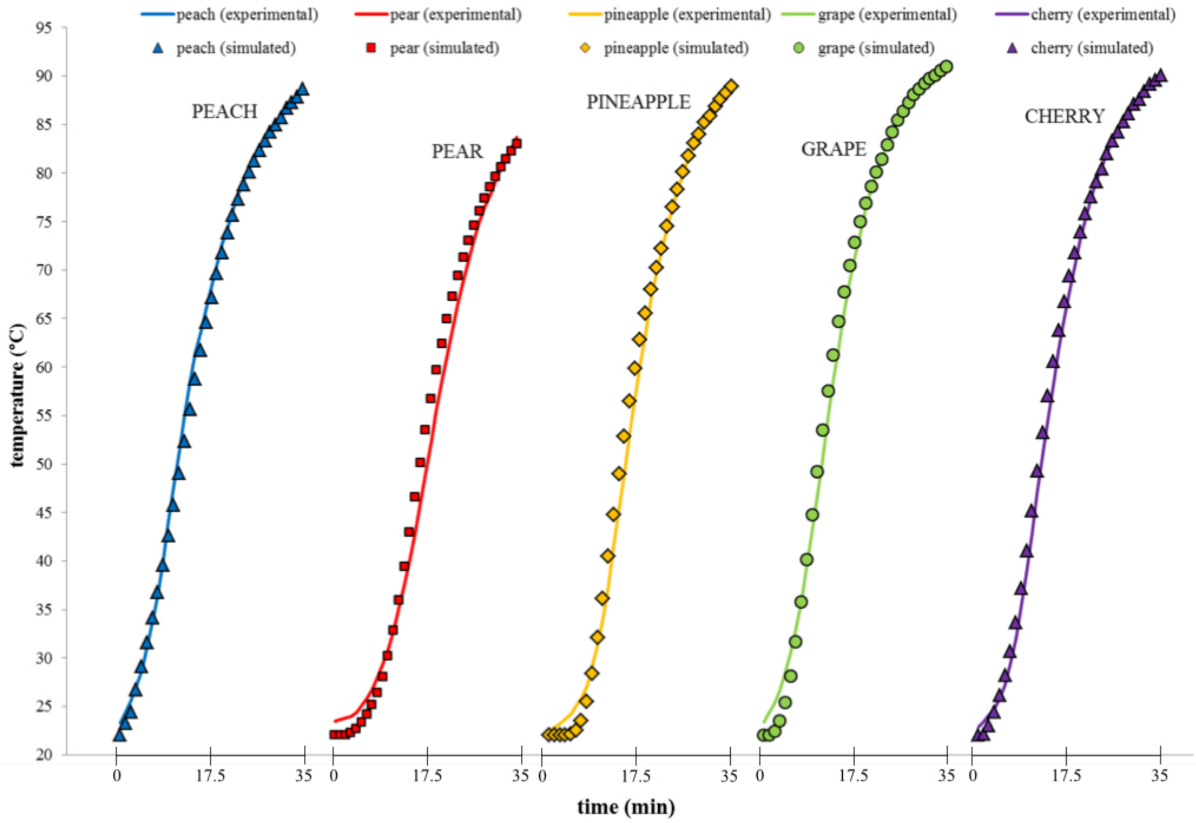

Figure 6. Temperature distribution of the syrup at 4 different time steps (from mathematical model).

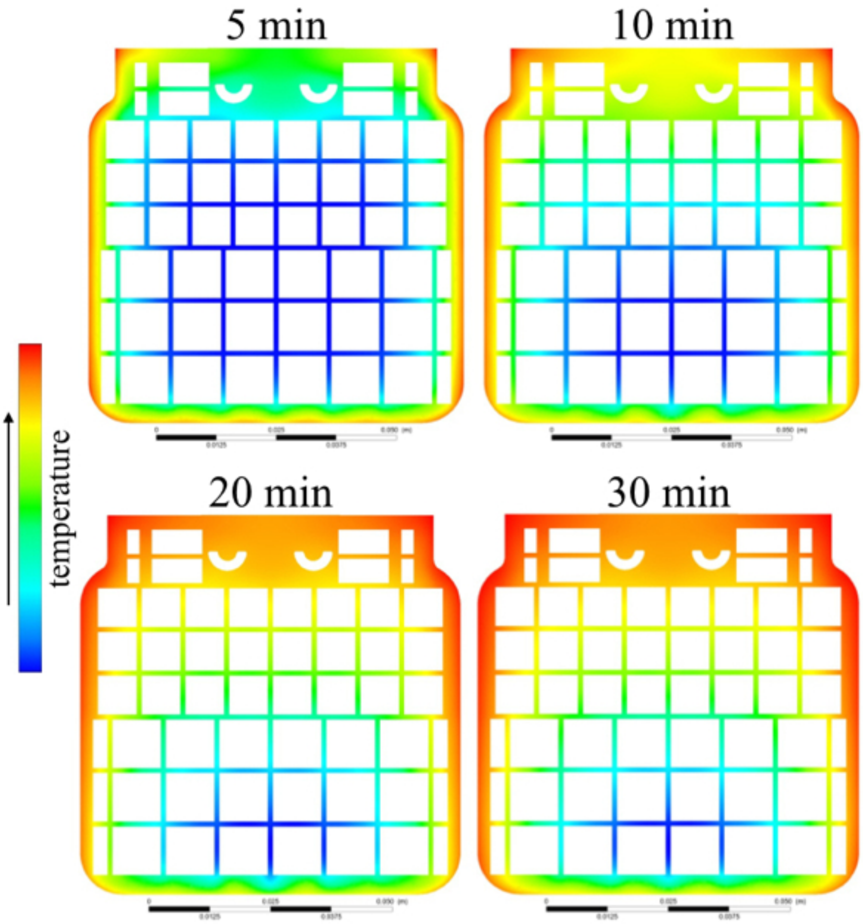

Figure 7. Temperature distribution of the fruit pieces at 4 difference time steps (from mathematical model).

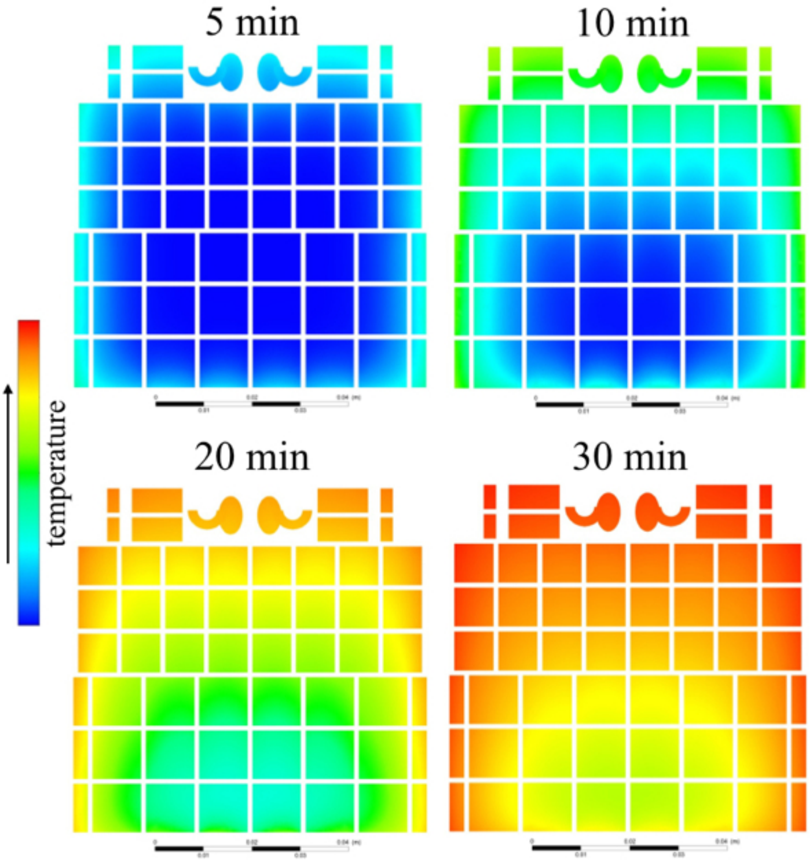

Investigation and modelling of natural convection and conduction heat exchange: study on food systems with modified starch by means of Computational Fluid Dynamics (CFD)

Matteo Cordioli, Massimiliano Rinaldi and Davide Barbanti

Department of Food Science, University of Parma, Parco Area delle Scienze 47/A, 43124
Parma, Italy

Published in *International Journal of Food Science and Technology*
DOI: 10.1111/ijfs.13039

Abstract

This experimental paper is focused on the effects of starch gelatinization on heat exchange in laboratory-made food systems containing four modified starch concentrations (0, 2, 6 and 10%). Viscosity profiles of samples were experimentally measured: the effect of gelatinization was evident, particularly at 6% and 10%, where the viscosity increased from 0.010 to 70 Pa s and to 1507 Pa s, respectively. The heat exchange rate showed a decrease with the increasing of starch concentration and the effects were observed until 6%. Four CFD models were also developed and, after an experimental validation (RMSE < 1.5°C), used to study the heat exchange in detail. Velocity profiles showed that the convective flows slowed down from 2.5 to 0 mm s^{-1} after the gelatinization phenomenon. Finally, the effects on the slowest heating/cooling zone (SHZ/SCZ) location in the CFD models were studied: at 0% and 2% the SHZ settled 15 and 80 mm from the bottom of jars in heating and cooling phase, respectively. At 6% and 10%, before the starch gelatinization phase, the SHZ was located in a similar position of the 0% and 2% while when the gelatinization occurred the SHZ slightly moved toward the geometric centre (50 mm) as expected for an only-conductive product.

Keywords: CFD, convective + conductive, starch gelatinization, slowest heating zone.

1. Introduction

Starch is a common ingredient which primary function is to thicken a liquid as a result of its gelatinization. In many foods, such as soups, salad dressing, gravies and sauces, it is present in excess of water. Because of the drastic increase in the apparent viscosity, the rheological behaviour during the transition from fluid-like to viscoelastic behaviour deeply affects heat transfer during thermal processing (Yang and Rao, 1998). The viscosity of a fluid containing starch increases first with temperature during thermal processing because of the amylose release and swelling of the starch granules after the initial temperature of gelatinization has been reached. After the starch dispersion attains its maximum viscosity, the granules begin to break and the viscosity decreases with temperature, as consequence (Liao et al., 2000). As a result, broken heating curves are encountered during batch sterilization of many foods containing starch (Yang and Rao, 1998).

In thermal processing of canned foods, heat transfer usually occurs by means of either convection or conduction or more frequently by both mechanisms. The fluid viscosity is one of the major factors affecting heating rate in convective-heating foods: the higher the viscosity of the fluid, the more resistant it would be to movement and, thus, the heat transfer rate inside the can content would be slower (Tattiyakul et al., 2002). Ramaswamy et al. (1993) reported that change in viscosity due to increase in starch concentration from 3% to 4% accounted for about 60% of decrease in heating rate. Berry et al. (1979) and Berry and Bradshaw (1980) conducted heat penetration tests on soups and reported a decrease in sterilization value with the increase in the product viscosity. As a consequence, the thermal process of such kind of foods must be properly designed by studying both the rheological and thermal properties of foods and the mechanism of heat transfer during the treatment. These purposes are normally achieved by a relevant number of experimental trials with an increase in cost and time consumption; as a consequence, a reduced possibility to have fast, efficient and in-depth results has to be accounted (Sun, 2007).

With the development of computer technology, the design of thermal processes underwent tremendous development. Use of advanced modelling techniques, such as computational fluid dynamics (CFD) reduces the complexity in solving the non-linear partial differential equation of heat transfer. CFD is a modelling tool that can be used to develop three-dimensional models representative of a physical system and can produce results with high accuracy in less time. CFD is based on numerical methods that can predict the governing heat transfer mechanism over 3D domain of interest (Singh et al., 2015); as a consequence, it is an excellent tool to understand transient heat transfer phenomena occurring inside a can. For example, by CFD analysis, it is easy to find the slowest heating zone, which can be further used for calculating the accurate process time, as well as illustrating the sharp heterogeneity in temperature profile of the product when no agitation is applied to the can (Singh et al., 2015).

In the last decade few works have been published on the CFD simulation studies of canned foods with breaking curve behaviour, where the heat exchange began with convection and continued by convection+conduction or mainly conduction. Tattiyakul et al. (2001) simulated starch solution undergoing transient gelatinization and concluded that uniform heating could be obtained by rotating the can intermittently during the sterilization process. Subsequently, Tattiyakul et al. (2002) investigated heating rate and temperature distribution in three canned fluids with different thermo-rheological behaviours undergoing intermittent agitation.

However, the scientific literature still lacks of in-deep studies concerning the heat treatment on food systems showing starch gelatinisation during heating phase and the use of mathematical models to predict the effects of starch concentration on heat penetration and sterilizing/pasteurizing values.

The objectives of the present study were (i) to experimentally study the thermal processing of food systems at different starch concentrations (0, 2, 6 and 10%), (ii) to develop and validate a CFD model of each product and (iii) to evaluate the effect of the starch concentration on the heat transfer rate and slowest heating zone (and slowest cooling zone) location of each food system.

2. *Materials and methods*

2.1. Food systems characteristics

Modified waxy maize starch (Frutarom, Parma, Italy) dispersion at different concentrations were prepared with an electric blender (Oster®, New York, USA) at room temperature for 10 minutes. To guarantee a sufficient stability of the dispersion along the entire treatment, an emulsion with sunflowers oil (12% w/w), modified starch (0, 2, 6 or 10% w/w), soy lecithin (5% w/w) and water was prepared. The percentage of each component was selected after a brief testing phase to identify the best composition from the emulsion stability point of view by evaluating both the gel formation and the absence of phase separation. The system, after emulsification, was allowed to rest for at least 1 hour to ensure a good deaeration. The glass jar used for the trials had a volume of 203 ml, diameter = 56 mm and height = 115 mm. Glass thickness, measured with a calliper at different locations on the side and bottom surface of the container, resulted in an average value of about 3 mm. All the jars were hermetically closed with a screw metal cap after filling. Three replicates for each sample were prepared and analysed.

2.2. Rheological data

The rheological measurements were made in a concentric cylinder rotational viscometer (Brookfield, Middleboro, MA, USA). The apparatus measures the shear rate and the apparent viscosity of a fluid at fixed temperature. The apparent viscosity, η, is defined as the ratio of shear stress (τ) to the shear rate (γ) ($\eta = \tau/\gamma$). Two cylindrical spindles were used for the rheological analyses. The ULA spindle (Brookfield, Middleboro, MA, USA) was used for 0% (100 rpm, 10-15% torque range) and 2% samples and for 6% and 10% samples before starch gelatinization (viscosity range from $6*10^{-4}$ to 2 Pa s, 20 rpm, 15-45% torque range). Viscosity measurements after gelatinization for 6% and 10% samples were carried out by means of SC4-25/13R spindle (Brookfield, Middleboro, MA, USA) (viscosity range from 0.479 to 1600 Pa s): rotation speed/torque range were 20/(45-75%), 5/(40-80%) and 0.3/(50-98%) for 2, 6 and 10%, respectively. The viscometer was connected to a computer for the data acquisition and collection in an Excel® ASCII worksheet. The viscosity value of each sample was measured from 20 to 85°C and from 85 to 40°C with temperature step of 1°C (20 points for each temperature degree) to study the heating and the cooling phase, respectively.

2.3. Sample processing details

The heat penetration inside the food systems was studied taking into consideration both heating and cooling phase in order to emphasize the difference between the systems where the heat exchange was convective in both the phases and the systems where, after gelatinization, the heat exchange occurred by convection + conduction or mainly by conduction. The tests were carried out in a stirred thermostatic bath (MPM Instruments S.r.l., Bernareggio, Italy) with an internal volume of 17 L. The jars were immersed in the water up to the base of the cap: the heat exchange thus took place mainly through the side walls and the bottom of the jar. During the heating phase water temperature was set at 89±1°C and samples were heated from 25°C until the slowest multipoint sensor reached 85°C (see *section 2.4*). In the cooling phase, the water temperature was 34±3°C and the treatment was stopped when the slowest multipoint sensor reached 40°C. Three repeated thermal treatments on three different jars for each sample were performed.

2.4. Heat penetration data

The temperatures inside the jar were measured using wire thermocouples (K-type; Ni/Al-Ni/Cr) connected to a multimeter acquisition system (Yokogawa Electric Corporation, Tokyo, Japan). In addition, a multipoint temperature probe was positioned along the central axis of the jar through a hole made in the centre of the cap as previously reported (Cordioli et al., 2015). The multipoint probe (length = 97.5 mm; diameter = 3.5 mm) recorded temperature at four different heights (31.5, 57.5, 70.5 and 96.5 mm) from the bottom of the jar. The temperatures at half the height of the outer wall of the jar were also measured by sticking a wire thermocouple (diameter = 0.9 mm, Gauge number = 20) on the external surface with a 1 cm^2 of an appropriate scotch tape. Data obtained from the external wall of jars were used as temperature values for boundary conditions of the model. Both for multipoint probe and single thermocouple, an acquisition rate of 1 s was used and time-temperature data were collected in an Excel® ASCII worksheet.

2.5. Statistical analysis

Means and standard deviations (SD) were calculated with STATISTICA (release 8.0, Statsoft Inc., Tulsa, Oklahoma, USA) statistical software. One-way-analysis of variance (ANOVA) and least significant difference test (LSD) at a 95% confidence level ($P \leq 0.05$) was applied to identify differences of evaluated parameters among samples.

3. CFD modelling

3.1. Defined domain and mesh details

Thermal treatments were simulated by means of a multidimensional CFD (Computational Fluid Dynamic) model. First, a 3D CAD model was developed to replicate the glass jar and the fluid within it. The 3D geometry model was developed with SolidWorks® 2013 software (Dassault systèmes, Vélizy-Villacoublay, France). In order to reduce the computational effort required by the solution of the CFD model, the spatial domain was assumed to be symmetric with regard to two perpendicular planes through the vertical axis of the jar, hence only a quarter of the jar needed to be simulated.

Following the approach used by Kiziltaş et al. (2010), Dimou and Yanniotis (2011) and Cordioli et al. (2015), in order to reduce the complexity of multiphase fluid calculation, the headspace (equal to 3 mm in the experimental test) was not considered in the simulation assuming the jar completely filled with product.

The model geometry was then imported into the ICEM CFD® software (Canonsburg, Pennsylvania, USA) and discretized into an unstructured tetrahedrical mesh. The values of maximum and minimum element edge dimension both for the jar and fluid was $2.21*10^{-3}$ and $1.11*10^{-5}$ m, respectively. In order to accurately calculate the flow field near the wall of the jar, five layers of flat prismatic wedge element were used for the discretization of the fluid domain. The optimal number of wall boundary layers, needed to obtain an appropriate level of accuracy, was identified by means of a layer-independence analysis, which suggested that the dimension of the first element near the wall equals to 1.1*10^{-4} m with a height ratio of 1.2 between layers. The final mesh with jar and fluid elements consists of 1320641 elements and 319300 nodes. The mesh was optimized and finalized for better accuracy and computational time. From a quality point of view, the value of skewness was 0.21±0.12, which represent a good value (ANSYS Icepak User's Guide, 2011).

3.2. Numerical model

The software ANSYS® CFX v15 (Canonsburg, Pennsylvania, USA), run on HP Z420 Workstation (Palo Alto, California, USA), was used to solve the governing continuity, momentum and energy equations for the defined geometry and associated boundary conditions. The domain was defined in the global co-ordinate frame in which the solver carries out the calculations. The generalized transport equations solved are:

a) The continuity equation

$$\frac{\partial \rho}{\partial t} + \nabla \cdot (\rho V) = 0 \quad (1)$$

b) The momentum equation

$$\frac{\partial \rho V}{\partial t} + \nabla \cdot (\rho V \cdot V) = \nabla \cdot \left(-p\delta + \mu(\nabla V + (\nabla V)')\right) + S_M \qquad (2)$$

c) The energy equation

$$\frac{\partial \rho h_{total}}{\partial t} - \frac{Dp}{Dt} + \nabla \cdot (\rho V h_{total}) = \nabla \cdot (k\Delta T) + S_E \qquad (3)$$

Where t is the time (s), V is the velocity vector (m s^{-1}), ρ is the density (kg m^{-3}), p is the pressure (Pa), μ is dynamic viscosity (Pa s), h_{total} is the specific total enthalpy (J), k is thermal conductivity (W m^{-1} K^{-1}).

Natural convection was modelled using the Boussinesq approximation, which uses a constant density fluid model, but applies a local body gravitational force throughout the fluid that is a linear function of thermal expansivity β and of the local temperature difference. The buoyancy source is added to the momentum equation as follows:

$$S_M = -\rho_{REF} \cdot \beta \cdot (T - T_{REF}) \cdot g \quad (4)$$

Where ρ_{REF} and T_{REF} are the density and temperature at the boundary wall condition and g is the gravitational force.

No internal energy source terms (S_E) were taken into account.

The liquid inside the jar at time 0 was assumed to be at rest and at uniform temperature while a laminar flow mode was assumed to occur throughout the thermal processing (where the heat transfer was convective).

3.3. Boundary conditions

In this study, a transient simulation was carried out and a uniform time varying temperature condition was applied to all the external surfaces of the jar. For the model validation, time-temperature profiles imposed on the external surface of the jar were obtained from the value measured on jar surface in experimental tests. Finally, to compare the effect of thickening agent concentration on heat transfer by means of the validated models, a treatment curve at 95°C for 50 minutes followed by a cooling phase at 25°C of the same time with an initial temperature of the samples equal to 20°C was simulated.

A no-slip condition was applied with velocity = 0 m s^{-1} of the fluid relative to the internal jar surface. A good accuracy was reached setting the time steps value at 1 s: this guaranteed a low Courant number and ensured a right compromise between the solver time and the quality of the results. High resolution advection schemes were adopted for all simulations, in order to achieve second order accuracy. The convergence criterion was defined as residual root mean square (RMS) value lower than 10^{-4}.

3.4. Thermal and physical properties

Four different materials were created in the pre-processor library to define thermal and physical properties of the fluid inside jar. For all the food systems studied, the same thermal and physical properties were chosen, except from the viscosity value, which is different for each system. This assumption has been taken by considering the large variation of viscosity value between the samples and for each sample as a function of the temperature. From preliminary sensitivity analysis, the viscosity therefore resulted the physical parameter which manly influences the heat exchange. The data, obtained from Tattiyakul et al., (2001), were: thermal conductivity (k) 0.66 W m^{-1} K^{-1}, specific heat (c_p) 4180 J kg^{-1} K^{-1}, volumetric expansion coefficient (β) 0.00053 K^{-1} and density (ρ) 1000 kg m^{-3}. Conversely, the viscosity was assumed to be a function of temperature and obtained from the experimental rheological measures (*section 2.2*). With regard to the glass, thermal and physical properties were obtained from the software library.

3.5. Model validation

The developed models were validated by comparing experimental temperature measurements at specific points inside the glass jar with the predicted ones.

The accuracy of the model prediction was assessed by determining root mean square error (*RMSE*) with the following:

$$RMSE = \sqrt{\frac{\sum_{i=1}^{n}(T_E - T_P)^2}{N}} \qquad (5)$$

where T_P is simulated temperature (°C) and T_E is measured temperature (°C), at time t.

4. *Results and discussion*

4.1. Viscosity

The first objective of the work was to define a thermo-rheological profile of the four different food systems. Three replicates of viscosity measures on three samples for each model system were performed: the overall coefficient of variation resulted lower than 5% and hence, for a clear reading, in figures only average values (without error bars) are reported. In **Figure 1**, the viscosity experimental data (in logarithmic scale), vs. temperature, are reported. The viscosity changed from 0.011 to 0.015 Pa s in 2%, from 0.010 to 70 Pa s in 6% starch concentration samples (three orders of magnitude) and from 0.012 to 1507 Pa s in 10% (six orders of magnitude) by varying the temperature from 25 to 85°C. As expected, a great increase in the viscosity was observed only in 6% and 10% samples, due to gelatinization of modified starch with a lower increase in the 2% sample. Despite the differences in viscosity value, it's possible to note that the gelatinization process began around 50°C in all samples. Finally, in the sample without starch, the viscosity linearly varied with the sample temperature and showed the same viscosity values both in heating and cooling phases (**Figure 1**).

4.2. Heat penetration curves and validation of developed mathematical models

The simulated results for the four food systems were in agreement with the experimental data, as shown in **Table 1**. The global mean RMSE values for all samples resulted below 1.5°C and no significant differences were observed between experimental and simulated temperature data. In addition, in **Figure 2**, experimental and simulated temperature profiles at 57.5 mm from the bottom of the jar are compared for each food systems. As previously reported, since the overall coefficients of variation were lower than 5%, only average values (without error bars) are shown. The little variation in the calculated data may be due to the combined effects of the experimental and model assumptions such as Boussinesq approximation and thermal and physical properties of the materials. Furthermore, during the experiments, the presence of the multipoint temperature sensor may have changed the liquid flow pattern and, hence, affected the temperature profile of the fluid flow inside the jar. In the simulation, small-scale instabilities, mainly at the bottom of the jar, were observed probably due to the buoyancy effect: these helical and wavy helical vortices, coupled with the existing local turbulence and laminar flow model, could have generated little deviations between experimental and simulated data.

4.3. Results of in-silico simulations with CFD models

4.3.1. Comparison of temperature profiles

Initially, in order to evaluate the difference between the four food systems, the calculated time-temperature profiles at geometric centre (49.5 mm from the bottom) were compared (**Figure**

3): it's evident the effect of starch gelatinization on 6% and 10% samples with an evident change in the heating rate at about 55°C. This change was caused by the end of the convective heat mechanism as a consequence of the viscosity increase inside the system (**Figure 1**). The change in the heating and cooling rate was analysed by quantifying the global heating and cooling rate of the four samples, at three different distances from the bottom of the jar along the central axis (**Table 2**). The heat exchange rate decreased with increasing the starch concentration from 0 to 6% while, on the contrary, no significant differences were observed between 6% and 10% samples both in heating and cooling phase.

The differences in the temperature profile have been analysed also through the temperature contours obtained from the mathematical models: in **Figure 4** temperature contours of all the samples at difference time steps (5, 10, 25, 57 and 90 min) are reported. Initially (5 min), it's possible to note that the temperature contours were similar for all the samples because the convective heat exchange was predominant and SHZ was positioned near to the bottom of the jar, as expected. When the starch gelatinization temperature (about 50°C) was reached, approximately at 10 min, it began to emerge the different behaviour of the sample. 0% (**a2**) and 2% (**b2**) samples continued to show a convective heat exchange, while in 6% (**c2**) and 10% (**d2**) the temperature contours considerably changed. This is due to the transition from convection to convection+conduction/conduction as consequence of viscosity increase inside the systems (**Figure 1**). After 25 minutes, the samples 0% (**a3**) and 2% (**b3**) continued to maintain the same trend while, in the 6% (**c3**) and 10% (**d3**) samples the effect of convection to conduction heat exchange was very evident, especially in 10% where the SHZ moved to the geometric centre. The differences between samples were evident also in the cooling: 0% (**a4**, **a5**) and 2% (**b4**, **b5**) showed a convective heat exchange for the entire phase and the SCZ, as expected, moved from the bottom position to a position near the top in both samples. On the contrary, samples 6% (**c4**, **c5**) and 10% (**d4**, **d5**) followed the trend shown in the last part of the heating phase, conductive heat exchange resulted evident in both cases, especially in the last where the SCZ resulted located at the geometric centre. In the sample 6% (**c4**, **c5**) it's possible to observe that the SCZ didn't match the geometric centre despite the heat exchange took place by conduction: probably in this system fluid flows induced by natural convection were still present.

4.3.2. Comparison of velocity profiles

In a body uniformly heated at the surface and containing a cold liquid, the temperature differences between the wall and the core in turn lead to corresponding density differences. These induce buoyancy forces in the liquid resulting in natural convection flow patterns. The flow motions inside the jars are illustrated in **Figure 5**, where time-velocity profiles at geometric centre are reported. Analysing the first 20 minutes of heating it can be observed the effect of starch gelatinisation. The 6% and 10% samples curve showed a rapid slowdown from about 5 to 0 mm s^{-1} after 10 minutes (corresponding to the time necessary to reach 50°C in this position) and maintained the same values until the end of the treatment. For the 0% and 2% samples the velocity value tend to 0 mm s^{-1} only after 20 minutes and it was probably due to a gradual evening out of the temperature gradients (Varma and Kannan, 2006). The effects of convective motions returned evident during the initial phase of cooling, but only for 0% and 2% samples where the gelatinization did not occur and viscosity did not reach conduction to convection threshold value.

In order to study the velocity profile normal to the radial direction, a plane at 49.5 mm from the bottom was chosen. Initially, the convective flow patterns resulted evident in all the samples (**Figure 6a**) with upward movements near the wall surface (positive values) and downward movements along the centre of the jar (negative values). When the starch gelatinization occurred (around 10 min) it's possible to note a slowdown to 0 mm s^{-1} of fluid velocity in 6% and 10% samples while the samples 0% and 2% maintained the same trend previously observed (**Figure 6b**). Also during the cooling phase natural convection flow can be noted but in the opposite direction with respect to the heating phase. In **Figure 6c** it's evident a descending flow along the jar wall (negative value) and ascending ones along the central axis (positive value). This phenomenon was evident only in 0% and 2% samples, where the starch gelatinization did not prevent fluid flow. In samples 6% and 10% the speed values remained at 0 mm s^{-1} due to the absence of convective motions.

In **Table 3**, the thickness of the layer pertaining to the upward and downward moving velocity at mid-plane (49.5 mm from the bottom), along the entire treatment, is reported. After 5 minutes, when the convective motions were high, the thickness of upward layer was in agreement with Varma and Kannan (2006) who reported a thickness equal to 15% of the radial distance. This trend was evident in all the samples, except from the 2% sample, where the thickness of upward moving layer was slightly lower. The same value of thickness was observed also in the cooling phase, for the samples 0% and 2%, obviously referred to downward movement. For the samples 6% and 10% only data until 10 minutes are reported, because of starch gelatinisation that stopped the convective motions.

4.3.3. Comparison of slowest heating/cooling zone

Providing an adequate heat treatment means to ensure that the slowest heating zone (SHZ) receives the necessary heat for a sufficient period of time able to inactivate the most damaging microorganisms with the maximum maintaining of sensory and nutritive properties (Varma and Kannan, 2006). In most food products the SHZ has not a constant location inside the glass jar as it changes with process time and on the heating transfer mechanism. In this study, the point in the domain with lowest temperature was taken as the representative of SHZ/SCZ. The temperature and movement of this point obtained by means of the developed CFD models were traced for the four studied systems. **Figure 7** reports the variation of SHZ and SCZ position along the jar vertical axis during the heating (from 0 to 50 minutes) and cooling phase (for the remaining 50 minutes), respectively.

In all the four systems, the SHZ initially settled near the bottom between 15 and 20% of total height; it is basically due to convective currents that were established within liquid systems subjected to heat exchange. These movements created a recirculating flow, increasing the rate of heat transfer and also moved the SHZ from the geometric centre down near the bottom of the jar (Cordioli et al., 2015). However after first 10 minutes, for 6% and 10%, where the gelatinization of starch increased viscosity by several orders of magnitude, it's possible to observe the interruption of the convective movement. The heat exchange shifted from convection to conduction and thus caused the geometric centre to become the SHZ of the jar (**Figure 7**); this effect was more evident in 10%, where after 30 minutes of treatment the SHZ was near the geometric centre. Finally, in 6% the shift is reduced, but also present. The effect of starch gelatinization can also be evidenced by analysing the heating time (from 20 to 90°C) of different samples at SHZ. Sample 0% needed 12 minutes and heating time increased with starch concentrations as expected: 27 minutes for 2%, 36 minutes for 6% and 38 minutes for 10%. Values confirm the above observations: the highest differences were observed among 0, 2 and 6% samples while, on the contrary, the time difference between 6 and 10% samples may be negligible.

In the cooling phase, it's possible to note many of the effects already observed in the heating one. The 0% and 2% systems, where the heat exchange depends on pure convection, the SCZ moved close to the top of the jar at 74% and 85% of total axial distance, respectively. This shift of SCZ is due to inversion of convective movements inside jar. The cold fluid, with higher density compared to hot one, moved downward along the jar wall, then was deflected by the bottom surface of the can and starting moving in radial direction before go up along the central axis. These recirculating flows, like those previously seen in the heating phase (although in the opposite direction), induce a shift of SHZ towards the top of the jar.

5. *Conclusions*

In this study, the effect of four starch concentrations (0, 2, 6 and 10%) on heat exchange in food emulsion systems submitted to in-container thermal process was studied. From the thermo-rheological data, results showed that the effect of starch gelatinization deeply influences both viscosity and temperature profile of the samples, particularly at 6% and 10% starch concentration, where the viscosity increased by three and six orders of magnitude, respectively. With the data obtained from rheological analysis, four different 3D CFD mathematical models were developed to simulate the thermal treatment of such food systems taking into account also the gelatinization process. All the models were then successfully validated through experimental tests and an appreciable agreement between simulated and experimental data was obtained for all the samples (average RMSE value lower than 1.5°C).

Starting from the validated models, four simulations (one for each food system) with the same treatment conditions were carried out to compare the effect of starch concentration on heat treatment. During the heating phase, the change in heat exchange, caused by the starch gelatinisation and the increase in viscosity, resulted evident and the heating rate decreased with starch concentration in particular from 0 to 6% while only little differences were observed between 6 and 10%. With regard to the cooling phase, 6 and 10% samples showed a mainly conductive heat exchange mechanism with the slowest cooling point located at the geometrical centre of the jar; on the contrary, 2% samples continued to exhibit the “piston effect” typical of convective fluids.

In addition, the SHZ/SCZ moved differently among the samples. In 0% and 2% samples, where the convective motions were predominant, the SHZ and SCZ was positioned at 15-20% and 74-85% of total height in heating and cooling phase, respectively. In 6% and 10% samples, before the starch gelatinization the SHZ was positioned in the same position of the other samples; however, when the gelatinization took place, the SHZ tends to move toward the geometric centre, as expected.

In conclusion, this work shows the feasibility of mathematical models to be used in complex systems with significant changes in viscosity during the thermal process, such as soups or sauces with added starch. Data from models could be useful to fasten process design leading also to costs reduction.

References

ANSYS®, (2011). *ANSYS® Icepak User's Guide* (release 14, p. 700). Canonsburg, Pennsylvania, USA.

Berry Jr, M. R., Savage, R. A. & Pflug, I. J., (1979). Heating characteristics of cream-style corn processed in a Steritort: effects of head space, reel speed and consistency. *Journal of Food Science*, 44, 831-835.

Berry Jr, M. R. & Bradshaw, J. G., (1980). Heating characteristics of condensed cream of celery soup in a Steritort: heat penetration and spore count reduction. *Journal of Food Science*, 45, 869-879.

Cordioli, M., Rinaldi, M., Copelli, G., Casoli, P. & Barbanti, D., (2015). Computational fluid dynamics (CFD) modelling and experimental validation of thermal processing of canned fruit salad in glass jar. *Journal of Food Engineering*, 150, 62–69.

Dimou, A. & Yanniotis, S., (2011). 3D numerical simulation of asparagus sterilization in a still can using computational fluid dynamics. *Journal of Food Engineering*, 104, 394–403.

Kiziltaş, S., Erdoğdu, F. & Palazoğlu, T. K., (2010). Simulation of heat transfer for solid–liquid food mixtures in cans and model validation under pasteurization conditions. *Journal of Food Engineering*, 97, 449–456.

Liao, H., Rao, M.A. & Datta, A.K., (2000). Role of thermo-rheological behaviour in simulation of continuous sterilization of starch dispersion. *Food and Bioproducts Processing*, 78(1), 48-56.

Ramaswamy, H. S., Abbatemarco, C. & Sablani, S. S, (1993). Heat transfer rates in a canned food model as influenced by processing in an end-over-end rotary steam/air retort. *Journal of Food Processing and Preservation*, 17, 269-286.

Singh, A., Singh, A.P. & Ramaswamy, H.S., (2015). Computational techniques used in heat transfer studies on canned liquid-particulate mixtures – A review. *Trends in Food Science & Technology*, 43, 83-103.

Sun, D.W., (2007). *Computational fluid dynamics in food processing*. Boca Raton: CRC.

Tattiyakul, J., Rao, M.A. & Datta, A.K., (2001). Simulation of heat transfer to a canned corn starch dispersion subjected to axial rotation. *Chemical Engineering and Processing*, 40, 391–399.

Tattiyakul, J., Rao, M. & Datta, A.K, (2002). Heat transfer to three canned fluids of different thermo-rheological behaviour under intermittent agitation. *Food and Bioproducts Processing*, 80(1), 20-27.

Varma, M.N. & Kannan, A., (2006). CFD studies on natural convective heating of canned food in conical and cylindrical containers. *Journal of Food Engineering*, 77, 1024–1036.

Yang, W.H. & Rao, M.A., (1998). Transient natural convection heat transfer to starch dispersion in a cylindrical container : numerical solution and experiment. *Journal of Food Engineering*, 36, 395-415.

Table 1. RMSE values (°C) obtained for the model validation.

Sample	***location in the jar***				
	31.5 mm	*57.5 mm*	*70.5 mm*	*96.5 mm*	***average***
0 %	1.43	1.09	1.07	1.22	**1.20**
2%	1.30	1.03	1.64	1.58	**1.39**
6%	1.84	1.31	1.23	1.25	**1.41**
10%	1.62	1.81	1.05	1.28	**1.44**

Table 2. Global heating and cooling rate of the four systems at three different positions along the central axis. Values in the same row with different letters showed statistically difference ($p < 0.05$).

	Height from bottom (mm)	***0%***	***2%***	***6%***	***10%***
heating (°C min^{-1})	24.8	5.35	2.39	1.70	1.68
	49.5	5.65	2.70	1.70	1.62
	74.3	5.97	3.34	1.97	1.79
	mean	**5.66**^{a}	**2.81**^{b}	**1.79**^{c}	**1.69**^{c}
cooling (°C min^{-1})	24.8	-5.82	-3.01	-2.02	-1.89
	49.5	-5.64	-2.47	-1.76	-1.71
	74.3	-5.79	-2.20	-1.82	-1.89
	mean	**-5.75**^{A}	**-2.56**^{B}	**-1.87**^{C}	**-1.83**^{C}

Table 3. Comparison of thickness (mm) of the upward moving flow (up) and of the downward moving flow (down), along the radial direction (at 49.5 mm from the bottom). Values at different time steps were reported (5, 10, 25, 45, 57, 70 and 90 minutes).

	Time	***0%***		***2%***		***6%***		***10%***	
	(min)	***up***	***down***	***up***	***down***	***up***	***down***	***up***	***down***
heating	***5***	3.8	21.2	2.6	22.4	4.0	21.0	3.9	21.1
	10	3.6	21.4	2.7	22.3	-	-	-	-
	25	6.5	18.5	3.3	21.7	-	-	-	-
	45	10.0	15.0	4.4	20.6	-	-	-	-
cooling	***57***	16.1	4.5	21.7	3.3	-	-	-	-
	70	19.2	5.8	21.4	3.6	-	-	-	-
	90	15.3	9.7	20.5	4.5	-	-	-	-

Figure 1. Thermo-rheological profiles of the four different food systems (viscosity in logarithmic scale).

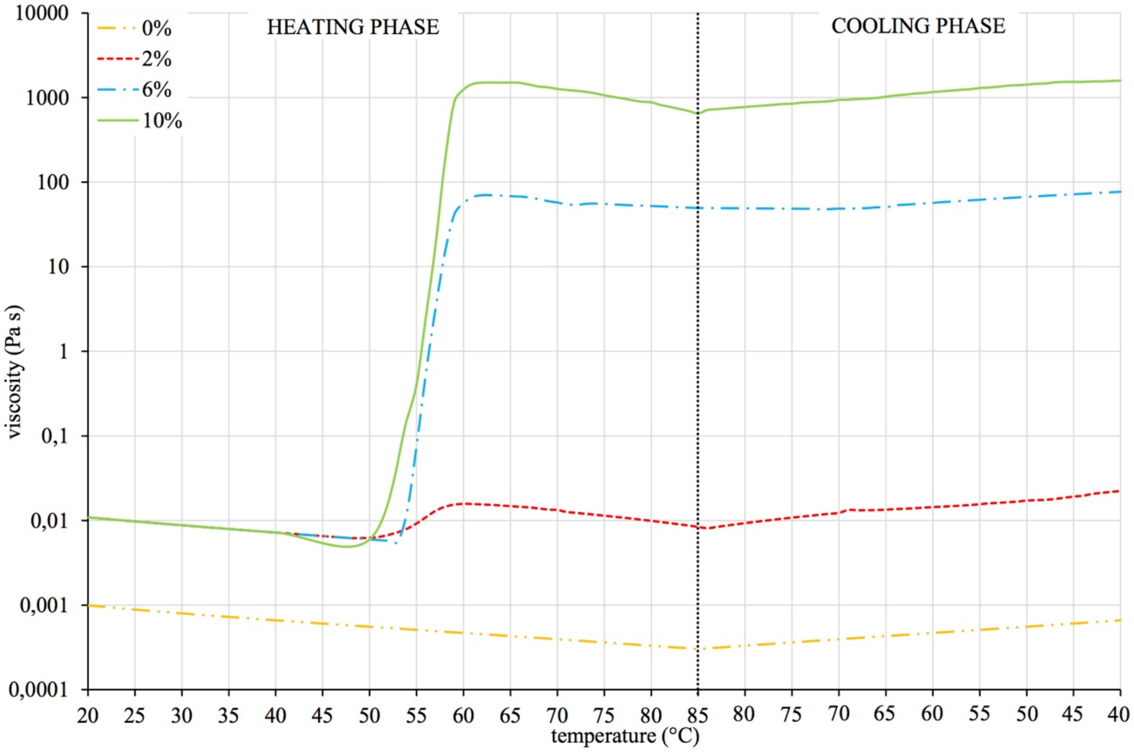

Figure 2. Comparison of the temperature profiles between experimental data and mathematical model results: (**a**) 0%, (**b**) 2%, (**c**) 6% and (**d**) 10%.

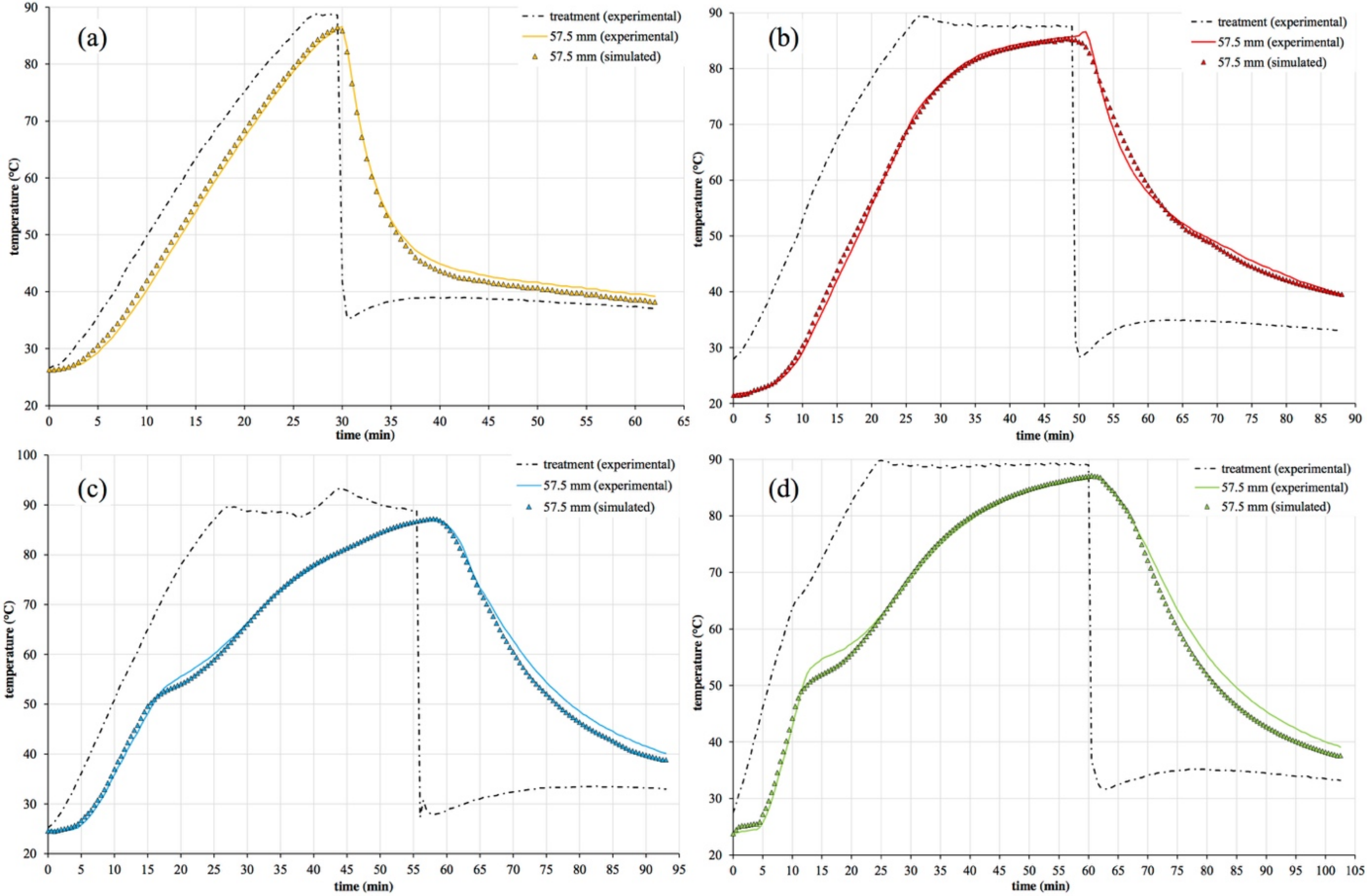

Figure 3. Comparison of time-temperature profiles at geometric centre of the four food systems.

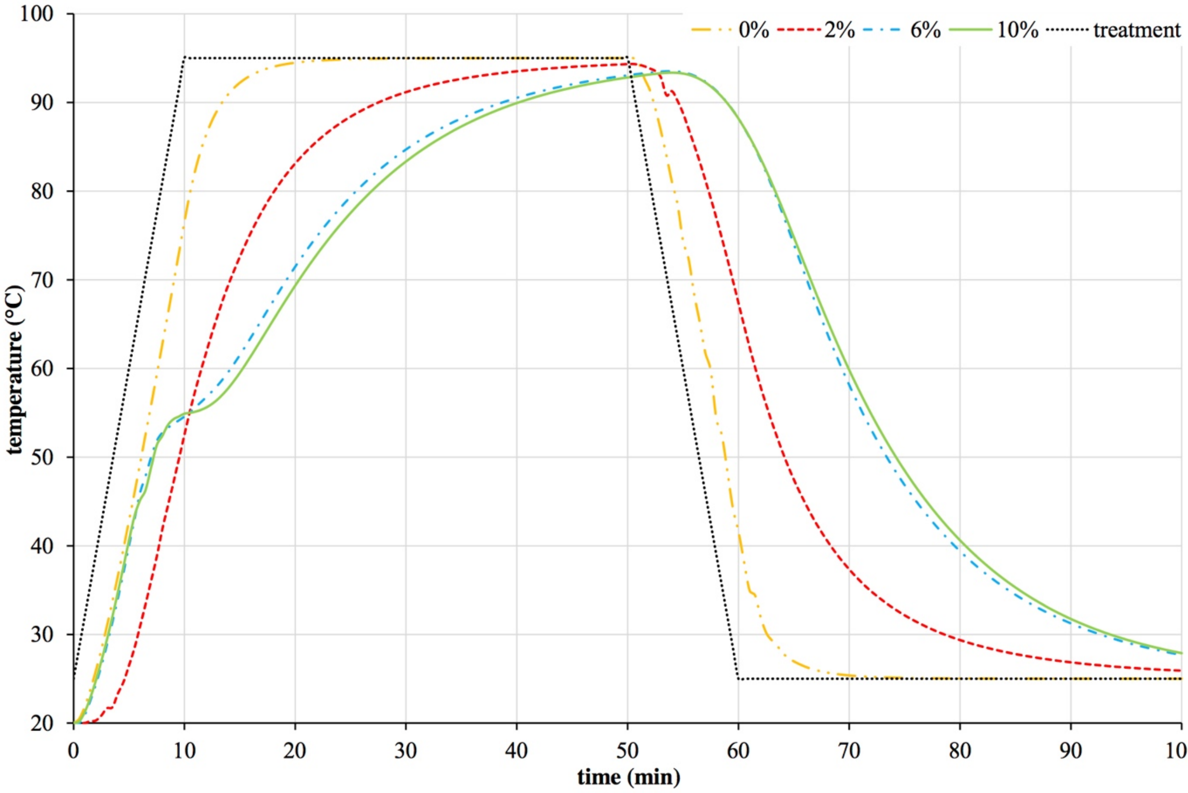

Figure 4. Temperature contours at 5 (**1**), 10 (**2**), 25 (**3**), 57 (**4**) and 90 (**5**) minutes: (**a**) 0%, (**b**) 2%, (**c**) 6% and (**d**) 10%.

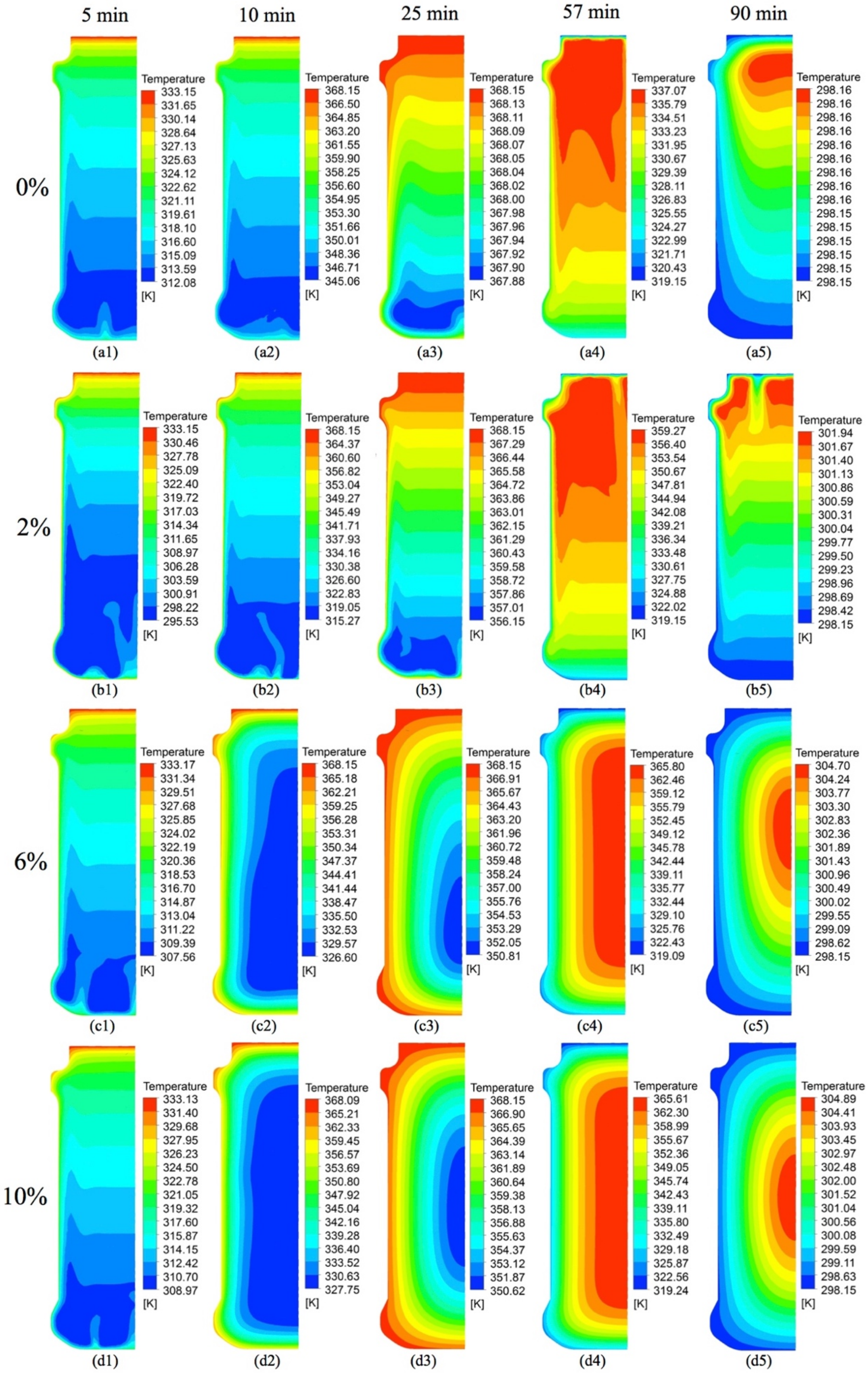

Figure 5. Time-velocity profiles at geometric centre of the four food systems calculated by means of the developed models.

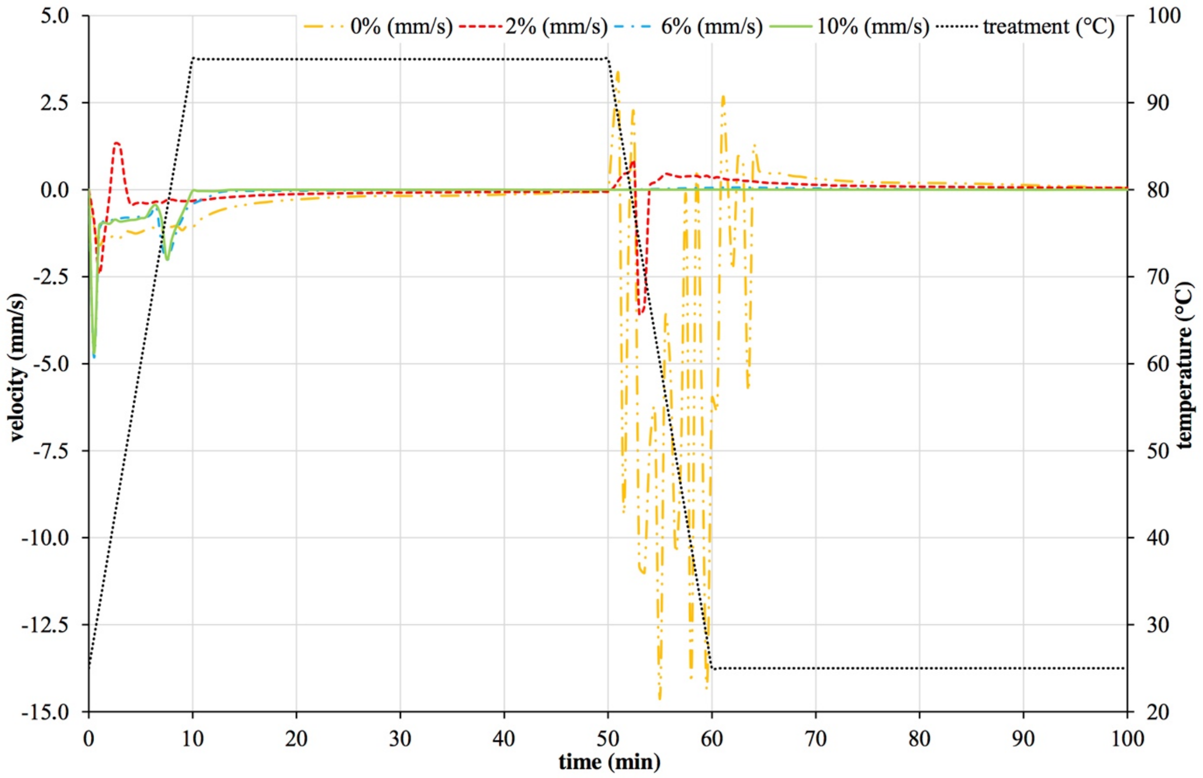

Figure 6. Comparison of the velocity profiles normal to the radial direction at 49.5 mm from the bottom: (**a**) 5, (**b**) 10 and (**c**) 70 minutes.

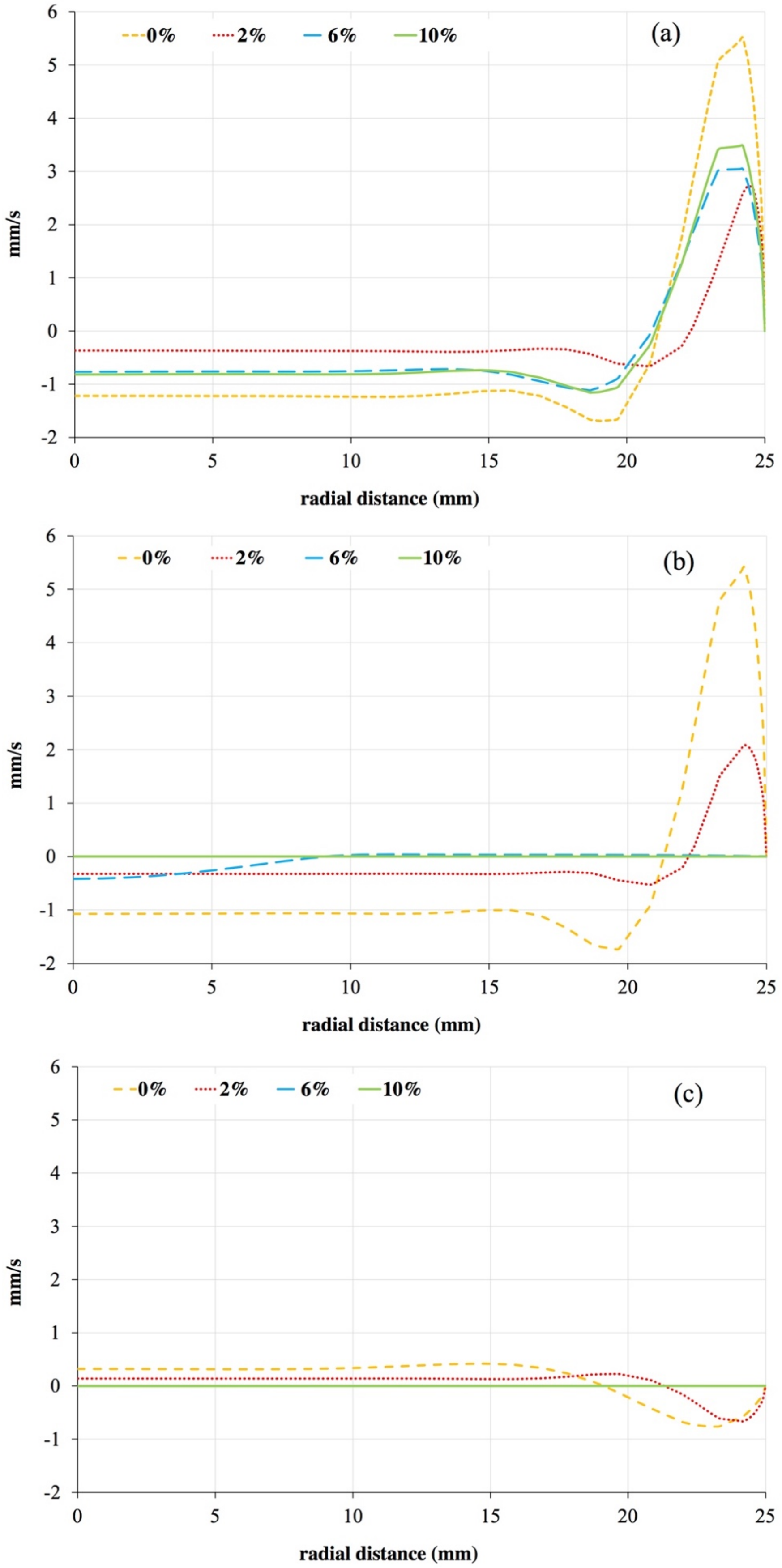

Figure 7. Comparison of the SHZ/SCZ locations during heat treatment.

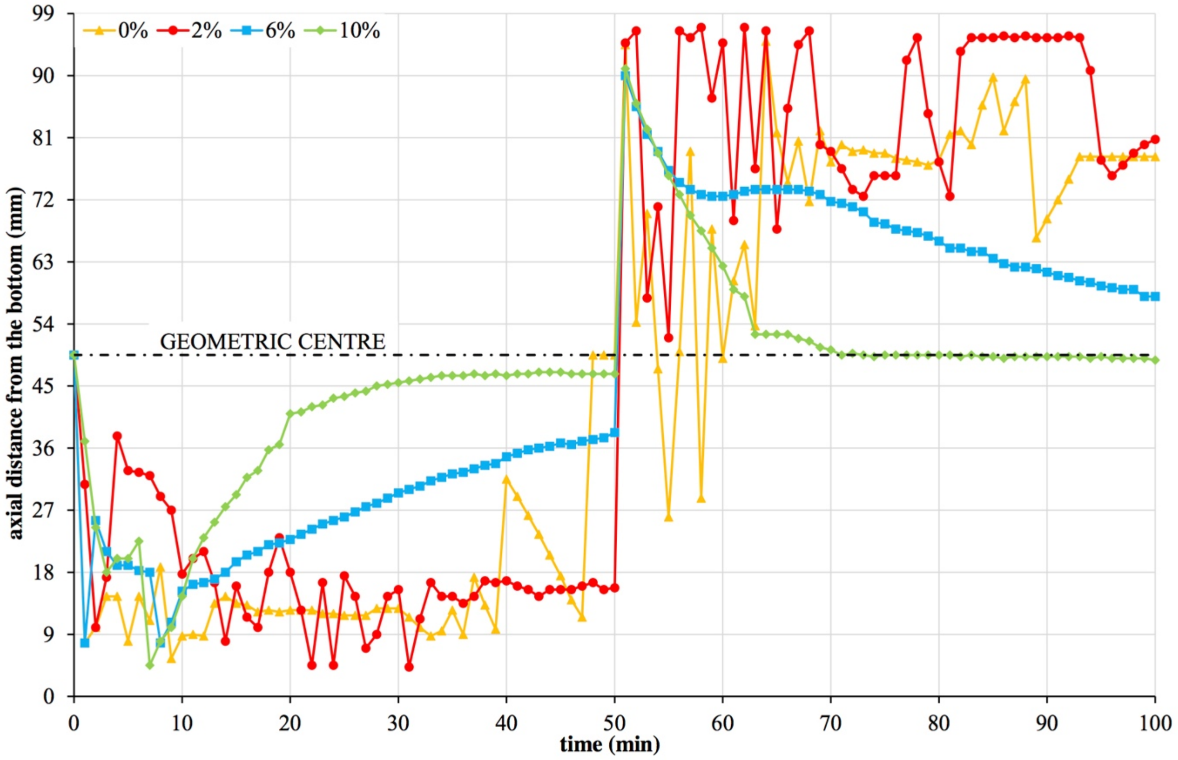

Computational Fluid Dynamics (CFD) techniques to investigate the effects of jar geometry and starch concentration on thermal treatment of food systems

Matteo Cordioli, Matteo Malavasi, Massimiliano Rinaldi and Davide Barbanti

Department of Food Science, University of Parma, Parco Area delle Scienze 47/A, 43124
Parma, Italy

To be submitted

1. Introduction

Thermal treatment is one of the most common preservation process for foods. It permits to increase the storage life of a food and make it safer for human consumption, by destruction of pathogenic microorganism and inactivation of deleterious enzymes. Over the years two different method regard conventional thermal treatment were developed: aseptic processing where the food is sterilized prior to packaging and canning where the product is packed and then sterilized (Ghani et al., 2002). As regard the thermal process of canned food, Kumar et al. (1990) reported that magnitude of thermal process depends upon the product, container type, size and orientation and heating medium characteristics.

In particular, the heat transfer modes in a canned food can occur by conduction or by either natural or forced convection according to food structure and characteristics of the heating system (Lespinard and Mascheroni, 2012). One of the variables which affect the type of heat exchange involved in thermal treatment was the presence of thickening agents such as starch. Many foods contain starch either as a natural component or that was added to impart viscosity (Tattiyakul et al., 2001). The behaviour of starch component in a food system submitted to thermal treatment can affects greatly the results of process itself. When a starch dispersion is heated above the gelatinization temperature, the granules swell and form a viscous dispersion. This process induce a great increase of apparent viscosity of the food system and the transition from fluid-like to viscoelastic behaviour deeply influence the heat transfer during thermal process (Yang and Rao, 1998). The viscosity is one of the major factors affecting the heat exchange: the higher the viscosity of the fluid, more resistant it would be to movement and thus heat exchange inside the food system would be slower (Tattiyakul et al., 2002). As reported by Cordioli et al. (2016) the heat exchange mode inside a system containing starch changes along the thermal treatments. Until the gelatinization temperature the system results fluid and the heat exchange was mainly by convection (conduction can be considered negligible), while above this critical value, as results of increasing of viscosity, the convective current tend to disappear and heat exchange became mainly by conduction. Not only the presence or absence of starch affect the heat exchange but also the percentage as reported by Ramaswamy et al. (1993), which indicate a reduction of heating rate of 60% passing from 3 to 4% of starch concentration. Also Cordioli et al. (2016) investigated the effect of starch concentration on the heat exchange and demonstrate that above 6% of starch concentration no significant differences were obtained. Therefore, knowledge of the critical concentration of starch which separate the convective from conduction heat exchange behaviour results of great importance because it affect not only the efficiency but also the efficacy of a thermal treatment.

As introduced previously, also the container type must be considered in a design of a thermal treatment. In particular the geometries of the container in which the food system is placed can affect the result of a thermal treatment as investigated by Varma and Kannan (2006), where the focus was to enhance the natural convection heat transfer rates through geometry modification and varying its orientation. The Authors concluding that container geometries affect greatly heat exchange, mainly regard the convective mode, where the convective currents results influenced by the shape of container. Also Lespinard and Mascheroni (2012) investigated the effect of different geometries on thermal treatment of viscous food, in particular cylindrical glass container of different volume and dimensions. It concludes that when a container is replaced for another of the same volume but different height/diameter ratio, the needed sterilization time varies.

In all the works previously reported the parameters taken into consideration to evaluate the performance of thermal treatments were various, the temperature and velocity profile, the position of slowest heating zone and the sterilization time. In some cases, however, the experimental measurement of these parameters result difficult due to low magnitude of values (such as fluid velocity) and the risk to disturb the temperature-velocity field by inserting a probe inside the food system. Further, the slowest heating zone is not fixed at one location (especially in systems in which the heat exchange mode changes along thermal treatment). For these and other reasons, mathematical modelling approach has been extensively applied to predict the temperature patterns in the thermal treatments of canned foods. In particular, numerical methods involving Computational Fluid Dynamics (CFD) to map the temperature-velocity profiles as well as the movement of the slowest heating zone have received attention in recent time due to the increase in computational speed and reliability as well as difficulties associated with conducting experiments (Varma and Kannan, 2006).

To the Authors best knowledge, in literature still lack a comprehensive and deep study on thermal treatments of food system in which the heat exchange mode change along treatment (due to starch gelatinization) and the evaluation how commercial glass jars of different geometries can affect the efficacy and efficiency of the process. The objective of this work was to investigate, by means of CFD models experimentally validated, the heat exchange in food systems with different starch concentrations packed in glass jars with different geometries.

2. *Materials and methods*

2.1. Food systems characteristics and jar geometry description

The liquids samples were prepared following the same steps reported in Cordioli et al. (2016): a dispersions of oil (12% w/w) in water were prepared at different modified waxy maize starch (Frutarom, Parma, Italy) concentrations (0, 2, 3, 4, 5 and 6%). To guarantee the stability of the dispersion along thermal treatment and prevent the separation of the two phases soy lecithin was added (5% w/w) to the solution. The system, after the preparation, was allowed resting for at least 1 hour to ensure a good deaeration.

Five different jar shapes with the same nominal volume (314 mL) and about the same weight/diameter ratio (around 1) were tested to evaluate the effect of geometry on the heat exchange (**Figure 1**): glass thickness, measured with a calliper at different locations of the jars, resulted in an average value of about 3 mm. All the jars were hermetically closed with a screw lid after filling.

2.2. Rheological characterization

As regard the rheological profile, two different parameters were investigated: temperature of gelatinization and maximum viscosity value: in this way, it’s possible to obtain the viscosity value in function of the temperature for all the different tested solutions.

The temperature of gelatinization was studied by means of concentric cylinder geometry mounted on ARES rheometer (Ta Instruments, New Castle, DE, USA) and the dimensions of the geometry were 34 mm cup diameter, 32 mm bob diameter and height of 33 mm. All the analyses were conducted at a shear rate of 50 s^{-1} (the minimum value to get accurate values also before the gelatinization) and temperature was linearly increased from 20 to 80°C with a heating rate of 2.2±0.1°C/min, through a thermostatic bath (Thermo Fisher Scientific, Waltham, MA, USA) connected to rheometer. All the trials were performed in triplicate.

Once identified the gelatinization temperature, to characterize the viscosity after gelatinization oscillatory tests with parallel plate (diameter = 50 mm) were run in triplicate. First, the linear viscoelastic region (LVR) was identified by means of strain amplitude sweeps (1 Hz) from 0.009% to 15% at 65°C for each solution. Then, a test at a constant strain (inside LVR region) and frequency (1 Hz) was carried out from 35 to 85°C (with a temperature ramp of 1°C/min) for each solution to identify the viscosity in function of temperature after gelatinization.

Because of the low shear rate, viscosity may be assumed to be independent of shear rate and the fluid as a Newtonian fluid: due to this consideration, in our model, viscosity was considered to vary only with the temperature.

2.3. Experimental thermal treatment

The experimental thermal treatments were conducted taken into account both heating and cooling phase in order to emphasize the difference between the systems where the heat exchange was convective in both the phases and the systems where, after gelatinization, the heat exchange occurred by convection + conduction or mainly by conduction, as reported by Cordioli et al. (2016). The tests were carried out in a small scale static pasteuriser (JBT FoodTech, Parma, Italy), controlled by PLC. Inside the pasteuriser (width = 550 mm; length = 730 mm) water was sprayed over the containers from two nozzles at a rate of 2800 l h^{-1} with a spread angle of 120°. The jars were positioned at the centre of the pasteuriser between the nozzles. As highlighted by Cordioli et al. (2015), during preliminary test no temperature variations were observed among jars placed in different positions of the plant and also along the circumference of a single jar: this was due to the high-water flow and to the high spreads angle of the nozzles, allowing homogeneous temperature distribution inside the plant. Three repeated thermal treatments were performed on three different jars to evaluate the average temperature and standard deviation of the treatments. The overall coefficients of variation resulted lower than 5% and hence, for a clear reading, in figures only average values are reported. The experimental thermal treatments were composed by a heating phase where the hot water temperature was set at 90°C and samples heated from 30 to 85°C at the slowest multipoint sensor point. In the cooling step, the water temperature was set at 25°C and the treatment was considered finished when the slowest multipoint sensor point reach 30°C.

The temperatures inside the jar were measured using wire thermocouples (K-type; Ni/Al-Ni/Cr) connected to MV100 acquisition system (Yokogawa Electric Corporation, Tokyo, Japan). In addition, a multipoint temperature probe was positioned along the central axis of the jar through a hole made in the centre of the lid. This probe (length = 97.5 mm; diameter = 3.5 mm) recorded the temperature at different height in functions of the type of the jar. In **Table 1** the height at which the multipoint probe measure the temperature for each geometry is reported. The temperature at half height of the outer wall, on the bottom outer side of the bottom of the jar and on the upper side of the lid were also measured by sticking a wire thermocouple (diameter = 0.9 mm, Gauge number = 20) on the external surface with a 1 cm^2 of an appropriate scotch tape. Data obtained from these wire thermocouples were used as temperature values for boundary conditions of the models validation stage. Both for multipoint probe and single thermocouple, an acquisition rate of 1 s was used and time-temperature data were collected in an Excel® ASCII worksheet.

2.4. Statistical analysis

Means and standard deviations were calculated with SPSS (release 23, IBM, Armonk, NY, USA) statistical software. SPSS was used to perform two-way-analysis of variance (ANOVA) and Tukey post hoc test at a 95% confidence level to evaluate the effect of starch concentration and jar geometry at a significance level of 0.05 ($P < 0.05$). Starch concentration and jar geometry were considered as variables.

3. CFD modelling

3.1. Define domain and mesh details

The thermal treatments were simulated by means of 3D CFD models, starting from geometries developed with SolidWorks® 2015 (Dassault systèmes, Vélizy-Villacoublay, France) software. To reduce the computational effort and improve the precision of the solution of CFD model, the domains were assumed to be symmetric regarding two planes through the vertical axis of each jar. Starting from the geometries reported in **Figure 1**, only a section was taken into consideration for the model development (as highlighted by the imagines on the right side of the **Figure 1**). During a preliminary study the differences between the results obtained from the model of the entire domain were negligible with respect to those obtained from domain sections and the lowest one was then used. In this way, it's possible to increase the density of mesh and obtain a better result.

The 3D geometries were then imported into the ICEM CFD® software (Canonsburg, Pennsylvania, USA) and discretized into an unstructured hexahedrical and wedge mesh. The mesh was optimized and finalized for a better accuracy and reducing computational time. The numbers of elements, the values of maximum and minimum element edge dimension and the skewness values of each geometries considered in this work were reported in **Table 2**. From a quality point of view good results were reached for every geometry (ANSYS Icepak User's Guide, 2011).

3.2. Numerical model

The software ANSYS® CFX v16 (Cannonsburg, Pennsylvania, USA), run on HP Z420 Workstation (Palo alto, California, USA), was used to solve the governing continuity, momentum and energy equations for the defined geometry and associated boundary conditions. The domain was defined in the global co-ordinate frame in which the solver carries out the calculations. To solve the coupled system of partial differential equations, the high-resolution scheme with second order backward Euler method was adopted.

The generalized transport equations solved are:

a) *The continuity equation*

$$\frac{\partial \rho}{\partial t} + \nabla \cdot (\rho V) = 0 \qquad (1)$$

b) *The momentum equation*

$$\frac{\partial \rho V}{\partial t} + \nabla \cdot (\rho V \cdot V) = \nabla \cdot \left(-\mathrm{p}\delta + \mu \cdot (\nabla V + (\nabla V)')\right) + S_M \quad (2)$$

c) *The energy equation*

$$\frac{\partial \rho h_{total}}{\partial t} - \frac{\mathrm{Dp}}{Dt} + \nabla \cdot \left(\rho V c_p T\right) = \nabla \cdot (\mathrm{k} \cdot \Delta \mathrm{T}) + S_E \qquad (3)$$

Where t is the time (s), V the velocity vector (m s^{-1}), p the pressure (Pa), μ dynamic viscosity (Pa s), k thermal conductivity (W m^{-1} K^{-1}), c_p the specific heat capacity (J kg^{-1} K^{-1}). Natural convection was modelled using the Boussinesq approximation, which uses a constant density fluid model, but applies a local body gravitational force throughout the fluid that is a linear function of water thermal expansivity $\beta = 2.57*10^{-4}$ K^{-1} (obtained from the software library) and of the local temperature difference. The buoyancy source is added to the momentum equation as follows:

$$S_M = -\rho_{REF} \cdot \beta \cdot (\mathrm{T} - T_{REF}) \cdot g \qquad (4)$$

Where ρ_{REF} and T_{REF} are the density and temperature at the boundary wall condition and g is the gravitational force. No internal energy source terms (S_E) were taken into account.

The liquid inside the jars at time = 0 s was assumed to be at rest and at uniform temperature while a laminar flow mode was assumed to occur throughout the treatment as consequence of convective heat transfer. In addition, a no-slip condition was applied with velocity = 0 m s^{-1} of the fluid relative to the internal jar wall.

A good accuracy was reached setting and adaptive time step with a value between 0.2 and 10 s: this guarantees a maximum Courant number of 1 (Boz et al., 2014) and ensures a right compromise between the solver time and the quality of the results. For all the models the initial time step was set at 0.1 s. High resolution advection schemes were adopted for all simulations, to achieve second order accuracy. The convergence criterion was defined as residual root mean square (RMS) value lower than 10^{-4}, as reported by others Authors for similar systems (Augusto and Cristianini, 2011; Kannan and Sandaka, 2008) and the overall imbalance in the domain less than 1% for all variables.

3.3. Boundary conditions

A transient simulation was carried out due to the variation of boundary conditions with time, in particular the temperature along the external surface of the jars. For the model validation, the time-temperature profiles get from the three thermocouples positioned along the outer surface of the jars (bottom, side and top) were imposed as boundary conditions. Then, starting from validated models, to evaluate the effect of starch concentration and geometry of the jars, different simulations were conducted with the same time-temperature profile. The treatment was composed of heating phase at 95°C for 50 minutes followed by cooling step at 25°C for the same time.

3.4. Thermal and physical properties

Six materials were created in the pre-processor software with specific thermal and physical properties while the glass domain was already presents in the software library. The values for each starch concentration were quantified from analytical composition of solutions (Choi and Okos, 1985) except the viscosity values obtained from experimental measurements. Density, thermal conductivity and specific heat varied from 986 to 1001 kg m^{-3}, from 0.509 to 0.607 W m^{-1} K^{-1} and from 2994 to 4182 J kg^{-1} K^{-1}, respectively. Starting from preliminary sensitivity analysis, apparent viscosity resulted the physical parameter which mainly influenced the heat exchange due to the large variation as consequence of gelatinization process. Consequently, for the liquid domain, the variation of all thermal and physical properties of the fluid as consequence of temperature increase in the experimental range where considered negligible while the experimental apparent viscosity function with temperature was used.

3.5. Models validation

The developed models were validated by comparing experimental temperature values with the predicted ones. The accuracy of the prediction was assessed by determining root mean square error (*RMSE*) with the following:

$$RMSE = \sqrt{\frac{\sum_{i=1}^{n}(T_E - T_P)^2}{N}} \qquad (5)$$

Where T_P is simulated temperature (°C), T_E is experimental temperature (°C) and N number of value compared. The lower RMSE value demonstrated a better compatibility of the simulation results (Boz et al., 2014).

Starting from the results obtained by Cordioli et al. (2016), where experimentally validation was conducted on different starch concentrations, in this work the models regarding the different jars geometries were experimentally validated. As highlighted by Cordioli et al. (2016) this kind of CFD models followed very well the experimental trends also in systems with breaking heating curve. So, the focus of the validation phase, for this work, were the systems containing water, where the jar geometries can affect the convective heat transfer more than systems where, after passing the gelatinization temperature the heat exchange mode became conductive. Moreover, to reduce the time necessary for the experimental phase the cooling phase was validated only for two geometries. Only the hexagonal geometry and high cylinder ones were considered, which represent the two extreme geometries. The others can be considered included in these two extremes, so if these two geometries result validated also the other three can be considered validated.

4. Results and discussion

4.1. Validation of fluid dynamics models

The simulated results for the five geometries filled with water were in agree with the experimental tests as shown in **Table 3**, where the values of RMSE calculated on 5 points along the container central axis are reported. The little variations in the calculated data may be due to the combined effects of the experimental and model assumptions such as Boussinesq approximation and thermal and physical properties of the materials. Also the presence, during the experimental thermal treatments, of the multipoint temperature sensor may have changed the liquid flow pattern and, hence, affected the temperature profiles of the fluid as reported by Marra and Romano (2003). Moreover, in the simulation, small-scale instabilities were observed probably due to the buoyancy effect: these helical and wavy helical vortices, coupled with the laminar flow model, could have generated little deviations between experimental and simulated data. Besides these considerations, the global mean RMSE resulted of 1.03°C a value in accordance with the literature (Boz et al., 2014; Cordioli et al., 2016). Furthermore, taken into consideration the accuracy of thermocouples employed for the experimental test (±1°C), the RMSE values obtained could be considered acceptable and models resulted experimentally validated and useful for the study of fluid dynamics.

4.2. Temperature profiles

In **Figure 2** the temperature profiles at the geometric centre obtained from the simulations are reported. By considering samples with only water (**Figure 2,** panel **a),** there are little differences between high cylinder, short cylinder and hexagonal while the flared geometry gave the highest heating rate in both heating and cooling stages and on the contrary the squared geometry gave the lowest ones in both phases. Probably, square jar resulted the slowest in the thermal exchange due to the presence of shoulders with a very high angle that slowed down the convective motions; flared jar even if presented the greatest diameter presented a profile advantageous for convective motions.

In panel (**b**) the effect of starch concentration was highlighted by taking into consideration the flared geometry that, as seen before, gave the best performance among 0% samples. As expected, the temperature profile was highly influenced by the starch concentration and the temperature curves tended to shift to the right (which represents a slowing of heating and cooling rate) as viscosity increased. For the samples with higher starch concentrations (4, 5 and 6%) it's possible to clearly note the breaking curve effect due to the change from convective to conductive heat exchange mode. These results were confirmed by Cordioli et al. (2016), that reported both the effect of starch gelatinization and the change in the heating rate at about 55°C for samples at 6 and 10% of starch.

Temperature profiles can be easily compared by means of the temperature contours obtained from the CFD models referred to the two most different geometries (**Figure 3**) at different time steps (180 s, before gelatinization; 510 s, after gelatinization; 3330 s at the beginning of the cooling phase) and at 0 and 6% of starch concentrations.

Initially (180 s), for both the concentrations the effect of jar geometry appeared evident: flared jar (panel **F0p** and **F6p**) showed higher mean temperatures compared to the squared ones (panel **S0p** and **S6p**). From the temperature contours it's also possible to identify the regions of the jar whose influenced the convective currents and the heat exchange, as consequent: the presence of corners near the neck of the squared jar increased temperature stratification (**S6p**) probably due to the reduction of convective currents. Despite the differences in temperatures between the studied geometries and starch concentrations, the slowest heating zone (SHZ) resulted positioned near the container bottom at about 15/20% of total height for all the cases as a consequence of convective heat exchange.

At 510 s, above the gelatinization temperature, while the 0% samples (panel **F0g** and **S0g**) continued with the same behaviour observed in the previous time step for both geometries, in the 6% samples (panel **F6g** and **S6g**), the temperature stratification considerably changed due to the transition from convective to conduction heat exchange as a consequence of viscosity increase (Cordioli et al., 2016). The convective disappeared for both the geometries and the SHZ moved from the bottom of the jar toward the geometric centre. In addition, the differences between the two geometries tended to diminish as a consequence of conductive heat exchange which is affected mainly by the characteristic dimensions (like diameter and height) and less by the geometry of the jars, due to the absence of convective currents. The flared and squared geometries presents similar characteristic dimensions and the temperature stratification in conductive conditions resulted similar.

These differences can be better highiligheted by considering the temperature stratification after 3330 s, at the beginning of the cooling phase. For the systems in whom the gelatinization didn't take place and heat trasfer mode remained convective (panel **F0c** and **S0c**), the slowest cooling zone (SCZ) resulted positioned near the top of the jars due to inversion of convective movements inside jar, in accordance with natural convective heat exchange theory. For the highest concentration samples (panel **F6c** and **S6c**), the conductive heat exchange mode resulted clearly evident in both the geometries. The SCZ results positioned near the geometric centre, with a tendence toward the top of the jar. This is probably caused by the insulation effect of the headspace (static air layer with 10 mm thickness) while this effect resulted less evident in the heating phase because of the convective currents (before the gelatinization).

4.3. Heating/cooling rate and Overall heat transfer coefficient OHTC

Figure 4 reports the heating rate from 35 to 85°C (panel **a**) calculated from three points along the central axis (15, 50 and 85% of total height) and, as expected, the heating rate decreased with the increase of starch concentration. In particular, 5 and 6% samples can be considered similar for almost all geometries probably because of the exceeding of critical starch concentration. Above the 5% of concentration the heat transfer was no more influeced by the percentage of starch, maybe due to the complete disappereance of convective movements.

In order to compare the absolute heat transfer performances of the tested geometries, the mean overall heat transfer coefficients (OHTC) were calculated during the heating phase by the following equation (Bergman et al, 2011):

$$\bar{U} = \frac{\dot{m}c_p}{A_s} \cdot \ln\frac{(T_\infty - T_{m,o})}{(T_\infty - T_{m,i})} \qquad (6)$$

Where $\bar{U}$ is overall heat transfer coefficient (W m^{-2}), A_s jar outer surface (m^2), $\dot{m}$ mass flow rate (k s^{-1}), T_∞ treatment temperature (°C), $T_{m,o}$ initial temperature of the product inside the jar (°C) and $T_{m,i}$ temperature of the product inside the jar at time step i (°C). The obtained data are reported in **Table 4**. In general, short cylinder showed the lowest OHTC values and the lowest heat exchange performance probably due to its low specific surface compared to other geometries. Only at 6% flared geometry gave a lower value probably due to the rapid gelatinization of starch and viscosity increase. On the contrary the geometry with the overall best performances was the hexagonal one that gave the highest OHTC values followed by the high cylinder: cylinders with elongated shapes (H/D = 1.5) are well known to be very efficient in exchange phenomena; similarly results of hexagonal jar probaly are due to two facts: on one hand the studied geometry is regular and on the other presents a high H/D value of about 1.15. Regarding jar geometries, it's possible to note great differences between geometries mainly at lower starch concentrations. The standard deviation calculated between the mean heating rates obtained for each geometry (data not shown) tended to decrease linearly with the increasing of starch concentration. This reinforces the theory developed in the previous paraghrap: the geometry of the jar affected mainly systems in which the heat exchange occourred by convective mode.

The same analysis was carried out for the cooling step and reported in panel **b** with a similar behaviour. In particular, the cooling rates tended to decrease with increasing of starch concentration and also the temperature stratification followed the same trend. From the data reported in **Figure 4b** the difference between the sample 0% and all the others emerges more pronounced. This behaviour can be associated with the starch gelatinazion process. Along the heating phase, until the temperature of gelatinization was reached the heat exchange was mainly convective for all the samples contributing to reduce the differences between the samples. In the cooling phase, the samples in which gelatinization took place showed conductive heat exchange mode for the whole duration of cooling phase. On the contrary, in the samples, like the 0%, where the gelatinization didn't take place, showed yet convective heat exchange also in this stage. For the same reason, regarding the effect of geometries, the main difference can be observed only at low starch concentration (0 and 2%) where convective current remain present also in the cooling step. In this case, the standard deviation calculated between the mean cooling rate values obtained for each geometry (data not shown) can be approximated to an exponential trend, confirming the great difference between conductive and convective heat exchange on the heat transfer rate.

4.4. Velocity profile

The convective currents can be better understand by comparing the velocity profiles of the flow normal to a line positioned in radial direction at 50% of the jar height (**Figure 5**). In all the cases, it's possible to note for the heating phase (panel **a** and **c**) the ascending flows (positive velocity values) near the jar wall and the descending one (negative velocity values) near the jar axis. In the cooling step (panel **b** and **d**) the movements resulted inverted; along the jar wall the flow results descending while along the central axis ascending. Furthermore, in panel **(a)** and **(b)** it's possible to evaluate the effect of starch concentration on the magnitude of flow velocity: as expected, both for the heating and cooling phase the maximum velocity tended to decrease with the increasing of starch concentration. Also the effect of jar geometries on 0% samples can be assessed (**Figure 5** panel **c** and panel **d)** by considering the velocity profile of different jars. First of all, the data obtained from the simulations, as regard to the order of magnitude, resulted in accordance with literature on similar systems (Lespinard and Mascheroni, 2012). As possible to note, all the geometries seem to give the same behaviour with little discrepancy both in heating and cooling phases. Probably the most important difference can be observed near the bottom and the top of the jars, where the geometries difference resulted more pronounced. The effect of starch concentration and jars geometries can be observed also by comparing the velocity profiles at the geometric centre along the thermal treatment of the same samples considered in the *Section 4.2*. In **Figure 6** the differences between flared and square geometries at 0 and 6% are reported: as expected, the velocity profile resulted affected mainly by the starch concentration. Moreover, at 6% of starch the differences between the two geometries tended to reduce by conductive heat exchange modes. However, at low starch concentration (0%) this trend confirmed what observed previously about temperature profile: the flared geometry seems to has higher flow velocity values probably related to a greater heat exchange rate and to a more efficient thermal treatment as consequence.

4.5. Comparison of cook values

To evaluate the global effect of both starch concentration and jar geometry the cook values calculated at the geometric centre of each jar and for every concentration were compared.

The cook value, starting from the data obtained from simulations, was calculated as follows:

$$C_0 = \int_0^t 10^{\frac{(T_{sim}-T_{ref})}{z}} dt \qquad (7)$$

where T_{sim} (°C) was the product simulated temperature, T_{ref} (°C) the reference temperature (100°C), z the constant value equal to 33°C (Holdsworth, 1985) and dt (min) the time interval (0.5 min).

Regarding the heating step (data not shown), it’s possible to note how the cook values decreased with increase the starch concentration, for all the geometries. Moreover, each starch concentration presented significant differences each other. From the geometry point of view the samples can be divided into two groups the first composed by the high and short cylinders and the other by hexagonal and flared ones with the square geometry positioned between the two groups.

About the cooling stage (data not shown) the trend in function of starch concentration can be approximated to the previous one. Only for the samples 2 and 3% the results can be considered no significantly different. Concerning the geometry effect on the heat exchange in this case only the short cylinder and flared geometries seem to give the same results, the others gave cook values with significant differences each other's.

Finally, to give an overview of the entire treatments also the cook values obtained from the entire thermal process were compared, analysed and reported in **Table 5**. As can be expected, the results appear a mean of the heating and cooling steps: the cook values tended to decrease with increasing the starch concentration and results appear significantly different each other's, except for the samples 0 and 2%, probably due to the low starch concentration which didn't affect greatly the heat exchange. About the effect of geometries, samples can be divided in two groups with similar behaviour: one composed by short cylinder and the other composed by flared geometry. The remaining geometries can be positioned between these two groups. Moreover, as reported in the **Table 5**, both variable as well as the combination of them resulted significant.

4.6. Slowest heating/cooling zone analysis

The aim of thermal treatment is to give adequate amount of heat for a sufficient period of time at the SHZ to reduce the most damaging microorganisms and at the same time keep an higher level of sensory and nutritive properties (Varma and Kannan, 2006). The slowest heating zone is considered the region inside a jar that can take the longest time relative to the other positions to reach the reference temperature and which receives the least amount of heat along the thermal treatment. On the other hand the SCZ, or slowest cooling zone, is refers to the region during cooling stage which has the lowest heat exchange and takes the longest time to reach the target temperature. This behaviour can affect not only the sensory and nutritional characteristics of a products but is dangerous because it can favour the growth of damaging microorganism.

After these premises it's evident the importance of knowing of SHZ and SCZ, which can be affected mainly by the type of products but also from the kind of treatment. In most food products, these target points haven't a constant location inside the glass jar as it changes with the heating transfer mechanism involved in the process. In this work, thanks to the developed CFD models it's possible to follow the movements of SHZ and SCZ along the thermal treatment, considering them the point in the domain with the lowest and highest temperature in heating and cooling phase, respectively.

As expected the SHZ resulted afected greatly by the starch concentration. The mean positions obtained from the five different geometries were 18.4, 15.8, 17.2, 20.2, 27.5 and 42.4% for samples at 0, 2, 3, 4, 5 and 6%, respectively. These results were in accordance with data obtained by Cordioli et al. (2016). The shift of SHZ was the consequence of change from convective to conductive heat exchange due to the starch gelatinization along the thermal treatment. Where present, convective current pushed down the SHZ as already explained in Cordioli et al. (2016). This shift can be observed in **Figure 7a**, where the tracking of SHZ in the high cylinder geometry at different starch concentration is reported. Initially, it was positioned near to the bottom of the jar, then once reached the starch gelatinization temperature, for the higher starch concentrations, tended to move towar geometric centre. In **Figure 7b** it's possible to appreciate the effect of jar geometry on the SHZ movements and as expected the geometry slightly affected the target point, both at low and high starch concentrations.

As regard the cooling phase and the SCZ position obtained from the five different jar geometries were 98.8, 97.6, 97.1, 96.4, 84.1 and 70.4% for samples at 0, 2, 3, 4, 5 and 6% of starch, respectively. These results are quite different respect to data reported in Cordioli et al. (2016), where for low starch concentrations SCZ was positioned at about 80% of total height while for high starch concentrations tended to be near the geometric centre. This upward shift was probably caused by the presence of head space inside the jars, as explained in *Section 4.2*.

The position and the motion of SHZ/SCZ can also affect the design process of a thermal treatment. Usually the process was dimensioned on the temperature at the geometric centre of the jar considered, for simplicity, the slowest heat exchange zone of the product. But by means of the results obtained in this work it's possible to show that if the design of thermal process is done exclusively taking into account the values at the geometric centre it will be done an evident and coarse mistake. In **Figure 8** is reported a comparison between the cook values estimated at the geometric centre and those calculated at SHZ (panel **a**) and SCZ (panel **b**). In the heating phase (panel **a**) the cook value at geometric centre resulted higher than the values calculated at the SHZ (mean increases of 10%) while regarding the cooling step, the cook values estimated at geometric centre result lower than values estimated at SCZ (mean decreases of 82%).

5. Conclusions

In this study the effects of six starch concentrations (0, 2, 3, 4, 5 and 6%) on the heat exchange of glass jars with five different geometries were investigated. Starting from experimental test, such as thermal treatment and rheological characterizations, several 3D CFD models were developed and experimentally validated (mean RMSE of 1°C).

By means of the validated models, thirty simulations (one for each starch concentration/jar geometries combination) at the same process conditions were carried out: as expected the starch concentrations greatly affected the temperature profile at the geometric centre, while regard the jar geometries only at low starch concentration can be noted relevant difference between the samples. The differences between the samples can be highlighted by comparing the heating and cooling rates: the values tended to decrease with increasing of starch concentrations both for heating and cooling stages. The geometry of the jar mainly affected systems in which the heat exchange occurred by convective mode because the convective currents can be greatly influenced by the shape of the container.

Moreover, the cook values at the geometric centre of each jar and for every concentration were compared. The cook values tended to decrease with the increasing of the starch concentration and resulted appear significant different each other's (except for the samples 0 and 2%). Regarding the geometry, three groups can be identified: one with the short cylinder another with the flared geometry, while the remaining geometries can be positioned between them.

Finally, the position of SHZ in heating phase and SCZ in the cooling one were also investigated. As expected, the target point moved along the treatment as consequence of shift from convective to conduction heat exchange due to starch gelatinization. In particular, the mean position of SHZ along the heating phase were 18.4, 15.8, 17.2, 20.2, 27.5 and 42.4% of the total height for samples at 0, 2, 3, 4, 5 and 6% of starch concentration, respectively. Knowledge of the position of SHZ/SCZ result of great importance also for the design process of a thermal treatments. In this work, thanks to the power and flexibility of CFD models is possible to track the real position of SHZ/SCZ along the treatments and quantify the cook value in this position, which result great different (+10% and -82% for the heating and cooling phase, respectively) respect the ones measured at the geometric centre, the position usually considered for process dimension.

Concluding, in this work, thank's to the powerfull of CFD technique, it was possible to perform analysis and quantification of parameters in positions and conditions difficult (if not impossible) to achieve in the reality. So, these mathematical models (and in general this techique) can be an usefull tools to fasten the process design of new product, optimize exsisting processes and better understand the variables and conditions which mainly affect the food submitted to transformation process.

References

ANSYS®, (2011). *ANSYS® Icepak User's Guide* (release 14). Canonsburg, Pennsylvania, USA.

Augusto, P. E. D. & Cristianini, M., (2011). Numerical evaluation of liquid food heat sterilization in a brick-shaped package. *Procedia Food Science*, *1*(Icef 11), 1290–1294.

Bergman, T., Lavine, A., Incropera, F. & Dewitt, D., (2011). Fundamentals of Mass and Heat Transfer, seventh edition. John Wiley & Sons. Page 553

Boz, Z., Erdogdu, F. & Tutar, M., (2014). Effects of mesh refinement, time step size and numerical scheme on the computational modeling of temperature evolution during natural-convection heating. *Journal of Food Engineering*, *123*, 8–16.

Choi, Y. & Okos, M., (1985). Effects of temperature and composition on the thermal properties of foods. In *Proceedings of the Fourth International Congress on Engineering and Food*, Etnisnton, Alberta, Canada.

Cordioli, M., Rinaldi, M. & Barbanti, D., (2016). Investigation and modelling of natural convection and conduction heat exchange: study on food systems with modified starch by means of computational fluid dynamics. *International Journal of Food Science & Technology*, *51*(4), 854–864.

Cordioli, M., Rinaldi, M., Copelli, G., Casoli, P. & Barbanti, D., (2015). Computational fluid dynamics (CFD) modelling and experimental validation of thermal processing of canned fruit salad in glass jar. *Journal of Food Engineering*, *150*, 62–69.

Ghani, A. G. A., Farid, M. M. & Chen, X. D., (2002). Numerical simulation of transient temperature and velocity profiles in a horizontal can during sterilization using computational Fluid dynamics. *Journal of Food Engineering*, 51(1), 77–83.

Holdsworth, S. D., (1985). Optimisation of thermal processing–A review. *Journal of Food Engineering*, *4*(2), 89–116.

Kannan, A. & Sandaka, P. C. G., (2008). Heat transfer analysis of canned food sterilization in a still retort. *Journal of Food Engineering*, *88*(2), 213–228.

Kumar, A., Bhattacharya, M. & Blaylock, J., (1990). Numerical simulation of natural convection heating of canned thick viscous liquid food products. *Journal of Food Science*, *55*(5), 1403–1411.

Lespinard, A. R. & Mascheroni, R. H., (2012). Influence of the geometry aspect of jars on the heat transfer and flow pattern during sterilization of liquid foods. *Journal of Food Process Engineering*, *35*(5), 751–762.

Marra, F. & Romano, V., (2003). A mathematical model to study the influence of wireless temperature sensor during assessment of canned food sterilization. *Journal of Food Engineering*, *59*(2–3), 245–252.

Ramaswamy, H. S., Abbatemarco, C. & Sablani, S. S., (1993). Heat transfer rates in a canned food model as influenced by processing in an end-over-end rotary steam/air retort. *Journal of Food Processing and Preservation*, *17*, 269–278.

Tattiyakul, J., Rao, M. A. & Datta, A. K., (2001). Simulation of heat transfer to a canned corn starch dispersion subjected to axial rotation. *Chemical Engineering and Processing: Process Intensification*, *40*(4), 391–399.

Tattiyakul, J., Rao, M. & Datta, A., (2002). Heat transfer to three canned fluids of different thermo-rheological behaviour under intermittent agitation. *Food and Bioproducts Processing*, 80(1), 20-27.

Varma, M. N. & Kannan, A. (2006). CFD studies on natural convective heating of canned food in conical and cylindrical containers. *Journal of Food Engineering*, *77*(4), 1024–1036.

Yang, W. H. & Rao, M. A. (1998). Complex viscosity-temperature master curve of cornstarch dispersion during gelatinization. *Journal of Food Process Engineering*, *21*(315), 191–207.

Table 1. Position of the thermocouples along the central axis for the different jar geometries.

	Distance from the bottom of the jar (mm)				
	High cylinder	***Low cylinder***	***Hexagonal***	***Square***	***Flared***
CH01	30	13	13	13	13
CH02	43	26	26	26	26
CH03	56	39	39	39	39
CH04	69	52	52	52	52
CH05	82	65	65	65	65
CH06	95	-	78	-	-
Total height of the jar	99	75	84	76	75

Table 2. Characteristic dimensions and qualitative parameters of meshing for the five geometries studied.

	Min element edge (m)	***Max element edge (m)***	***Growth rate***	***Skewness***	***Number of elements***	***Number of nodes***
Hexagonal	$1*10^{-5}$	$2*10^{-3}$	1.10	0.23±0.15	715415	182254
Square	$9.8*10^{-6}$	$2*10^{-3}$	1.10	0.24±0.17	700038	238871
Short cylinder	$8.9*10^{-6}$	$1.8*10^{-3}$	1.10	0.21±0.13	369342	102750
Flared	$9.1*10^{-6}$	$1.8*10^{-3}$	1.10	0.21±0.12	370548	83912
High cylinder	$1.1*10^{-5}$	$2.2*10^{-3}$	1.10	0.21±0.12	280630	64523

Table 3. RMSE value (°C) obtained for the model validation.

		Location in jar					***mean***
		CH01	***CH02***	***CH03***	***CH04***	***CH05***	
High cylinder	*Heating*	0.75	0.74	0.72	0.78	0.70	**0.74**
	Cooling	2.02	2.38	2.34	2.07	1.95	**2.15**
Short cylinder	*Heating*	0.75	0.73	0.61	0.40	0.20	**0.54**
Flared	*Heating*	0.86	0.91	0.86	0.70	0.64	**0.79**
Square	*Heating*	1.53	1.32	1.08	0.75	0.54	**1.04**
Hexagonal	*Heating*	1.59	1.66	1.51	1.33	1.07	**1.43**
	Cooling	0.78	0.50	0.17	0.52	0.71	**0.54**

Table 4. Overall Heat Transfer Coefficient (W m^{-2}) referred to heating step.

	High cylinder	***Short cylinder***	***Hexagonal***	***Squared***	***Flared***
Water	0.065	0.060	0.064	0.062	0.071
2%	2.261	1.857	2.328	1.965	2.208
3%	1.365	1.191	1.464	1.445	1.390
4%	0.035	0.030	0.037	0.034	0.035
5%	0.024	0.024	0.026	0.027	0.025
6%	0.024	0.020	0.022	0.022	0.019

Table 5. Global cook values obtained for the different samples studied. The values between the brackets were the standard deviation calculated starting from the variability of the treatment temperature (±0.5°C).

	Cook value (min)				
	High cylinder	***Short cylinder***	***Hexagonal***	***Square***	***Flared***
0%	29.88$^{a/AB}$ (1.04)	30.29$^{a/A}$ (1.06)	30.23$^{a/B}$ (1.05)	29.75$^{a/AB}$ (1.04)	31.35$^{a/B}$ (1.09)
2%	30.82$^{a/AB}$ (1.08)	29.00$^{a/A}$ (1.01)	30.23$^{a/B}$ (1.05)	27.96$^{a/AB}$ (0.98)	30.11$^{a/B}$ (1.05)
3%	26.98$^{b/AB}$ (0.94)	26.04$^{b/A}$ (0.91)	27.11$^{b/B}$ (0.95)	28.32$^{b/AB}$ (0.99)	27.97$^{b/B}$ (0.98)
4%	23.62$^{c/AB}$ (0.82)	22.96$^{c/A}$ (0.80)	25.16$^{c/B}$ (0.88)	23.94$^{c/AB}$ (0.84)	24.94$^{c/B}$ (0.87)
5%	19.84$^{d/AB}$ (0.69)	20.75$^{d/A}$ (0.72)	21.13$^{d/B}$ (0.74)	21.80$^{d/AB}$ (0.76)	20.69$^{d/B}$ (0.72)
6%	18.46$^{e/AB}$ (0.64)	17.13$^{e/A}$ (0.60)	17.72$^{e/B}$ (0.62)	18.49$^{e/AB}$ (0.65)	17.40$^{e/B}$ (0.61)

	P (< 0.05)	
Starch %	***Geometry***	***Starch %*Geometry***
0.000	0.009	0.004

$^{a-e}$ different small letters indicate significantly difference of values in function of starch concentration ($P < 0.05$)

$^{A-B}$ different capital letters indicate significantly difference of values in function of jars geometries ($P < 0.05$)

Figure 1. 3D geometries of the compared commercial jars, with the characteristics dimensions. Perspective view on the left and top view on the right. On the right images was highlighted the domain considered for the CFD models development respect to total domain.

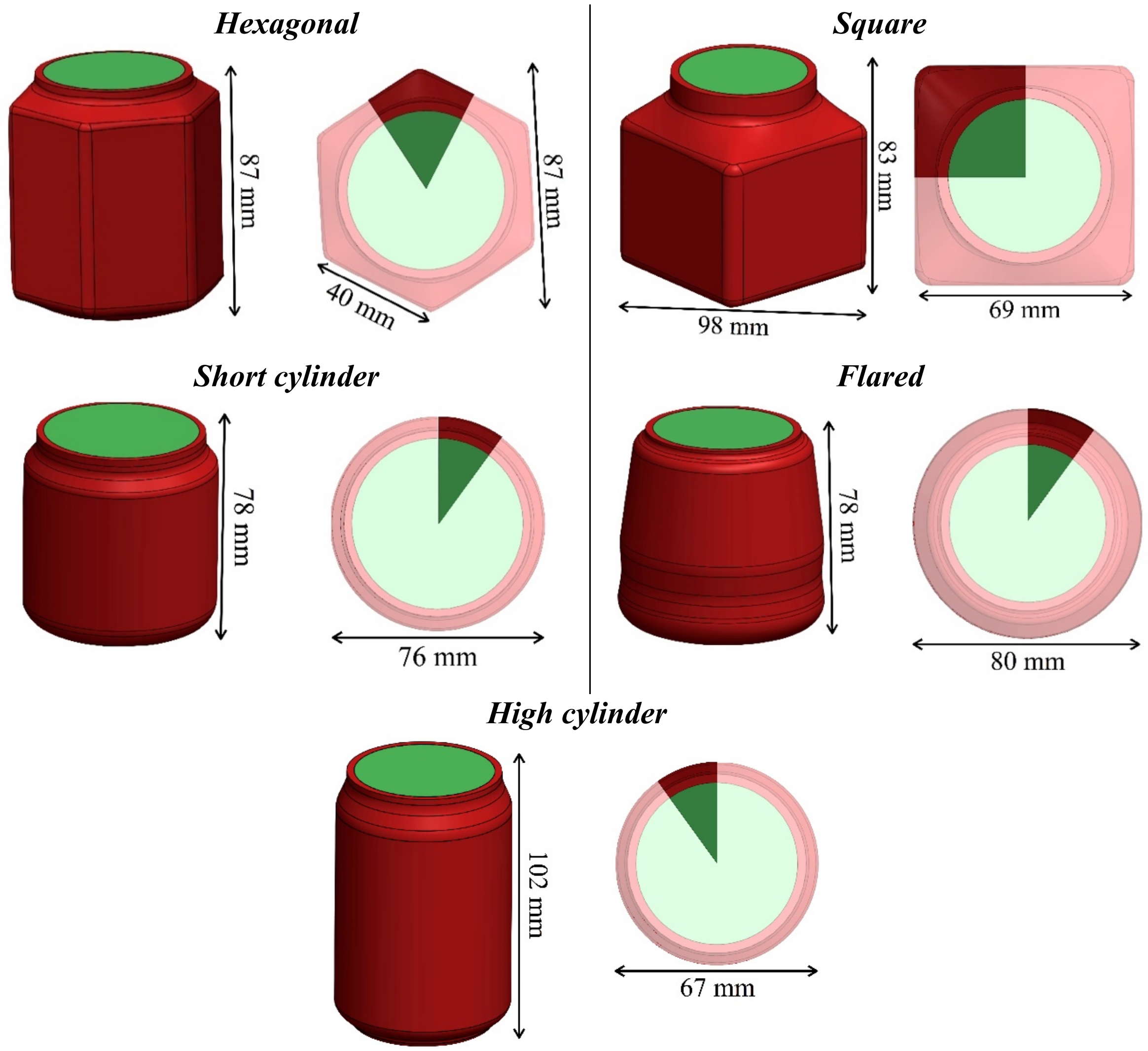

Figure 2. Comparison of temperature profile at the geometric centre from the simulated treatments, in function of geometries for 0% sample (panel **a**) and in function of starch concentration for the flared geometry (panel **b**).

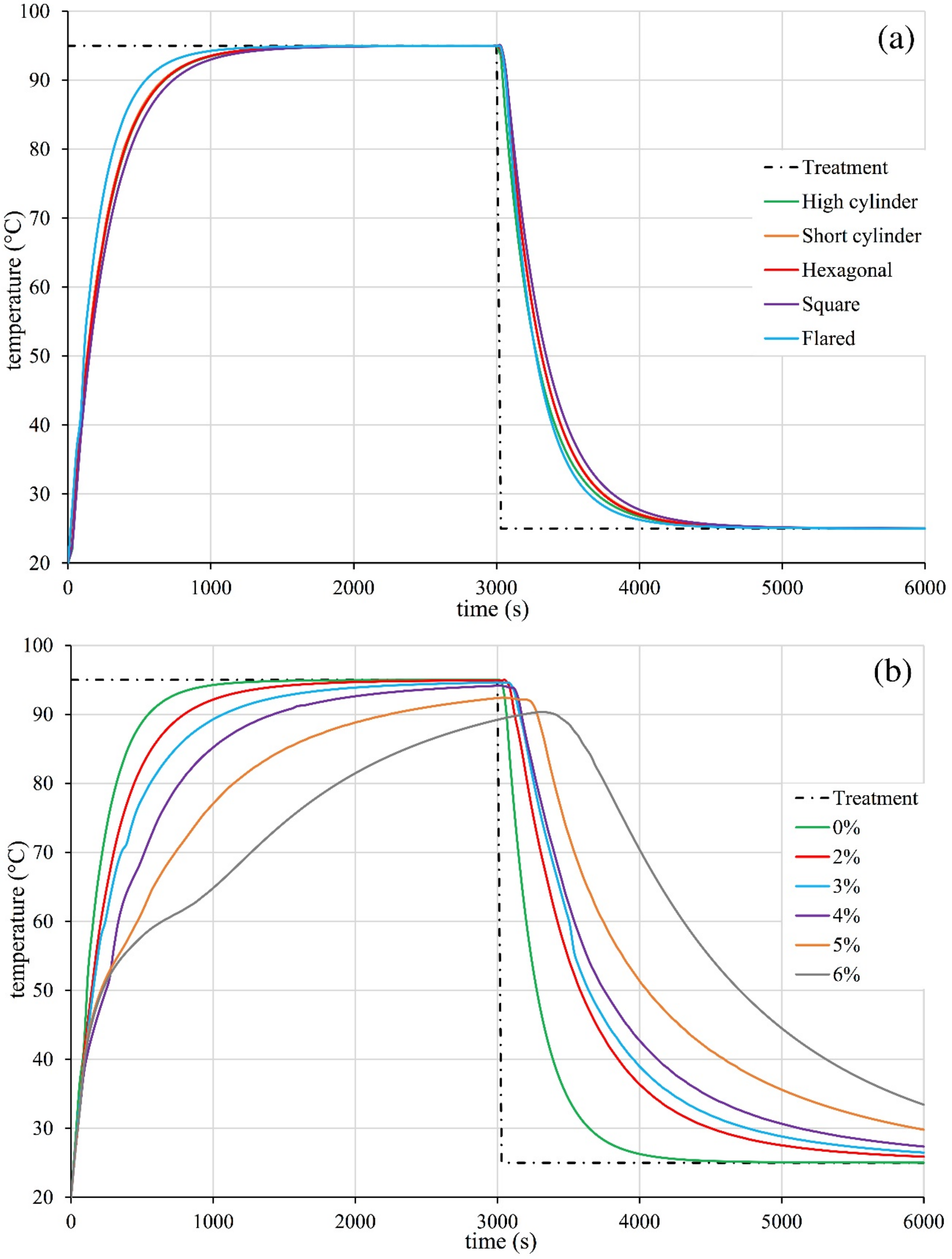

Figure 3. Temperature contours at difference time steps [180(**p**), 510(**g**) and 3330(**c**) s] for flared (**F**) and square (**S**) geometries at the two extremes starch concentrations: 0(**0**) and 6(**6**)%.

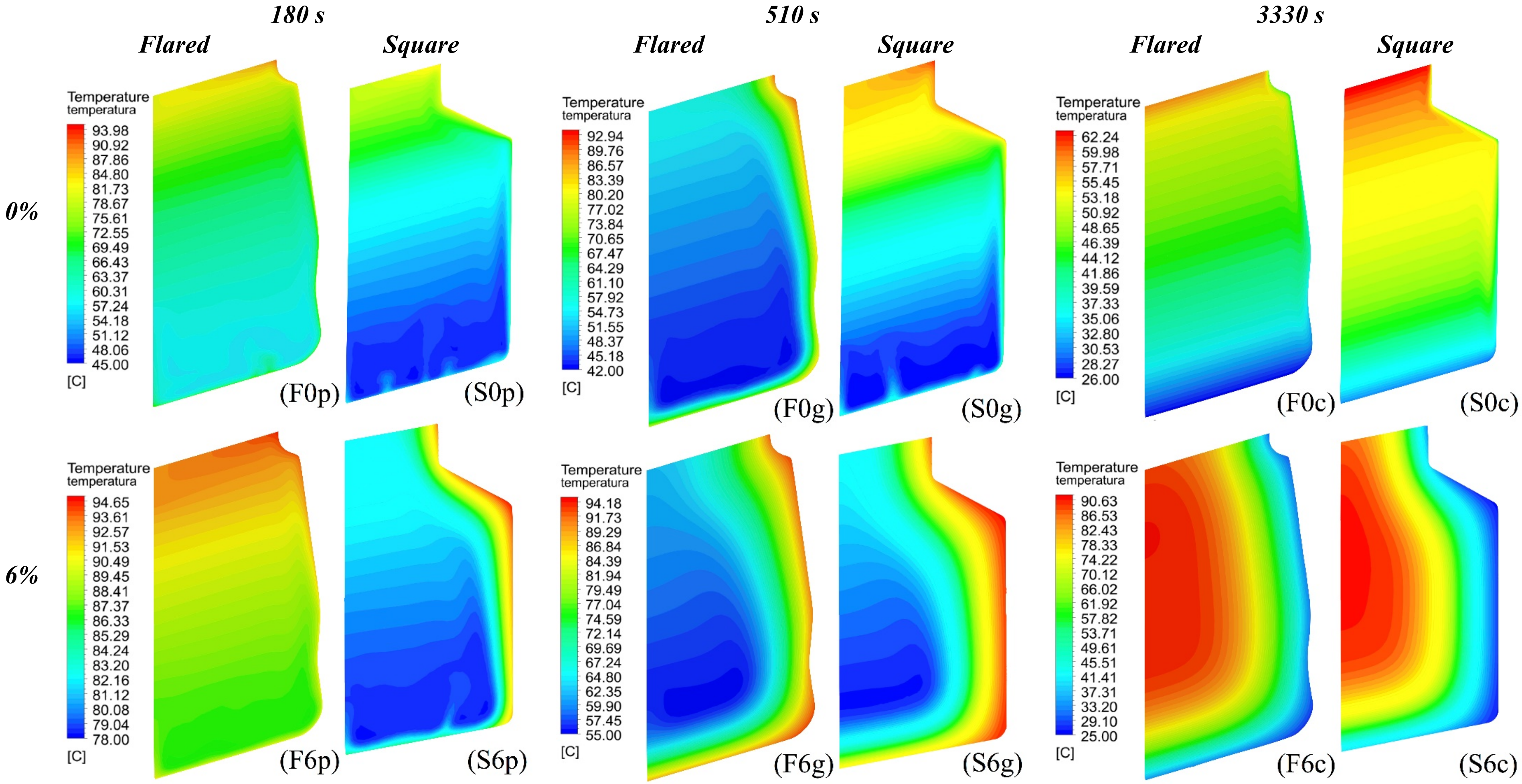

Figure 4. Mean heating (panel **a**) and cooling (panel **b**) rate of the samples obtained from three points along central axis (15, 50 and 85% of the height).

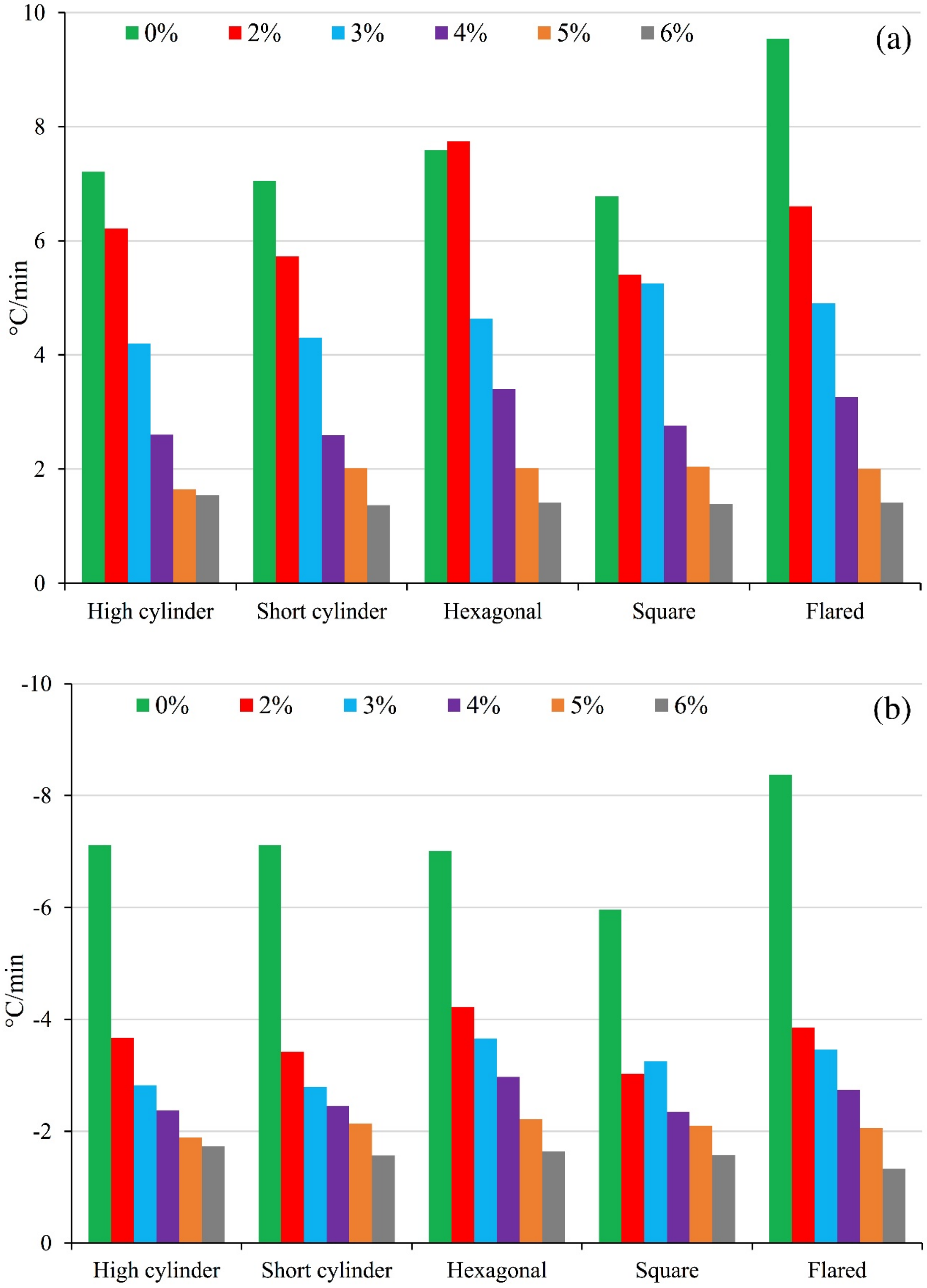

Figure 5. Comparison of velocity profiles normal to the radial direction at 50% of the total jar height. Effect of the starch concentrations on flared geometry at 2520 s (panel **a**) and 4500 s (panel **b**). Effect of jar geometries on 0% sample at 2520 s (panel **c**) and 4500 s (panel **d**).

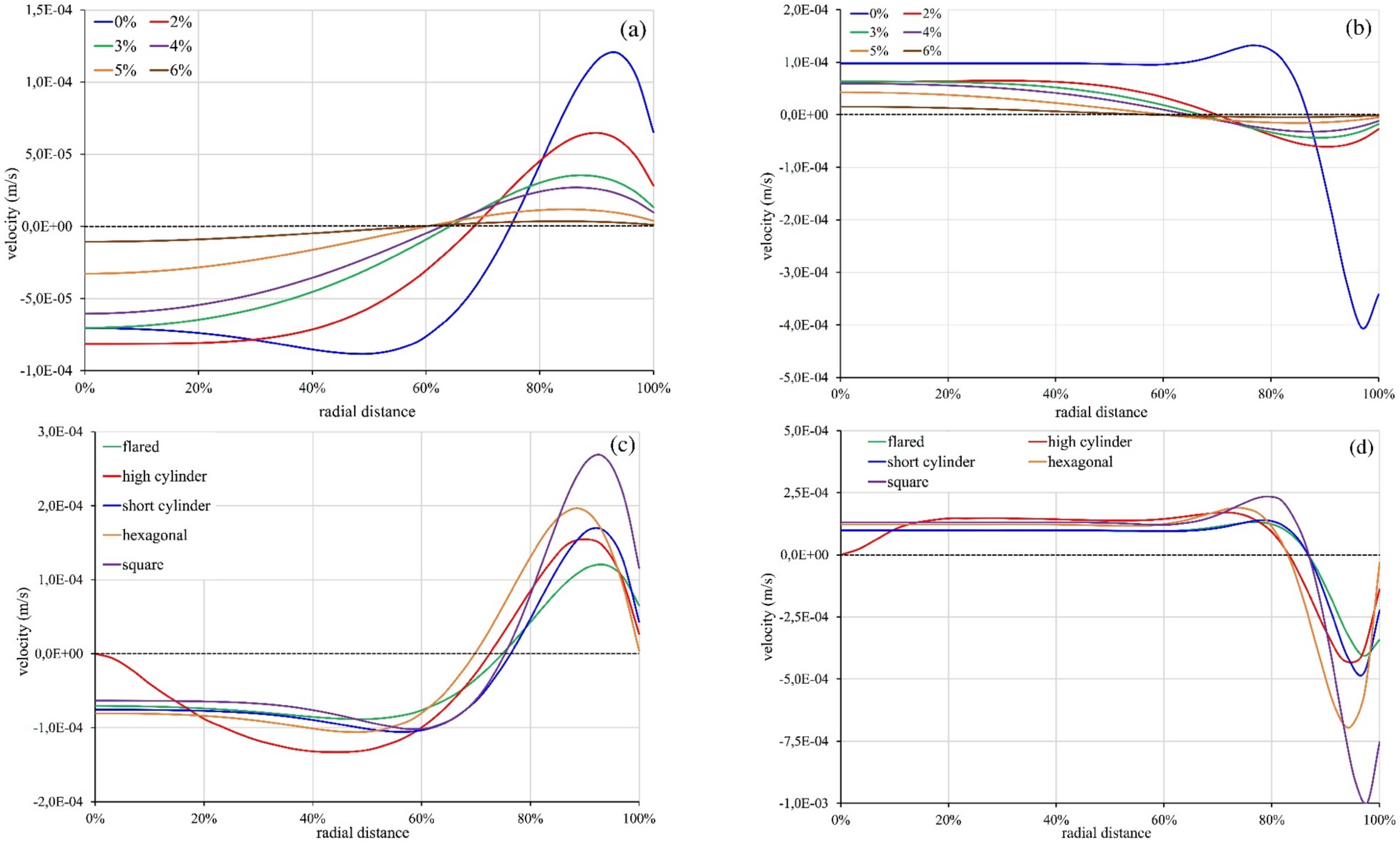

Figure 6. Comparison of time-velocity profiles at the geometric centre of flared and square geometries at 0 and 6% of starch concentration.

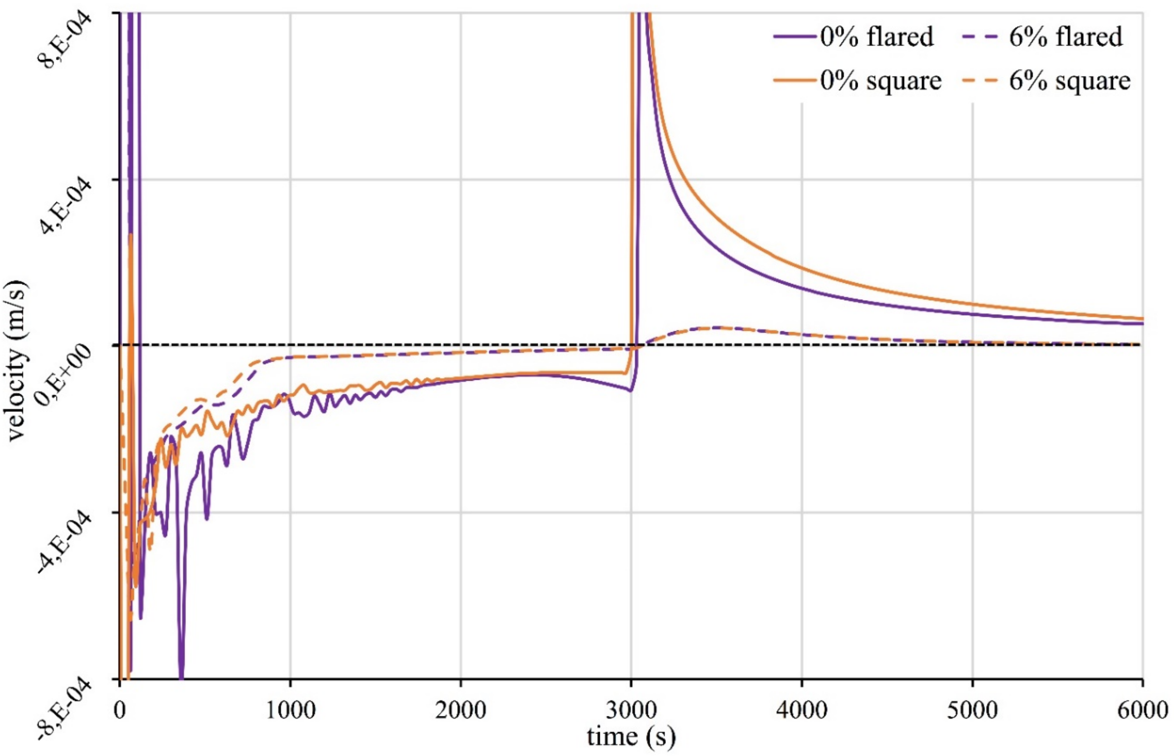

Figure 7. SHZ locations during heating phase of thermal treatment by means of the developed models. Comparison of different starch concentrations for the high cylinder geometry (panel **a**). Effect of starch concentration on different jar geometries (panel **b**).

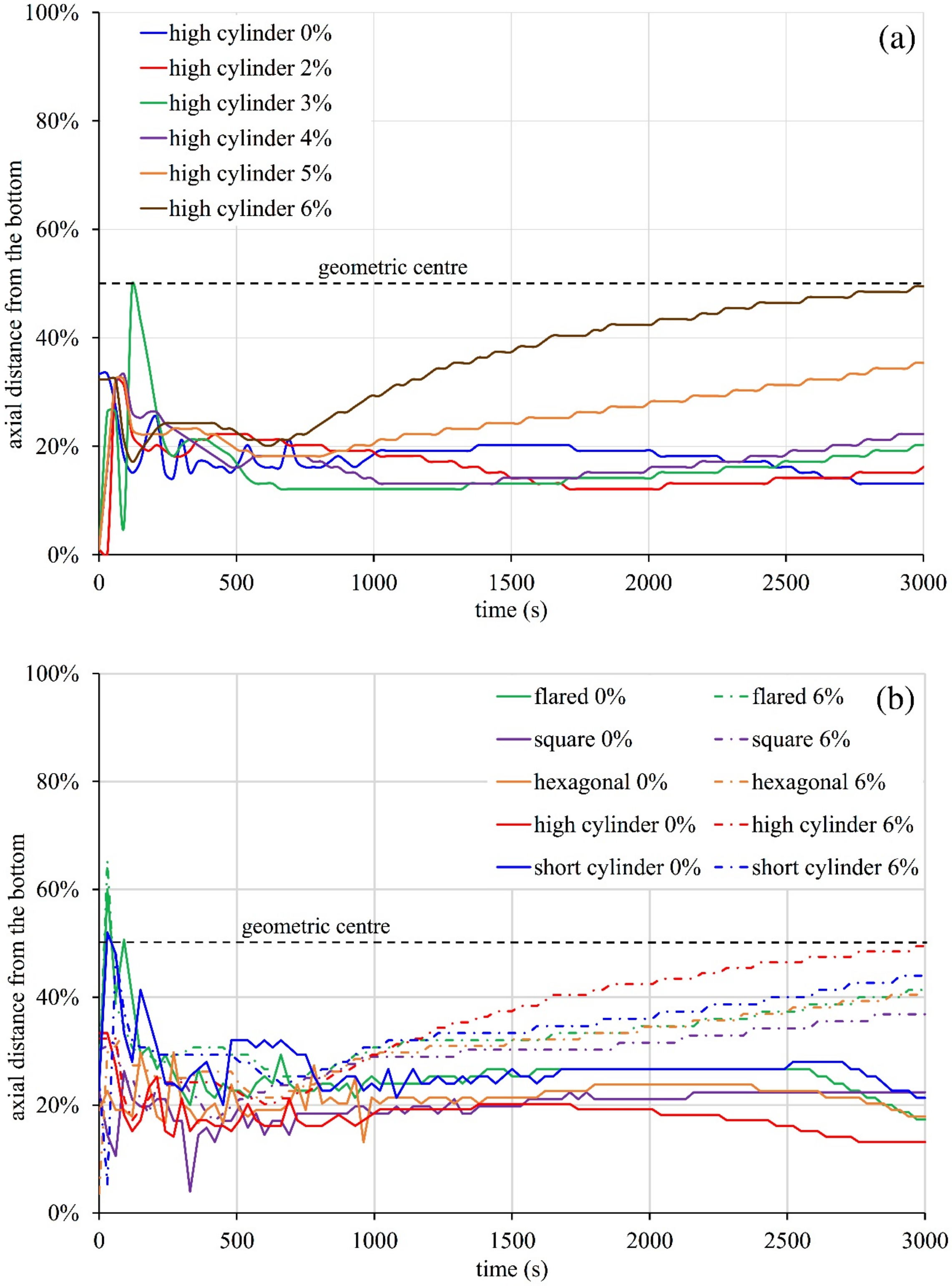

Figure 8. Comparison of the cook values calculated at the geometric centre and at the SHZ/SCZ in the heating (panel **a**) and cooling (panel **b**) phases.

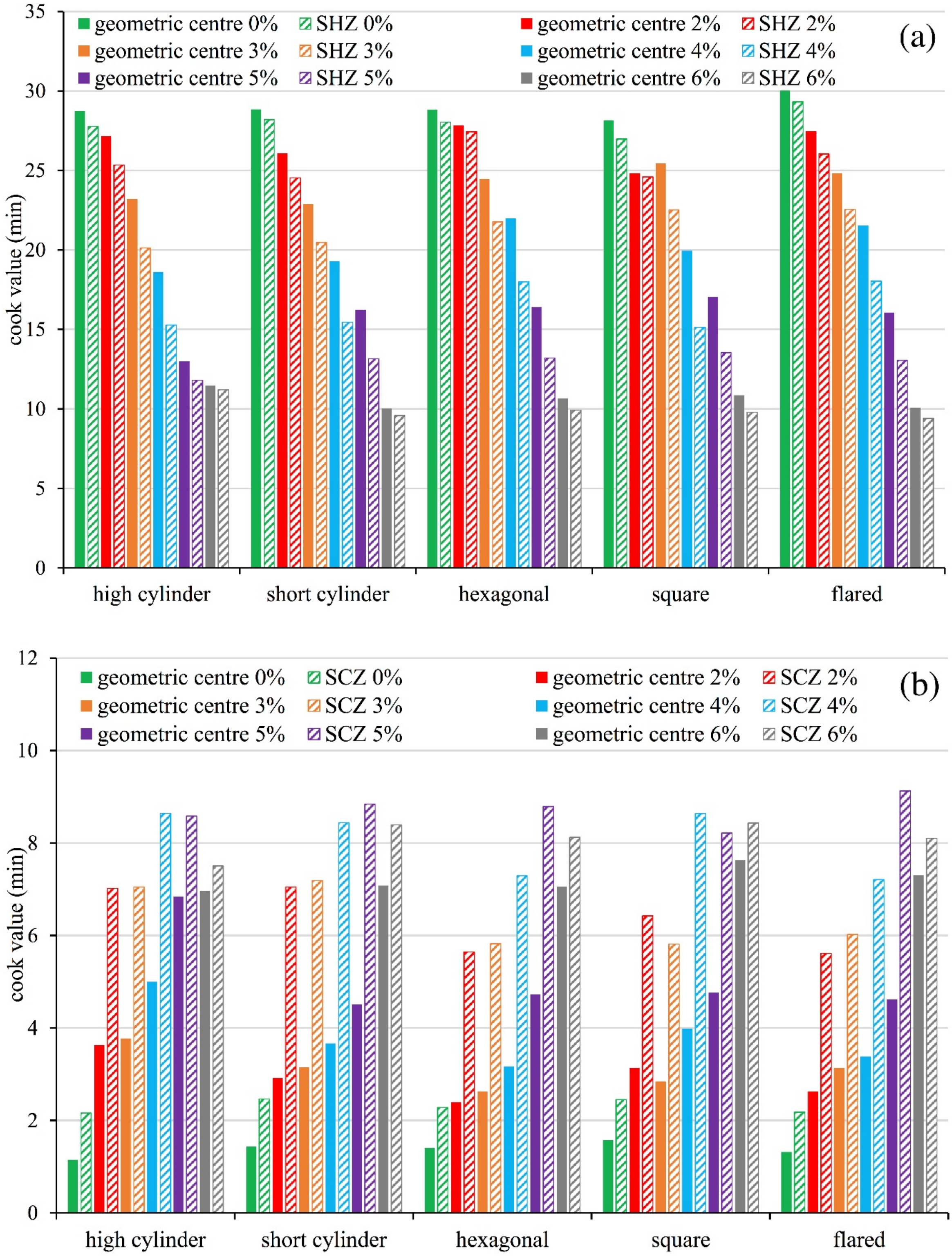

Development and validation of CFD models of thermal treatment on milk whey proteins dispersion in static and continuous process condition

Matteo Cordioli, Massimiliano Rinaldi, Germano Mucchetti and Davide Barbanti

Department of Food Science, University of Parma, Parco Area delle Scienze 47/A, 43124
Parma, Italy

Submitted to *Journal of Food Engineering*

Abstract

The objective of this study was to develop and to experimentally validate Computational Fluid Dynamics (CFD) models of thermal treatments on whey protein (WP) dispersions both in static and continuous conditions, at several processing times, shear rates and treatment temperatures. First, thermo-rheological properties of WP dispersions were investigated: the viscosity peak (raising up at 66°C) decreased as the shear rate increased. Then, two different CFD models were developed to simulate the thermal process: results showed a good fitting between experimental and simulated data (RMSE lower than 1.7°C for static model and mean temperature difference of 0.93°C for the continuous one). Thanks to the developed models, cook values of both static and continuous treatments were calculated, slowest heating points were exactly located and by means of these data equations for estimating the cook value in processing conditions within experimental range were obtained overcoming the need of experimental tests or in-silico calculations.

Keywords: thermal treatments, whey proteins, denaturation, CFD modelling, continuous process.

1. Introduction

In the last 2 decades, whey proteins (WP) became far more than a by-product of the cheese industry because of environmental and economic aspects and because of the growing consumers' demand for foods with specific nutritional and functional attributes (Alvarez et al., 2015). Thus, WP are nowadays widely used as ingredients to improve food quality, especially food texture, water holding capacity (WHC) or emulsion stability (Ndoye et al., 2012); whey proteins are often subjected to heat treatment in order to change their physical and functional characteristics and the variation of their properties can be achieved by controlled denaturation (Wolz et al., 2016). The denaturation-aggregation of β-lactoglobulin, the most abundant protein in the whey fraction of cow milk and also the dominant protein in heat-induced sol-gel transition, occurs following three different stages. First, when the temperature reaches 40°C, a dissociation of native dimers, existing under physiological conditions, into native monomers occurs; then, when the temperature increases above 60°C, a partially reversible unfolding of monomers and the formation of thermally induced molten globules takes place; finally, depending on process conditions, irreversible intra-molecular interactions occur resulting in the formation of protein aggregates (Tolkach and Kulozik, 2007). Several factors affect the denaturation-aggregation process such as protein concentration, as generally the reaction rate increases with concentration, due to the increased probability of collision between molecules (Wolz and Kulozik, 2015), as well as concentration influences the aggregate size (Wolz et al., 2016). Heating time and temperature are the most important process parameters influencing the denaturation/aggregation process with a direct effect of both on the degree of denaturation-aggregation. In addition, a decrease of aggregate diameter with increasing shear rate during continuous processes was also reported due to the reduced efficiency of the collisions at high shear rate (Wolz et al., 2016).

Management of shear rate together with WP concentration, pH, mineral balance and heat treatment is currently used to produce microparticulated WPC, used as fat mimetic (Spiegel and Huss, 2002).

Knowledge of WP behaviour as a function of variable shear rate is also crucial to industrialize the production of Ricotta cheese favouring the development of the continuous operation mode (Modler and Emmons, 2001) without negatively affecting the product rheology.

Due to the complexity of the above-mentioned phenomena, food industry needs more and more knowledge about whey protein denaturation for a higher comprehension, evaluation and analysis with reduced time and costs for process design and optimization (Erabit et al., 2016). Mathematical models could represent useful tools for this purpose: various modelling approaches are reported in the literature starting from kinetic modelling using Arrhenius equation that provides information about the characteristics of the initial step of the aggregation process but not about aggregation with any prediction of the final aggregates size as well as the viscosity of the WP suspension. To the best of our knowledge, only mathematical modelling of fouling of heat exchangers has been carried out with reference to whey protein solutions (Blanpain-Avet et al., 2016; Petit et al., 2013). Population Balance Equation (PBE) was reported to be a way to model the evolution of a size distribution to study thermo-mechanical process conditions that allow obtaining whey protein aggregates with specific functionalities (Erabit et al., 2015 and 2016). Several authors proposed Response Surface Methodology (RSM) as a way to reduce the need for full factorial designs, thus reducing the number of experimentations, and to study a complex situation such as whey protein denaturation/aggregation under continuous treatments (Alvarez et al., 2015). However, RSM models need a certain numbers of samples to be validated and can be used only within studied conditions. Despite CFD models could allow predicting protein gelation under continuous thermal treatment, the literature for the modelling of whey protein solutions is very limited: in the work of Chantoiseau et al. (2012) Computational Fluid Dynamics (CFD) was used for solving the fluid-flow and heat-transfer problem and coupled with a population balance equation (PBE) for evaluating particle aggregation. CFD technique represents a powerful numerical instrument that became widely used in the last years to simulate different processes in food industry (Norton et al., 2013). CFD technique uses numerical algorithms to solve the non-linear partial differential equations of fluid mechanics (Navier-Stokes equations) and heat transfer in a given geometry. In this way, many complex mechanisms governing food-processing systems can be solved with a reduction of the empiricism associated with a food process design (Mirade and Daudin, 2006; Norton et al., 2013). Problem complexity becomes higher when a suspension of WP is treated in continuous thermal treatment because induced protein gelation affects flow properties and heat transfer. These processes are coupled: on one hand, the product transformation depends on the operation conditions (velocity, shear rate and temperature); on the other hand, the thermal and rheological properties of a liquid food are themselves modified as a result of the product transformation (Chantoiseau et al., 2012).

Hence the objective of this work was to design, develop and validate CFD models, using commercial software, for predicting the temperature variation during thermal process applied for denaturing and coagulating concentrated WP dispersions in both static and continuous conditions. WP gels were obtained at different processing times, shear rates and treatment temperatures while CFD models used experimental thermo-rheological properties of WP dispersions. The results were then discussed by means of cook value, a universal parameter which permits to quantify and compare the relative thermal effects at different process conditions (Wang et al., 2003).

2. Materials and methods

2.1. Samples preparation

Milk whey protein concentrate (WPC 80) was provided by S.C.A Srl (Fiorenzuola D'Arda, Italy). The composition of the powder, as reported by the supplier, was as follows: protein 80 g/100g, lactose 7.2 g/100g, water 5.0 g/100g, fat 3.5 g/100g, minerals 3.1 g/100g and lactic acid 1.2 g/100g. The WPC 80 powder was dispersed in water to obtain a final protein concentration of 15% w/v and, in order to guarantee a complete hydration, the dispersion was continuously stirred for 3 hours at room temperature and then stored at 5°C for 12 hours before the experimental tests (pH was constantly equal to 6.7).

2.2. Experimental thermal treatment

2.2.1. Static thermal treatment

The WPC dispersion rested in a stirred water bath at 16°C until it reached this temperature; then it was transferred in a polypropylene tube (diameter = 18 mm; height = 100 mm; thickness = 1 mm) filled with a volume of 18 mL and finally it was treated for different times (2, 4, 6 and 8 min) and bath temperature (75, 80 and 85°C) combinations. After the heating phase, all samples were cooled in a stirred cold bath (10°C) for 8 min. Three replicates for each time/temperature combination were prepared and analysed. The static thermal treatment was carried out in a stirred thermostatic bath (MPM Instruments Srl, Bernareggio, Italy) with an internal volume of 17 L. The test tube was put in the water up to the base of the cap in order to allow heat exchange through the side walls and the bottom.

The temperatures inside the test tube were measured using four wire thermocouples (K-type; Ni/Al-Ni/Cr; ∅ = 0.9 mm, Gauge number = 20) connected to a multimeter acquisition system (Delta Ohm Srl, Padova, Italy). The thermocouples were positioned at the geometric centre of the test tube, in the headspace of test tube, on the wall outer surface at the middle height and inside thermostatic water bath near the external surface of the test tube. The data were acquired with an interval of 2 s and collected in an Excel® ASCII worksheet by a software developed with LabView®. Data obtained from the thermocouples positioned in the water bath and in the head space were used for boundary conditions of the models, while the values measured at the geometric centre and on the outer wall surface were used to validate the models.

2.2.2. Continuous thermal treatment

The continuous thermal treatments were carried out in a small pilot plant (Valfor Srl, Parma, Italy). Schematically the plant consisted of a feeding tank, a volumetric piston pump (OBL Srl, Milano, Italy) and a heat exchange section that consisted of stainless steel pipe with a nominal diameter of 6 mm and a wall thickness of 1 mm (total length at the central axis = 86 m). The whole tube was divided into 5 sections bent like a spiral coil and connected each other. The spiral coils were immersed into three stirred thermostatic baths (Julabo Italia Srl., Milano, Italy; MPM Instruments Srl, Bernareggio, Italy) filled with a total volume of 70 L of water. The section of the pipe, connecting one bath to the following, was lower as possible and preliminary test demonstrated that heat losses in these connections were negligible. However, this critical point has been taken into account on the development of the fluid dynamics models; consequently, specific boundary conditions for this zone were imposed. The total internal volume of the heating zone was 2.43 L. The flow rate of the pump varied from 10.9 to 39.8 L/h. In **Figure 1,** a schematic view of the heat exchange zone with the disposition of the different spiral coils has been reported.

Also for the continuous thermal treatments three different process temperatures (75, 80 and 85°C) and up to four residence times (9.92, 6.82, 4.91 and 3.66 min) were adopted. In this case, the cooling step was not considered. Three replicates for each time/temperature combination were prepared and analysed after equilibration of the feeding tank at 16°C by means of a water jacket.

The temperatures along the heat exchange zone were measured using 16 wire thermocouples (K-type; Ni/Al-Ni/Cr; ∅ = 0,9 mm, Gauge number = 20) connected to a multimeter acquisition system (Delta Ohm Srl, Padova, Italy). The thermocouples were positioned at the inlet and at the outlet of each section (9 thermocouples), 5 in the thermostatic baths (to obtain a specific treatment temperature for each section) and 2 in the ambient temperature around heating zone. Data obtained from the thermocouples positioned in the thermostatic baths and in the ambient were used as temperature values for boundary conditions of the model, while the temperature measured at the inlet and the outlet of each section were used to validate the models. Also in this case, the data were acquired with an interval of 2 s and collected in an Excel® ASCII worksheet by a software developed with LabView®.

2.3. Thermo-rheological properties

The apparent viscosity profile of the WPC solution was measured with concentric cylinder geometry (Couette cell) mounted on ARES rheometer (Ta Instruments, New Castle, DE, USA). The dimensions of the geometry were 34 mm cup diameter, 32 mm bob diameter and height of

33 mm. 8 mL of the whey protein solution were transferred using a graduate cylinder to the rheometer cup set at 16°C and sample temperature left to equilibrate for 2 min before starting the test. Temperature was linearly increased from 16 to 85°C with a heating rate of 2.2±0.1°C/min, through a thermostatic bath (Thermo Fisher Scientific, Waltham, MA, USA) connected to rheometer. The tests were performed at 4 different shear rates, correlated with the calculated flow rate values in the pilot plant. All the trials were performed in triplicate.

The correlation between flow rate and shear rate was obtained from the simplified Rabinowitsch-Mooney equation as reported from Arellano et al. (2013):

$$\gamma_w = \frac{(3n+1)}{4n}\frac{4V}{\pi R^3} \qquad (1)$$

Where γ_w is the shear rate (s^{-1}), n flow behaviour index, V volumetric flow rate (m^3 s^{-1}) and R radius of the pipe (m). From preliminary rheological tests the obtained flow behaviour index n was equal to 1.029.

To define the turbulence inside the pipe, also the Reynolds number (*Re*) was calculated:

$$Re = \frac{D \cdot v \cdot \rho}{\mu} \qquad (2)$$

Where D is pipe diameter (m), v mean velocity of the flow (m s^{-1}), ρ density (kg m^{-3}) and μ apparent viscosity (Pa s). From the rheological measurements (**Figure 2**), the apparent viscosity slowly decreased from 0.011 to 0.004 Pa s (due to Arrhenius effect) until a critical temperature of about 66°C was reached, while, above this value, a rapid increase of viscosity was instead observed. The viscosity peak decreased with the shear rate increasing: 0.151, 0.065, 0.054 and 0.047 Pa s for 191, 278, 386 and 519 s^{-1}, respectively. These results are in accordance with Fernández Farrés et al. (2014), who reported for whey protein a decrease of the aggregate diameter of the particles with increasing shear rate as the imposed shear limited the growth of aggregates during the gelation process.

A quadratic response surface was obtained with TABLECURVE 3D software (release 4.0, Systat Software Inc., San Jose, CA, USA) by means of polynomial fitting method using the Levenberg-Marquardt algorithm from the thermo-rheological experimental data (**Figure 2**) and, after a preliminary sensitivity analysis, the best fitting equation (R^2 = 0.993) was:

$$\mu = \frac{(0.011 - 0.00037 \cdot T + 3.1757 \cdot 10^{-6} \cdot T^2 + 5.1322 \cdot 10^{-7} \cdot \gamma)}{(1 - 0.026 + 0.00017 \cdot T^2 + 5.1449 \cdot 10^{-5} \cdot \gamma)} \qquad (3)$$

where μ is apparent viscosity (Pa s), T is treatment temperature (°C) and γ shear rate (s^{-1}). Equation (3) allowed calculation of the dispersion viscosity at any treatment temperature and shear rate combinations without any other rheological test and with a good degree of accuracy with respect to experimental data (RMSE = 0.007 Pa s). Obtained function is an approximation of the thermo-mechanical history of fluid particles and is limited to the heating rate used in the experimental tests.

3. CFD modelling

3.1. Static thermal treatment modelling

3.1.1. Defined domain and mesh details

Both thermal treatment processes, in static and continuous conditions, were simulated by means of 3D CFD models. The first step in model development was to replicate the 3D geometry of the domain of interest, thanks to SolidWorks® 2015 (Dassault systèmes, Vélizy-Villacoublay, France) software.

Regarding the static thermal treatment, in order to reduce the computational effort and to improve the precision of the solution of CFD model, the spatial domain was assumed to be symmetric with regard to two planes through the vertical axis of the test tube, hence only a portion of 6 degrees was simulated: during a preliminary study the differences between the results obtained from the model of the entire domain were negligible with respect to those obtained from domain sections and the lowest one was then used. In this way it's possible to increase the density of mesh and obtain a better result. The developed domain was composed by the test tube wall and sample dispersion. In the model it wasn't possible to neglect the wall of the test tube due to the high wall thickness/tube radius ratio (>16%) and to the low value of polypropylene thermal conductivity (0.22 W m^{-1} K^{-1}), lower than the value of the sample (0.56 W m^{-1} K^{-1}).

The model geometry was then imported into the ICEM CFD® software (Canonsburg, Pennsylvania, USA) and discretized into an unstructured hexahedrical and wedge mesh. In order to accurately calculate the flow field near the wall of the test tube, as reported also by Boz et al. (2014), 10 layers of flat prismatic wedge element, with a growth rate of 1.2 between layers and a transition ratio (the size change between the last layer of elements in the inflation layer and the first elements in the hexahedron region) of 0.2 were used for the discretization of the fluid domain. Also for all the domains of interest, the mesh was optimized and finalized for a better accuracy and reducing computational time. The values of maximum and minimum element edge dimension both for the test tube wall and fluid dispersion were $2.0*10^{-4}$ and $7.2*10^{-6}$ m, respectively. The final mesh number after mesh independent analysis, with solid and fluid elements, consists of 480069 elements and 120770 nodes. From a quality point of view, the value of skewness was 0.22±0.14, while the mean growth rate value was 1.10, which represent good results (ANSYS Icepak User's Guide, 2011).

3.1.2. Numerical model

The software ANSYS® CFX v16 (Canonsburg, Pennsylvania, USA), run on HP Z420 Workstation (Palo Alto, California, USA), was used to solve the governing continuity, momentum and energy equations for the defined geometry and associated boundary conditions. The domain was defined in the global co-ordinate frame in which the solver carries out the calculations. To solve the coupled system of partial differential equations, the high-resolution scheme with second order backward Euler method was adopted. The generalized transport equations solved are:

a) The continuity equation

$$\frac{\partial \rho}{\partial t} + \nabla \cdot (\rho V) = 0 \qquad (4)$$

b) The momentum equation

$$\frac{\partial \rho V}{\partial t} + \nabla \cdot (\rho V \cdot V) = \nabla \cdot \left(-\mathrm{p}\delta + \mu \cdot (\nabla V + (\nabla V)')\right) + S_M \qquad (5)$$

c) The energy equation

$$\frac{\partial \rho h_{total}}{\partial t} - \frac{\mathrm{Dp}}{Dt} + \nabla \cdot \left(\rho V c_p T\right) = \nabla \cdot (\mathrm{k} \cdot \Delta \mathrm{T}) + S_E \qquad (6)$$

Where t is the time (s), V the velocity vector (m s^{-1}), p the pressure (Pa), k thermal conductivity (W m^{-1} K^{-1}), c_p the specific heat capacity (J kg^{-1} K^{-1}). Natural convection was modelled using the Boussinesq approximation, which uses a constant density fluid model, but applies a local body gravitational force throughout the fluid that is a linear function of water thermal expansivity $\beta = 2.57 * 10^{-4}$ K^{-1} (obtained from the software library) and of the local temperature difference. The buoyancy source is added to the momentum equation as follows:

$$S_M = -\rho_{REF} \cdot \beta \cdot (\mathrm{T} - T_{REF}) \cdot g \qquad (7)$$

Where ρ_{REF} and T_{REF} are the density and temperature at the boundary wall condition and g is the gravitational force.

No internal energy source terms (S_E) were taken into account.

The liquid inside the test tube at time = 0 s was assumed to be at rest and at uniform temperature while a laminar flow mode was assumed to occur throughout the thermal processing (where the heat transfer was convective).

A no-slip condition was applied with velocity = 0 m s^{-1} of the fluid relative to the internal test tube surface. A good accuracy was reached setting an adaptive time step with a value between

0.1 and 2 s: this guarantees a small Courant number (Boz et al., 2014) and ensures a right compromise between the solver time and the quality of the results. High resolution advection schemes were adopted for all simulations, in order to achieve second order accuracy. The convergence criterion was defined as residual root mean square (RMS) value lower than 10^{-4} and the overall imbalance in the domain less than 1% for all variables.

3.1.3. Boundary conditions

In the static thermal treatment, a transient simulation was carried out due to the variation of boundary conditions with time (in particular the temperature along the external surface). For the model validation, three different time-temperature profiles imposed on the external surface of the domain were obtained from the experimental values measured with thermocouples positioned on the outer surface of test tube inside thermostatic bath and near the head space (75, 80 and 85°C for 8 minute of heating, followed by cooling phase at 10°C for 8 min). Then, starting from the validated models different treatments were simulated. In particular the same treatment temperatures (75, 80 and 85°C) with a heating phase of different duration (2, 4, 6, 8, 12, 16 and 20 minutes), followed by the same cooling phase at 10°C for 8 minute.

3.1.4. Thermal and physical properties

In the pre-processor library two materials with specific thermal and physical properties were created: one for the test tube wall and the other for the protein dispersion. With regard to the first one, the physical and thermal properties data, obtained from Lienhard and Lienhard (2008), were: density (μ) 905 kg m^{-3}, thermal conductivity (k) 0.20 W m^{-1} K^{-1} and specific heat (c_p) 1900 J kg^{-1} K^{-1}.

The viscous dissipation generally quantified by the Brinkman number (Br) which is defined as the ratio of the heat generated by the viscous action of the dissipation to the conduction was also taken in consideration. The values of Br number were calculated from:

$$Br = \frac{\mu \cdot V^2}{k \cdot (T_w - T_0)} \qquad (8)$$

Where T_w is wall temperature (°C) and T_0 bulk fluid temperature (°C). The maximum value obtained in both test tube and pilot plant resulted 0.005 due to the low velocity of the fluid and since the viscous dissipation effects will be important when the Brinkman number is bigger than unity (Yataghene et al., 2009), heat generation due to viscous dissipation was neglected.

Regarding the whey protein dispersion, from preliminary sensitivity analysis, viscosity therefore resulted the physical parameter which manly influenced the heat exchange due to the whey proteins coagulation/aggregation. From this assumption, variation of all other thermal and physical properties of the fluid as consequence of temperature increase in the experimental range were considered negligible and the terms of the equations (Choi and Okos, 1985) accounting for the influence of temperature discarded. Hence, in order to simplify the fluid dynamic model, the values were quantified by starting from the solution composition (Choi and Okos, 1985). The data obtained ($\rho = 1035$ kg m^{-3}, $k = 0.56$ W m^{-1} K^{-1}, $c_p = 2906$ J kg^{-1} K^{-1}) were then inserted as constant in the software library. Conversely, the apparent viscosity was assumed to be a function of temperature as obtained from the experimental rheological measures (*section 2.3*).

3.2. Continuous thermal treatment model

3.2.1. Defined domain and mesh details

As already seen for the procedure development of fluid dynamics model of treatment in static conditions (*section 3.1.1*), the first step was to create a 3D CAD model of the domain, also in this case performed with SolidWorks® 2015 software. In order to reduce the computational effort required by the solution of the CFD model and increase the accuracy, and taking into account the higher ratio between the length and the diameter of pipe in the pilot plant, the entire domain was separated in 5 subdomains. Another strategy implemented to reduce the calculation was to ignore the stainless steel wall of the pipe in the domain development and substitute the physical wall with a heat transfer coefficient (h) calculated by:

$$h = \frac{k}{s} \qquad (9)$$

Where h is heat transfer coefficient (W m^{-2} K^{-1}) and s tickness of tube wall (m). The 5 subdomains reported in *Section 2.2.2* were then imported into the ICEM CFD® software and discretized into an unstructured hexahedrical and wedge mesh. In order to accurately simulate the flow field near the tube wall, 3 layers of flat prismatic wedge element, with a growth rate of 1.2 between layers and a total thickness of $1*10^{-3}$ m, were used for the discretization of the fluid domain in all the sections. For all the domain of interest, the mesh was optimized and finalized for better accuracy and reduce computational time. The values of maximum and minimum element edge dimension, the skewness value, the number of elements and nodes for each subdomain were reported in **Table 1**. The number of elements for the entire system was 63837128, while from a quality point of view the mean growth rate and skewness for each section reach good values (ANSYS Icepak User's Guide, 2011).

3.2.2. Numerical model

The software ANSYS® CFX v16, run on CELSIUS M740 Fujitsu Workstation (Tokyo, Japan), was used to solve the equations (4), (5) and (6) reported in *Section 3.1.2*. Regarding the natural convection, this effect wasn't taken into consideration due to the presence of forced convection caused by the flow inside the pipe which makes negligible the natural one. Moreover, the inertia forces due to secondary flow in the bend sections of pilot plant can be considered negligible: weighted Dean's number result 17.2, lower than critical value of 20 reported by Kreith et al. (2011). No internal energy source terms (S_E) were taken into account and in the continuous thermal treatment a laminar flow mode was assumed as the maximum flow rate didn't exceed 450 Reynold.

3.2.3. Boundary conditions

In the continuous thermal treatment, a stationary simulation was carried out because the boundary conditions didn't change with time. For the model validation, six different residence time/process temperature conditions were taken into consideration. In particular, the maximum (9.92 min) and minimum (3.66 min) residence time at the three different process temperatures (75, 80 and 85°C). The boundary conditions imposed at pipe surface in the different sections were obtained from the experimental tests, specifically from the thermocouples positioned inside the water baths near the pipe. Starting from the validated models, also in this case different treatment were simulated. Particularly, three different temperatures (75, 80 and 85°C) and seven residence times (2, 4, 6, 8, 12, 16 and 20 minutes), the same simulated for the static thermal treatment, were adopted. The heat transfer coefficient, between the outer and inner wall surface, had a value of 60500 W m^{-2} K^{-1}. Also the inlet flow rate and temperature for the first subdomain of the plant (Section 1) were experimentally measured. For the subsequent sections the inlet flow rate and temperature values were obtained from the previous section (the outlet value of one section becomes the inlet value for the next) with a cascading resolution system. A no-slip condition was applied with velocity = 0 m s^{-1} of the fluid relative to the internal pipe wall surface. Also in this case high resolution advection schemes were adopted for all simulations, in order to achieve second order accuracy. The convergence criterion was defined as residual root mean square (RMS) value lower than 10^{-4} and the overall imbalance in the domain less than 1% for all variables.

3.2.4. Thermal and physical properties

Taking into account the considerations made in *Section 3.1.4*, the influence of the temperature on the thermal and physical properties of fluid dispersion was considered negligible with respect to the variation of the apparent viscosity along the heat treatment due to the whey proteins denaturation-aggregation. As a consequence, the same properties reported in the *Section 3.1.4* were chosen for these fluid dynamics models. Nevertheless, in this case the apparent viscosity was assumed to be function not only of temperature but also of the shear rate inside the pipe; therefore, the temperature-apparent viscosity profile was experimentally determined at every flow rate of interest.

3.3 Models validation

The developed models for the static and continuous thermal treatment were validated by comparing experimental temperature values with the predicted ones.

For the static CFD models, the accuracy of the prediction was assessed by determining root mean square error (*RMSE*) with the following:

$$RMSE = \sqrt{\frac{\sum_{i=1}^{n}(T_E - T_P)^2}{N}} \qquad (10)$$

Where T_P is simulated temperature (°C), T_E is experimental temperature (°C) and N number of value compared. The lower RMSE value demonstrated a better compatibility of the simulation results (Iezzi et al., 2011, Boz et al., 2014).

However, for the continuous CFD models, considering the stationary conditions of the domain, the goodness of the models was evaluated quantifying the percentage difference between the experimental and simulated temperature, and model was considered validated when the value was lower the 5% (Aguiar and Gut, 2014).

4. Results and discussion

4.1. Validation of fluid dynamics models

4.1.1. Static thermal treatment

The results obtained from fluid dynamics models of the different static thermal treatments were in agreement with the experimental data (**Table 2**): the global RMSE values for the different processes resulted below 1.7 °C, according with data reported in literature (Iezzi et al., 2011; Boz et al., 2014; Cordioli et al., 2016). Furthermore, in **Figure 3**, experimental and simulated temperature profiles (at geometric centre and at outer wall of the test tube) at the three different temperatures are reported, confirming that the fluid dynamic models well fitted with the trend of experimental tests. The main deviations between experimental and simulated data appeared in the first part of both heating and cooling phases, probably due to the rapid variation of the boundary conditions and to the magnitude of phenomena. This hypothesis is strengthened by the fact that the discrepancy is noted mainly on the outer wall of the test tube, the region mostly affected by this rapid change. Precision of mathematical model could be reduced by increasing the number of the mesh elements, choosing a suitable adaptive time step method but with the need of higher computational effort and a less flexibility of the model. Thus the fluid dynamics models developed for the static thermal treatment could be considered validated and hence usable for industrial application to simulate treatments at different time and temperature combinations.

4.1.2. Continuous thermal treatment

Also for the fluid dynamics models developed for the continuous treatments an experimental validation took place by considering six different process conditions: minimum (3.66 min) and maximum (9.92 min) residence times for each process temperature (75, 80 and 85 °C). Data from models resulted in good agreement with the experimental ones (**Table 3**): the discrepancy might be caused by models' approximations needed to reduce the time of calculation and imposed by the hardware limitation. The most important approximation was the low number of meshes along the tube section, which represented the principal direction of heat exchange, mainly due to the high length/diameter ratio of the tube. Hence, it caused a reduction of the goodness of models, but for the aims of this work a mean difference of 0.93°C (0.67%) could be considered acceptable, in agreement with data reported in literature (Aguiar and Gut, 2014); consequently, these models can be considered successfully validated.

4.2. In-silico simulations by means of validated CFD models

4.2.1. Static thermal treatments

Starting from validated fluid dynamics models, three different temperatures (75, 80 and 85 °C) and seven times (2, 4, 6, 8, 12, 16, 20 min) were simulated and compared. To easily compare the effects of different process conditions the cook values (C_0) were calculated as follows:

$$C_0 = \int_0^t 10^{\left(\frac{T_{sim} - T_{ref}}{z}\right)} dt \qquad (11)$$

where T_{sim} (°C) was the product simulated temperature, T_{ref} (°C) the reference temperature (100°C), z the constant value equal to 33°C (Holdsworth, 1985) and dt (min) the time interval. In **Table 4** minimum (11.75 mm from the bottom), maximum (internal wall) and cook values calculated as a mean of 9 points inside the tube test, 5 along axis (at 11.75, 23.50, 35.25, 47.00, 58.75 mm from the bottom of test tube) and 4 along radius (at 0, 1.75, 3.50, 5.25 mm from the internal wall of test tube at half height) are reported. In this way, also the convective motions were taken into consideration and cook value estimation resulted more precise. Considering the difference between the cook values reported in **Table 4**, the temperature stratification inside the test tube decreased with the treatment time and increased with the treatment temperature. As expected, the temperature stratification tended to disappear once the test tube reached an equilibrium temperature. The results were confirmed by analysis of the coefficient of variation: the values decreased with the temperature and increased with the time of process. Data presented in **Table 4** shows that precise cook value, or in general thermal treatment, estimation could be very difficult by using experimental heat penetration data and that mathematical models could be very useful in this purpose eliminating over-estimation risk.

Starting from the data obtained from the simulated static thermal treatment, a response surface, linear with time and quadratic with temperature, was developed in Matlab® environment with an equation describing the relationship between the mean cook value and the treatment conditions:

$$C_0 = 25.85 - 0.6169 \cdot T_t - 1.041 \cdot t_t + 0.003569 \cdot {T_t}^2 + 0.01601 \cdot T_t \cdot t_t \qquad (12)$$

where C_0 is forecast cook value (min), T_t is treatment temperature (°C) and t_t is time of treatment (min). The equation, with R^2 value of 0.995, allowed predicting cook value within the temperature range of validation without experimental tests or in-silico simulations.

4.2.2. Continuous thermal treatments

In order to compare the results of the simulation at different conditions (75, 80 and 85 °C for 2, 4, 6, 8, 12, 16 and 20 min) also for the continuous thermal treatments the cook values were calculated both along the axis of the tube that represented the slowest heating zone (as in laminar flow regime the axis presents the highest velocity and so the minimum residence time) and near the tube wall (where the product was submitted to the higher thermal treatment due the lower fluid velocity near wall and the proximity with the heating medium). In **Table 5** the cook values for the different process conditions are reported. The effects of laminar flow appear evident: along the tube wall the cook value presents the higher results, however along the central axis, where the velocity was double respect the mean value, the cook value results lower. The difference between cook values along the axis and near the tube wall tended to increase with the time of treatment and with the temperature of treatment. Actual cook value calculation along the axis and near the wall in a pipeline is possible only by using validated mathematical models that allow miming temperature profile in every geometry. To compare these treatments with the statics ones, also the mean cook value, calculated at mean flow velocity, was taken into account and reported in **Table 5**.

As seen before, the mean cook values obtained from the simulation of continuous treatments were used to develop a quadratic response surface with Matlab® describing the relationship between the mean cook value and the treatment conditions:

$$C_0 = 34.189 - 0.854 \cdot T_t - 1.130 \cdot t_r + 0.0053 \cdot {T_t}^2 + 0.0004 \cdot {t_r}^2 + 0.0172 \cdot T_t \cdot t_r \quad (13)$$

Where C_0 is forecast cook value (min), T_t is treatment temperature (°C) and t_r is residence time (min). The equation, with R^2 value of 0.999, allows predicting cook value inside the temperature range of validation without experimental tests or in-silico simulations.

4.2.3. Comparison of static and continuous in-silico treatments

In **Figure 4** a comparison of the mean cook value between static and continuous simulated thermal treatments, at all process conditions, is reported. As expected, the effect of fluid flow inside the tube was evident: in all the conditions, the continuous treatment showed a higher cook value due to a faster warm up that happened in dynamic system in comparison with the static one: the lower the treatment time the higher the difference (about 84% for 2 min and 15% for 20 min treatment time). So, in the continuous conditions, where a slight forced convection induced by laminar flow took place, the warm up time it's significantly reduced compared to the static treatment where only natural convection was present.

5. Conclusion

In this study, starting from experimental tests, two different CFD models for thermal treatment of WP solutions under static and continuous conditions were designed and successfully validated, as confirmed by the low RMSE values. An equation for predicting the change of apparent viscosity as a function of the sample temperature was developed and used for the prediction of the transition from convective to conductive heat exchange mode along the whole thermal treatment. Moreover, the temperature data resulting from validated CFD models, were used to calculate the cook values allowing to quantify the cook value in several points of both static and continuous system and compared with experimental ones. In addition, two different equations for the prediction of the cook value at different process conditions were obtained. Finally, this work showed the feasibility of CFD modelling in a pilot tubular heat exchanger for predicting the relationship between gel formation and heat transfer when concentrated whey protein dispersions are processed at different shear rates and temperatures. A better knowledge of the behaviour may be useful to improve the design of mass continuous treatments and make more profitable the production of Ricotta cheese and/or other protein-based gels. By means of mathematical models it's also possible to study the residence time distribution of the product in the heat exchanger in order to predict gel properties on the basis of thermos-rheological history of whey proteins.

References

Aguiar, H.F. & Gut, J.A.W., (2014). Continuous HTST pasteurization of liquid foods with plate heat exchangers: Mathematical modeling and experimental validation using a time-temperature integrator. *Journal of Food Engineering*, 123, 78–86.

Alvarez, P.A., Emond, C., Gomaa, A., Remondetto, G.E. & Subirade, M., (2015). Predictive Response Surface Model for Heat-Induced Rheological Changes and Aggregation of Whey Protein Concentrate. *Journal of Food Science*, 80, 326–333.

ANSYS®, (2011). *ANSYS® Icepak User's Guide* (release 14, p. 700). Canonsburg, Pennsylvania, USA.

Arellano, M., Flick, D., Benkhelifa, H. & Alvarez, G., (2013). Rheological characterisation of sorbet using pipe rheometry during the freezing process. *Journal of Food Engineering*, 119, 385–394.

Blanpain-Avet, P., André, C., Khaldi, M., Bouvier, L., Petit, J., Six, T., Jeantet, R., Croguennec, T. & Delaplace, G., (2016). Predicting the distribution of a whey protein fouling in a plate heat exchanger using the kinetic parameters of the thermal denaturation reaction of β-lactoglobulin and the bulk temperature profiles. *Journal of Dairy Science*, 99(12), 9611-9630.

Boz, Z., Erdogdu, F. & Tutar, M., (2014). Effects of mesh refinement, time step size and numerical scheme on the computational modeling of temperature evolution during natural-convection heating. *Journal of Food Engineering*, 123, 8–16.

Chantoiseau, E., Plana-Fattori, A., Doursat, C. & Flick, D., (2012). Coupling fluid flow, heat transfer and thermal denaturation-aggregation of beta-lactoglobulin using an Eulerian/Lagrangian approach. *Journal of Food Engineering*, 113(2), 234-244.

Choi, Y. & Okos, M., (1985). Effects of temperature and composition on the thermal properties of foods. In *Proceedings of the Fourth International Congress on Engineering and Food*, Etninston, Alberta, Canada.

Cordioli, M., Rinaldi, M. & Barbanti, D., (2016). Investigation and modelling of natural convection and conduction heat exchange: study on food systems with modified starch by means of computational fluid dynamics. *International Journal of Food Science and Technology*, 51, 854–864.

Erabit, N., Ndoye, F. T., Alvarez, G. & Flick, D. (2015)., A Population Balance Model integrating some specificities of the β-lactoglobulin thermally-induced aggregation. Journal of Food Engineering, 144, 66-76.

Erabit, N., Ndoye, F. T., Alvarez, G. & Flick, D., (2016). Coupling Population Balance Model and Residence Time Distribution for pilot-scale modelling of β-lactoglobulin aggregation process. *Journal of Food Engineering*, 177, 31–41.

Fernández Farrés, I., Moakes, R.J.A. & Norton, I.T., (2014). Designing biopolymer fluid gels: A microstructural approach. *Food Hydrocolloids*, 42, 362–372.

Holdsworth, S.D., (1985). Optimisation of thermal processing–A review. *Journal of Food Engineering*, 4, 89–116.

Iezzi, R., Francolino, S. & Mucchetti, G., (2011). Natural convective cooling of cheese: Predictive model and validation of heat exchange simulation. *Journal of Food Engineering*, 106, 88-94

Kreith, F., Manglik, R. M. & Bohn, M. S., (2011). *Principal of Heat Transfer* (p. 401). Cengage Learning, Stamford, Connecticut, USA.

Lienhard IV, J. H. & Lienhard V., J. H., (2008) *A Heat Transfer Textbook* (p. 706). Phlogiston Press, Cambridge, Massachusetts, USA.

Mirade, P.S. & Daudin, J.D., (2006). Computational fluid dynamics prediction and validation of gas circulation in a cheese-ripening room. *International Dairy Journal*, 16, 920–930.

Modler, H.W. & Emmons, D.B., (2001). The use of continuous ricotta processing to reduce ingredient cost in “further processed” cheese products. *International Dairy Journal*, 11, 517–523.

Ndoye, F.T., Erabit, N., Alvarez, G. & Flick, D., (2012). Influence of whey protein aggregation on the residence time distribution in a tubular heat exchanger and a helical holding tube during heat treatment process. *Journal of Food Engineering*, 112, 158–167.

Norton, T., Tiwari, B. & Sun, D.-W., (2013). Computational fluid dynamics in the design and analysis of thermal processes: a review of recent advances. *Critical Reviews in Food Science and Nutrition*, 53, 251–75.

Petit, J., Six, T., Moreau, A., Ronse, G. & Delaplace, G., (2013). β-lactoglobulin denaturation, aggregation, and fouling in a plate heat exchanger: Pilot-scale experiments and dimensional analysis. *Chemical Engineering Science*, 101, 432-450.

Spiegel, T. & Huss, M., (2002). Whey protein aggregation under shear conditions-effects of pH-value and removal of calcium. *International Journal of Food Science and Technology*, 37, 559-568.

Tolkach, A. & Kulozik, U., (2007). Reaction kinetic pathway of reversible and irreversible thermal denaturation of β-lactoglobulin. *Le Lait (INRA Editions)*, 87(4-5), 301–315.

Wang, Y., Wig, T.D., Tang, J. & Hallberg, L.M., (2003). Sterilization of Foodstuffs Using

Radio Frequency Heating. *Journal of Food Science*, 68, 539-544.

Wolz, M. & Kulozik, U., (2015). Thermal denaturation kinetics of whey proteins at high protein concentrations. *International Dairy Journal*, 49, 95–101.

Wolz, M., Mersch, E. & Kulozik, U., (2016). Thermal aggregation of whey proteins under shear stress. *Food Hydrocolloids*, 56, 396–404.

Yataghene, M., Fayolle, F. & Legrand, J., (2009). Experimental and numerical analysis of heat transfer including viscous dissipation in a scraped surface heat exchanger. *Chemical Engineering and Processing: Process Intensification*, 48(10), 1447-1458.

Table 1. Characteristic dimensions and qualitative parameters of meshing in the five subdomains of continuous thermal treatment plant.

	Length (m)	***Volume (L)***	***Min element edge (m)***	***Max element edge (m)***	***Growth rate***	***Skewness***	***Number of elements***	***Number of nodes***
Section 1	11.466	0.3243	$4.9*10^{-5}$	$9.8*10^{-3}$	1.10	0.21±0.1	$10.5*10^{6}$	$3.3*10^{6}$
Section 2	5.113	0.1446	$7.6*10^{-5}$	$1.5*10^{-2}$	1.10	0.22±0.1	$4.8*10^{6}$	$1.5*10^{6}$
Section 3	30.608	0.8655	$1.3*10^{-4}$	$2.7*10^{-2}$	1.16	0.22±0.1	$19.3*10^{6}$	$6.6*10^{6}$
Section 4	28.326	0.8011	$1.3*10^{-4}$	$2.6*10^{-2}$	1.16	0.22±0.1	$18.9*10^{6}$	$6.4*10^{6}$
Section 5	10.451	0.2962	$6.7*10^{-5}$	$1.3*10^{-2}$	1.10	0.22±0.1	$10.1*10^{6}$	$3.2*10^{6}$

Table 2. Maximum RMSE values (°C) obtained for the static thermal treatment model validation.

	Heating phase		***Cooling phase***		***Global treatment***	
	centre	***wall***	***centre***	***wall***	***centre***	***wall***
75°C	1.70	0.66	0.75	1.42	1.32	1.10
80°C	1.89	1.18	1.32	1.93	1.63	1.59
85°C	1.99	0.97	1.29	1.10	1.67	1.04

Table 3. Absolute and percentage (in brackets) temperature differences between experimental data and simulations for continuous thermal treatments.

	Residence time (min)	***Section 1***	***Section 2***		***Section 3***		***Section 4***	***Section 5***		***Mean***
		Outlet	***Inlet***	***Outlet***	***Inlet***	***Outlet***	***Outlet***	***Inlet***	***Outlet***	
75°C	3.66	0.45	1.60	0.55	0.36	0.17	0.21	3.21	1.10	***0.96***
		(0.65)	(2.32)	(0.78)	(0.53)	(0.25)	(0.29)	(4.41)	(1.57)	***(0.82)***
	9.92	1.22	0.98	0.39	0.05	0.16	2.45	0.68	1.67	***0.95***
		(1.70)	(1.38)	(0.55)	(0.07)	(0.22)	(3.55)	(0.95)	(2.36)	***(0.34)***
80°C	3.66	0.43	0.45	0.21	1.16	0.17	0.53	0.09	2.20	***0.65***
		(0.56)	(0.60)	(0.27)	(1.59)	(0.21)	(0.70)	(0.12)	(2.96)	***(0.46)***
	9.92	0.26	0.46	0.57	1.53	0.62	2.18	1.30	1.10	***1.00***
		(0.35)	(0.61)	(0.76)	(2.10)	(0.81)	(2.99)	(1.70)	(1.46)	***(1.11)***
85°C	3.66	0.15	0.89	0.86	1.34	0.99	2.16	0.92	1.22	***1.07***
		(0.19)	(1.08)	(1.07)	(1.72)	(1.23)	(2.77)	(1.13)	(1.54)	***(0.74)***
	9.92	0.50	0.96	1.19	1.42	0.61	1.36	0.54	1.06	***0.95***
		(0.63)	(1.20)	(1.49)	(1.80)	(0.75)	(1.76)	(0.66)	(1.34)	***(0.55)***

Table 4. Simulated cook values (min) between nine points for the static thermal treatment.

min	***75°C***					***80°C***					***85°C***				
	mean	***cv***	***min***	***max***	***diff***	***mean***	***cv***	***min***	***max***	***diff***	***mean***	***cv***	***min***	***max***	***diff***
2	0.06	*35%*	0.03	0.09	*67%*	0.08	*37%*	0.04	0.12	*69%*	0.09	*39%*	0.04	0.16	*72%*
4	0.27	*20%*	0.18	0.35	*48%*	0.34	*23%*	0.22	0.47	*53%*	0.43	*26%*	0.27	0.64	*58%*
6	0.55	*14%*	0.43	0.67	*36%*	0.73	*16%*	0.55	0.92	*41%*	0.97	*18%*	0.70	1.26	*44%*
8	0.88	*10%*	0.73	1.01	*27%*	1.19	*11%*	0.97	1.40	*31%*	1.60	*12%*	1.29	1.94	*33%*
12	1.57	*6%*	1.41	1.70	*17%*	2.16	*7%*	1.93	2.38	*19%*	2.98	*7%*	2.64	3.33	*21%*
16	2.26	*4%*	2.10	2.40	*12%*	3.15	*5%*	2.91	3.37	*14%*	4.38	*5%*	4.04	4.73	*15%*
20	2.96	*3%*	2.80	3.10	*10%*	4.14	*3%*	3.90	4.36	*11%*	5.78	*4%*	5.44	6.14	*11%*

Table 5. Simulated cook value (min) for the continuous thermal treatment along the axis (maximum flow velocity), near the wall (minimum flow velocity) and at mean flow rate.

min	*75 °C*			*80 °C*			*85 °C*		
	axis	*wall*	*mean*	*axis*	*wall*	*mean*	*axis*	*wall*	*mean*
2	0.17	2.69	0.34	0.24	3.81	0.47	0.34	5.40	0.67
4	0.34	5.46	0.67	0.47	7.73	0.95	0.67	10.96	1.34
6	0.51	8.09	1.01	0.71	11.46	1.42	1.00	16.24	2.01
8	0.67	10.79	1.34	0.96	15.29	1.91	1.34	21.67	2.67
12	1.02	16.19	2.03	1.45	22.95	2.88	2.03	32.52	4.05
16	1.36	21.60	2.73	1.97	30.62	3.87	2.73	43.39	5.45
20	1.71	27.01	3.42	2.51	38.28	4.86	3.42	54.26	6.84

Figure 1. Schematically view of the continuous heat exchanger: the different colours represent the segmentation of the CFD model domains while the dashed lines are the volume occupied by the water. The arrows show the position of the thermocouples.

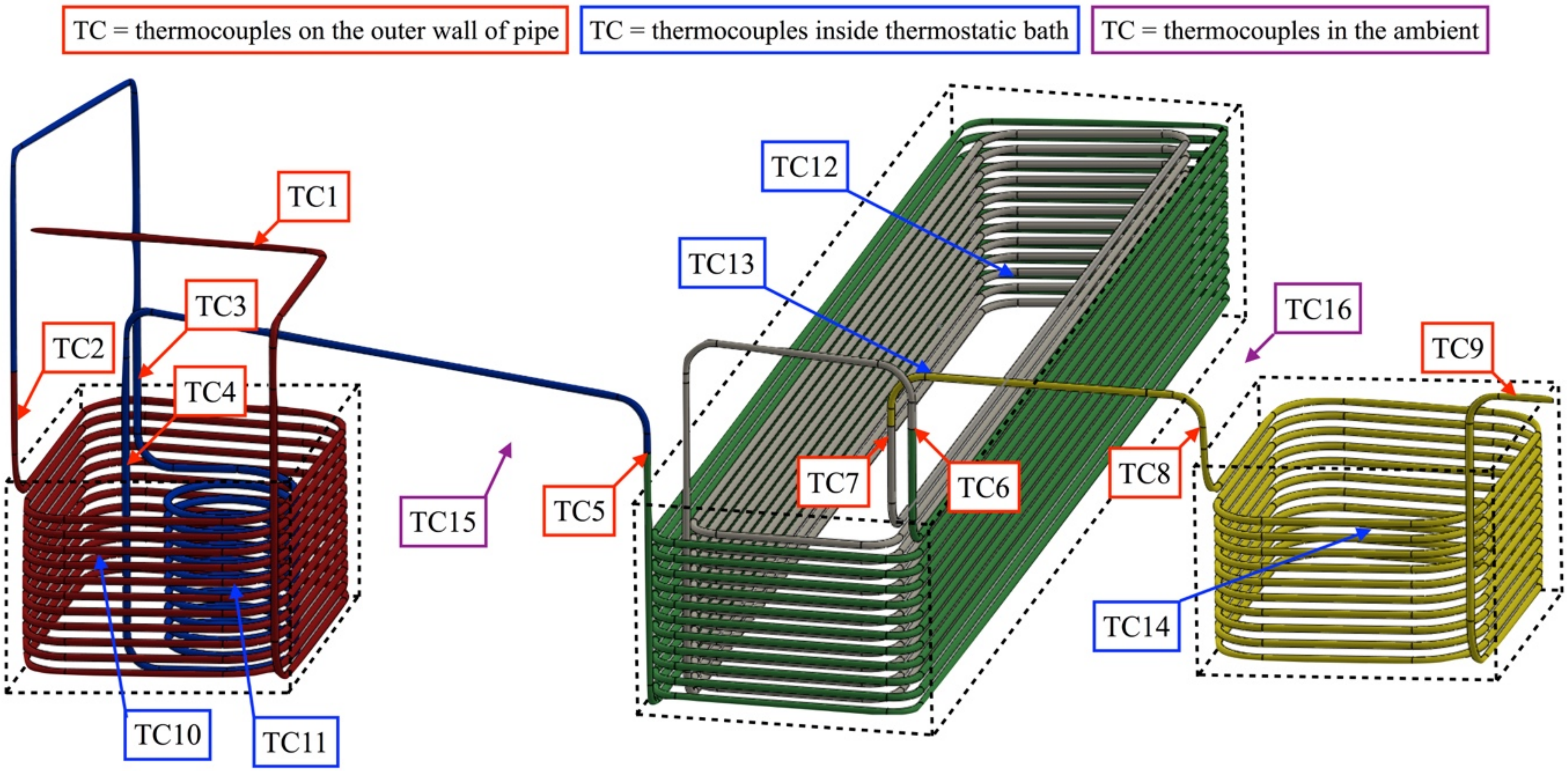

Figure 2. Response surface by fitting experimental data from thermo-rheological analysis of whey protein dispersion at different shear rate.

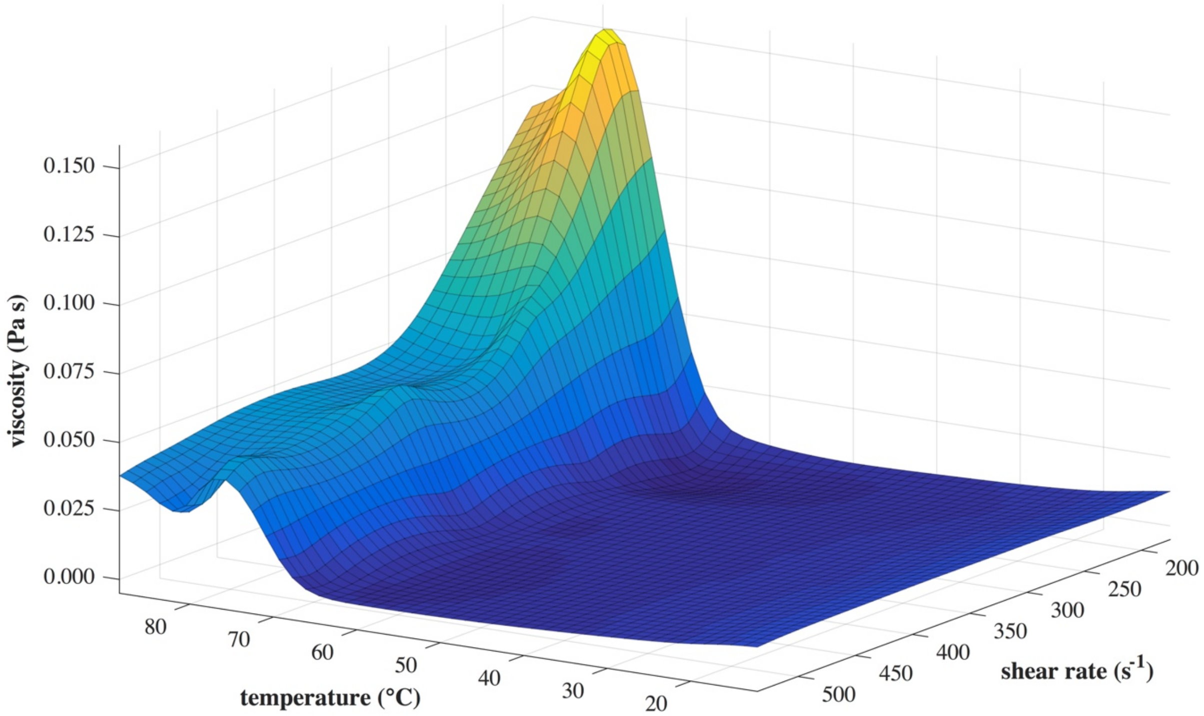

Figure 3. Comparison of temperature profile between experimental test (RSD < 5%) and mathematical model for the static thermal treatment at 75 (panel **a**), 80 (panel **b**) and 85 °C (panel **c**).

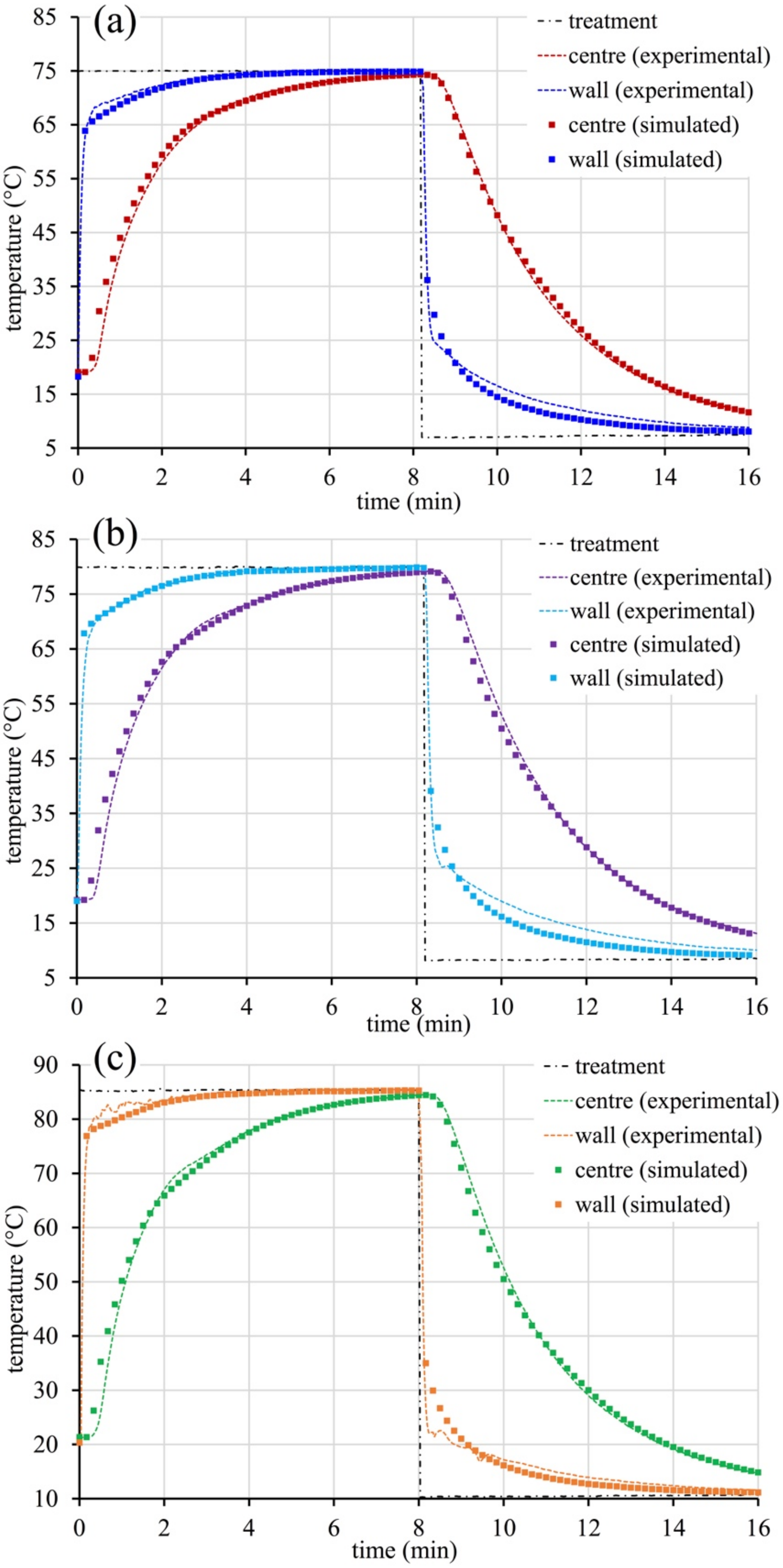

Figure 4. Comparison of cook value obtained from static and continuous in-silico treatments: (panel **a**) 75°C, 80°C (panel **b**) and 85°C (panel **c**) at different process time.

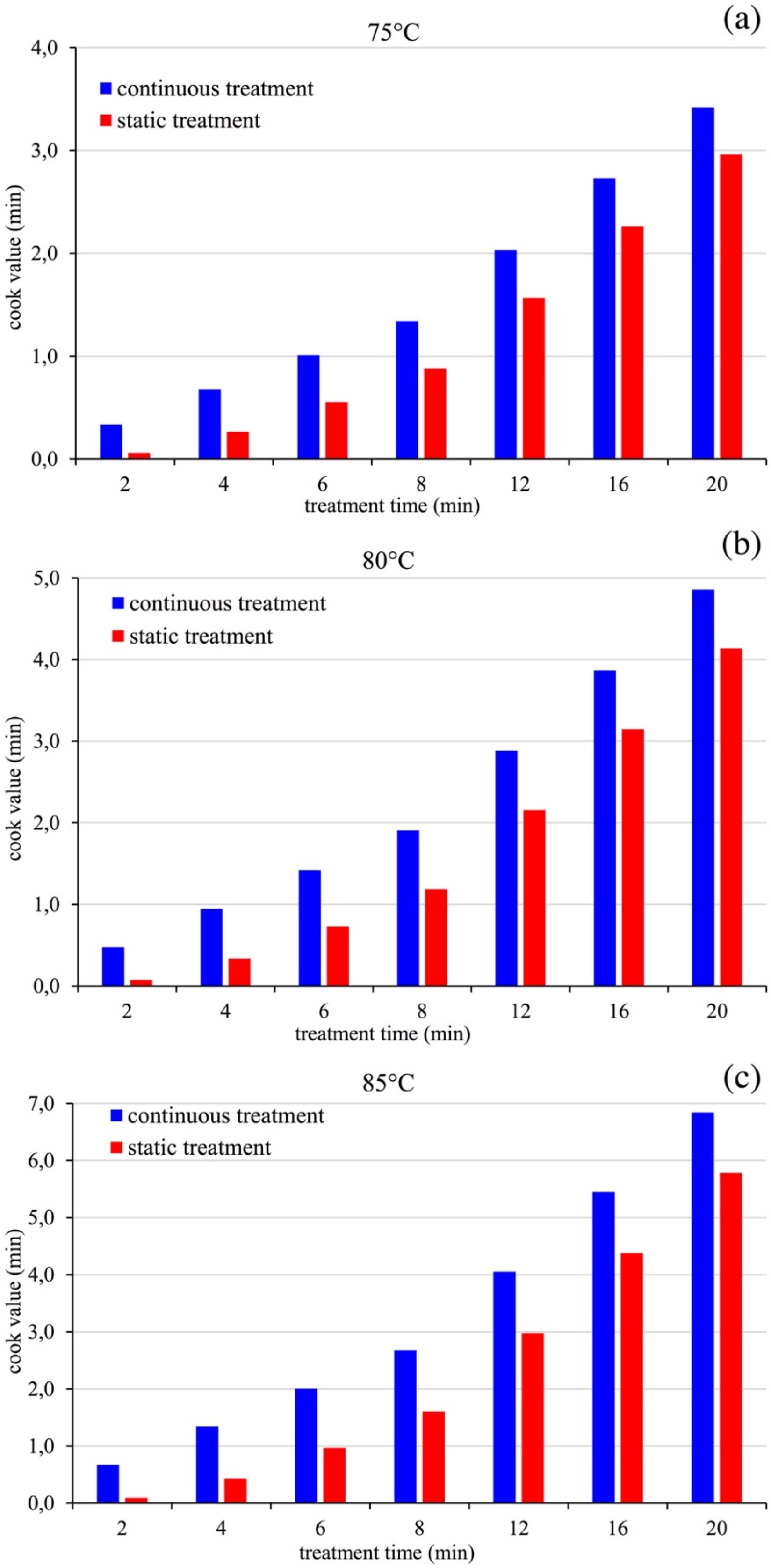

Study of fluid motion

Study and optimization of a CO_2 sparger for carbonated beverages and beer by means of CFD modelling

Massimiliano Rinaldi[1], Matteo Cordioli[1], Davide Barbanti[1] and Marco Dall'Aglio[2]

[1]Department of Food Science, University of Parma, Parco Area delle Scienze 47/A, 43124 Parma, Italy
[2]Valfor Srl, Via Achille Grandi, 1, 43045 Fornovo di Taro, Italy

Published in *International Journal of Food Engineering*
DOI: 10.1515/ijfe-2016-0083

Abstract

In the present work, two different geometries of spargers for beverage carbonation were modelled by means of CFD technique, taking into consideration three different flow rates. The first geometry presented a radial inlet of liquid food while the second one a tangential one. Calculation allowed to study the effect of fluid velocities on mixing and to identify the best solution; mathematical results were then confirmed from a qualitative point of view by experimental tests with both water and apple juice. CFD resulted a very useful technique for in-silico designing, not only for technically-simple parts of plants, but also for very complicated ones such as carbon dioxide spargers in which gas and liquid are mixed together.

Keywords: carbonated beverage, computational fluid dynamic, fluid flow

1. Introduction

The consumption of soft drinks in their various forms has taken place for many centuries in order to meet the body's fundamental requirement for hydration. The discovery of the means of artificially carbonating water by dissolution of CO_2 under pressure is attributed to Dr. Joseph Priestley in the late 1760s, though there were many other workers active in this field at the same time which probably deserves equal credit.

Production of carbonated drinks was traditionally carried out by means of adding concentrated syrup to the bottle and then topping it up with carbonated water. A considerable improvement in speed was achieved in 1937, when the Mojonnier Brothers Corporation of Chicago introduced a continuous blending/cooling/carbonating system (Steen and Ashurst, 2006).

In general, two basic methods for carbonating a drink are possible: the injection and dispersion of carbon dioxide into the liquid to be carbonated, and the fine spraying of the product into a carbon dioxide atmosphere. However, in-line carbonation methods are being used increasingly. These either sparge carbon dioxide into the liquid or inject the liquid into a gas stream. When the gas is sparged into the liquid small bubbles of gas are formed and hence easily absorbed by the liquid. The higher the pressure the smaller the gas bubbles formed at the sparger and the greater the gas bubbles surface area available for the gas to be absorbed by the liquid. In addition, also the inlet gas velocity, the physical properties of liquid, as well as the design of both the sparger and the housing of the sparger play an important role in optimal dissolution of gas into liquid (Ali et al., 2016). In the recent years, several efforts were spent for modelling carbonation process by means of numerical techniques and mathematical models: As an example, Ali et al. (2016) applied the Euler–Euler methodology to numerically investigate the gas–liquid flow mixing feature inside a continuously operated carbonating tank and studied various injecting nozzle designs, gas bubble sizes and liquid or gas velocities. Also Sanyal et al. (1999) develop and validate a transient, two-dimensional axisymmetric simulation of a laboratory-scale cylindrical bubble column with good results. A computational fluid dynamics model was developed to predict mixing time in a bubble column at higher gas velocity and results appear in good agreement with experimental data (Rampure et al., 2007). Lestinsky et al. (2012) carried out a study on the effect of different geometric parameters on the two phase inside an airlift reactor. Experimental results and numerical simulations were compared and a good agreement was find. For the best authors knowledge, no works were published on carbonation of beverage in continuous conditions. However, the Authors stated that large-scale experimental multiphase flow systems require a considerable amount of construction time and cost and thus mathematical models could be very helpful in designing mixing process with a great reduction of costs and time.

For this reason, the aim of this work was to study and optimize different designs of CO_2 sparger, at three different flow rates, for water or soft drink carbonation by means of CFD modelling. In this way, the time and cost needed for the development stage could be reduced and process can be optimized to guarantee the best results at every flow rates.

2. *Materials and methods*

2.1. Spargers geometry

Studied spargers for water and beverage carbonation process, made of sintered porous metal (mean pore size 1 μm) and designed for the food industry (Pall Corporation, Port Washington, NY, USA) had a diameter of 34 mm and a height of 145 mm. The housing of sparger presented an internal diameter and height of 40 and 200 mm, respectively. Both water and carbon dioxide inlets had an internal diameter of 8 mm and a section of 50.2 mm^2, as consequence. Between sparger upper surface and housing outlet there was a chamber for fluids mixing of 0.136 dm^3. In **Figure 1** the characteristic dimensions of geometry are reported.

The main difference between the two spargers taken into consideration in this work was the geometry of the water inlet into the mixing chamber: the first one presented a radial inlet while the second one a tangential water inlet (**Figure 2**). Furthermore, in order to evaluate also the effect of different flow rates on the mixing efficacy and efficiency three different process conditions were studied: flow rate of the water at INLET 1 was set at 8, 16 and 32 L h^{-1} while carbon dioxide at INLET 2 was set at 2.8, 5.6 and 13.2 L h^{-1} (hereinafter referred to process A, B and C, respectively).

2.2. CFD models development

Two sparger geometries were studied and modelled by means of multidimensional CFD (Computational Fluid Dynamic) model. The modelled sparger geometries were firstly drawn by means of SolidWorks® 2013 (Dassault systèmes, Vélizy-Villacoublay, France) in order to obtain two 3D CAD models. Only the fluid domain was taken into consideration in models development. The 3D geometry was then imported into the ICEM CFD® software (Canonsburg, Pennsylvania, USA) and discretized into an unstructured tetrahedrical mesh. The values of maximum and minimum element edge dimensions for both the spargers geometry were $6.6*10^{-2}$ and $3.3*10^{-4}$ m. In order to accurately calculate the flow field near the wall of the sparger, five layers of flat prismatic wedge element were used for the discretization of the fluid domain. For the optimization of an appropriate level of accuracy, a maximum dimension of mesh near the wall of $5.0*10^{-4}$ m and of $2.5*10^{-4}$ m at the contact surface of the two fluids was imposed. The final mesh consists of 7275016 elements for radial geometry (Sparger 1) and 7304227 elements for tangential one (Sparger 2). The mesh was then optimized and finalized for better accuracy and computational time. From a quality point of view, the values of skewness for radial and tangential geometry were 0.23±0.13 and 0.23±0.13, respectively, that represent a good value (ANSYS Icepak User's Guide, 2011).

The software ANSYS® CFX v15 (Canonsburg, Pennsylvania, USA), on HP Z420 Workstation (Palo Alto, California, USA), was used to solve the governing continuity and momentum equations for the defined geometry and associated boundary conditions (heat exchange wasn't take into consideration). The domain was defined in the global co-ordinate frame in which the solver carries out the calculations. The generalized transport equations solved are:

a) *The continuity equation*

$$\frac{\partial \rho}{\partial t} + \nabla \cdot (\rho V) = 0 \qquad (1)$$

b) *The momentum equation*

$$\frac{\partial \rho V}{\partial t} + \nabla \cdot (\rho V \cdot V) = \nabla \cdot \left(-\mathrm{p}\delta + \mu \cdot (\nabla V + (\nabla V)')\right) + S_M \qquad (2)$$

Where t is the time (s), V is the velocity vector (m s^{-1}), ρ is the density (kg m^{-3}), p is the pressure (Pa), μ is dynamic viscosity (Pa s). In this study a stationary simulation was carried out and a no-slip condition was applied with velocity = 0 m s^{-1} of the fluid relative to the internal sparger surface. To model the turbulence inside the flow a Shear Stress Transport (SST) equation was chosen for all the models. High resolution advection schemes were adopted for all simulations, in order to achieve second order accuracy. The convergence criterion was defined as residual root mean square (RMS) value lower than 10^{-4}. The fluid domain was considered as a multiphase system with two different liquid phases, and to simplify the CFD models, the chemical interactions between the phases were not taken into consideration: hence, only the mixing effect due to the fluid flow was studied (and the two fluids were considered immiscible). To improve the accuracy of the solution a free surface model was choosen in addition to the models reported in this paragraph, this model reduces the computational effort but at the same time guarantee good results. The incoming fluid was considered water while carbon dioxide was considered as the gas phase: properties of studied fluids were obtained from scientific literature and are reported in **Table 1**.

2.3. CFD models development

After modelling, water carbonation was experimentally tested on a pilot plant (developed by Valfor Srl) located in University of Parma laboratories. The pilot plant presented a total volume of about 2 L and a flow rate varying from 2 to 50 L h^{-1}. The equipment could work up to 200 bar and it is implemented with several water baths to have constant temperature both of carbon dioxide and product to be carbonated. The carbonation efficacy was evaluated from a qualitative point of view with a camera that continuously captured images of gas-liquid mixture thanks to three inspection windows (**Figure 3**) made of transparent polycarbonate placed on the pipeline of the pilot plant: by means of qualitative analysis of number and dimensions of gas bubbles, mixing results of different conditions were compared.

3. Results and discussion

3.1. Mixing efficacy and efficiency from CFD models

In order to quantify mixing efficacy, water volume fractions on the outlet section of both spargers were calculated at 3 different flow rates. Theoretically, from the volume ratio between water flow inlet and gas flow inlet, the water volume fraction value is equals to 0.741. As reported in **Table 2**, tangential connection (Sparger 2) seemed to give a better mixing of gas and liquid at the outlet of the sparger as given by a lower water volume fraction values in all the studied conditions. In particular, the best process conditions were different for the two geometry: for the radial geometry (Sparger 1) the best mixing results were obtained at the process condition C (the highest flow rate), while for the tangential geometry (Sparger 2) the best mixing results were obtained at the process condition A (the lowest flow rate value). This different behaviour could be due to the different flows in the mixing chamber: when the water flow entered radially into the chamber a higher flow rate increased the turbulence as well as the degree of mixing. However, for the tangential water flow inlet, centrifugal motions set up along the housing's internal wall caused a lower degree of turbulence in the domain; as a consequence, in order to obtain a higher mixing value, a higher residence time (corresponding to lower flow rate) was necessary. These hypotheses are confirmed by streamlines reported in **Figure 4** where the turbulence vs. centrifugal motion behaviours are evident.

In order to quantify mixing efficiency, pressure drops, calculated as difference between average pressure at inlet and average pressure at outlet section of both spargers were compared. As reported in **Table 3**, the lowest pressure drop was obtained in the Sparger 2 (tangential injection) for all the conditions. This was probably the consequence of a lower turbulence inside the mixing chamber of the Sparger 2 with respect to Sparger 1 (**Figure 4**): in general, the pressure drop tended to reduce with the increasing of the flow rate.

3.2. Mixing efficacy from experimental test

From experimental tests, developed at the best conditions obtained from model data, Sparger 1 seem to give, from a qualitative point of view, a better mixing between water and CO_2 and a more stable carbonated water (**Figure 5**), as consequence. Sparger 1 gave more homogeneous and little bubbles in comparison to Sparger 2 without great bubbles along the internal wall of the inspection unit (**Figure 5**). From this point of view, the tangential inlet was not the best solution even if the liquid generated its own turbulence inside the housing and prevented fluid streamlines formation. Probably, turbulence inside the Sparger 2 and the spiral flux on the filter limited the spilling of CO_2 with great bubbles along pipeline walls as well shown in **Figure 5**. Results from experimental tests were confirmed by distribution of fluids at the outlet (**Figure 6**).

3.3. Mixing quality

For the evaluation of the mixing efficacy it is also necessary to study the degree of homogeneous distribution at the outlet section of the mixing chamber. In **Figure 6** water volume fraction contours were reported for the two different geometries at the three process conditions. As depicted, not homogeneous mixture distributions were reached at the outlet of any samples. As shown, the water inlet geometry didn't influence the mixture distribution and also the different fluid flow affected the results. In **Figure 7** a comparison between the process conditions for the different geometries is reported: no significant differences in water volume fraction were observed for the Sparger 1 (**Figure 7A**); however for the Sparger 2, water volume fraction profiles were slightly affected by the process conditions (**Figure 7B**). Process C seemed to generate a great unevenness in fluid mixing probably due to centrifugal forces, as stated above. The evaluation of the effect of the sparger geometry on the mixing quality was made and a comparison between water volume fraction profiles at each process condition was reported in **Figure 8**. Except for the process B (**Figure 8B**) where the geometry didn't affect the mixing homogeneity, the sparger inlet geometry changed the mixing quality. In the process A (**Figure 8A**) the trend was the same for most of the profiles except for those closer to the walls. Major differences could be evidenced in Process C conditions (**Figure 8C**) where the trend was significantly different between the two geometries.

4. Conclusion

This work demonstrated the effectiveness of mathematical model to predict fluid mixing also in complex systems and the usefulness of these models for designing and optimizing gas sparging systems for the beverage industry. Two sparger geometries and three flow rates were studied and best settings for each condition were identified. From the developed CFD models significant different results between the two geometries and at different inlet flow rate were obtained. However in both cases no homogenous mixtures were obtained with about the same results under all test conditions. Probably, for the increasing of the homogeneity of the output stream, a static turbulence generator could be added in the upper part of the mixing chamber: in this way the two fluids could mix better. Mathematical modelling and the proposed approach could be also used for designing new sparger geometries and achieve process optimization by reducing experimental tests and by reducing times in building new geometries.

References

Ali, H., Kim, K. W., Kwak, M. K., Kim, J. S., Choi, J. Y. & Park, C. W., (2016). Numerical investigation on the flow mixing feature inside a continuously carbonating process tank. *Computers & Electrical Engineering*, (51), 343-355.

ANSYS®, (2011). *ANSYS® Icepak User's Guide* (release 14). Canonsburg, Pennsylvania, USA.

Lestinsky, P., Vayrynen, P., Vecer, M. & Wichterle, K., (2012). Hydrodynamics of airlift reactor with internal circulation loop: Experiment vs. CFD simulation. *Procedia Engineering*, (42), 892-907.

Rampure, R. M., Kulkarni A. A. & Ranade, V.V., (2007). Hydrodynamics of Bubble Column Reactors at High Gas Velocity: Experiments and Computational Fluid Dynamics (CFD) Simulations. *Industrial and Engineering Chemistry Research*, (46), 8431-8447.

Sanyal, J., Vàsquez, S., Shantanu, R. & Dudukovic, M. P., (1999). Numerical simulation of gas-liquid dynamics in cylindrical bubble column reactors. *Chemical Engineering Science*, (54), 5071-5083.

Steen, D. & Ashurst, P.R., (2006). Carbonated soft drinks: formulation and manufacture. Oxford: Blackwell Publishing Ltd.

Table 1. Physical and thermal properties of modelled fluids.

	CO_2	*Water/Liquid food*
Molar mass (kg mol^{-1})	44.0	18.0
Density (kg m^{-3})	1.98	997
Dynamic viscosity (Pa s)	0. 0149	0.8899
Thermal expansivity (K^{-1})	0.00366	0.000257

Table 2. Mean water volume fraction value, obtained from CFD models, of the two sparger geometry in the three process conditions at the outlet region.

	Process condition		
	A	***B***	***C***
Sparger 1	0.820	0.867	0.817
Sparger 2	0.754	0.835	0.766

Table 3. Pressure drop value in absolute and in percentage, obtained from CFD models, of the two sparger geometry in the three process conditions.

	Process A				***Process B***				***Process C***			
	P_{inlet} (Pa)	P_{outlet} (Pa)	ΔP (Pa)	ΔP (%)	P_{inlet} (Pa)	P_{outlet} (Pa)	ΔP (Pa)	ΔP (%)	P_{inlet} (Pa)	P_{outlet} (Pa)	ΔP (Pa)	ΔP (%)
Sparger 1	6.8	1.0	5.9	86%	22.4	3.9	18.5	83%	80.5	17.3	63.2	79%
Sparger 2	5.9	1.0	4.9	83%	20.7	4.3	16.4	79%	76.2	18.4	57.8	76%

Figure 1. Sparger internal geometry with the main dimension (mm).

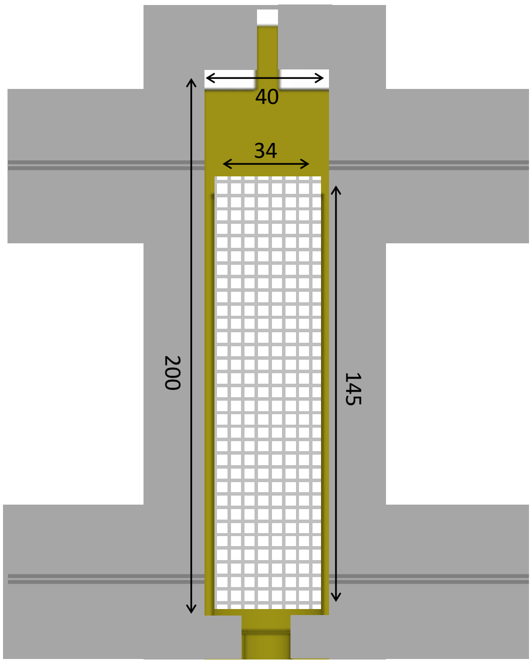

Figure 2. Radial (Sparger 1) and tangential (Sparger 2) sparger geometries obtained from 3D model, whole (upper) and section (below).

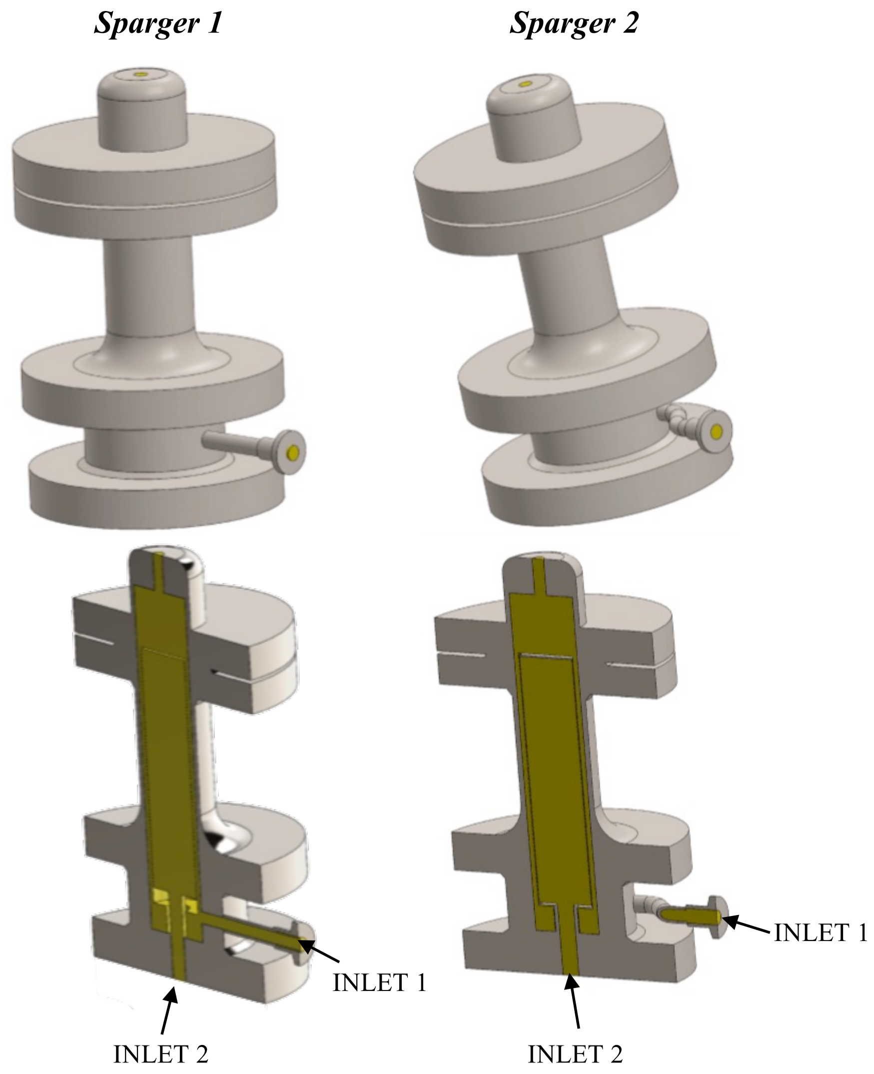

Figure 3. Inspection unit for bubble measurement mounted on the pilot plant.

Figure 4. Streamline obtained from CFD models inside the mixing chamber for the two geometries at the process conditions with the best mixing results (blue: water; red: carbon dioxide).

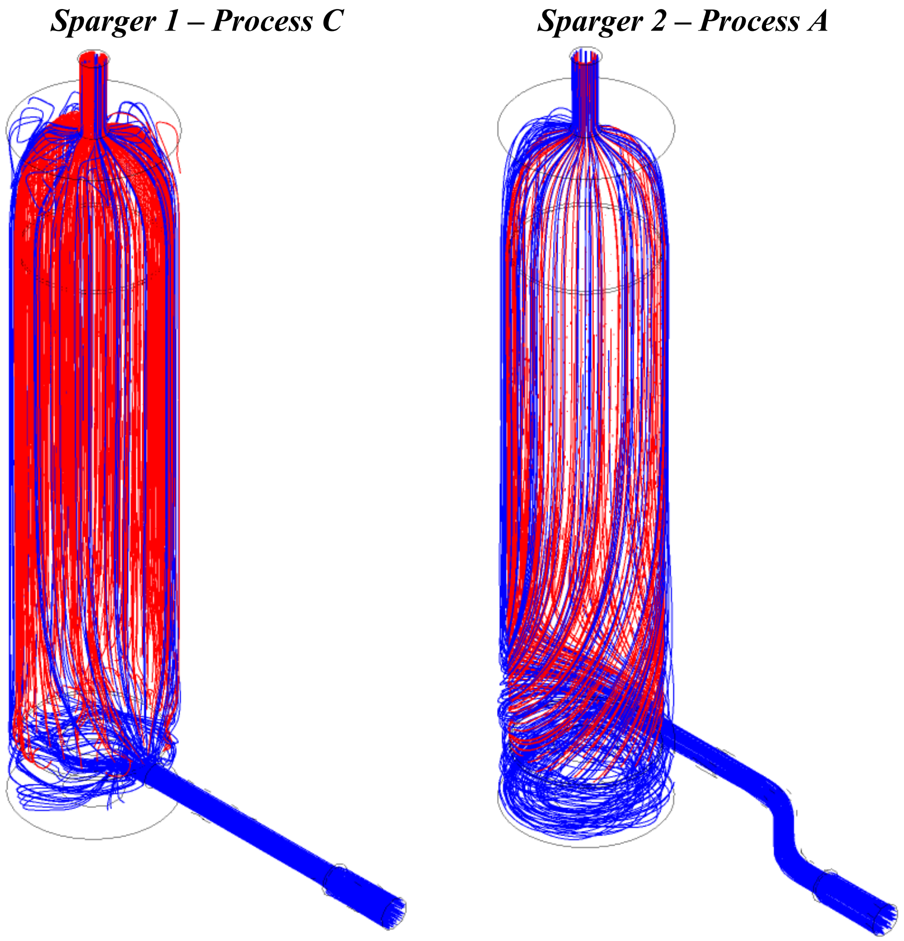
Sparger 1 – Process C

Sparger 2 – Process A

Figure 5. Bubbles inside the inspection unit after the mixing chamber for the two geometries at the process conditions with the best mixing results.

Sparger 1 ***Sparger 2***

Figure 6. Water volume fraction contours at the outlet section, obtained from CFD models, of the two sparger geometries in the three process conditions (blue: water 100%; white: carbon dioxide 100%).

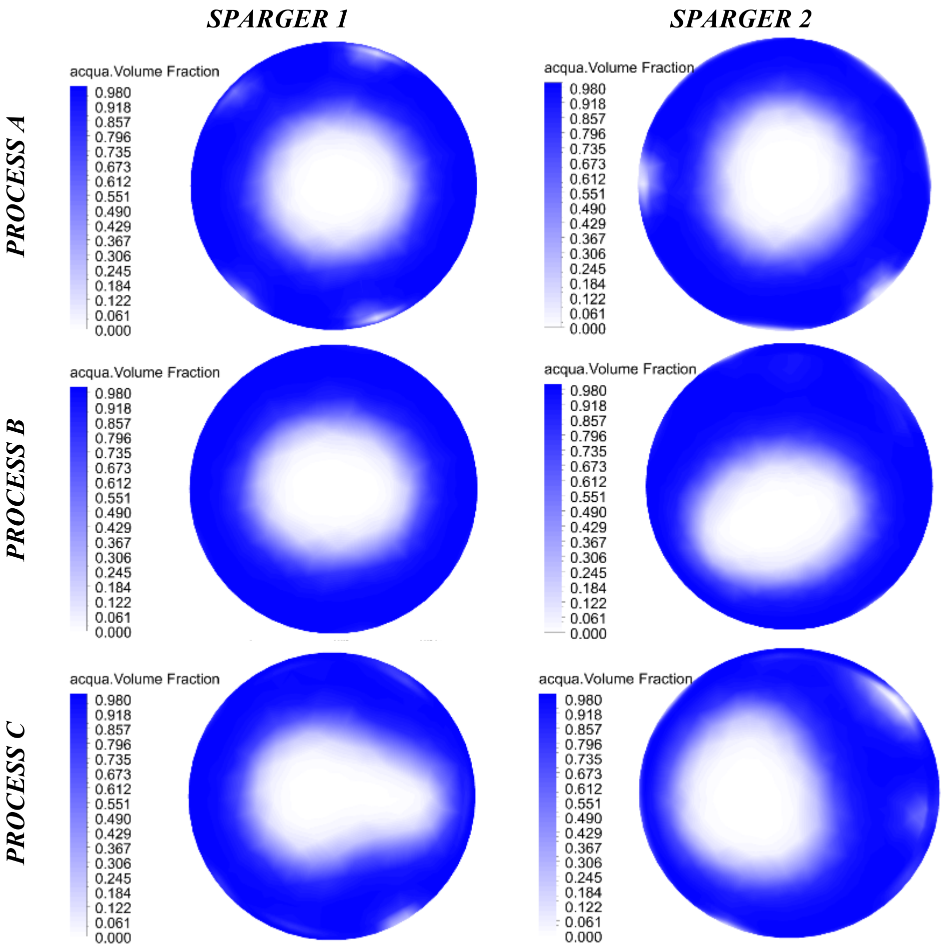

Figure 7. Comparison of water volume fraction profile at the outlet section at different process conditions for the Sparger 1 (panel **A**) and Sparger 2 (panel **B**).

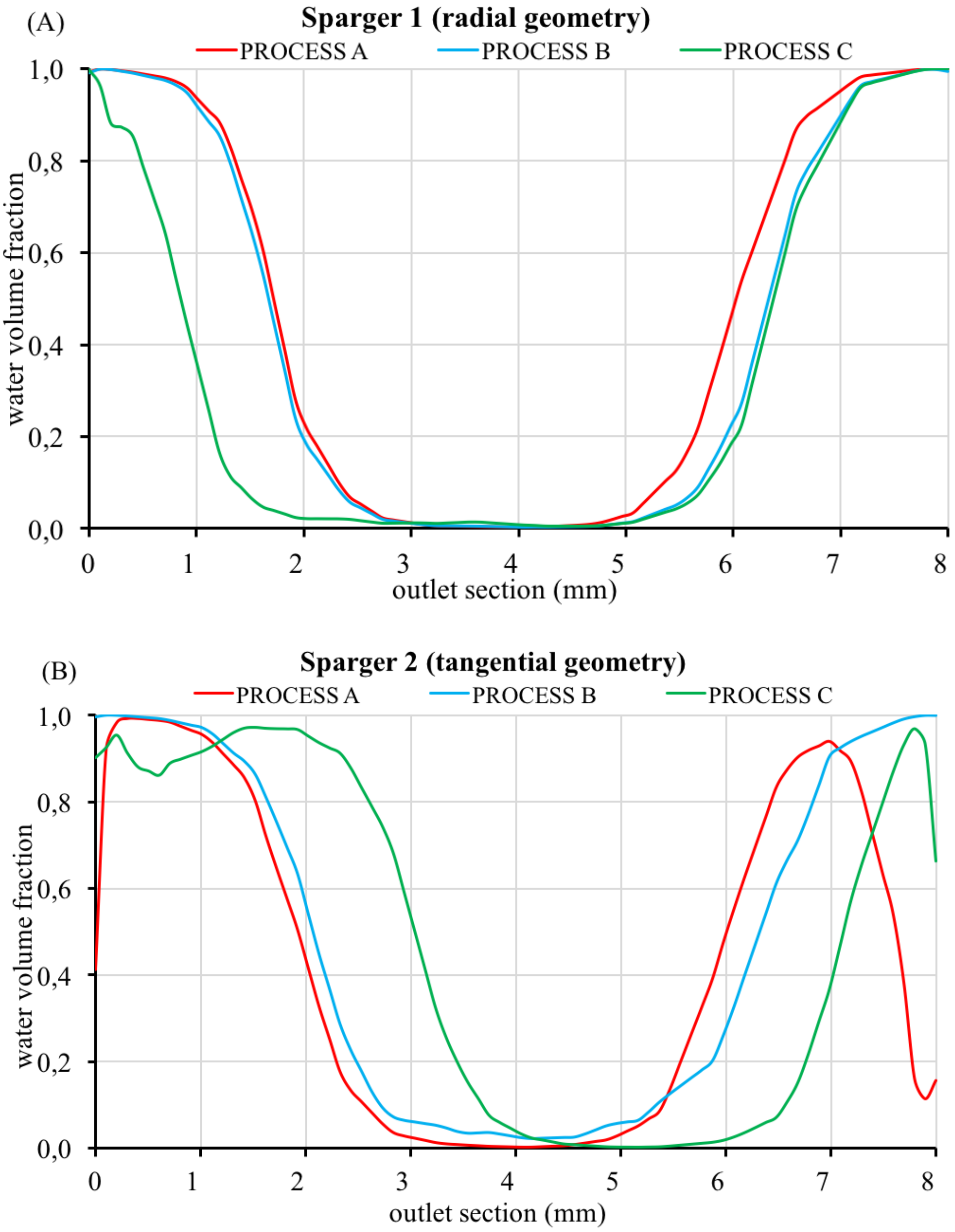

Figure 8. Comparison of the effect of the sparger geometry on water volume fraction profile, obtained from CFD models, at different process conditions.

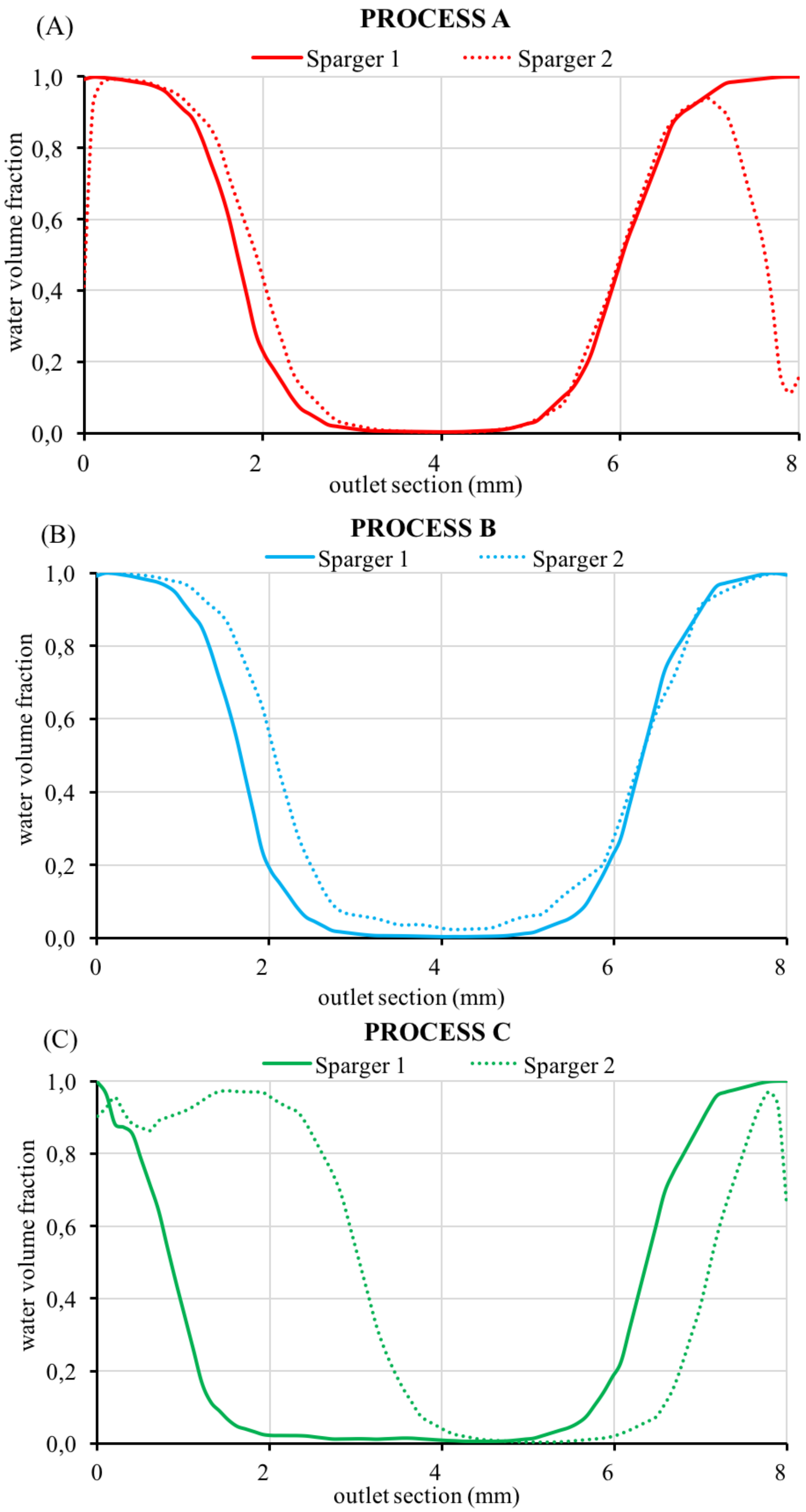

Development of a geometry with specific wall shear stress characteristics by means of Computational Fluid Dynamics (CFD) techniques

Matteo Cordioli, Giampaolo Betta and Davide Barbanti

Department of Food Science, University of Parma, Parco Area delle Scienze 47/A, 43124 Parma, Italy

Part of study under development

1. Introduction

In many areas of the food industry, production lines are daily cleaned to ensure product safety and quality, maintain heat transfer characteristics and reduce the pressure drop (Jensen et al., 2005). Cleaning is a complex operation, where its efficiency depends on four energy factors: mechanical energy (or hydrodynamic effect) used to physically remove soil, chemical energy used to break down soil and render it easier to remove, thermal energy which increases the effects of the two first factors and the cleaning time (the contact time between soil and cleaning solution). The combination of these factors and their relative efficiency varies with strain type. A restriction in one energy source may be compensated by increasing energy from the other factors. For economic and environmental reasons, it's good practice to increase the mechanical action and reduce the others three. Moreover, the increase of the cleaning efficiency is economically advantageous as a reduction in cleaning time (and, as consequence a reduction in effluent production), reduction of the amount of cleaning agents necessary, and energy consumption (Blel et al., 2007).

The mechanical effect is influenced by the shape and the geometry of the plant or single element, because it affects the flow inside itself. The shear forces of the cleaning fluid at fluid/equipment interfaces are of great importance in the cleaning mechanism (Lelièvre et al., 2002). Shear forces can be controlled by either design of the equipment or volumetric flow rate, with the former being preferred due to the cost of increasing the flow rate (Jensen et al., 2005). A parameter, namely wall shear stress, correlates the cleanability to the flow inside a plant (i.e., the tangential stress along the wall of the geometry). As reported by Lelièvre et al. (2003), the wall shear stress results the most suitable criterion governing the removal of colloidal particles and microorganism from a surface. Furthermore, Lelièvre et al. (2002) have shown the importance of the flow pattern in cleaning process: when the flow is undisturbed (e.g., in straight pipe) the relevant parameter is the mean local wall shear stress, otherwise in unsteady zones (e.g., close to the discharge part of a sudden expansion), wide variations in the local wall shear stress guarantee a good cleanability, despite the low level of the mean local wall shear stresses.

The aim of this study, part of a wider work not reported for industrial secret issues, was to develop a geometry with a surface of about 0.05 m^2 in which the wall shear stress varies within defined range, with an increasing trend along the surface as linear as possible. This objective was achieved by means of CFD (Computational Fluid Dynamics) technique, a mathematical tool which allows to predict the flow behaviour, the main parameter which influences all the four factors of the cleaning process. With this mathematical instrument, it is possible to reduce the time and the cost of development of new geometries and eliminate or reduce the need to build a huge number of prototypes. Moreover, by using these software it is possible to estimate parameters (e.g., wall shear stress value) without disturbing the flow and often under uncommon conditions.

The wall shear stress range, considered as the target for this study, was the same that can be found in the industrial application of cleaning in place (CIP) process of closed system (such as pipe). For this purpose, Jensen and Friis (2004) have conducted a cleanability test on a radial flow cell. Cleaning test were carried out on geometry with different radius. In this work the critical wall shear stress was estimated to be between 3 and 6 Pa. These values are considered as reference and starting point also for the present work, with the further objective to extend the range of wall shear stress, from 0 to value around 10 Pa.

2. *Wall shear stress theory*

In this paragraph, the wall shear stress has been analytically calculated and the results have been compared with the CFD models results in order to evaluate the goodness of the prediction. Pipes of cylindrical section with different diameters and lengths have been adopted as the reference geometries for this demonstration. This brief theoretical demonstration can be useful to highlight also the main parameters that influences the wall shear stress and how it is possible to improve this value.

Starting from head loss equation (3) for straight tube reported in White (1999) and Darcy-Weisbach equation in terms of head loss (eq. 4), both expressed as:

$$h_f = \frac{4\tau_w}{\rho g}\frac{L}{d} \quad (3)$$

$$h_f = f\frac{L}{d}\frac{v^2}{2g} \quad (4)$$

By replacing the head loss (h_f) in equation (3) with the formula of (4), the wall shear stress can be calculated as (eq. 5):

$$\tau_w = \frac{f}{8}\rho v^2 \quad (5)$$

Where τ_w is wall shear stress (Pa), L the length of tube section (m), ρ density of the flowing fluid (kg m^{-3}), g gravity acceleration (m^2 s^{-1}), d diameter of the tube section (m), v velocity of flow (m s^{-1}) and f friction factor. Friction factor is a tabulated constant and depends on Reynolds number and relative roughness of the surface. As known, Reynolds number (Re) is expressed by means of:

$$Re = \frac{\rho v d}{\mu} \qquad (6)$$

Where μ is dynamic viscosity (Pa s).

From these first assumptions, also the main parameters which affect the wall shear stress value emerge:

- Physical characteristics of the fluid (such as density and dynamic viscosity);
- Fluid dynamics behaviour (e.g., the flow velocity);
- Geometric parameters of the tube (such as diameter and roughness).

From an analytical point of view, three theoretical study were carried out on different tube diameters and lengths, at three different flow rates. The test condition and the obtained results are shown in **Table 1**.

3. CFD models development

The development of the geometry of interest was a step by step process, starting from a simple geometry and evaluating the results at each modification. The 3D geometry of the various domains was developed with SolidWorks® 2015 (Dassault systèmes, Vélizy-Villacoublay, France). The 3D geometries were then imported into the ICEM CFD® software (Canonsburg, Pennsylvania, USA) and discretized into an unstructured hexahedrical and wedge mesh for all the domains of interest. The quality and quantity of mesh are very important for the accuracy and time of CFD simulation. Therefore, care was taken in selecting the mesh type and size to optimize the CFD results (Khoshvaght-Aliabadi et al., 2014). A mesh independent analysis was conducted for each developed CFD model in order to guarantee the complete independence of results from the number of mesh. Finally, the mesh was optimized and finalized for a better accuracy, thus reducing the computational time.

After the meshing phase, the physical properties of the domain and the boundary conditions were set up. Water at 20°C was used as test fluid, and it was considered as incompressible, homogeneous and as a Newtonian fluid with negligible effect of viscous heating. Thermal and physical properties were obtained from the software library ($\rho = 997$ kg m^{-3}; $\mu = 8.9 \cdot 10^{-4}$ Pa s; $C_p = 4181.7$ J kg^{-1} K^{-1}; k = 0.61 W m^{-1} K^{-1}). In this study steady state simulations were carried out with no changes in boundary and domain conditions with the time (time independent analysis). The boundary of the computational domain consisted of an inlet fluid zone, wall zone and an outlet zone.

The software ANSYS® CFX v15 (Canonsburg, Pennsylvania, USA), run on HP Z420 Workstation (Palo Alto, California, USA), was used to solve the governing continuity, momentum and energy equations for the defined geometry. The domain was defined in the global co-ordinate frame in which the solver carries out the calculations. The governing equation were discretized by the finite volume method (FVM) and iteratively solved until the set residuals were obtained (value of 10^{-4} for the continuity, momentum and energy equations) and when imbalance value for the conservation equations reached 1%, which can be considered the solution converge value (ANSYS CFX Modelling Guide, 2015).

4. *Results and discussion*

4.1. Models validation

Simple cylindrical geometries with three nominal diameters of 50, 65 and 80 mm, length equal to 100 times the nominal diameter (to guarantee a full development of the flow inside the domain) and an inlet water velocity of 2.5, 1.5 and 1 m s^{-1} respectively, were developed in order to evaluate the goodness and accuracy of the results obtained with CFD models. The wall shear stress value obtained from the models were compared with the values calculated with the equation (5) reported in *Section 2*.

As shown in **Figure 1**, after initial turbulence due to fluid development, the values of wall shear stress tend to become constant. As expected, by decreasing of tube diameter the wall shear stress increases and the difference between dn65 and dn50 is more marked than the one between dn65 and dn80, indicating the key role of the diameter. When the fluid flow resulted completely developed inside the tube (and the wall shear stress value became stationary), the wall shear stress value for the different samples was very close to the values obtained with the analytical method as reported in **Table 1**. From these results, it's possible to consider the CFD models predictions useful for the aim of this work.

4.2. Design of test geometry

After this preliminary test, the next step was to use the CFD technique to compare different geometries with the objective to obtain a geometry with a surface around of 0.05 m^2 and with a wall shear stress that varies between 0 and 10 Pa (with the first derivative as constant as possible to guarantee a gradually increases along the surface). Starting from the results reported in Jensen and Friis (2004), the focus has been focused on wall shear stress values lower than 10

Pa; there were also considered higher values, keeping in mind the variability of the correlation between the wall shear stress and the cleanability due to the others boundary conditions.

Some constrains were defined in order to reduce the number of tests before starting the development process:

- Easiness of geometry construction;
- Possibility of treating the geometry with the higher number of surface treatments or coatings;
- Reduce the volume of test section keeping constant the surface dimension of the geometry.

As a consequence, the test section should have a simple geometry, with an adequate perimeter development to fulfil the requirements previously reported and with a volume or a displacement which avoid an excessive obstruction of the section. Hence, the test geometry should consist of a tube allowing the complete development of the flow but with the lowest encumbrance.

4.2.1. Simple geometry inserted into cylindrical tube

The first test was carried out by comparing the wall shear stress values calculated on the surface of five different samples inserted in the middle of a cylindrical tube (length 780 mm, diameter 80 mm), with axis orthogonal to the fluid flow. The section geometry of the samples with the characteristics sizes were reported in **Figure 2**. Despite the low surface available (far from the target of this work), these geometries result easy to construct and to manage. Water at 20°C was used as simulating fluid, with a mean inlet velocity of 1.5 m s^{-1}.

The wall shear stress values obtained at the samples surface along half-perimeter (parallel to fluid flow) were reported in **Figure 3**. From the results, it’s possible to divide the samples into two groups: the first one composed of circle and ellipse geometries, showing a symmetric behaviour between the front and the rear of the sample and a second one where the samples undergo a rapid reduction of the wall shear stress at the rear of the samples. Regarding the maximum reached value, the samples could be included into the same group, especially for tilted square, rhombus and square. In **Figure 4** the trend of the wall shear stress was analysed by dividing the surface of the sample in three zones, as a function of the wall shear stress value: the first where the value increases (blue in **Figure 4**), the second where the value decreases (red in **Figure 4**) and the last where the value remains constant (green in **Figure 4**). In the first three samples, the percentage of the length at which the wall shear stress value remains constant is greater than 50%, reaching up to 75% in the square sample. This characteristic makes them unfit for the objective of the study: only few initial centimetres fulfil the needed requirements, otherwise an increase in the size of the sample is required (with obvious disadvantages in the flow behaviour). Furthermore, also the decrease zone (red in **Figure 4**) it’s practically absent.

This behaviour is due to the presence of edges, that separate the flow from the surface of the samples. The circle and ellipse samples, shows a symmetric trend, with a zone where the value tends to be constant (and therefore not complying with the requirements) near 20%. This low percentage (in respect to the other samples) makes these geometries partially suitable with the aim of the study.

From this first phase it's possible to highlight some conclusions:

- The samples with flat surfaces give gradual increases in wall shear stress value on the frontal zone, while on the rear zone the values are low and unstable. Moreover, in these geometries, the maximum wall shear stress value seems to be lower than the one obtained with the curved surfaces samples, which can be an advantage if we consider the maximum wall shear stress target for this work (around 10 Pa).
- The curved surface samples give continuous patterns in the derivative value, both in the front and rear zone, but with the highest values.
- In all the samples studied, the section reduction cause a high increase in mean velocity and thus in wall shear stress value, up to 10 times higher when compared with the value calculated at the tube surface (about 5 Pa). Hence, it would be necessary to reduce the surface of the samples, a modification in conflict with the aim of the work, if we need to reduce this effect.

Starting from these brief conclusions, the next simulations will be carried out on flat geometry, which minimally reduces the section surface and seems to give the best value regard the wall shear stress (from the absolute values point of view).

4.2.2. Flat geometry with different inclination

In this second step of the geometry development, the sample was a plate of 84 mm length and 4 mm thicker, placed parallel to the flow in the middle of the test tube (cylindrical geometry with a length of 780 mm and a diameter of 80 mm) and tested at five different inclinations (from 5° to 45° with a step of 10°). The same domain and boundary conditions imposed in the previous test were chosen.

Also in this case, the different geometry placements were evaluated by comparing the wall shear stress value along the central axis of the plate, parallel to the fluid flow, both on the top and the bottom surface, as reported in **Figure 5a** and **5b**, respectively. In the figures, in order to simplify the comparison between the samples, a focus around the wall shear stress value of 10 Pa was carried out, omitting the highest values that aren't meaningful to the study goal. In **Figure 5a**, all the samples show an initial peak due to the impact of the flow with the edge of the sample. Out of the first millimetres of the plate, an increasing trend emerge for all the geometries until the last millimetres (where turbulence occurs because of the end of the plate). For the inclinations from 15° to 45° the wall shear stress values of 10 Pa exceeded at about half of the plate surface, so these samples can be considered not appropriate for the goal of the work. From this tests emerges how the sample with inclination of 5° shows the higher useful surface, but without interesting wall shear stress variation along the surface (except for the initial and final zones). Considering the bottom surface (**Figure 5b**) the behaviour results more variable in respect to the upper one. For inclination from 5° to 25° the wall shear stress ranges between 0 and 10 Pa while for the other cases the variations were even more evident.

In regards to the percentage of surface in which the wall shear stress has value less than 10 Pa, with the inclinations from 15° to 45° the useful surface is near 40% of the total one, as reported in **Figure 6**, while for the plate with the lowest inclination (5°) the useful surface is near 100%. Concerning the bottom surface of the plate and taking into consideration the useful surface, the maximum wall shear stress value and the regularity of its variation, the best solution seems to be the sample with 25° of inclination. However, the benefit is not liable to make such geometry adoptable and no one of the samples tested in this section fulfil the goal of the study.

In conclusion of this second step of designing process, it is outlined how with high inclination the problem of section reduction (highlighted in the *Section 4.2.1*) appears again, accompanied by high value of wall shear stress. On the contrary, for samples with low inclination, despite the high value of useful surface, the wall shear stress results constant without the necessary variation. In order to reduce the interferences of the sample on the fluid flow, in the next step, the plate, placed at the centre of the tube will be removed and the samples become the tube wall itself. Specifically, the cylindrical tube will be composed of divergent and convergent sections, and the wall shear stress will be quantified directly on it. The aim is to get slow variations of wall shear stress inside a lower range, with the most regular possible trends, without turbulence and for the higher possible length.

4.2.3. Cylindrical tube with convergent and divergent section

In this test, a geometry, made of cylindrical tubes with different diameter and length, with divergent and convergent section, was studied to know how these geometry variations can influence the wall shear stress value. In **Figure 7a** it has been reported the characteristic dimensions of the sample. The simulation was carried out with the same domain and boundary characteristics imposed in the previous tests (e.g., water at 20°C with an inlet flow velocity of 1.5 m s^{-1}).

The wall shear stress values were obtained from a straight line along the tube wall, parallel to the fluid flow and the results were shown in **Figure 8**. In order to evaluate the effect of the geometry variation on the wall shear stress, each section was individually analysed.

Section 1. In this 200 mm length section, for the 88% of the surface the wall shear stress shows a linear trend between 6 and 8 Pa; in the last 25 mm the values rapidly tend to zero due to the abrupt diameter restriction (from 65 to 50 mm).

Section 2. This section has the same length of the previous one but a smaller diameter. After the initial turbulence due to the restriction, the wall shear stress value increase from 8 to 13 Pa. The lower initial value is probably caused by the turbulence that prevents a good adherence between fluid and wall. Moreover, the increase of wall shear stress value, in respect to the previous section is in accordance with the reduction of the tube section.

Section 3. In this divergent section (diameter from 50 to 80) of 200 mm length, the wall shear stress value decreases from 13 to 0 Pa.

Section 4. In this straight section of 400 mm length, the wall shear stress value changes from 0 to 3 Pa, with a rapid increase near the last part of the section.

Section 5. This convergent section (from 80 to 65 mm of diameter) with a length of 200 mm, shows a linear increase of the wall shear stress value from 3 up to 7 Pa.

Section 6. In the last straight section (diameter 65 mm and length 200 mm), wall shear stress value was constant around 7 Pa, similar to the value obtained in *Section 1*.

After this brief analysis emerges that the best results were obtained in the *Section 4*. What makes this straight tube so interesting is its location within the whole geometry. In fact, a so different trend in respect to the other constant diameter tube sections (specially Section 1 and 6) is caused by the presence of a divergent section before and a convergent one after the section of interest. Furthermore, the obtainment of values of interest in a portion at a constant diameter is an advantage from a practical and constructive point of view.

Starting from this result, the next step will be to focus on correct position and dimension of divergent and convergent section as well as the length and the shape of the tube at constant diameter in order to obtain slightly higher wall shear stress values at the exit zone.

4.2.4. Square tube section preceded by divergent section

In this phase the goal was to investigate some behaviours appeared in the previous step. In **Figure 7b** the tested geometry was reported. The final convergent section was removed to investigate the real effect caused by the divergent section placed before the test section. Furthermore, with the aim to have geometries with a more practical shape, the cylindrical tube in Section 4 was replaced with a square section one. Also some dimensions were changed (e.g., side height and length), to improve the wall shear stress range obtained in the previous simulation. In particular, the tested section changes from diameter of 80 mm to a side of 50 mm, and the section before the divergence was reduced from 50 to 40 mm of diameter. The domain and boundary conditions were kept as previously imposed: water at 20°C with an inlet fluid velocity of 1.5 m s^{-1}.

From the CFD models were quantified the wall shear stress values along the top wall of the test section, parallel to the fluid flow at the middle position and at 12.5 mm from the middle position. The results, only regard to the square section tube, were reported in **Figure 9**. As expected, the trends along the two sampling lines result very similar, with lower values in the lateral line due to the proximity of the lateral side wall which causes a reduction in the fluid velocity. In both lines the results show an initial turbulence zone, higher in the central line. The geometrical modification implemented on this sample allowed to reach a higher wall shear stress range (from 0-3 Pa to 0.5-6, 1-7 Pa for lateral and central line, respectively). In the last 100 mm, the increase in wall shear stress value tend to disappear, so it is unnecessary to furtherly lengthen the test section.

In the next step, we will simply add a cylindrical section after the test section to have a more real context, as the square tube results difficult to insert in a real process conditions. The objective is to evaluate if this changes will modify the results obtained in this step. Another goal is to furtherly extend the range of wall shear stress values.

4.2.5. Square tube section succeeded by convergent section

In this phase it was added a convergent section (diameter from 50 to 40 mm and length of 200 mm) after the test section, the rest of the geometry being constant. Also the domain and boundary conditions were kept as previously described.

From the results reported in **Figure 9** the presence of a convergence tube (dotted line) after the test section doesn't affect the wall shear stress value except in the last millimetres due to the changes in section (from square to circle). Conversely a disadvantage effect appears in the first zone of the test tube where the wall shear stress start from higher values. Unfortunately, for the aim of this study it's necessary that the wall shear stress starting from value close to zero.

Whit this geometry modification the disadvantages were more than the advantages, so in the next step the convergent tube will be substituted with a divergent one to evaluate if the worsening of the results was due to the presence of a final section or to the geometry itself.

4.2.6. Square tube section succeeded by divergent section

In this stage, the final convergent section was replaced with a divergent one (from diameter 50 to 65 mm) of the same length.

From the data reported in **Figure 9** (point-dotted line) it seems to be confirmed that the geometry of final section influences more the initial zone of the test section than the final one. The values are similar to those previously seen: the presence of a cylindrical geometry after the test section greatly affects the results, more than the shape of geometry itself.

4.2.7. Summary of the first results

In **Table 2**, a summary of the tested geometry was reported, with the main identified advantages and disadvantages. The last two reported geometry appear to be the only suitable for the aim of this study. The choice of the square section sample should imply the simplicity in the management of this kind of geometry. For example it allows to reduce the time and use of material in the case of production of samples with different characteristics: instead of changing the entire test section only one side could be substituted. For these reasons, in the next step this geometry will be improved.

4.2.8. Improvements on square geometry section

Starting from the geometry chosen in the previous paragraph, some small variations were made to extend the range of wall shear stress value. As reported in **Figure 7c**, the two divergent sections were reduced from 200 to 100 mm of length in order to increase the turbulence effect due to geometry variation (from cylindrical to square and vice versa). Furthermore, the test section was elongated from 600 to 750 mm, in order to evaluate if a longer test section can increase furtherly the range of values. As seen before, water at 20°C was chosen as fluid and an inlet fluid velocity of 1.5 m s^{-1} was imposed.

From the data reported in **Figure 10**, the range has remained almost identical (between 2 and 8 Pa): the changes did not bring the expected improvements. A new simulation was made with the same geometry but with different inlet fluid velocity (2 m s^{-1}), in order to evaluate the effect of flow rate on the wall shear stress value. As can be seen from the blue line reported in **Figure 10**, the wall shear stress range varies between 3.5 and 14 Pa, values not satisfactory regard the minimum value, but with this test emerges how the flow rate can control the wall shear stress range (increasing the amplitude of it).

From these further tests, it results how the square geometry isn't versatile, as expected before. The next step will be to get back to cylindrical geometry with convergent and divergent section, previously discarded because less useful from the practical point of view.

4.2.9. Improvements on cylindrical geometry section

The main disadvantages of this geometry were the difficult to work with curved surface (from a practical point of view) and the large consumption of the materials: it was necessary to realize a complete tube section instead of only one side as can be already seen for the square tube section.

To overcame this limits, the divergent and convergent section was inserted directly on the test zone and no longer before or after the same. In this way it was possible to reduce the length of the test section. Furthermore, in order to overcome the limits imposed by cylindrical geometry, the surface of interest was a removable plate (thickness of 8 mm, to reduce the risk of vibrations) inserted in the centre of the tube, parallel to fluid flow. With these two modifications the advantages of the plate surface and of the convergent/divergent cylindrical tube were combined. First of all, it was necessary to study the behaviour of the fluid inside this geometry. A simple cylindrical convergent section, where the geometry changes from 65 to 50 mm, with a length of 600 mm, was tested alone without the plate in the centre of the tube. The flow conditions imposed for the CFD model was the same previously seen: water at 20°C with an inlet velocity of 1.5 m s^{-1}. The fluid dynamics study showed how the wall shear stress value linearly and slowly increased along all the plate surface, but the range of values resulted to high (between 10 and 22 Pa) for the aim of this study. It was necessary to reduce the initial wall shear value, making it as close as possible to zero.

Starting from these considerations some changes were made at the geometry in order to achieve desired results (**Figure 7d**). The inlet diameter was increased from 65 to 80 mm, in order to obtain lower wall shear stress value at the inlet zone. Moreover, two section were added before and after the test section allowing the fully development of the fluid. In order to allow the connection of this section with processing equipment (to carry out future experimental test), section with diameter of 65 mm were added at the beginning and at the end of the geometry. The same flow conditions were imposed and the results were shown in **Figure 11**: the lower value of the range was reduced from 10 to 5 Pa, a very good result. With the aim to furtherly reduce this value, a simulation with flow inlet velocity of 1 m s^{-1} was carried out. In this case the wall shear stress values ranged between 2 and 12 Pa, values of great interest but with still a small range.

In order to increase the range of interest, at the last geometry were modified the inlet and outlet diameter of the test section. In particular, the entrance change from 80 to 100 mm while the exit from 50 to 40 mm. Also the flow development section was changed to ensure the complete development of the fluid flow. The inlet section increased from 480 to 600 mm length whilst the outlet section decreased from 300 to 140 mm. In this simulation, water at 20°C was flushed with an inlet velocity of 1 m s^{-1}. With this geometry the wall shear stress linearly and gradually increased along the plate, as seen before, but the range was considerably amplified and values varied between 1.4 and 34 Pa. In the challenge to get values closer to 0 the same simulation was repeated with a lower flow inlet velocity (0.8 m s^{-1}). The results in this case were optimal (range 0.9-24 Pa). The increase of length of the fluid development section did not led to difference from the fluid development point of view, and the main effect on wall shear stress may be due the change of diameter (as already seen from the previous test). So, the geometry must be optimized to reduce the encumbrance keeping the same wall shear stress values.

From these considerations, a final geometry was chosen. In **Figure 7e**, the characteristic dimensions were reported. The results obtained by flushing water at 20°C with an inlet velocity of 1 m s^{-1} showed a range between 2 and 13 Pa, slightly less suitable for the test (as the width of the range and minimal wall shear stress value point of view) but the advantages of this geometry overcame these limits. Moreover, as seen before, to reduce the minimal wall shear stress value it's possible to set up test with lower flow velocity.

5. *Conclusion and future development*

In this study the power of CFD models was applied to develop a suited geometry with specific characteristics regarding wall shear stress values and their variation on the geometry surface. The starting point were some assumptions like the surface dimension of the geometry, the easiness of construction and management, and the possibility of treating the geometry with different number of surface treatments or coatings. The step by step process allowed to learn more about the effect of different geometries on the wall shear stress and how also little changing can greatly affect the results.

The future step will be to realize a prototype of the developed geometry to confirm experimentally the results obtained with this study.

References

ANSYS®, (2015). *ANSYS® CFX Modelling guide*. Canonsburg, Pennsylvania, USA.

Blel, W., Bénézech, T., Legentilhomme, P., Legrand, J. & Le Gentil-Lelièvre, C., (2007). Effect of flow arrangement on the removal of Bacillus spores from stainless steel equipment surfaces during a Cleaning In Place procedure. *Chemical Engineering Science*, 62, 3798–3808.

Jensen, B.B.B. & Friis, A., (2004). Critical wall shear stress for the EHEDG test method. *Chemical Engineering and Processing*, 43, 831–840.

Jensen, B.B.B., Friis, A., Bénézech, T., Legentilhomme, P. & Lelièvre, C., (2005). Local Wall Shear Stress Variations Predicted by Computational Fluid Dynamics for Hygienic Design. *Food and Bioproduct Processing*, 83, 53–60.

Khoshvaght-Aliabadi, M., Zangouei, S. & Hormozi, F., (2014). Performance of a plate-fin heat exchanger with vortex-generator channels: 3D-CFD simulation and experimental validation. *International Journal of Thermal Sciences*, 88, 180–192.

Lelièvre, C., Legentilhomme, P., Gaucher, C., Legrand, J., Faille, C. & Bénézech, T., (2002). Cleaning in place: Effect of local wall shear stress variation on bacterial removal from stainless steel equipment. *Chemical Engineering Science*, 57, 1287–1297.

Lelièvre, C., Legentilhomme, P., Legrand, J., Faille, C. & Bénézech, T., (2003). Hygienic design: influence of the local wall shear stress variations on the cleanability of a three-way valve. *Chemical Engineering Research and Design*, 81, 1071–1076.

White, F.M., (1999). Fluid mechanics. McGraw-Hill.

Table 1. Comparison between the wall shear stress values obtained analytically and through numerical method (CFD models).

Diameter (mm)	*Length (mm)*	*Velocity ($m\ s^{-1}$)*	*Wall shear stress (Pa)*	
			Analytical calculation	*Numerical solution*
50	5000	2.5	12.8	13.4
65	6500	1.5	5.1	4.8
80	8000	1.0	2.9	2.0

Table 2. Advantages and disadvantages of the different geometries tested with CFD models.

Geometry	***Advantages***	***Disadvantages***
Transversal samples (circle, tilted square, rhombus, ellipse, square)	- Simplicity of production; - Possibility of applying different treatments;	- Surface far from the target; - To high wall shear stress value and non-linear behaviour;
Plate samples (with different inclination)	- Simplicity of production; - Possibility of applying different treatments; - In some cases, not reduces the tube section;	- Surface far from the target; - Wall shear stress derivatives highly variable; - It isn't knowing the effect of any vibration for thin plates;
Cylindrical tube (with divergent and convergent section)	- Suitable surface dimension; - Linear trend of the wall shear stress derivatives in a small range; - Possibility to optimize the geometry;	- Difficulty in the production and in application of different test;
Square tube (with divergent and convergent section)	- Suitable surface dimension; - Linear trend of the wall shear stress variation in a small range; - Simplicity of production; - Possibility of applying different treatments;	- Variability not only longitudinal due to the presence of the corners; - Difficult to position into real process conditions;

Figure 1. Comparison of the wall shear stress value obtained from CFD models of a straight tube with three different geometry and three different inlet fluid flow velocity. The data were collected along the tube wall, parallel to the fluid flow.

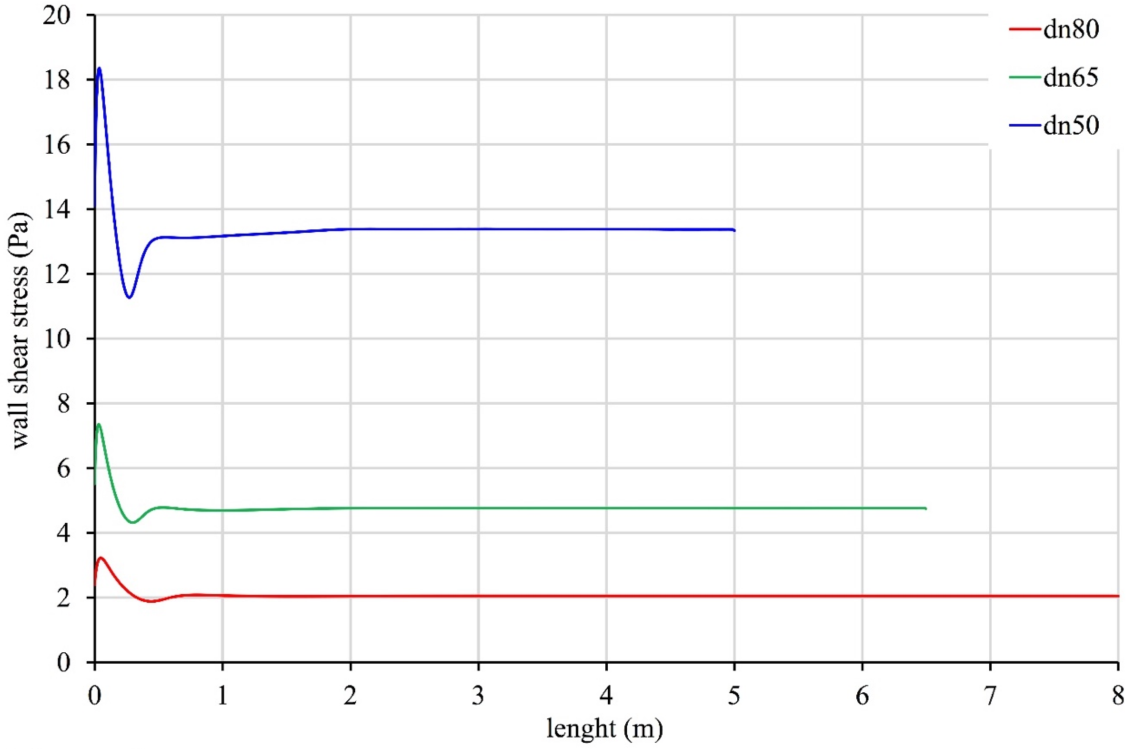

Figure 2. Different geometry section of the samples studied (the measures are reported in mm).

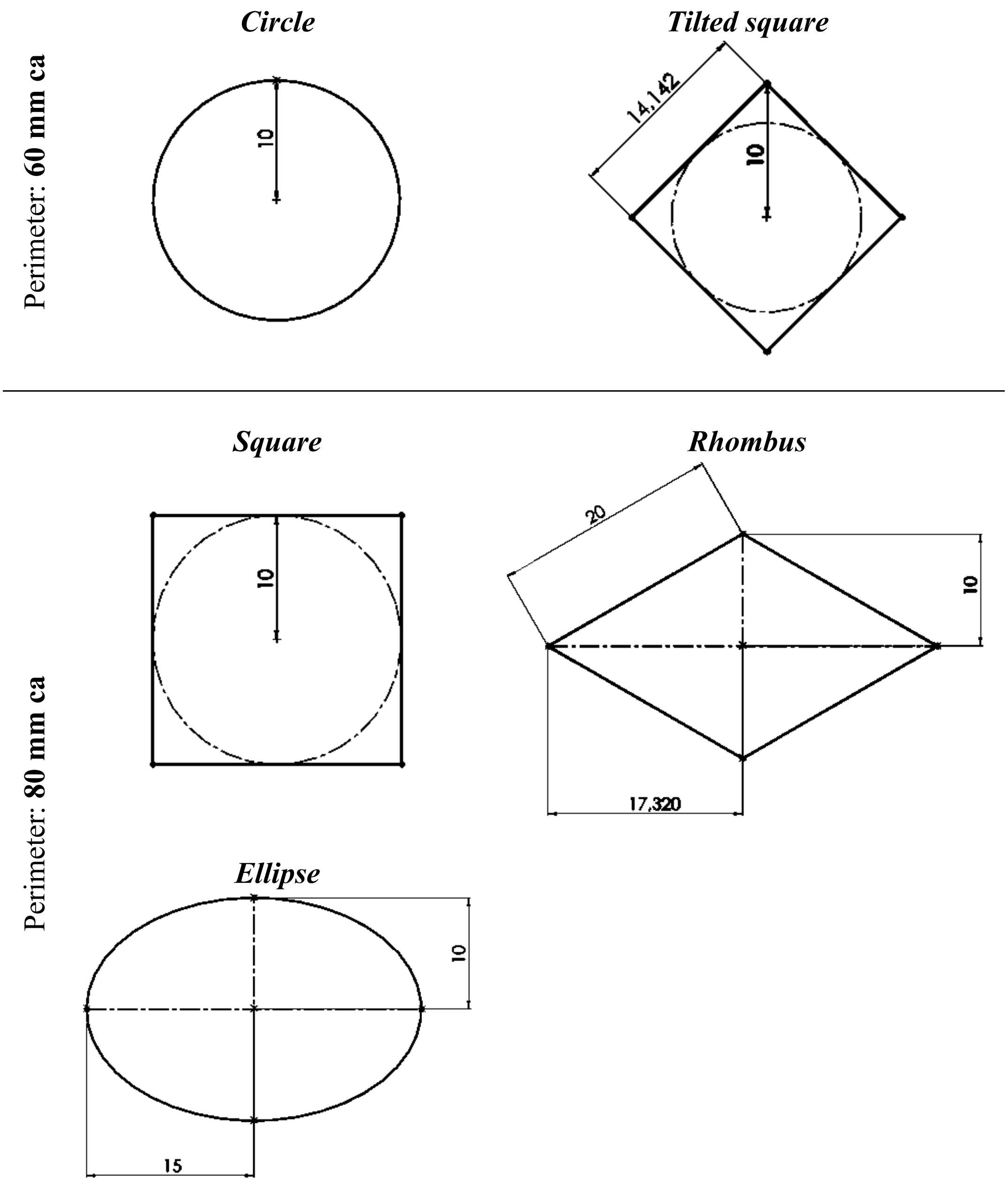

Figure 3. Comparison of the wall shear stress values obtained from CFD models on the surface samples along half-perimeter (parallel to fluid flow).

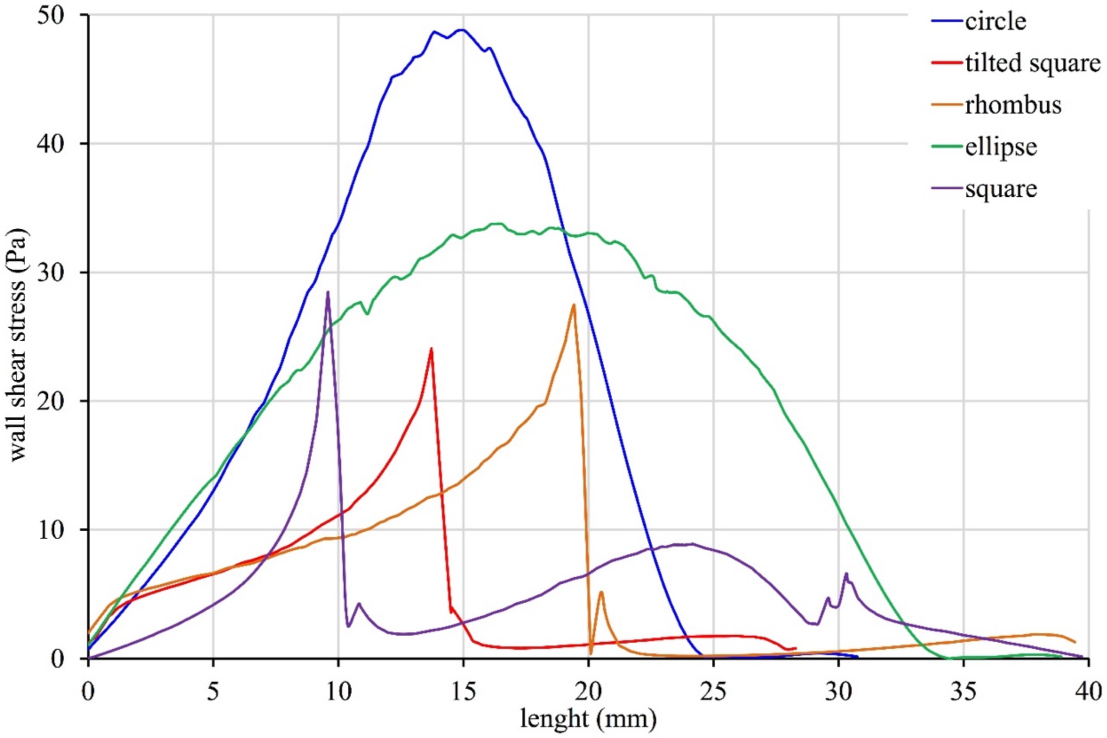

Figure 4. Analysis of the wall shear stress by dividing the surface of the sample in three zones in function of the wall shear stress value: the first where the value increase (blue section), the second where the value decrease (red section) and the last in which the value remains constant (green section).

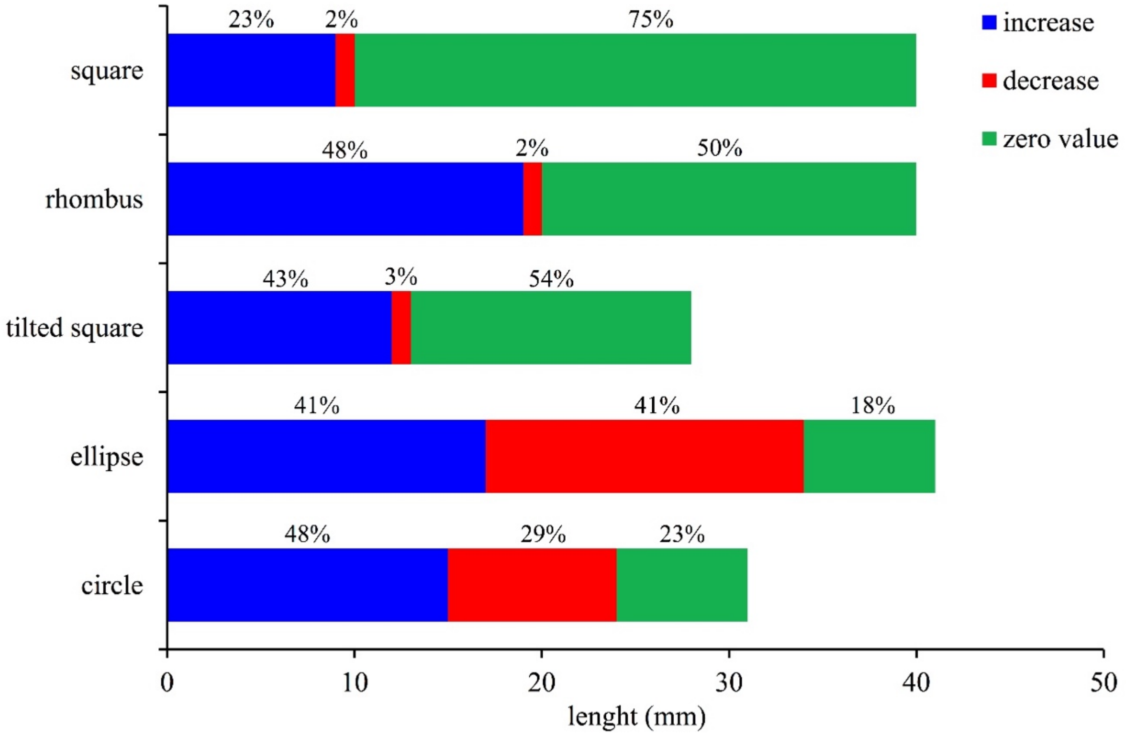

Figure 5. Comparison of the wall shear stress values obtained from CFD models along the central axis of the tested geometry (plate surface with different inclinations) parallel to the fluid flow, on the top (panel **a**) and on the bottom surface (panel **b**).

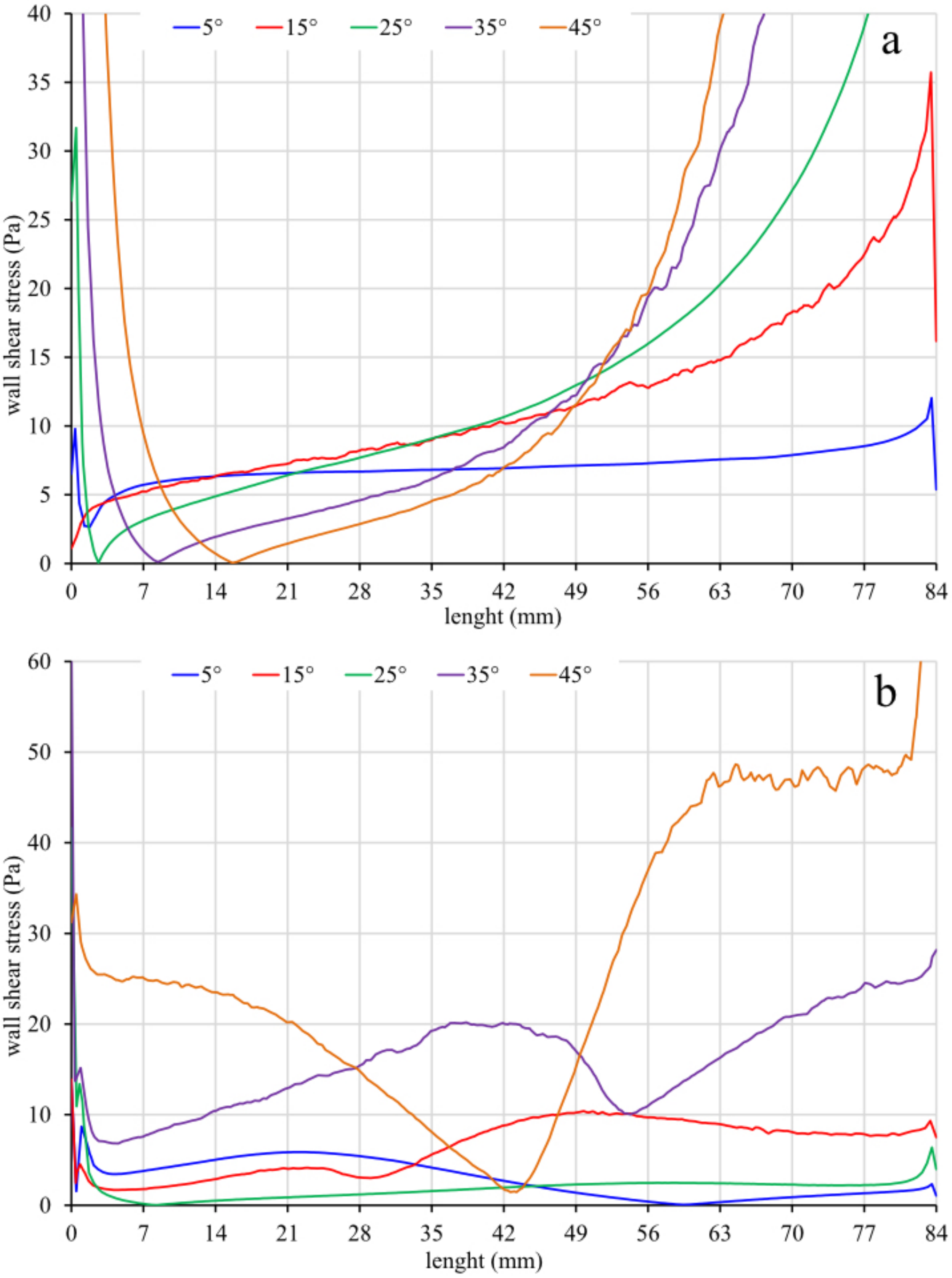

Figure 6. Comparison of the usefull surface (wall shear stress values lower than 10 Pa) between tested samples at different inclination, on top surface (blu columns) and bottom one (red columns).

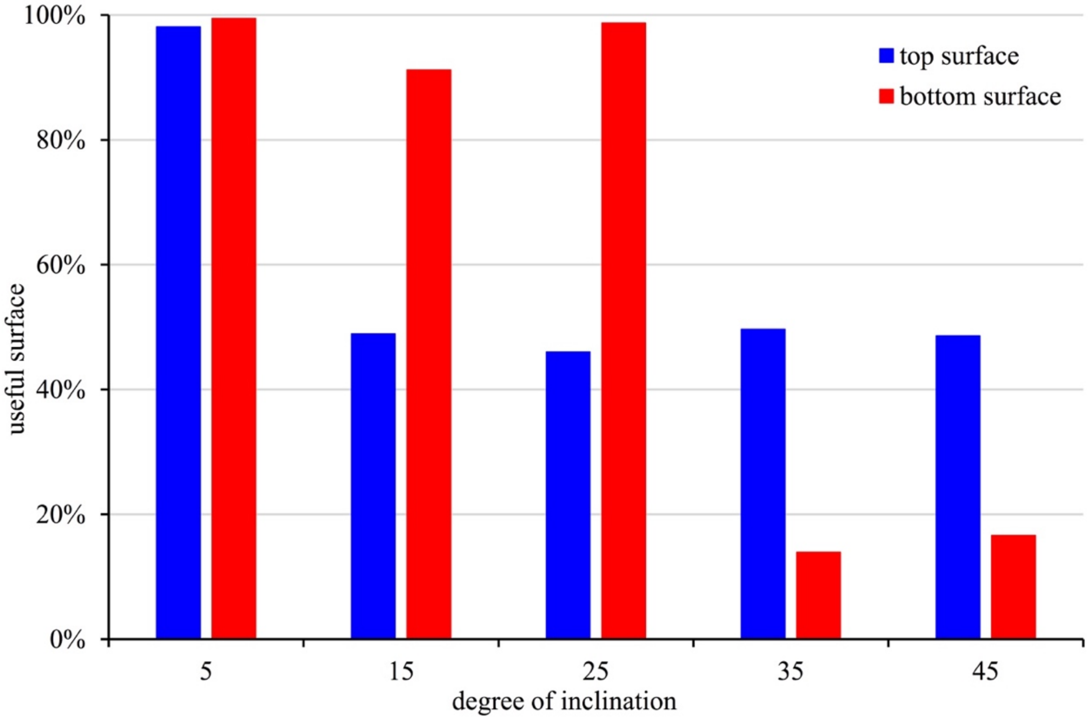

Figure 7. Characteristics dimensions of the most interesting test sections developed with CFD models.

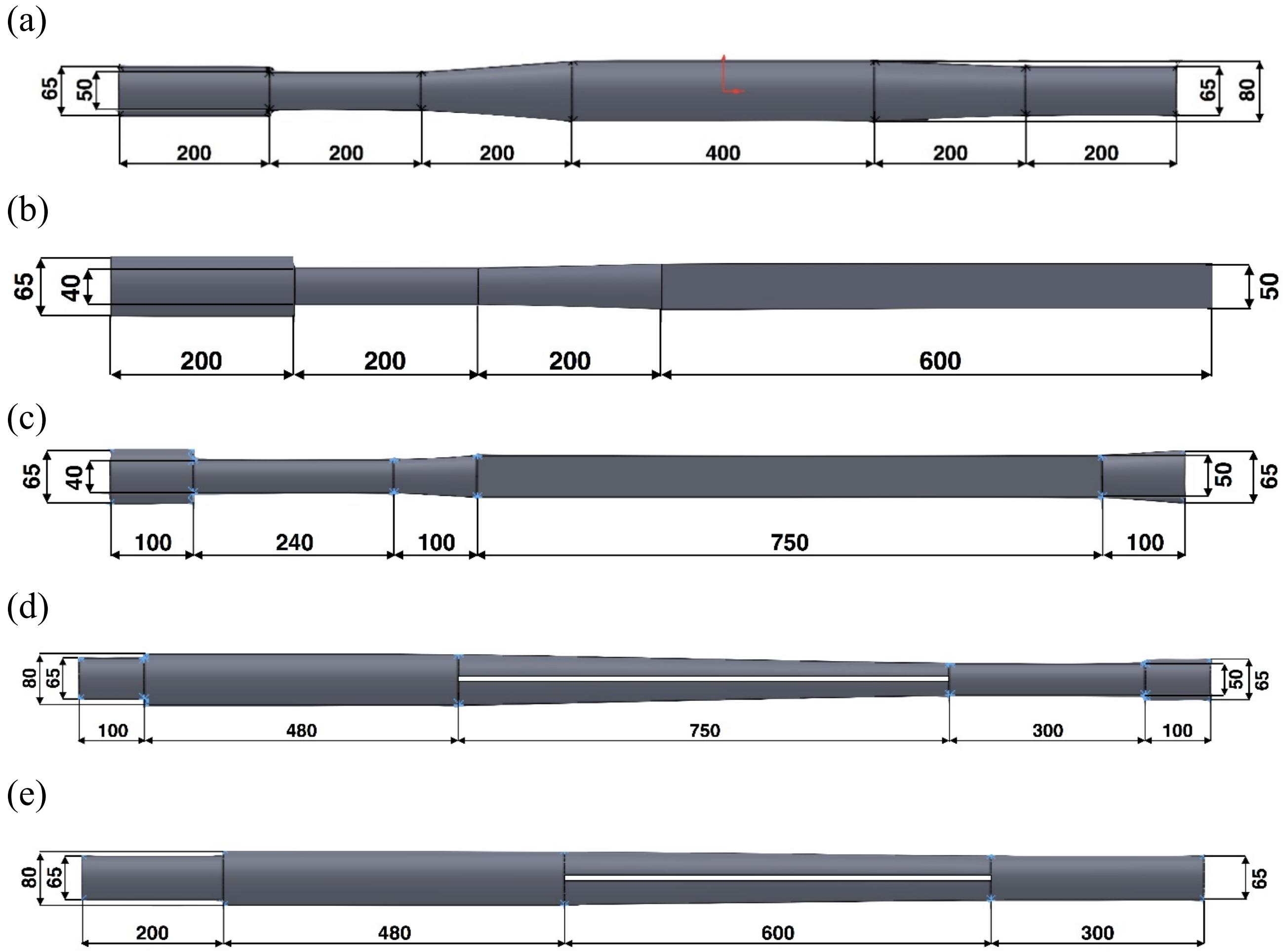

Figure 8. Wall shear stress values obtained from a straight line (parallel to fluid flow) along the tube wall for the geometry reported in **Figure 7a**.

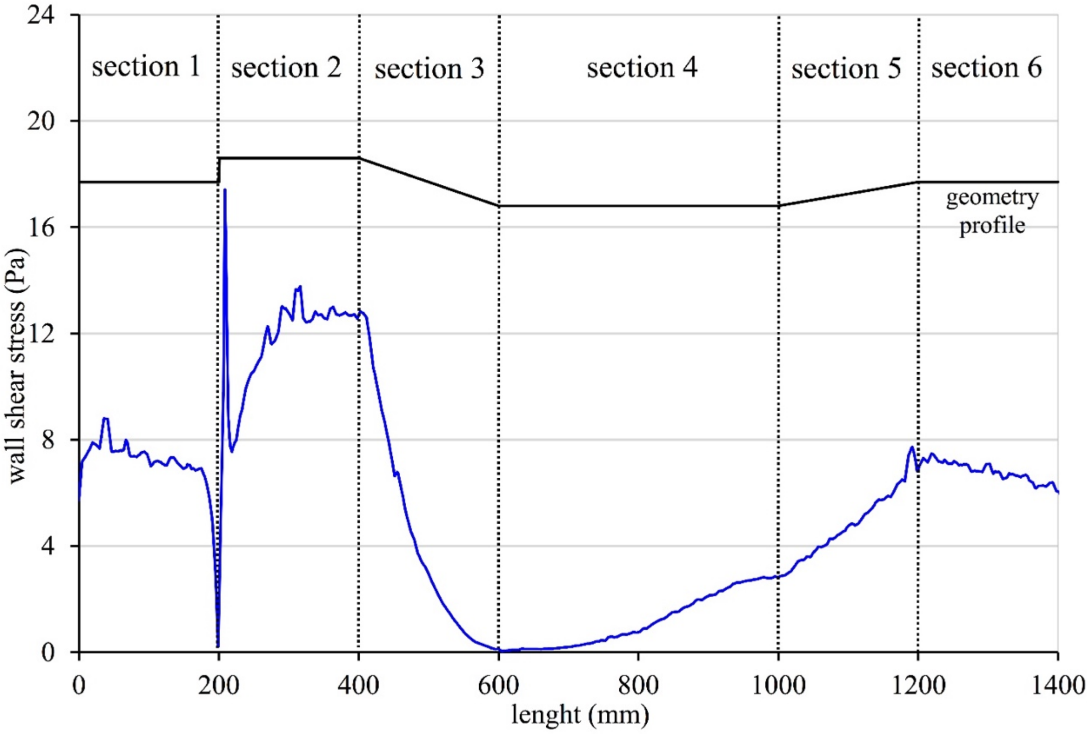

Figure 9. Wall shear stress profile obtained from CFD models in square tube section (the last region of tested geometry reported in **Figure 7b**). The continuos line is referred to standard geometry. The dotted line is reffered to standard geometry with a convergent section after the square one. The point-dotted line is reffered to standard geometry with a divergent section after the square one. The central line (blue in the figure) was obtained at middle position of the side wall, while lateral one (red in the figure) was positioned parallel to the first at a distance of 12.5 mm.

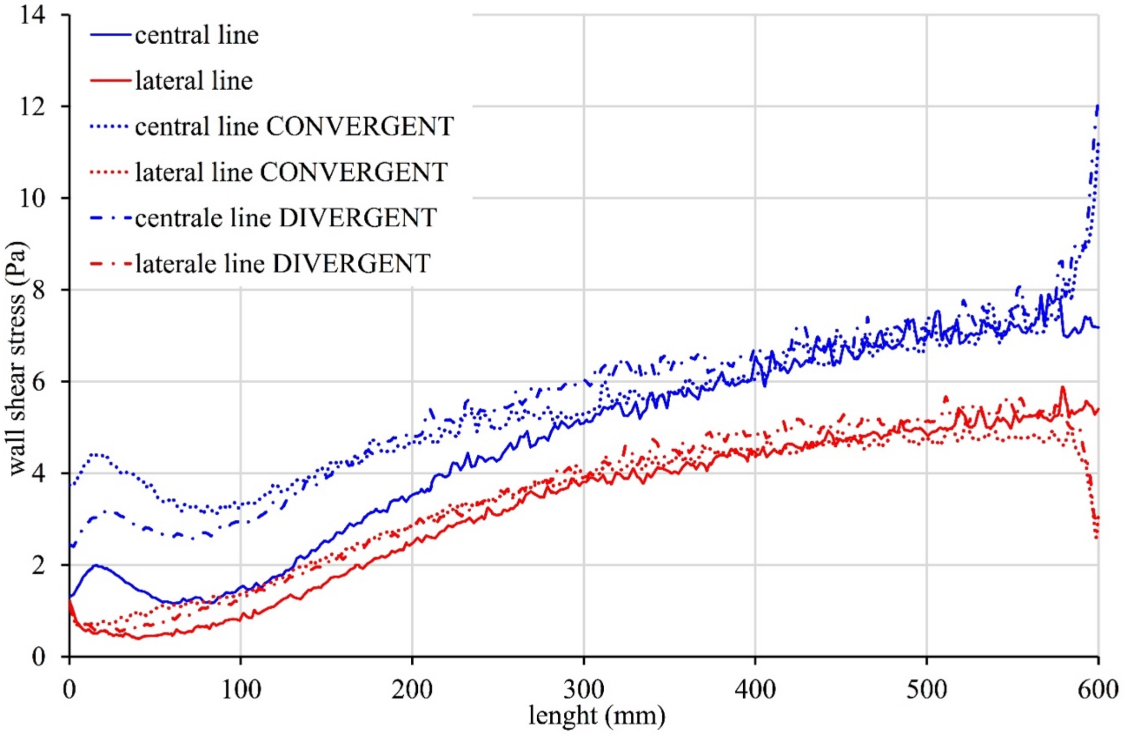

Figure 10. Comparison of the wall shear stress values obtained from CFD model on the square tube section with geometry reported in **Figure 7c** at two different flow rates.

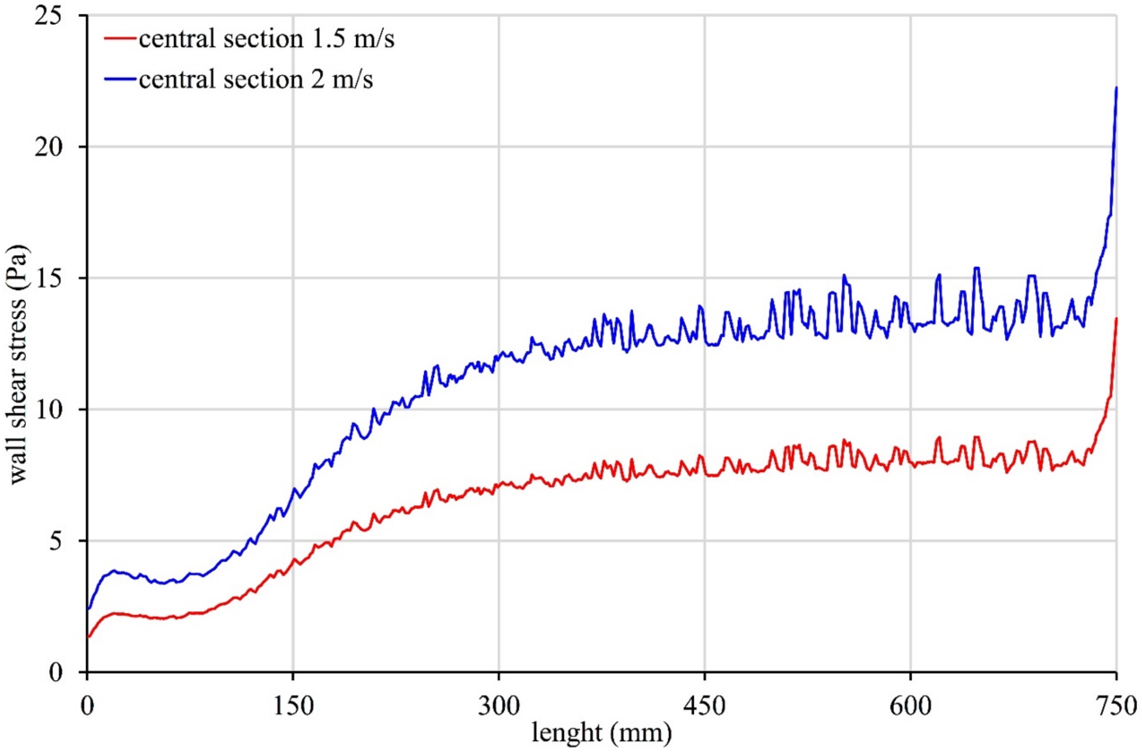

Figure 11. Comparison of the wall shear stress values obtained from CFD models along the central section of the plate positioned at the centre of the test tube, at two different flow rates.

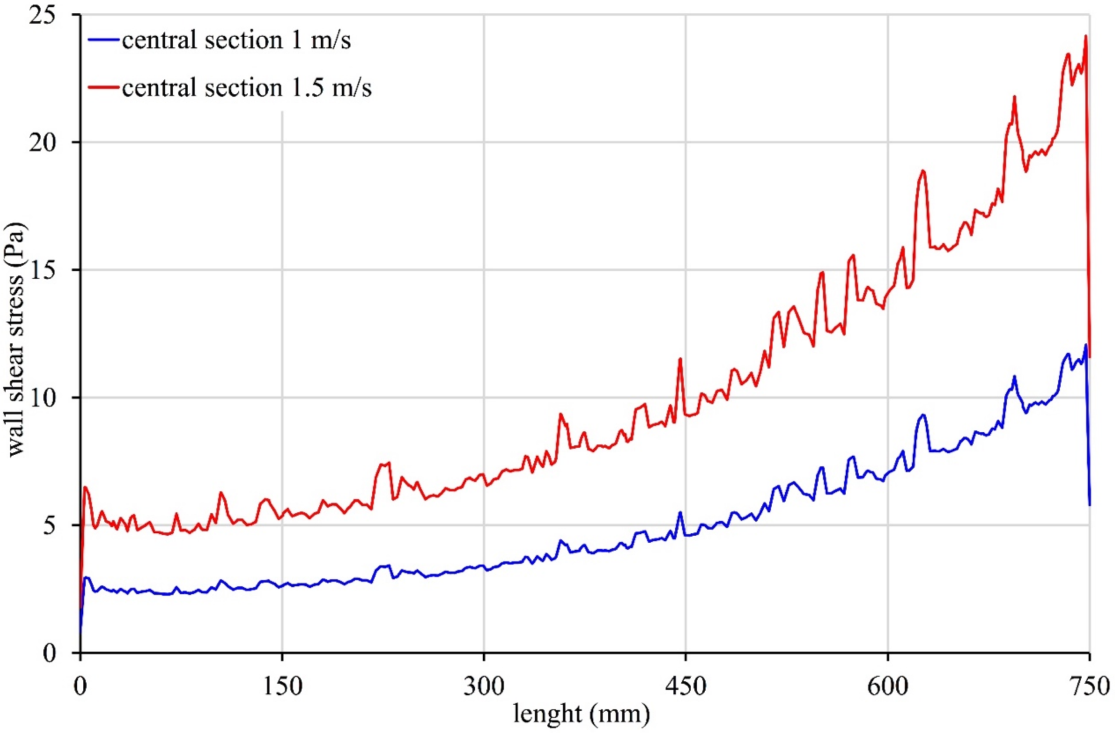

Evaluation of the performances of a plate fine heat exchanger for liquid food with different kinds of vortex generators using CFD methods

Matteo Cordioli, Massimiliano Rinaldi and Davide Barbanti

Department of Food Science, University of Parma, Parco Area delle Scienze 47/A, 43124
Parma, Italy

To be submitted

1. Introduction

Heating and cooling are common thermal processes in the food industry and are widely used to improve quality and safety of food products and also to extend the shelf life of them (Wang and Sun, 2003). Furthermore, the increasing attention on safety and quality of medium and long time shelf-life product had stimulated the optimization of thermal treatments, in order to get flavour and nutritional value closer to those of untreated foods (De Bonis and Ruocco, 2009).

Heat exchangers are used for continuous thermal treatment processing, while micro-organisms and enzymes are inactivated at high temperature in a holding tube. In particular, for the processing of liquid foods without particles in suspension and with low viscosity, like milk, beer, liquid egg or fruit juices, plate heat exchangers (PHEs) are extensively used. This type of exchanger provides high heat transfer rate with the important advantage that a heat regeneration step can be easily introduced in the process since more than one exchanger can be placed in the same frame (Aguiar and Gut, 2014).

In the heat exchanger practice it is imperative to increase the overall heat transferred between the operating fluids, while maintaining the pressure losses within acceptable limits. Therefore, the evaluation of the heat transfer should follow from a comparison between the heat transfer enhancement and the pressure loss enhancement (Rozzi et al., 2007). To increase the heat transfer rate and at the same time taking care of the augment pumping power, various techniques have been presented and can be classified in three main groups: active method, passive method and compound method. Active methods need external power input in order to augment the rate of heat transfer and for this reason this method present limit application in many practical applications. In the same way, the compound method that couples simultaneously two (or more) of the enhancing techniques uses complex design and has limited applications as well. Passive techniques showing the highest potential and among others swirl flow devices have widely been used for increasing the convective heat transfer (Sheikholeslami et al., 2015). Furthermore the heat transfer in the PHEs has been enhanced with various types of plate-fin channels geometries, such as plain, perforated, offset strip, louvered, wavy, vortex-generator and pin (Khoshvaght-Aliabadi et al., 2015). Brockmeier et al. (1993) compared five different heat transfer configurations: two plain fin, an offset strip, a louvered fin geometry and one with vortex generator. In comparison to the plain fin surface with a rectangular cross section, the vortex generator surface showed best performance characteristics allowing a reduction in heat transfer surface area of about 76%. Vortex generators, as a passive heat transfer enhancement technique in a channel, not only disturb the flow field but also make the fluid swirling and cause a heavy exchange between the core and the wall fluids (Ahmed et al., 2012). The vortex generators may be divided into transverse and longitudinal types in according with the position respect to the main flow direction: transverse will be perpendicular while longitudinal will be parallel with the flow field. Jain et al. (2003) reported that the longitudinal vortex generators showed a great enhancing of the heat transfer rate in plate-fin heat exchangers and fin-tube heat exchangers. Gentry and Jacobi (1997) studied the effect of delta-wing vortex generator embedded in a flat plate and found that the heat transfer was enhanced up to 50% compared to plain flat plate. Wu and Tao (2012) investigated the heat transfer characteristics of a plain plate and four plates with a pair of delta-winglet longitudinal vortex-generator with attack angles ranged from 15° to 60°: the Nusselt number of plate with attack angle of 60° is slightly higher than that of plate with attack angle of 45° yet may bring larger pressure drop.

The process of heat exchanger development necessitates work on efficient and reliable designs leading towards an optimal overall system performance: this iterative process need to implement many prototype in the design stage. Due to this reason, this method result time consuming as well as expensive especially for large scale models. However, economical access to powerful microprocessors has open the way for devolvement of Computation Fluid Dynamics (CFD) during the design phase (Aslam Bhutta et al., 2012). The application of numerical modelling will benefit the understanding of the physics of a food processing operation and thus aid in design, optimisation and control of a processing system. In the recent years, between numerical methods, CFD has been increasingly used to simulate thermal processes of foods. In CFD calculation, the continuity, momentum conservation and energy conservation equations are numerically solved, after a discretization process in small cell elements of the entire system, to give predictions of velocity, temperature, pressure profiles, and other parameters in a fluid flow system (Xia and Sun, 2002). These techniques is equally helpful in designing a heat exchanger system from a scratch as well as in troubleshooting/optimization by suggesting design modification.

The aim of this work was to improve the results obtained by Khoshvaght-Aliabadi et al. (2015), were the performance of PFHE with different plate-fin channels was investigated. Starting from their results, who reported that PFHE with vortex-generators seem to give the best results, in this work a deepening of this kind of geometries where conducted. In particular, different shape and characteristic dimensions of vortex-generators were investigated by means of CFD techniques to identify the best solution from efficacy (heat transfer coefficient) and efficiency (pressure drop) point of view.

2. Materials and methods

2.1. Geometry of PHEs with vortex generators

The domain of interest was composed of heat exchanger section made-up of bottom plate, top plate, two side bar, a header and a nozzle. The heat exchange zone presented a rectangular section of 30 mm in width and 12 mm in height and a length of 500 mm. The vortex generators inside the heat exchange zone consists of three wings in each row: one mounted on the top plate and the other ones mounted on the bottom plate. This trend alternately changes between the top and the bottom plates for a total of 57 wings. Three different shapes of the wings were taken into consideration: rectangular base (*RE*), rhombus base (*RH*) and elliptical base (*EL*). Also two geometrical parameters were choosing to evaluate the performance of PHEs: three different wing heights (w_h) and three wing widths (w_w). In **Table 1** a summary of the geometries with different geometrical parameters taken into consideration in this study was reported; also a geometry without wings, named PFHE, was considered to compare also the effect of wings presence on the heat exchange.

In addition, to guarantee the complete development of the fluid flow at the inlet section and to ensure that no flow recirculation appear at the outlet section of domain of interest a section of tube (diameter 12 mm) was added before and after the heat exchange zone. The lengths of these inlet and outlet zones were 240 and 360 mm, respectively. In **Figure 1** was reported a longitudinal section of the PFHE (panel **a**) and the shape of the different wings geometries inside the heat exchanger (panel **b**, **c** and **d**).

2.2. CFD modelling

2.2.1. 3D models and mesh details

The fluid flow and heat exchange inside the PHE were simulated by means of a multidimensional CFD (Computational Fluid Dynamic) model. First, a 3D CAD model for the fluid flow inside each geometry reported in **Table 1** was developed with SolidWorks® 2015 software (Dassault systèmes, Vélizy-Villacoublay, France). The effect of the wall of PHE was considered negligible due to the material (stainless steel shown a thermal conductivity almost 10 time greater than water) and the small thickness value of the wall (1 mm). This means a reduction of calculation time and possibility to improve the precision inside the fluid flow.

Water was used as test fluid, and has been treated as incompressible, homogeneous and Newtonian fluid with negligible effect of viscous heating. Thermal and physical properties were obtained from the software library.

The quality and quantity of mesh are very important for the accuracy and time of CFD simulation. Therefore, care must be taken in selecting the mesh type and size, so not to affect the CFD results (Khoshvaght-Aliabadi et al., 2015). The model geometry was imported into the ICEM CFD® software (Canonsburg, Pennsylvania, USA) and discretized into an unstructured tetrahedrical and hexaedrical mesh. The mesh was optimized by increasing the mesh density till the average temperature at the outlet fluid zone became constant. This process, named mesh independent analysis, was carried out for each geometry at the higher velocity value of fluid flow (1 m s^{-1}). The value of the minimum element edge dimension, for all geometries, was $1*10^{-4}$ m; however, the value of the maximum element edge dimension, dependent on the type of geometry, was lower than $1*10^{-3}$ m, for all the geometries. Moreover, to accurately calculate the flow field near the wall of the heat exchanger, five layer of flat prismatic wedge element (with a total thickness of 1 mm and growth rate of 20%) were added to the domain. From a mesh quality point of view, the value of the skewness was taken into consideration and a good value of skewness was reached for everyone geometry (ANSYS Icepack User's Guide, 2011).

2.2.2. Boundary conditions

In this study a steady state simulations were carried out with no changes in boundary and domain conditions with the time. As illustrated in *Section 2.1*, the computation domain consists of an inlet fluid zone (red in **Figure 1**), a heat exchange zone (green in **Figure 1**) and an outlet zone (blue in **Figure 1**). The applied boundary conditions in these regions are described as follows.

- *Inlet fluid zone*

At the inlet boundary:

$$u_y = u_z = 0 \qquad u_x = u_{in} = constant \qquad T = T_{in} = constant \quad \text{(1a)}$$

At the inlet zone surface:

$$u_x = u_y = u_z = 0 \qquad \frac{\partial T}{\partial y} = \frac{\partial T}{\partial z} = 0 \quad \text{(1b)}$$

- *Heat exchange zone*

At the heat exchange zone surface:

$$u_x = u_y = u_z = 0 \qquad T = T_{wall} = constant \quad \text{(2)}$$

- *Outlet fluid zone*

At the outlet zone surface:

$$u_x = u_y = u_z = 0 \qquad \frac{\partial T}{\partial y} = \frac{\partial T}{\partial z} = 0 \quad \text{(3a)}$$

At the outlet boundary:

$$\frac{\partial u_x}{\partial x} = \frac{\partial u_y}{\partial x} = \frac{\partial u_z}{\partial x} = 0 \qquad \frac{\partial T}{\partial x} = 0 \qquad (3b)$$

Where u is flow velocity (m s^{-1}), T is temperature (°C). x, y, z the spatial coordinates. A no-slip condition was applied with a zero velocity of the fluid relative to the surface of the PHE. In particular, T_{in}, the temperature of the fluid entering the system, was set at 20°C; T_{wall}, the temperature of the heating zone, was set at 90°C. u_{in}, the fluid velocity entering the system, was set at different value: 0.01, 0.02, 0.05, 0.1, 0.2, 0.5 and 1 m s^{-1}, to study the behaviour of the geometry at different Reynolds numbers.

2.2.3. Numerical model

The software ANSYS® CFX v15 (Canonsburg, Pennsylvania, USA), run on HP Z420 Workstation (Palo Alto, California, USA), was used to solve the governing continuity, momentum and energy equations for the defined geometry and for various Reynolds number. The domain was defined in the global co-ordinate frame in which the solver carries out the calculations and the governing equations for the mathematical model were as follows:

a) *Conservation of mass (continuity equation)*

$$\frac{\partial \rho}{\partial t} + \nabla \cdot (\rho V) = 0 \qquad (4)$$

b) *Conservation of momentum (momentum equation)*

$$\frac{\partial \rho V}{\partial t} + \nabla \cdot (\rho V \cdot V) = \nabla \cdot (-p\delta + \mu(\nabla V + (\nabla V)^t)) \qquad (5)$$

c) *Conservation of energy (energy equation)*

$$\frac{\partial \rho C_p T}{\partial t} - \frac{Dp}{Dt} + \nabla \cdot (\rho V C_p T) = \nabla \cdot (k\Delta T) \quad (6)$$

Where t is the time (s), V is the velocity vector (m s^{-1}), ρ is the density (kg m^{-3}), p is the pressure (Pa), μ is dynamic viscosity (Pa s), T is the temperature (°C), C_p specific heat capacity (J kg^{-1} $°C^{-1}$) and k is thermal conductivity (W m^{-2} $°C^{-1}$). The governing equations were discretized by the finite volume method (FVM) and to solve the coupled system of partial differential equations, the high-resolution scheme with second order backward Euler method was adopted. The solution was considered convergent when the residuals values of each equations reach the value of 10^{-4} and the imbalance value for the conservation equations reach 1% (ANSYS CFX Modelling Guide, 2015). Regarding the natural convection, the contribution wasn't taken into consideration due to the presence of forced convection caused by the flow inside the pipe which makes negligible the natural one.

2.3. Data processing method

The performance of a heat exchanger usually are evaluated in terms of the heat transfer and pressure drop performance characteristics (Khoshvaght-Aliabadi et al., 2014a).

To calculate heat transfer coefficient, first was compute the heat transfer rate by means of the following equation:

$$Q_{conv.} = \dot{m}C_P(T_{f,out} - T_{f,in}) \qquad (7)$$

Where $Q_{conv.}$ is heat exchange rate (W), $\dot{m}$ is mass flow rate (kg m^{-3}), C_P is specific heat (J kg^{-1} °C^{-1}), $T_{f,in}$ and $T_{f,out}$ inlet and outlet temperature (°C) of fluid, respectively. The effective heat transfer coefficient (h) was then estimated from the ratio between the heat transfer rate and the total heat exchange surface area and logarithmic mean temperature difference (between the wall and the fluid inside the heat exchanger):

$$h = \frac{Q_{conv.}}{A_t(T_w - T_f)_{LMTD}} \qquad (8)$$

Where h is heat transfer coefficient (W m^{-2} °C^{-1}), A_t is the total heating surface (m^2), $(T_w\text{-}T_f)_{LMTD}$ is the logarithmic mean temperature difference (°C), calculated by:

$$(T_w - T_f)_{LMTD} = \frac{(T_w - T_{f,in}) - (T_w - T_{f,out})}{log[(T_w - T_{f,in})/(T_w - T_{f,out})]} \qquad (9)$$

Where T_w is the treatment temperature (°C).

As well as the heat transfer coefficient, the thermal performance can be illustrated also in a non-dimensional form, with a parameter named Colburn factor. Whit this parameter also the properties of the fluid was considered in heat exchange. It can be calculated as:

$$j = \frac{h}{\rho u C_P} Pr^{2/3} \qquad (10)$$

Where ρ is density (kg m^{-3}), u is the mean velocity (m s^{-1}) at the minimum cross sectional flow area inside the heat exchanger, Pr is Prandtl number expressed as:

$$Pr = \frac{\mu C_P}{k} \qquad (11)$$

Where μ is dynamic viscosity (Pa s) and k thermal conductivity (W m^{-1} °C^{-1}).

Regard the pressure drop, in addition to the simple difference between the pressure at the outlet section and the pressure estimated at the inlet one, the performance can be assessed by the non-dimensional parameter named Fanning friction factor, calculated as:

$$f = \frac{2\rho \Delta P D_h}{L u^2} \qquad (12)$$

Where ΔP is the pressure difference (Pa) between inlet and outlet section, L is the section length (m) and D_h is the hydraulic diameter (m), expressed as:

$$D_h = \frac{4LA_c}{A_t} \qquad (13)$$

Where A_c is the minimum cross sectional flow area (m^2) inside heat exchange zone.

The global performance, taking into account both the heat transfer and pressure drop, of a heat exchanger can be estimated in different ways. Along the years several criteria were developed to evaluate the performance of heat exchanger and to select the optimum geometry with a larger *j* factor and smaller *f* factor. The easiest parameter is the *j*/*f* ratio, named surface performance factor, but Bhowmik and Lee (2009) demonstrated that this criterion could not be considered suitable for fluid with Prandtl number like those used in this study. From fluid like water, with a Prandtl number around 7 the better criterion seems to be JF criterion, expressed as:

$$JF_i = \frac{(j_i/j_{PFHE})}{(f_i/f_{PFHE})^{1/3}} \qquad (14)$$

Where j_i/f_i and j_{PFHE}/f_{PFHE} are the Colbourn/Fanning factor calculated at each process conditions for any geometry tested and one obtained from the PFHE geometry respectively.

Another objective in heat exchanger design is to reduce the total surface keeping constant the heat and pressure drop performances, or from the opposite point of view, increase the performance keeping the same surface of heat exchanger. To measure the possible reduction of the surface relative to each tested geometry compared to the PFHE one, the VG-I criterion reported by Webb was considered. The A_i/A_{PFHE} ratio was calculated, by means of the following equation,

$$\frac{A_i}{A_{PFHE}} = \left(\frac{j_{PFHE}}{j_i}\right)^{3/2} * \left(\frac{f_i}{f_{PFHE}}\right)^{1/2} \qquad (15)$$

The A_i/A_{PFHE} ratio represent the possible reduction, in percentage, of surface area volumes of each tested geometry respect to the standard one.

3. *Results and Discussion*

3.1. Grid independency analysis

The quality and quantity of grids are both very important for the accuracy and time required for CFD simulations, therefore, care must be taken in selecting the mesh type and size, so not to affect the CFD results. The grid dependence was investigated by simulation for each PFHE geometry at the highest fluid velocity (1 m s^{-1}) with 7 different mesh densities of about 300000, 600000, 1200000, 2400000, 4800000, 9600000 and 19200000 cells.

3.2. Heat transfer results

The effects of geometries and dimensions of vortex generators were investigated by means of dimensional and non-dimensional parameters as reported in *Section 2.3*. For each configuration, the results were obtained at 7 volumetric flow rates in the range of 134-12395 Re. The results of the plain channel (named PFHE) were considered to establish a baseline for comparison. In **Figure 2a** a comparison of the heat transfer coefficient for the various wing shapes at different volumetric flow rates is reported: the heat transfer coefficient increased linearly with raising of the flow rate, as expected (Khoshvaght-Aliabadi et al., 2015). The PFHE geometry gave the worst results while the best was obtained with the rhombus geometries probably due to the high turbulence caused by their shape. These results were confirmed also from a numerical point of view: the mean increase of heat transfer coefficient between the PFHE geometry and the remaining geometries was 71, 64 and 58 % for rhombus, rectangular and elliptical, respectively. Moreover, the difference between the base geometries and the investigated ones tended to increase with the raising of the flow rate until 1315 Re, while above this value the differences resulted no more significant. Probably, this fact could be a consequence of turbulence increasing generated by the fluid flow which overcame the turbulence effect made by the vortex-generator and so covered up the differences between geometries.

For a further comparison of heat transfer performance, non-dimensional parameters were introduced for easily comparing different heat exchangers. As introduced in *Section 2.3* the Colburn *j factor* was usually employed to evaluate the efficacy of the heat exchange. The ratio between *j factor* of three different geometries and that related to PFHE geometry (**Figure 2b**) confirmed what previously reported: the rhombus wings geometries gave the best results at almost all flow rates (except for 267 Re). Moreover, at 1315 Reynolds the rhombus geometry resulted 1.6 times more effectiveness with respect to the PFHE one.

Moreover, the local velocity contour maps obtained from CFD models of different geometries were compared at 3 different flow rates (0.01, 0.1 and 1 m s^{-1}) (**Figure 3**). From the lateral view, it's possible to note that differences between the geometries can be considered negligible, mainly at low flow rates. In all cases the presence of the vortex generators greatly affected the flow, producing dead spots which negatively affected the efficiency of heat exchanger. From the top view (**Figure 3**), the differences between the geometries became more evident with the increasing of the flow rate. From this colour map, it is possible also to highlight the "obstruction effect", which affected not only the heat exchange and pressure drop values but also the global efficiency regard also to the cleanability of heat exchanger. The "obstruction effect" due to the presence of vortex generators seem to be different between the different shapes only at the highest flow rate (1 m s^{-1}).

Once identified the best geometry (in this case the rhombus one), the effect of different dimensions of vortex-generators was also investigated. Starting from the width of the wing, 3 different width values were tested (3, 5 and 7 mm) and results are reported in **Figure 4a**. Also in this case the heat transfer coefficient linearly increased with the flow rate for all the geometries. Furthermore, as expected, the heat exchange linearly increased with the wings' width. PHE geometries for 3, 5 and 7 mm of width gave a heat transfer coefficient increase of 38, 71, 102%, respectively, compared to PFHE. In this case the intensification of turbulence and secondary flows due to the presence of larger vortex-generators positively affected the heat exchange. The trend of the ratios between *j factor* of different widths and the value referred to PFHE geometry (**Figure 4b**) appeared similar to those reported in **Figure 2b**. The highest ratios were obtained, for all the geometries, at Reynolds number of 1315 and the highest one (wing width of 7 mm) exceeded 1.7 times the value of the PFHE geometry. Also in this case, it's possible to note how at higher Reynolds number the ratios tended to decrease probably for the same reason previously reported.

The different wings' widths affected local velocity profile at almost all velocity (**Figure 5**): from the lateral view, the difference in local velocity profile increased with the increasing of flow velocity and, as expected, the highest discrepancy can be observed for the highest widths due to a reduction of flow section. Moreover the "obstruction effect" seemed reduced at higher flow rates, probably as consequence of increasing of global turbulence in the system. From the top view, the same behaviour can be observed and the differences between the three widths resulted evident both at lowest and at highest velocities.

Finally, starting from the geometries with the best heat transfer coefficient in function of wing width (rhombus geometry with a wings' width of 7 mm), three different wings' heights were tested (3, 6 and 9 mm, **Figure 6a**): as expected, also in this case the highest heat transfer coefficient for all Reynolds numbers was observed at the geometry with the highest wings' height. The values linearly increased both at increasing of Reynolds number and of wings' height. From the ratio between *j factor* of each geometry and that calculated for the PFHE geometry (**Figure 6b**) the best geometry for almost all flow rates (except for the lowest Reynolds number) resulted the 6 mm height geometries. Probably, the reduction of section area due to the presence of the wings of 7 mm of width and 9 mm height, increased greatly the mean velocity inside the heat exchange zone, reducing the heat transfer coefficient as consequence.

The effect of section reduction resulted evident also from the local velocity profile map (**Figure 7**): also in this case the differences increased with the increasing of the flow rate. The reduction of the heat transfer for the highest wings' height can be explained also by the images of the top view reported in **Figure 7**: the flow inside the heat exchange zone seemed to avoid the vortex generators, passing mainly through the zone between the wings and side wall of the heat exchanger.

3.3. Pressure drop results

The pressure drop is the other fundamental parameter to be considered during the design of a heat exchanger. In **Figure 8a** a comparison of pressure drop at different flow rates between the geometries with different shapes is reported: for all the geometries, the pressure drop exponentially increased with raisin up of the Reynolds number. As expected, the differences between the geometries resulted more evident at higher flow rates, as already reported regard the heat transfer coefficient. However, in this case two geometries seemed to have the same performances: the pressure drop obtained for rectangular and rhombus wing shapes resulted very similar, while for the elliptical one the values were clearly lower. These results were confirmed also from numerical point of view, the mean increase of pressure drop between the PFHE geometry and the three studied were 143, 149 and 126% for rectangular, rhombus and elliptical, respectively. Probably the "soft edge" geometry of elliptical wings reduced the interferences to the main flow, with lower secondary turbulence inside the heat exchange zone. These results are in accordance with the data shown in **Figure 2a**: the reduced interference on the fluid flow directly affected the heat transfer coefficient (the elliptical wing shape gave the worst result regard heat performance). In other terms the enhancement of heat transfer is usually penalized by the increase in the pressure drop (Khoshvaght-Aliabadi et al., 2014a).

Also for the pressure drop analysis a non-dimensional parameter was investigated to compare the performance of different geometries. The Fanning friction factor (f) was calculated following the equation (12) reported in *Section 2.3* and the ratios f_i/f_{PFHE} at different Reynolds numbers for the various wings geometries are reported in **Figure 8b**. Confirming what reported in the previous paragraph, the rhombus geometry gave the highest ratios in all process conditions. In all the tested channels, the ratio gradually decreased with the increasing of Reynolds number until a value where the ratio remained the same (for rhombus and elliptical geometries) or tended to slightly increase (for rectangular one). This behaviour was associated to the development of the fluid flow inside the heat exchange section: at higher Re number the flow resulted fully developed and the friction factor tended to reduce (Khoshvaght-Aliabadi et al., 2014a). In some cases (e.g., elliptical geometry at higher Reynolds number), this effect produced a ratio lower than 1, meaning that the pressure drop caused by the presence of wings can be negligible with respect to the PFHE geometry. From these results it's evident how the flow rate can greatly affect the efficiency of a thermal treatment. Moreover, the best geometry varied in function of the Reynolds number: until a value of 664, the lowest f_i/f_{PFHE} ratio was presented by the rectangular geometry, while above this value the elliptical one gave the best results.

As regard the local velocity profile of the three geometries the colour maps are reported in **Figure 3**. From the top view, the elliptical geometry seemed to give the best homogeneity regard the flow velocity, thus resulted in a lower interference in the fluid flow and a reduction of pressure drop between inlet and outlet section, as consequence.

As already done for the heat transfer coefficient, starting from the shape with the lowest pressure drop, in this case the elliptical one, 3 different widths were tested. In **Figure 9a** the pressure drop trends vs. Re numbers for elliptical wings with widths of 3, 5 and 7 mm are reported. The pressure drop increased (following a power equation) with the raising up of the flow rate for every width. As expected, the highest value was observed for the widest wings at each Reynolds number. Moreover, the differences between the different wings' widths increased with increasing of the Reynolds number and the trend between three different values can be approximated to an exponential equation at all flow rates. The mean increase of pressure drop between standard geometry and the tested ones resulted equal to 59, 126 and 236% for the wings height of 3, 5 and 7 mm, respectively. By comparing the f_i/f_{PFHE} ratio (**Figure 9b)** it's evident that for two widths (5 and 7 mm) the friction factor resulted similar at almost all flow rates. Probably over a defined width, a further increase doesn't affect the friction factor (however the pressure drop still increases due to the reduction of the heat exchanger section). In **Figure 9b** it's possible to note that, overcoming a defined Reynolds number (in this case equal to 2568) the ratio became lower than 1 for all the widths. In these cases, the turbulence generated by the flow overcame the effect of vortex-generators, making negligible their presence.

In **Figure 10** the local velocity profile obtained from the developed CFD models is reported. The width of the wings greatly affected the flow velocity as can be see both from the lateral view and from the top view. The differences between the geometries increase with the increasing of flow rate as already observed in **Figure 9a** regard the pressure drop. Moreover, as expected, the best results from local velocity point of view were obtained for the lowest wing width where the values seem to be more homogenous. These considerations confirm the relation between the local velocity range and the pressure drop: if the local velocity presents a reduced range of variation the pressure drop will result lower.

Finally, taking into consideration the elliptical geometry with width of 3 mm, the effects on pressure drop of three different wings' heights (3, 6 and 9 mm) were investigated. The results followed the same behaviour saw for the wings width (**Figure 11a**) and the pressure drop increased with the increasing of wings' height. The mean pressure drop enhancement between the PFHE geometry and tested geometries were of 26, 59 and 101% for the wings' height of 3, 6 and 9 mm, respectively. The f_i/f_{PFHE} ratio (**Figure 11b**) showed behaviour different between those obtained with wings' width: at low Re numbers the differences between the studied heights were evident and these differences tended to reduce as the flow rate increased. In this case the worst ratio was obtained with the highest height. However, once reached a defined Reynolds number (equal to 1315), the ratio became lower than 1 and the effect of different height seemed to inverted. As already illustrated, probably, at higher flow rate, the effect of vortex generators can be negligible compared to the turbulence generated by the flow.

The effect of restriction on the section surface of the heat exchanger in function of increasing of wings height can be appreciate in the local velocity profile from the lateral point of view (**Figure 12**). Also in this case the differences between various heights growth with the enhance of the flow rate. From the homogeneity of local flow velocity, as can be seen from the top point of view in **Figure 12**, the best results were obtained with the lowest wings height.

3.4. Global performance evaluation

As cited in the previous section, an improvement in the heat transfer performance is associated with an increase in the pressure drop. Consequently, it's necessary to identify the geometry which guarantees the best compromise between heat transfer coefficient and pressure drop.

First of all, to give an overview of the results obtained from the different geometries tested, the mean deviations of the heat transfer coefficient and pressure drop values between each geometries (shape, width and height) and the PFHE are summarized in **Table 2**, according to the following definition reported by Khoshvaght-Aliabadi et al. (2014a):

$$mean\ deviation\ (\%) = \frac{1}{N}\left(\sum\left|\frac{\emptyset_i-\emptyset_{PFHE}}{\emptyset_{PFHE}}\right|\right) \quad (16)$$

where ϕ is the heat transfer coefficient h (in the case of heat exchange study) or pressure drop ΔP (for the pressure drop analysis). N is the number of flow rate tested, in this case 7. From the tabulated data appears evident that general trend follow the behaviour explained in the previous paragraphs: both the heat transfer coefficient and pressure drop tend to increase with the increasing of wings width and height for all the different shapes tested.

Starting from the evaluation performance criteria explained in *section 2.3*, in **Table 3** were reported the values obtained for each geometry. Usually, high values of the $j_i/f_i^{1/3}$ meaning a heat exchanger with a good heat transfer and pressure drop performance. As can be noted, the highest value was obtained at the same characteristic dimensions for all the tested shapes: 5 and 9 mm of wings width and height, respectively. Moreover, in all the cases studied the values decrease with raising of the Reynolds number, following a power law tendency (data not shown).

Regard the thermal-hydraulic performance factor (JF_i), where a high value mean a heat exchanger with superior heat exchange and pressure drop performance, the same behaviour already of the previous parameter can be noted. However, from the flow rate point of view the best results were obtained at Reynolds number of 1315, this meaning that the flow rate affect directly the performance of a heat exchanger. Moreover, at specific flow rate (e.g., flow with Reynolds number of 134) the performance of the heat exchanger with vortex generators result worsen respect the geometry without them.

Finally, the last parameter taken into consideration was the possible reduction of the surface area of the heat exchanger respect the standard one (A_i/A_{PFHE}). In the last column of the **Table 3**, the highest reduction of surface was obtained with the same geometries previously highlighted for the other performance criteria. As can be seen the possible mean reduction of surface were of 25, 26 and 23% for rectangular, rhombus and elliptical wings shape, respectively.

4. Conclusion

In this work the performance of heat exchanger with different kind of vortex generators were investigated by means of CFD techniques. Starting from the standard plate fine heat exchanger, 3 different wing shapes (rectangular, rhombus and elliptical) and 2 geometric parameters were tested. As regard geometric parameters, three different wings' widths (3, 5 and 7 mm) and heights were compared (3, 6 and 9 mm). Finally, in order to investigate also the effect of flow rate on the performance of the heat exchanger, 7 different flow rates (from 0.01 to 1 m s^{-1}) were tested. Overall, 196 samples were compared by means CFD mathematical models and useful information were obtained without any experimental test.

Heat transfer coefficient and pressure drop were taken into consideration to evaluate the performance of the heat exchanger in the various consideration. Moreover, to make these results comparable among them, two non-dimensional parameters were calculated: Colburn *j* factor (for the heat exchange) and Fanning *f* factor (for the pressure drop).

The best heat exchange results regard were obtained for the rhombus wings shape and in particular the highest Colburn j factor, for almost all flow rates were estimated for wings width of 7 mm and height of 6 mm.

On the other hand, the best pressure drop results were obtained with the elliptical wing shape, and in particular with wings width of 3 mm and height of 3 mm, as expected. The low interference caused on the flow by the vortex generators affect directly the pressure drop. Moreover, in some flow rate conditions (e.g., high flow rate) the presence of vortex generators can be considered negligible respect the standard geometry, regard the pressure drop variation. From these results emerge how an improvement in the heat transfer performance is associated with an increase in the pressure drop. Consequently, one of the main step in heat exchanger design is to identify the geometry which guarantees the best compromise between heat transfer coefficient and pressure drop. To achieve this goal different performance evaluation criteria were developed in the years. After the calculation of $j/f^{1/3}$ ratio, JF_i factor and surface reduction criteria the best result for all the three different geometries were the vortex generators with a width of 5 mm and a height of 9 mm, with a possible mean reduction of surface of 25, 26 and 23% for rectangular, rhombus and elliptical geometry, respectively.

Starting from the results obtained in this work, future developments can be hypothesized such as the construction of experimental test pilot plant to validate the result of this work. Moreover, different fluids can be used as fluid flow, particularly fluid with non-Newtonian behaviour such as fruit juices or other liquid food matrix to evaluate also the effect of the viscosity on the heat exchange.

References

Aguiar, H.F. & Gut, J.A.W., (2014). Continuous HTST pasteurization of liquid foods with plate heat exchangers: Mathematical modeling and experimental validation using a time-temperature integrator. *Journal of Food Engineering*, 123, 78–86.

Ahmed, H.E, Mohammed, H.A. & Yusoff, M.Z., (2012). Heat transfer enhancement of laminar nanofluids flow in a triangular duct using vortex generator. *Superlattices and Microstructures*, 52, 398-415.

ANSYS®, (2011). *ANSYS® Icepack User's Guide* (release 14, p.700). Cannonsburg, Pennsylvania, USA.

ANSYS®, (2015). *ANSYS® Modelling Guide* (release 16). Cannonsburg, Pennsylvania, USA.

Aslam Bhutta, M.M., Hayat, N., Bashir, M.H., Khan, A.R., Ahmad, K.N. & Khan, S., (2012). CFD applications in various heat exchangers design: A review. *Applied Thermal Engineering*, 32, 1–12.

Bhowmik, H. & Lee, K.S., (2009). Analysis of heat transfer and pressure drop characteristics in an offset strip fin heat exchanger. *International Communications in Heat and Mass Transfer*, 36, 259–263.

Brockmeier, U., Guentermann, Th. & Fiebig, M., (1993). Performance evaluation of a vortex generator heat transfer surface and comparison with different high performance surfaces. *International Journal of Heat and Mass Transfer*, 36(10), 2575-2587.

De Bonis, M.V. & Ruocco, G., (2009). Conjugate fluid flow and kinetics modeling for heat exchanger fouling simulation. *International Journal of Thermal Sciences*, 48, 2006–2012.

Gentry, M.C. & Jacobi, A.M., (1997). Heat transfer enhancement by delta-wing vortex generators on a flat plat: Vortex interactions with the boundary layer. *Experimental Thermal and Fluid Science*, 14(3), 231-242.

Jain, A., Biswas, G. & Maurya, D., (2003). Winglet-type vortex generators with common-flow-up configuration for fin-tube heat exchangers. *Numerical Heat Transfer, Part A*, 43, 201-219

Khoshvaght-Aliabadi, M., Hormozi, F. & Zamzamian, A., (2014a). Role of channel shape on performance of plate-fin heat exchangers: Experimental assessment. *International Journal of Thermal Sciences*, 79, 183–193.

Khoshvaght-Aliabadi, M., Zangouei, S. & Hormozi, F., (2015). Performance of a plate-fin heat exchanger with vortex-generator channels: 3D-CFD simulation and experimental validation. *International Journal of Thermal Sciences*, 88, 180–192.

Rozzi, S., Massini, R., Paciello, G., Pagliarini, G., Rainieri, S. & Trifirò, A., (2007). Heat treatment of fluid foods in a shell and tube heat exchanger: Comparison between smooth and helically corrugated wall tubes. *Journal of Food Engineering*, 79, 249–254.

Sheikholeslami, M., Gorji-Bandpy, M. & Ganji, D. D., (2015). Review of heat transfer enhancement methods: Focus on passive methods using swirl flow devices. *Renewable and Sustainable Energy Reviews*, 49, 444-469.

Wang, L. & Sun, D.-W., (2003). Recent developments in numerical modelling of heating and cooling processes in the food industry—a review. *Trends in Food Science and Technology*, 14, 408-423.

Wu, J.M. & Tao, W.Q., (2012). Effect of longitudinal vortex generator on heat transfer in rectangular channels. *Applied Thermal Engineering*, 32, 67-72.

Xia, B. & Sun, D.W., (2002). Applications of computational fluid dynamics (CFD) in the food industry: a review. *Computers and Electronics in Agriculture*, 34, 5–24.

Table 1. Characteristic dimensions of different PHE geometry studied.

	wing length (w_l)	***wing width (w_w)***	***wing height (w_h)***	***code***
rectangular	2	3	3	RE.w3.h3
			6	RE.w3.h6
			9	RE.w3.h9
		5	3	RE.w5.h3
			6	RE.w5.h6
			9	RE.w5.h9
		7	3	RE.w7.h3
			6	RE.w7.h6
			9	RE.w7.h9
rhombus	2	3	3	RH.w3.h3
			6	RH.w3.h6
			9	RH.w3.h9
		5	3	RH.w5.h3
			6	RH.w5.h6
			9	RH.w5.h9
		7	3	RH.w7.h3
			6	RH.w7.h6
			9	RH.w7.h9
elliptical	2	3	3	EL.w3.h3
			6	EL.w3.h6
			9	EL.w3.h9
		5	3	EL.w5.h3
			6	EL.w5.h6
			9	EL.w5.h9
		7	3	EL.w7.h3
			6	EL.w7.h6
			9	EL.w7.h9

Table 2. Mean differences of the convective heat transfer (*h*) and pressure drop (*ΔP*) values between each geometry tested (shape, width and height) and the PFHE.

Wings		***rectangular***		***rhombus***		***elliptical***	
width (mm)	***height (mm)***	***h***	***ΔP***	***h***	***ΔP***	***h***	***ΔP***
3	**3**	21%	31%	23%	30%	16%	26%
3	**6**	37%	77%	38%	73%	27%	58%
3	**9**	58%	131%	55%	119%	44%	101%
5	**3**	33%	52%	32%	55%	29%	46%
5	**6**	64%	143%	71%	149%	58%	126%
5	**9**	96%	282%	99%	271%	87%	240%
7	**3**	46%	77%	53%	82%	42%	71%
7	**6**	92%	249%	101%	271%	90%	232%
7	**9**	130%	547%	145%	586%	133%	523%

Table 3. Comparison of the performance evaluation criteria obtained from the different tested geometry (mean value from the average of the flow rate). The best results for each wing shape where highligheted.

	wings width (mm)	*wings height (mm)*	*Performance evaluation criteria*		
			$j/f^{1/3}$ ratio	*JF_i factor*	*A_i/A_{PFHE}*
rectangular	3	3	0,0345	1,14	17%
	3	6	0,0357	1,20	21%
	3	9	0,0376	1,29	27%
	5	3	0,0360	1,21	22%
	5	6	0,0379	1,30	28%
	5	9	**0,0392**	**1,38**	**30%**
	7	3	0,0373	1,27	26%
	7	6	0,0387	1,35	**30%**
	7	9	0,0380	1,34	27%
rhombus	3	3	0,0344	1,14	16%
	3	6	0,0356	1,20	21%
	3	9	0,0372	1,27	26%
	5	3	0,0367	1,24	25%
	5	6	0,0381	1,31	29%
	5	9	**0,0393**	**1,38**	**31%**
	7	3	0,0375	1,28	27%
	7	6	0,0386	1,35	30%
	7	9	0,0385	1,36	28%
elliptical	3	3	0,0336	1,10	11%
	3	6	0,0345	1,14	15%
	3	9	0,0363	1,23	23%
	5	3	0,0354	1,18	19%
	5	6	0,0373	1,28	26%
	5	9	**0,0387**	**1,35**	**30%**
	7	3	0,0368	1,24	24%
	7	6	0,0383	1,33	29%
	7	9	0,0382	**1,35**	27%

Figure 1. Longitudinal section of the PFHE (panel **a**) with the fluid inlet zone (red), the heat exchange zone (green) and outlet zone (blu). Magnification of the heat exchange zone with the disposition and geometry of vortex generators for rectangular (panel **b**), rhombus (panel **c**) and elliptical (panel **d**) shape.

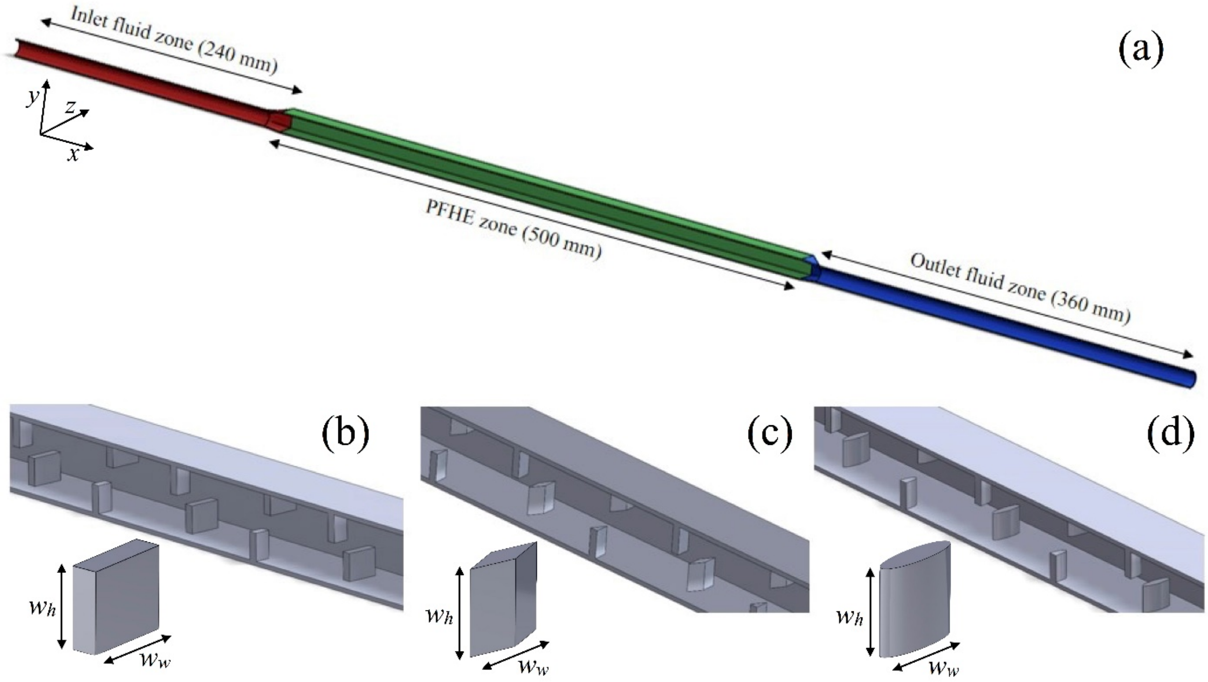

Figure 2. Comparison of the convective heat transfer coefficient in function of the Reynolds number between vortex generators with different shape (panel **a**) and the ratio between *j factor* in function of the Reynolds number of the three geometries and the one related to PFHE geometry (panel **b**).

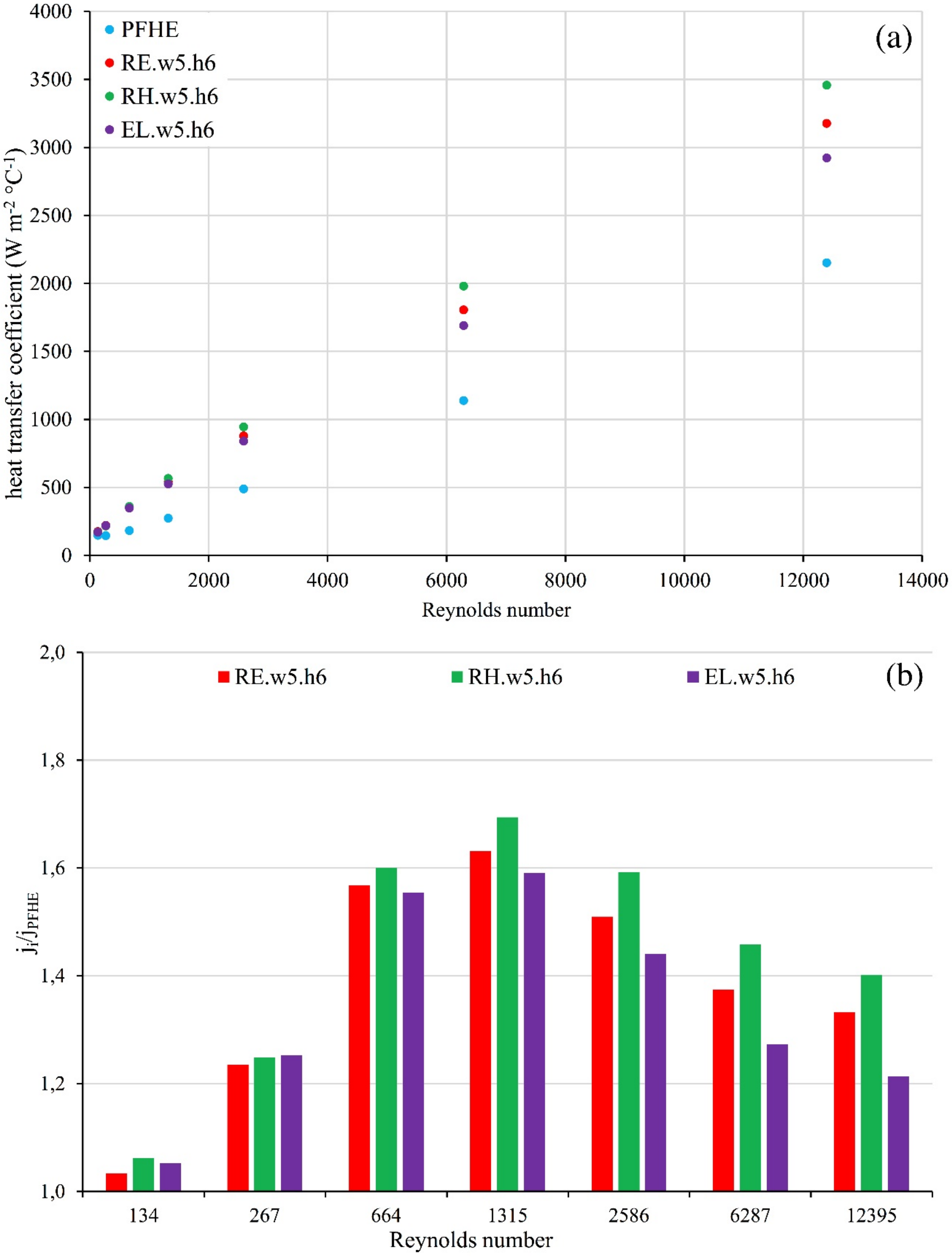

Figure 3. Local velocity profile of the flow inside heat exchanger, at three different flow velocity for the different wing shapes. The reported pictures, parallel to fluid flow was from a lateral point of view and from a top point of view.

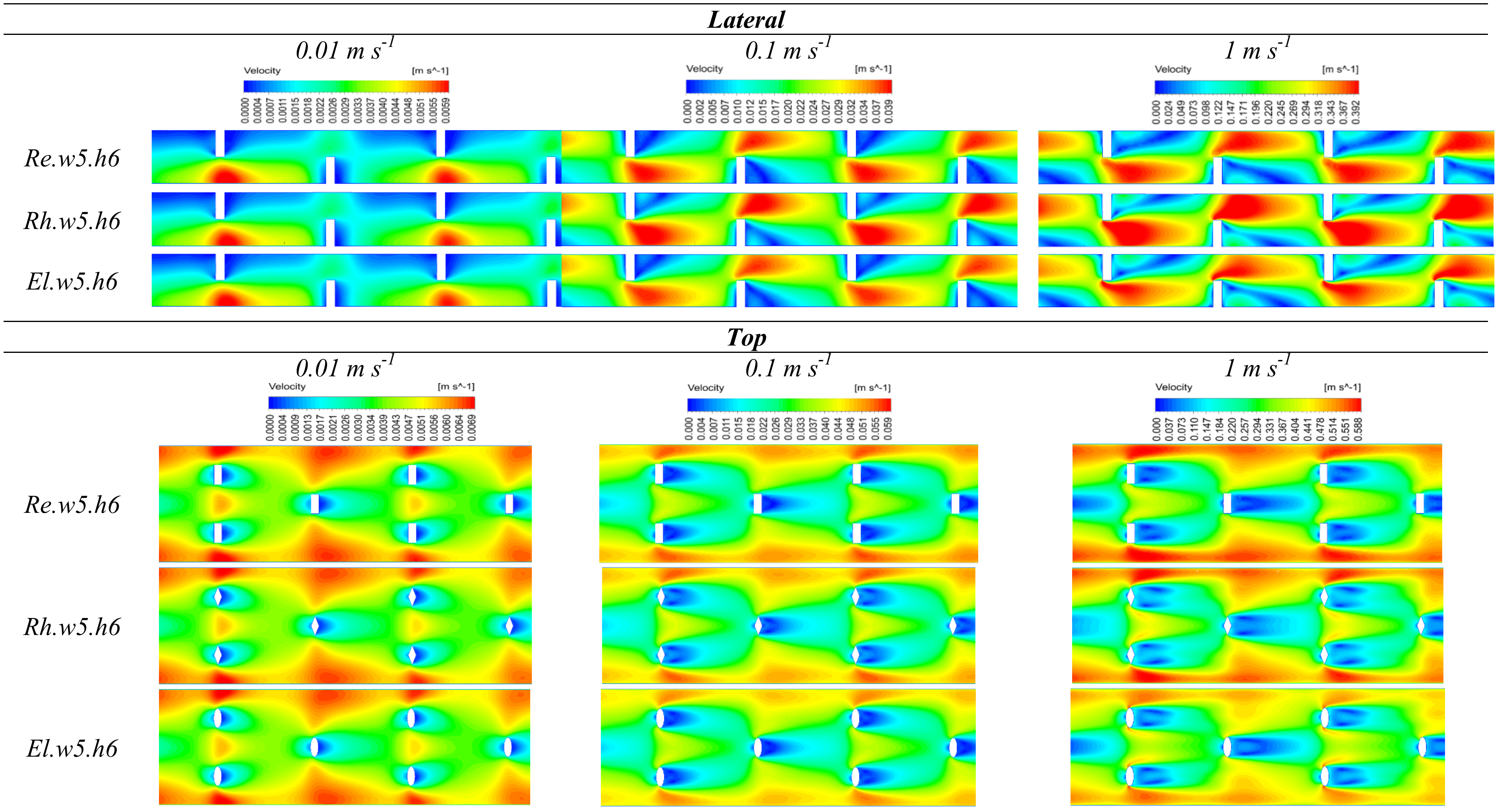

Figure 4. Comparison of the convective heat transfer coefficient in function of the Reynolds number between rhombus vortex generators with three different wing width (panel **a**) and the ratio between *j factor* obtained from the three different rhombus wing widht and the one related to PFHE geometry (panel **b**).

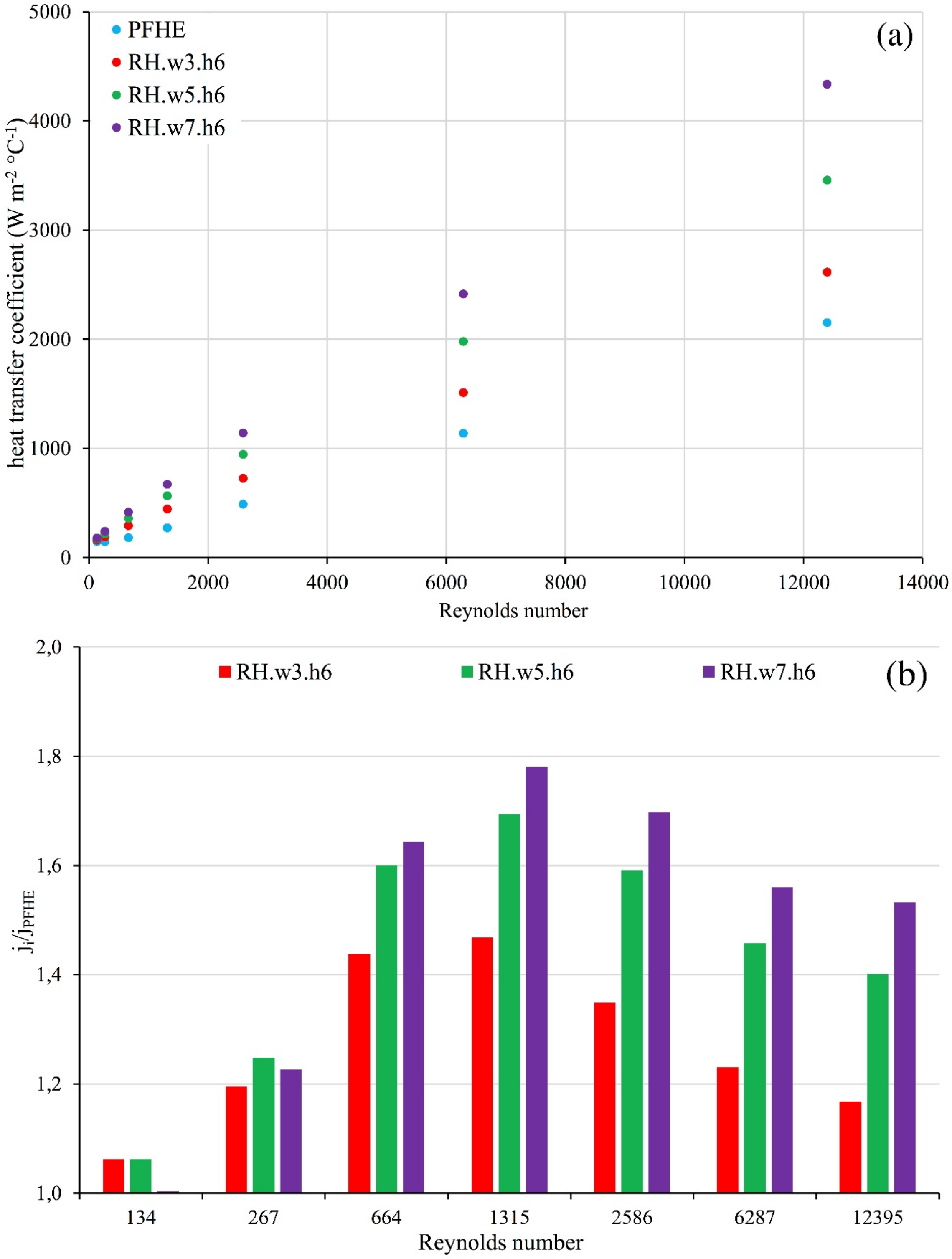

Figure 5. Local velocity profile of the flow inside heat exchanger, at three different flow velocity for the three different wings width for the rhombus geometry. The reported pictures, parallel to the fluid flow, was from a lateral point of view and from a top point of view.

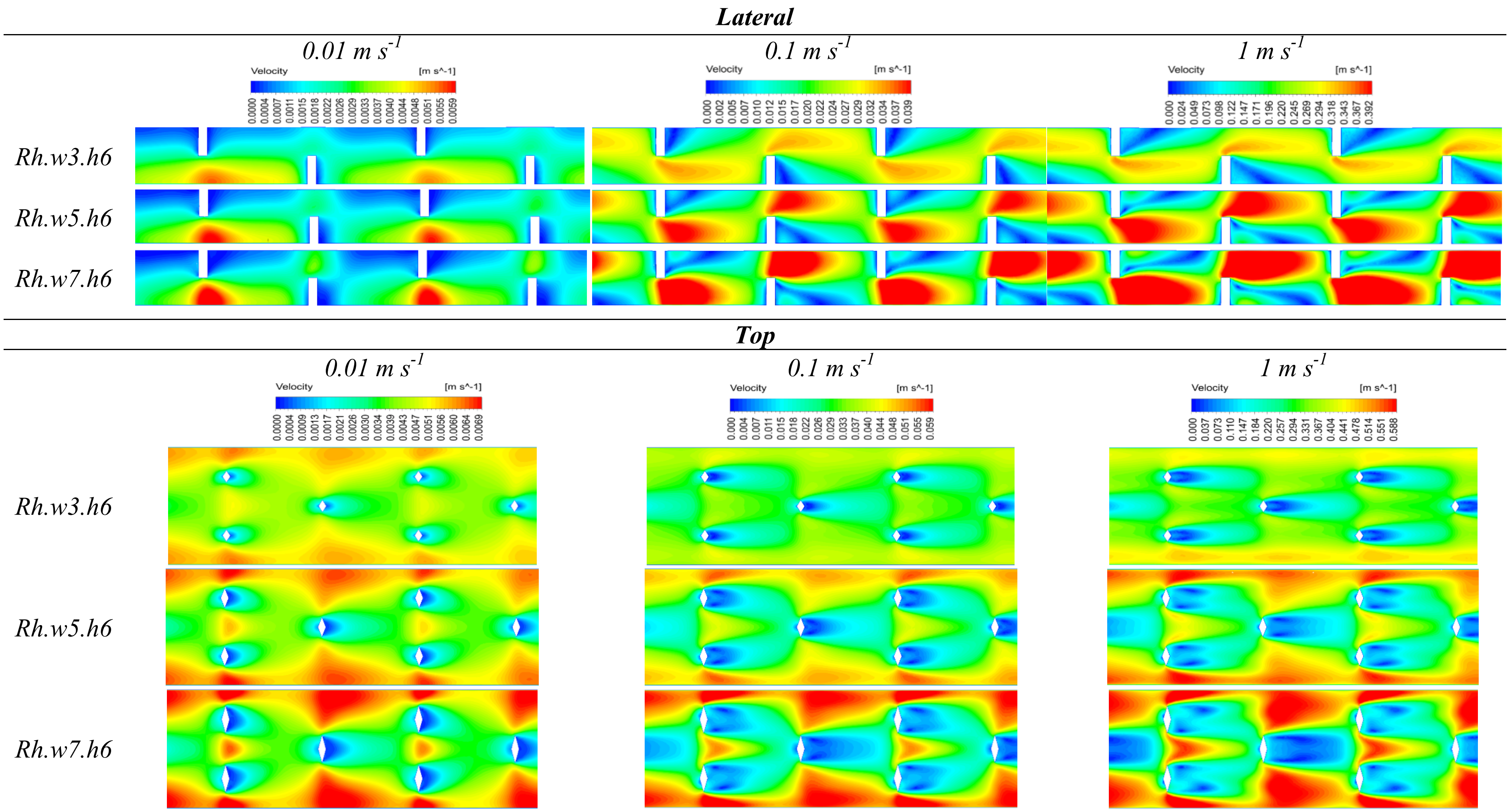

Figure 6. Comparison of the convective heat transfer coefficient in function of the Reynolds number between rhombus vortex generators with a width of 7 mm and three different wing height (panel **a**); ratio between *j factor* obtained from the three different rhombus wing heights and the one related to PFHE geometry (panel **b**).

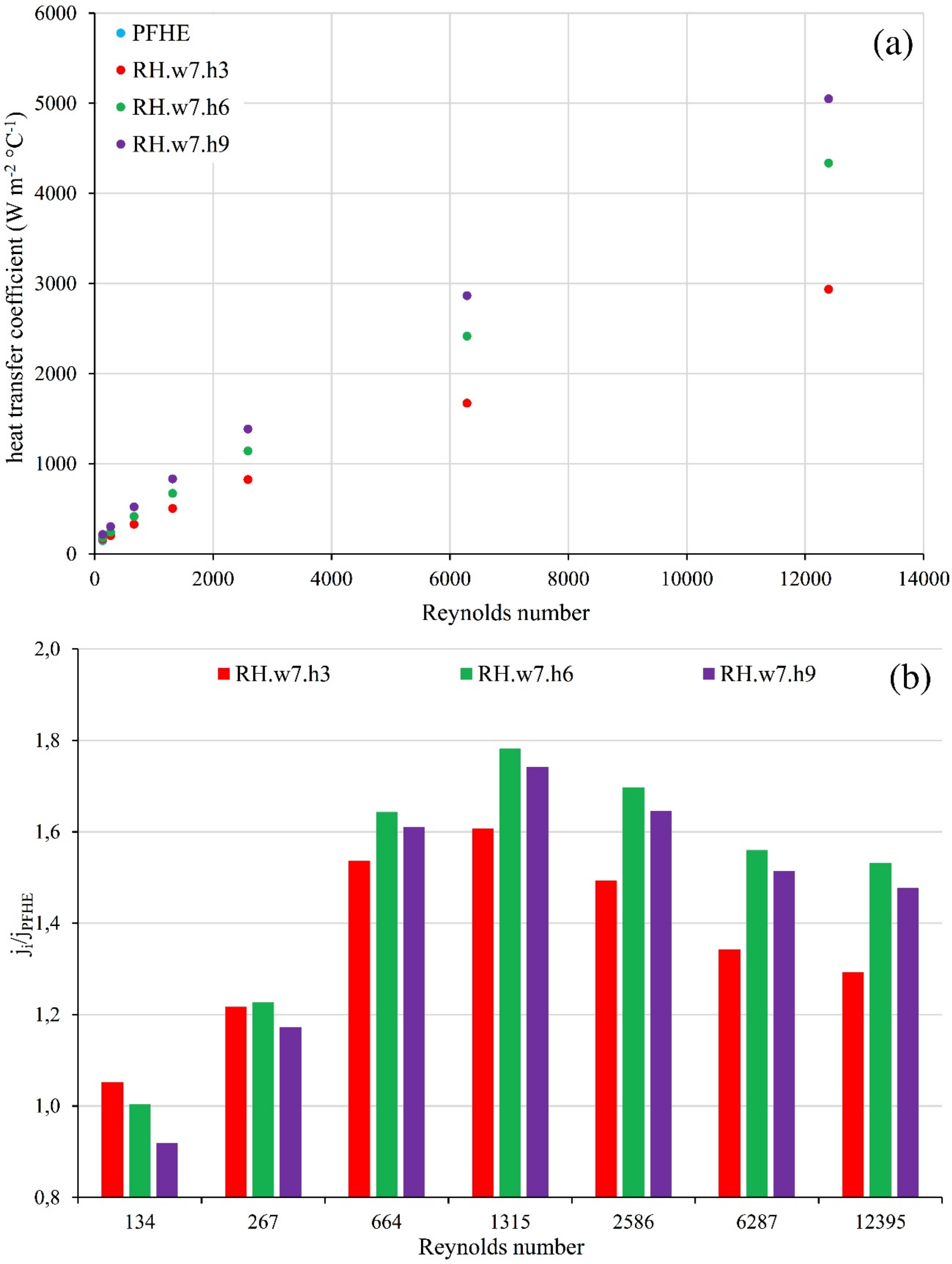

Figure 7. Local velocity profile of the flow inside heat exchanger, at three different flow velocity for the three different wings height for the rhombus geometry. The reported pictures, parallel to the fluid flow, was from a lateral point of view and from a top point of view.

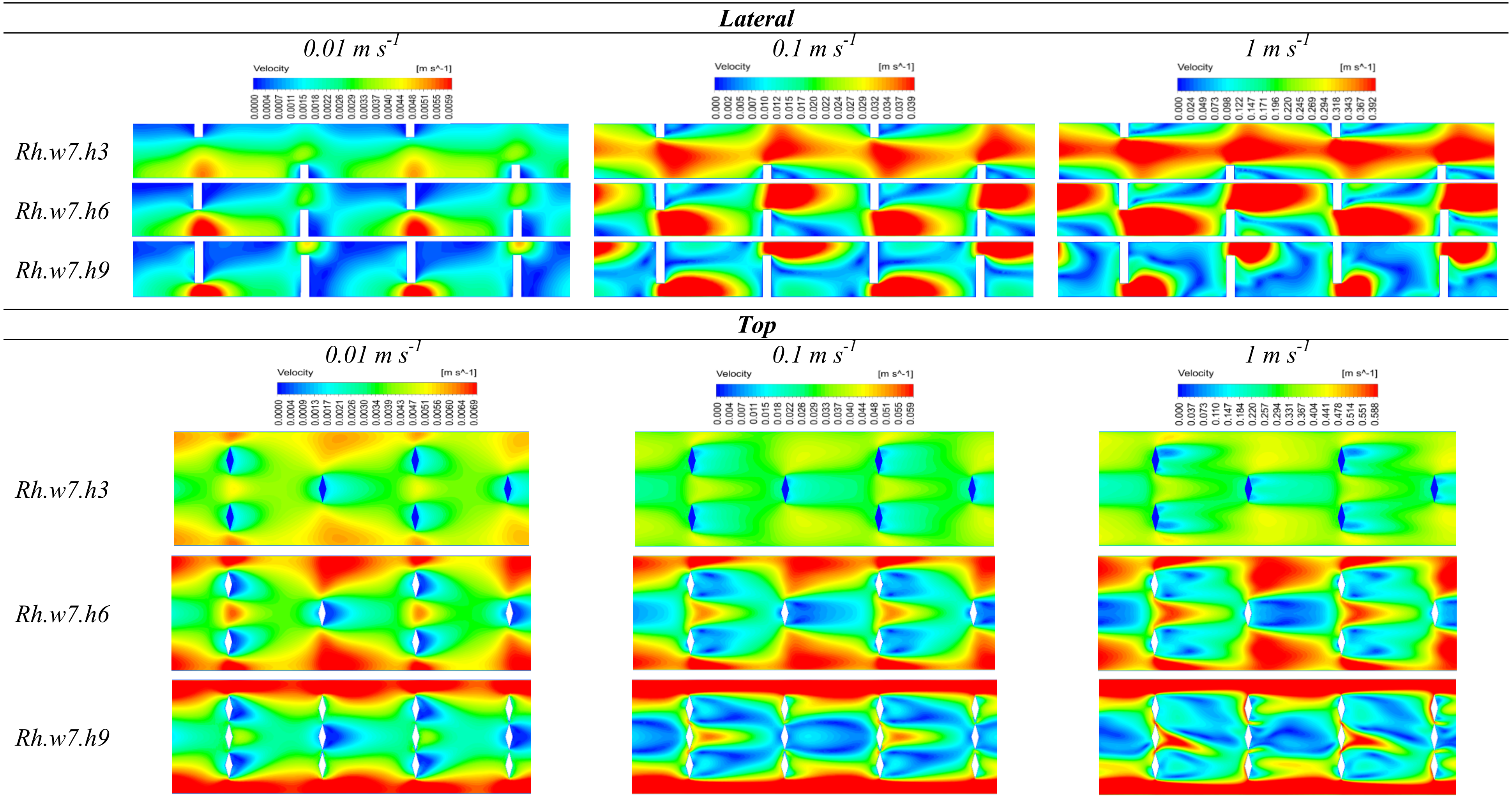

Figure 8. Comparison of the pressure drop in function of the Reynolds number between vortex generators with different shape (panel **a**) and the ratio between *f factor* in function of the Reynolds number of the three geometries and the one related to PFHE geometry (panel **b**).

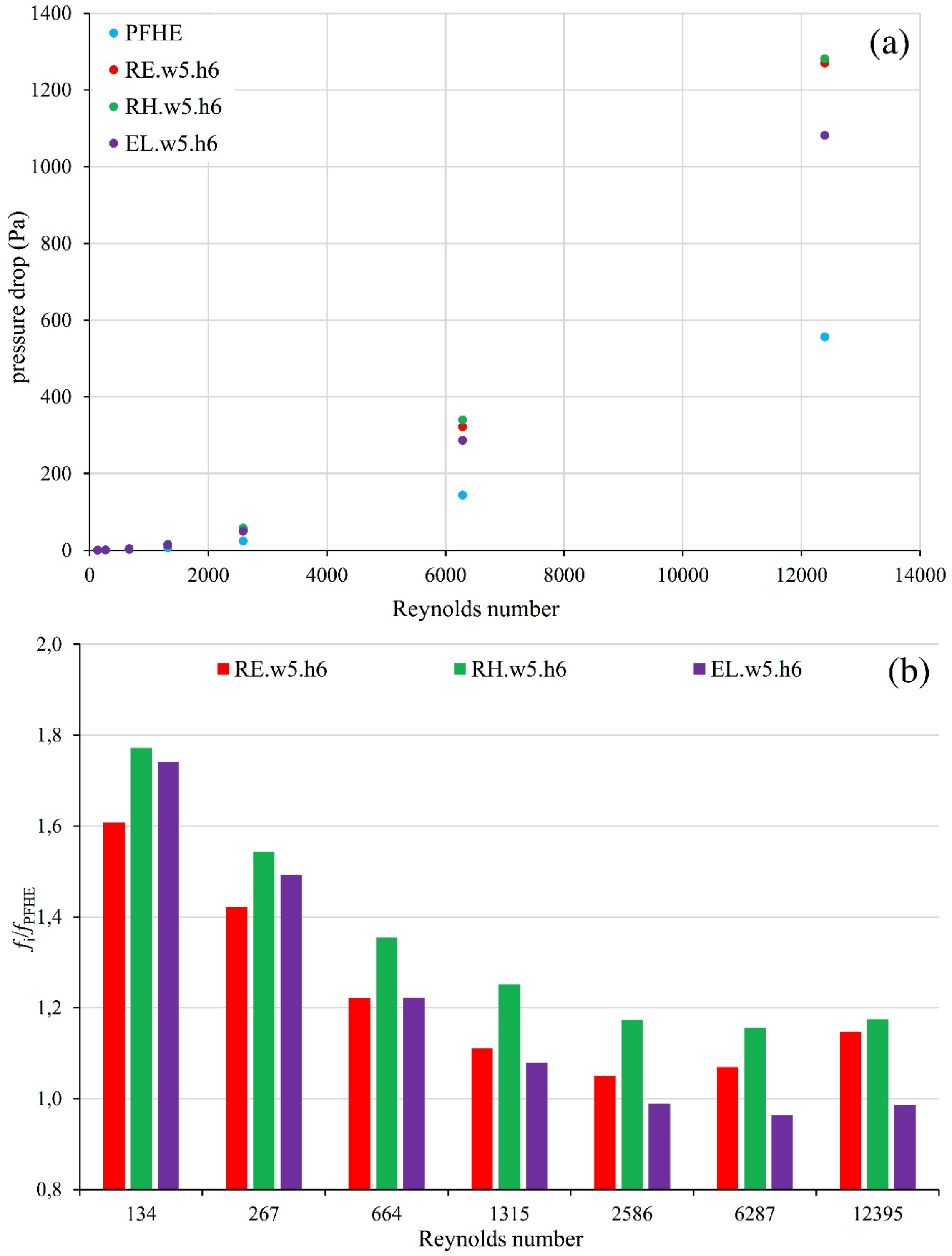

Figure 9. Comparison of the pressure drop in function of the Reynolds number between elliptical vortex generators with three different wing width (panel **a**) and the ratio between *f factor* obtained from the three different rhombus wing width and the one related to PFHE geometry (panel **b**).

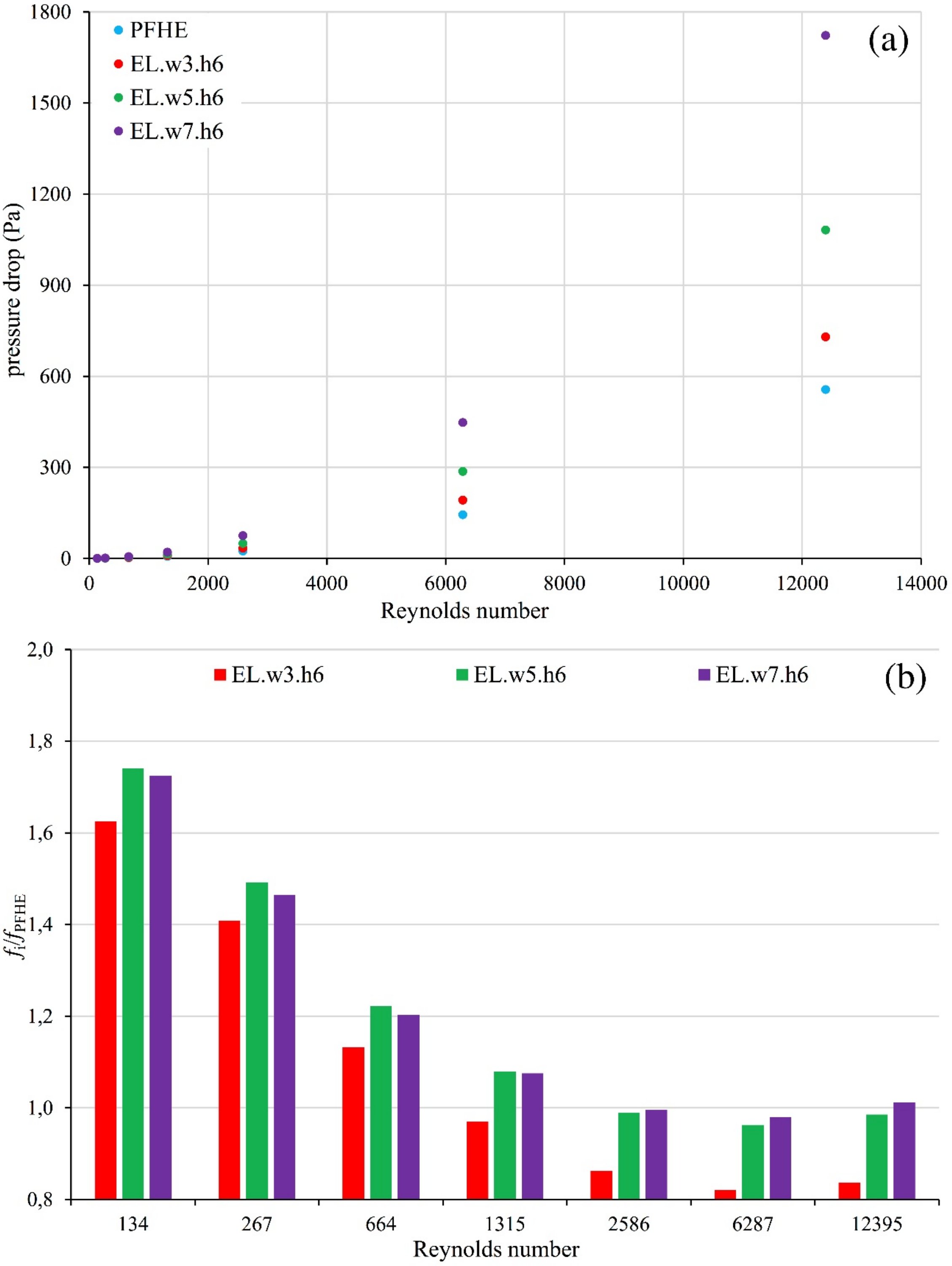

Figure 10. Local velocity profile of the flow inside heat exchanger, at three different flow velocity for the three different wings width for the elliptical geometry. The reported pictures, parallel to the fluid flow, was from a lateral point of view and from a top point of view.

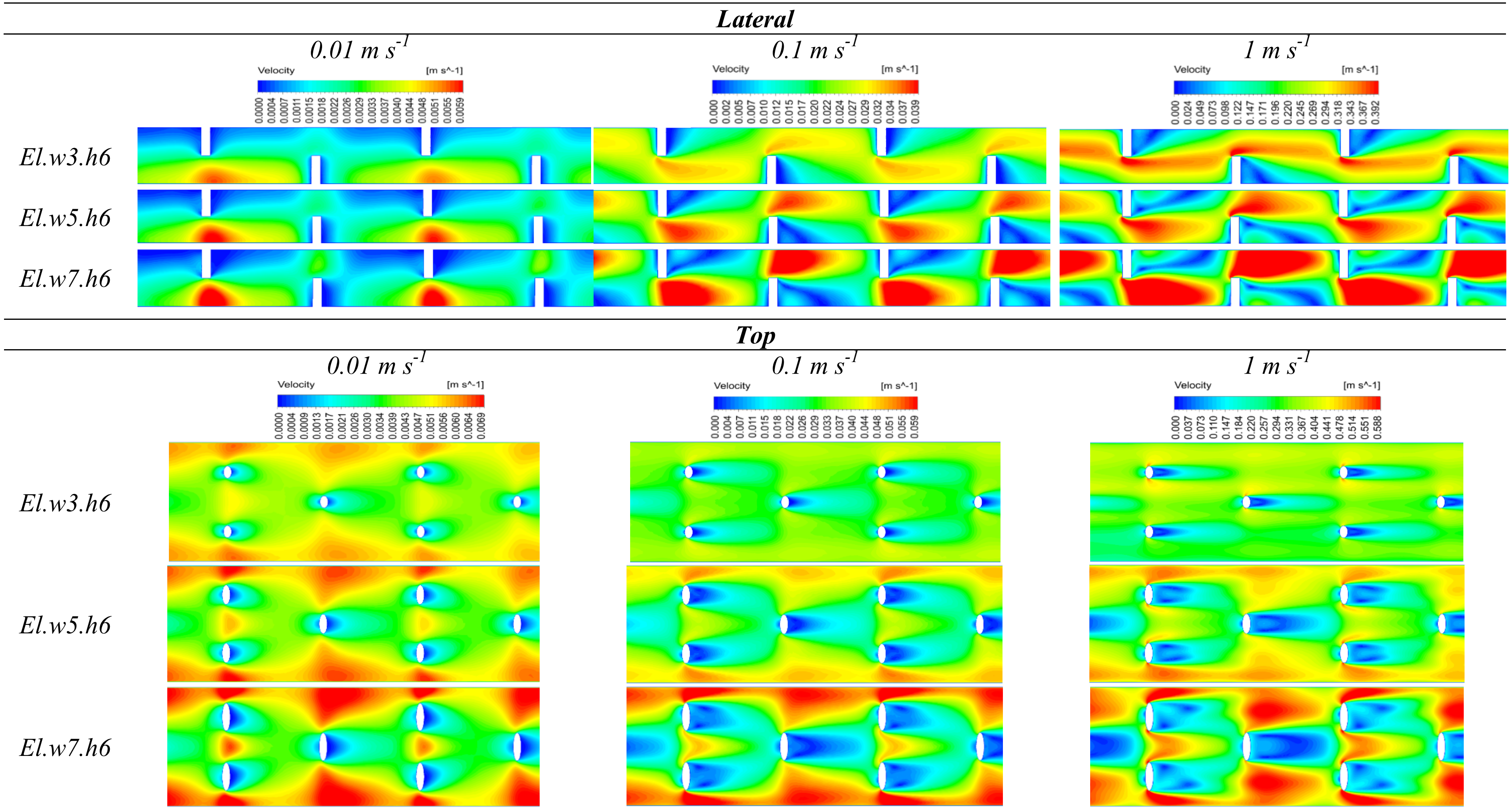

Figure 11. Comparison of the convective heat transfer coefficient in function of the Reynolds number between elliptical vortex generators with a width of 3 mm and three different wing height (panel **a**); ratio between *f factor* obtained from the three different elliptical wing heights and the one related to PFHE geometry (panel **b**).

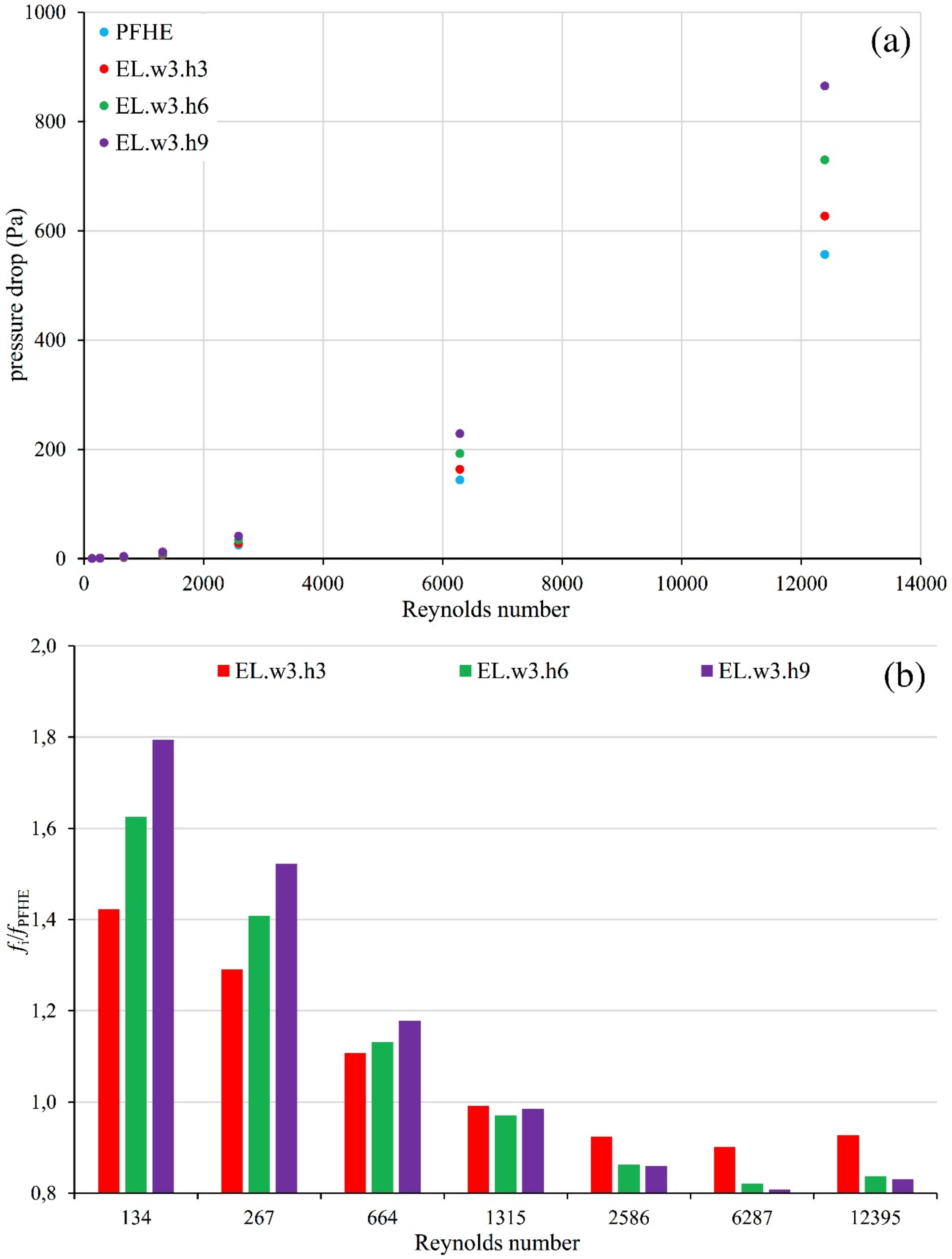

Figure 12. Local velocity profile of the flow inside heat exchanger, at three different flow velocity for the three different wings height for the elliptical geometry. The reported pictures, parallel to the fluid flow, was from a lateral point of view and from a top point of view.

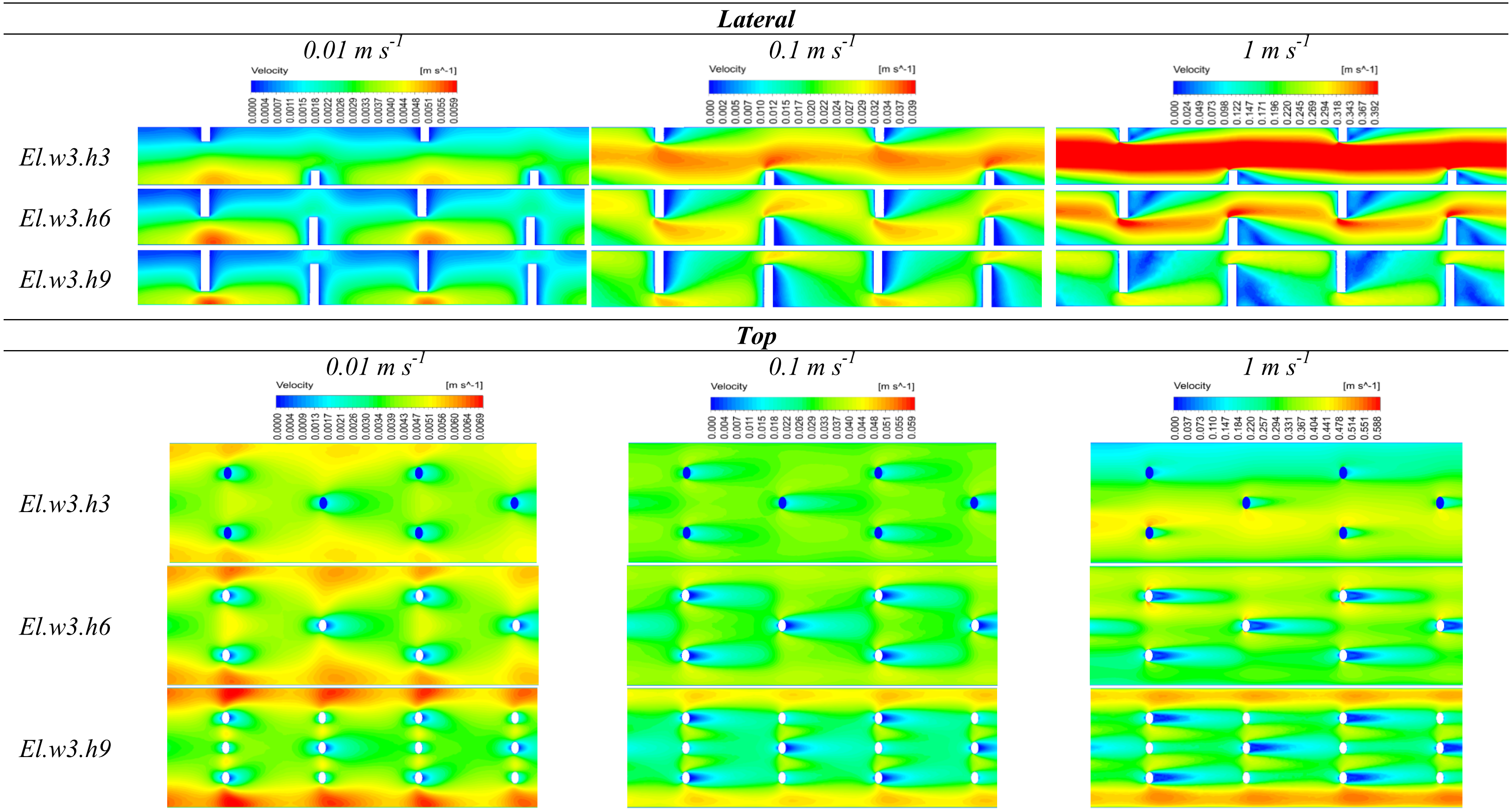

Short educational CV

- 2002-2007: Technical high school diploma (100/100), I.T.A.S. M.A. Bentegodi, Buttapietra (VR), Italy.
- 2007-2011: Bachelor's degree in Food Science and Technology (110/110 summa cum laude), University of Parma, Italy.
- 2011-2013: Master's degree in Food Science and Technology (110/110 summa cum laude), University of Parma, Italy
- 2014-2016: Ph.D. in Food Science, University of Parma, Italy.

List of publications

Scientific published papers

- Matteo Cordioli, Massimiliano Rinaldi, Gabriele Copelli, Paolo Casoli & Davide Barbanti. 2015. Computational fluid dynamics (CFD) modelling and experimental validation of thermal processing of canned fruit salad in glass jar. *Journal of Food Engineering. 62-69 (150).* DOI: 10.1016/j.jfoodeng.2014.11.003. IF (2015): 3,199
- Matteo Cordioli, Massimiliano Rinaldi & Davide Barbanti. 2016. Investigation and modelling of natural convection and conduction heat exchange: study on food systems with modified starch by means of computational fluid dynamics. *International Journal of Food Science and Technology. 854-864 (51).* DOI: 10.1111/ijfs.13039. IF (2015): 1,504
- Massimiliano Rinaldi, Matteo Cordioli, Davide Barbanti & Marco Dall'Aglio. 2016. Study and optimization of CO2 sparger for carbonated beverages and beer by means of CFD modelling. *International Journal of Food Engineering*. DOI: 10.1515/ijfe-2016-0083. IF (2015): 0,712
- Massimiliano Rinaldi, Matteo Cordioli & Davide Barbanti. 2016. Investigation on temperature fields in industrial chilling of pork legs for PDO Parma ham production and coupled temperature/microbial growth simulation. *Journal of Food Science & Technology*. DOI: 10.1007/s13197-016-2397-3. IF (2015): 1,241
- Massimiliano Rinaldi, Matteo Cordioli & Davide Barbanti. 2016. Pomegranate: Production, Products and Processing. Chapter in *Pomegranate: chemistry, processing and health benefits*. Chapter 3 (pages 57-74). ISBN: 978-1-63485-687-4

Papers under review (on 7/12/2016)

- Matteo Cordioli, Massimiliano Rinaldi, Davide Barbanti & Germano Mucchetti. 2016. Development and validation of CFD models on thermal treatment on milk whey proteins dispersion in static and continuous process condition. Sent 03/08/2016. *Journal of Food Engineering*. IF (2015): 3,199
- Marcello Alinovi, Matteo Cordioli, Salvatore Francolino, Francesco Locci, Roberta Ghiglietti, Flavio Tidona, Germano Mucchetti, Giorgio Giraffa. 2016. Effect of different clotting enzymes on textural and rheological properties of Crescenza cheese during refrigerated shelf-life. Sent 09/11/2016. *Journal of Dairy Science.* IF (2015): 2,408

Conferences contribution

- Davide Barbanti, Matteo Cordioli, Massimiliano Rinaldi & Alessandro Pugliese. 2015. Recovery and drying of manna exudates from Sicilian *Fraxinus excelsior L*. POSTER. 12th International Congress on Engineering and Food (ICEF12). Québec City Convention Centre, Québec City | June 14-18, 2015.
- Massimiliano Rinaldi, Matteo Cordioli, Davide Barbanti & Giampaolo Betta. 2015. Design and optimization of a heat pump dryer for apple slices. POSTER. 12th International Congress on Engineering and Food (ICEF12). Québec City Convention Centre, Québec City | June 14-18, 2015.
- Matteo Cordioli, Massimiliano Rinaldi, Davide Barbanti & Alessandro Pugliese. 2015. The carbon footprint of pasteurization step in canned fruit salad process: CO_2 quantification through mathematical model. POSTER. 12th International Congress on Engineering and Food (ICEF12). Québec City Convention Centre, Québec City | June 14-18, 2015.
- Massimiliano Rinaldi, Matteo Cordioli, Davide Barbanti & Marco Dall’Aglio. Study and optimization of a CO_2 sparger for carbonated beverages and beer by means of CFD modelling. POSTER. The International Food Operations & Processing Simulation Workshop. Bergeggi, Italy | September 21-23 2015.
- Massimiliano Rinaldi, Maria Paciulli, Matteo Cordioli, Davide Barbanti & Germano Mucchetti. Characterization of whey protein gel with near-infrared spectroscopy. POSTER. The Food Factor. Barcellona, Spain | November 2-4 2016.